KYOTO UNIVERSITY

DOCTORAL THESIS

Study on the temporal and spatial variations of total OH reactivity and ozone production sensitivity in Tsukuba, Yokohama, and Kyoto in Japan

---

Author:
Jiaru LI

Supervisor:
Prof. Yoshizumi KAJII

Graduate School of Global Environmental Studies

Global Environmental Studies

2021

Study on the temporal and spatial variations of total OH reactivity and ozone production sensitivity in Tsukuba, Yokohama, and Kyoto in Japan

By

Jiaru Li

A dissertation submitted in the requirements for the degree of

Doctor of Philosophy

in

Global Environmental Studies

in the

Graduate School of Global Environmental Studies

of the

Kyoto University, Japan

Committee in Charge:

Professor Dr. Yoshizumi Kajii, Chair
Dr. Yosuke Sakamoto
Dr. Christa Fittschen
Dr. Kayo Ueda
Dr. Shuhei Tanaka

Summer 2021

To my grandpa

Abstract

Exposure to air pollution is one of the top-ranking human health risk factors globally. It is well established that HO_x radicals, which including hydroxyl radicals (OH) and peroxy radicals (HO_2 and RO_2), are propagated from the photochemical process and substantially change the composition of the air. HO_x cycle is of paramount importance for atmospheric reactions and photochemical process, which may cause environmental problems such as the formation of ozone and secondary organic aerosol. Specifically, OH radicals is considered as one of the most important species that dominates reactive short-lived trace species especially in the degradation of organic compounds. Although, more than hundreds of reactants make it impossible to detect all reaction pathways. OH reactivity measurement is used to diagnose air quality and explore unknown trace species in many existing field observations. At present we can detect the total reactivity of HO_x radicals via several techniques. On the other hand, it is not yet certain about the effects of the HO_x cycle that driving photochemical oxidant generation process, especially, the mechanism of ozone production.

This research focused on three intensive field campaigns in contrasting urban sites in Japan. Total OH reactivity and trace species were detected concurrently to diagnose the air quality. Unknown trace species were quantified from the interpretation of total OH reactivity, and their influence on ozone production potential and ozone production regime was estimated. For the first time, heterogeneous effects on ozone production potential was assessed quantitatively and NO (NO_x) concentration was found to be the key factor. Aerosol uptake effects also indicated a shift on the regime of ozone production, pointing to the significance of heterogeneous effects when considering ozone production mechanism and for mitigation policy.

Three intensive field studies were conducted in contrasting locations in Tsukuba (2017), Yokohama (2019), and Kyoto (2020) in Japan during summer. Total OH reactivity was detected by laser pump and laser induced fluorescence spectroscopy. Calculated OH reactivity estimated from the chemical analysis of concurrent trace species helps to quantify the missing OH reactivity, and the later can unveil the existence of unknown OH-reactants in different places quantitatively. Ozone production analysis was conducted based on the results from three field studies. As the main by-products of HO_x cycle, ozone's relationship with its precursors (VOCs

and NO_x) and HO_x radicals was reported to be non-linear and complex. Mitigation of main precursors in the air cannot bring same reduction of ozone. Among the three campaigns, high level of NO_x was found in the coastal industrial area Yokohama, which, as a result, constrained the oxidative capacity in the air. The highest level of ozone production rate was assessed in Tsukuba, especially when polluted air masses transported from Tokyo and surrounding urban areas. Missing OH reactivity exhibited critical contributions to total OH reactivity in Tsukuba and Kyoto, which indicated a moderate corresponding relationship with OVOCs, and BVOCs, respectively. Missing OH reactivity could enhance the ozone production potential to a factor as high as 4 in Kyoto and 3 in Tsukuba. The aerosol uptake effects on HO_2 radicals was also estimated for ozone production potential and ozone regime assessment. The uptake coefficient was adapted from either concurrently measured HO_2 reactivity or literature value when the real-time value is not available. Depends on the location and period, aerosol effects also varied in relation to ozone production. Simply put, ozone production in Yokohama is least affected by particles because of high NO_x level and as such, HO_x cycle reactions were quickly terminated. Ozone production potential in Tsukuba and Kyoto was declined when considering aerosol uptake effects. Generally, all locations pertained to VOC-sensitive regime with some exceptions of NO_x-limited regime appeared in Tsukuba and Kyoto. Interestingly, missing OH reactivity and aerosol uptake effects can alter VOC-limited conditions into NO_x-limited in Tsukuba and Kyoto some time. The mechanism triggered for such alternation might be considerable to determine ozone production and mitigation policy.

Keywords: Total OH reactivity, field study, missing OH reactivity, LP-LIF, Ozone production sensitivity

Contents

List of Figures

List of Tables

Chapter 1

Introduction

The past several decades have seen tremendous development in urbanization and industrialization. As a consequence, we are facing with severe unprecedented environmental deterioration problems. Air pollution problem has become one of the most harmful and mortal threats to us since the mid of last century when "the great smog of London" and "the Los Angles photochemical smog" events occured. Since then, a number of air pollution episodes have been quite dramatic and caused over thousands of deaths worldwide [Finlayson-Pitts and Pitts Jr, 1999]. On the other hand, the science of atmospheric chemistry has forwarded greatly at the same time. Ozone depletion in the stratosphere in the late 20 century and its later recovery is a good example of how atmospheric science helps to solve environmental problems. Although a possible super recovery of ozone might be on the way because of anthropogenic climate change, which leads to a cooler stratosphere and accelerates ozone production. However, [Maliniemi et al., 2021] also reported such super recovery might get cancelled in the Antarctic stratosphere due to the excess of NO_x formed in the mesosphere and thermosphere. Focus in Japan, photochemical smog occurred in Tokyo in 1970, and after that people over Japan and the society suffered from the acid rain for some time. Although soon after the government published environmental regulations to control emissions from industrial, traffic, and other human activities. The modern society still faces in great challenges of environment protection. Especially in recent years, the increase of oxidants (mainly ozone and nitrogen dioxide) have risen public attention even under stringent reduction policy of primary emissions. Such oxidation process is closely related to radicals-involving reactions, which play a critical role in the secondary pollutants generation.

1.1 Science and challenges in Atmospheric Environment: HO_x cycle

Atmospheric photochemical process generates a series of radicals and these radicals substantially alter the air composition in the atmosphere [Monks, 2005]. Hydroxyl radicals (OH), as first discovered in 1934 by [Haber and Weiss, 1934] in a Fenton reaction as known today, OH was found to be one of the most important radicals in the air, can dominate the degradation of other trace species and convert per se into other radicals. OH radicals propagate hydroperoxy radicals (HO_2) after reacting with CO or formaldehyde, or produce various peroxy radicals (RO_2) when reacting with volatile organic compounds [Atkinson, 1986]. OH, HO_2, and RO_2 make up a circling reaction because HO_2 and RO_2 oxidize NO and eventually re-form OH to some extent (Figure 1.1).

The schematic diagram is displayed in Figure 1.1, in which the production, decomposition pathways and chain propagation in detail are provided. Section 1.2 and Section 1.3 will introduce OH and HO_2/RO_2 radicals from their source and sink in detail. In Figure 1.1, secondary production processes in black recount the whole HO_x cycle. Blue arrows indicate the primary source and red means sink routine removed from HO_x cycle. The cyclic reaction in black won't change the total amount of radicals but only transform the proportion of each radical group. Because the forward of HO_x cycle reaction produce NO_2, which can be photolyzed to generate ozone. Therefore, HO_x cycle can maintain the generation of oxidants.

$$NO_2 + h\nu\,(\lambda < 398\,\text{nm}) \longrightarrow O(^3P) + NO \tag{1.1}$$

$$O(^3P) + O_2 + [M] \longrightarrow O_3 + [M] \tag{1.2}$$

The photolysis of NO_2 is displayed in (1.1) and (1.2), which is pretty reactive because NO_2 can absorb visible light. In the case with wavelength below 398 nm under room temperature, the photolysis occurs with nearly 100% yield. Between 398 nm and 415 nm, NO_2 partially photodissociates because the internal energy and collisions contribute to the process, but the quantum yield declines quickly over this range and falls down to 0.1 with wavelength above 410 nm. Figure 1.2 shows the experimental results (hollow circle), calculated quan-

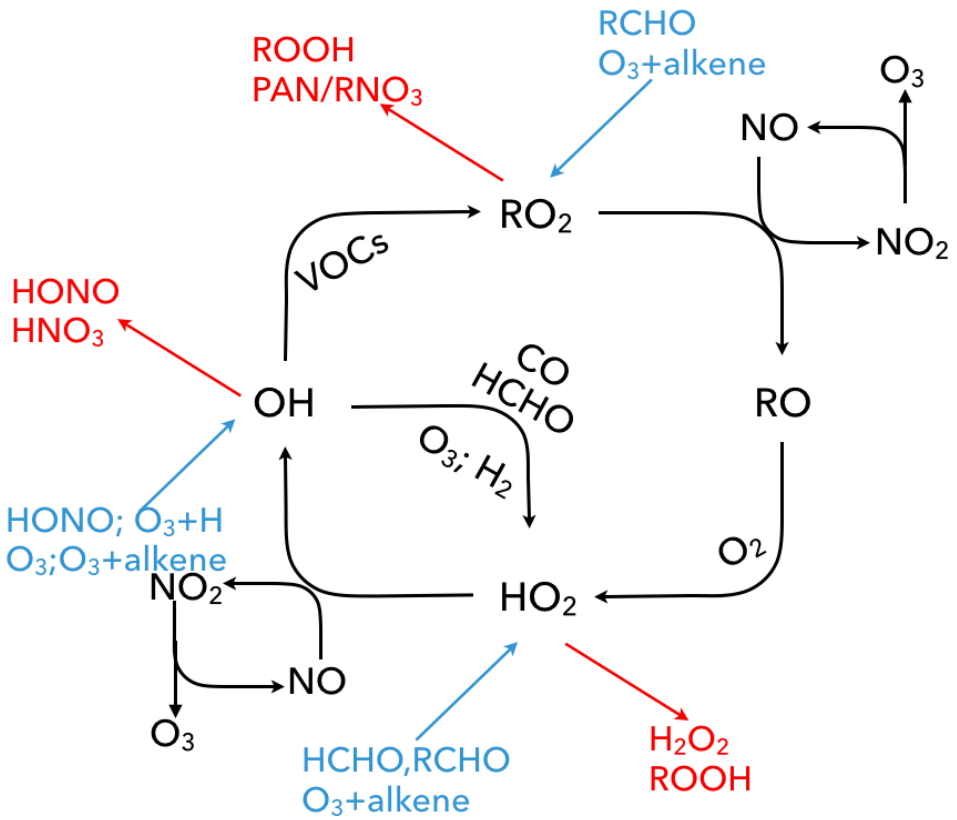

Figure 1.1: Schematic diagram of HO_x cycle.

tum yields from internal energy (dotted line) and collisions (dashed line), and the sum of two calculations (solid line) (experimental results adapted from [Roehl et al., 1994]; figure from [Finlayson-Pitts and Pitts Jr, 1999]). Note that the reverse of (1.1) and (1.2) destroys ozone and regenerates NO_2.

The occurrence of HO_2 cyclic reactions lead to the accumulation of ozone. In addition, peroxy radicals are able to form aerosol either directly or through heterogenous reactions (even multiphase reactions). The radical initiated oxidation reactions play a central role for low volatility products, which assembles secondary organic aerosol (SOA) [Kroll and Seinfeld, 2008]. On the other hand, ozonolysis also contributes to SOA formation, such as alkenes reaction with ozone. This reaction pathway forms a carbonyl and an energetically excited carbonyl oxide (also called as "Criegee Intermediate"), products from such a channel also make SOA importantly [Yu et al., 1999]. It's also notable to mention that peroxy radicals self-reaction is of importance to form low volatility products, especially among these "big radicals" with larger carbon number.

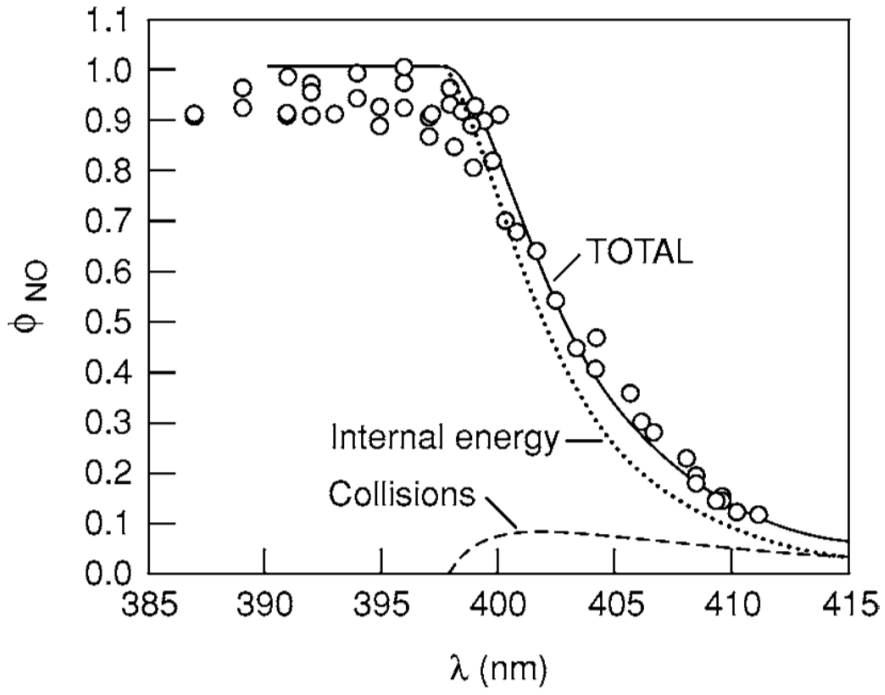

Figure 1.2: Quantum yields for NO production in the photodissociation of NO_2 at room temperature (298 K) as a function of wavelength (adapted from [Roehl et al., 1994]) [Finlayson-Pitts and Pitts Jr, 1999].

1.2 Foci of HO_x cycle: source, fate, and sink of OH radicals

As the initiating point of HO_x cycle, OH radicals are of paramount importance in the atmosphere. They react with countless trace species, further boost oxidizing processes, and control the degradation of most VOCs in the air, which, as a result, changes the air composition. Although OH concentration (varies from several to dozens of 10^6 molecule cm^{-3}) and lifetime (less than 1 s) can be disregarded in the air, its role should be underscored in the field of atmospheric chemistry. This section will tell the story of OH radicals from three viewpoints including source, fate, and termination.

1.2.1 OH sources

The major source of OH radicals in remote areas comes from ozone photolysis, the products subsequently react with water vapor to form OH (1.3). The detail of ozone photolysis will be introduced in Section 1.5.

$$O_3 + h\nu + H_2O \longrightarrow 2\,OH + O_2 \tag{1.3}$$

Moreover, photolysis of HONO (1.4), and ozonolysis of alkene (1.5) are alternative important

channels to primary OH production. HONO's photolysis happens with long wavelength range, which is crucial during the morning. Although (1.4) is a reversible reaction, in which OH react with NO forms HONO. This backward reaction is not the major source of HONO. HONO sources in the air come from the heterogenous reaction of NO with HNO_3 adsorbed on surface, this is a dominate channel in polluted urban area [Saliba et al., 2000]. In addition, surface hydrolysis of NO_2 might be important in a humid condition with high NO_2 concentration [Svensson et al., 1987].

$$\mathrm{HONO} + \mathrm{h}\nu \longrightarrow \mathrm{OH} + \mathrm{NO} \tag{1.4}$$

$$\mathrm{alkene} + \mathrm{O_3} \longrightarrow ... \longrightarrow \mathrm{OH} + \mathrm{products} \tag{1.5}$$

The contribution of aforementioned three primary sources for OH has been reported to be HONO photolysis (62.5%), ozone photolysis (33.3%), and ozonolysis (4.2%) in a case study conducted in a suburban area [Yang et al., 2021]. (1.6) shows a minor production channel of OH, by photolysis of H_2O_2. In (1.7), anther quite important reaction channel of OH source was expressed with reported rate constant of 2.84×10^{-11} $cm^3molecule^{-1}s^{-1}$ under the room temperature [Seeley et al., 1993].

$$\mathrm{H_2O_2} + \mathrm{h}\nu\,(\lambda < 300\,\mathrm{nm}) \longrightarrow 2\,\mathrm{OH} \tag{1.6}$$

$$\mathrm{O_3} + \mathrm{H} \longrightarrow \mathrm{OH} + \mathrm{O_2} \tag{1.7}$$

Except these primary source of OH, HO_x cycle also produces OH via the reaction of HO_2 with NO (1.8). OH derived from radical propagation is concluded as secondary production. Such secondary production plays a vital role in the presence of NO concentrations above 10 ppbv. Those HO_2 radicals should be generated from HO_x cycle or thermal decomposition of PAN and peroxynitric acid (HO_2NO_2) [Finlayson-Pitts and Pitts Jr, 1999].

$$\mathrm{HO_2} + \mathrm{NO} \longrightarrow \mathrm{OH} + \mathrm{NO_2} \tag{1.8}$$

Although OH is mainly produced during the daylight hours, nighttime reactions of NO_3 also form OH as showed in (1.9). The recommended rate constant is 4×10^{-12} cm^3 $molecule^{-1}$

s^{-1} [Brown and Stutz, 2012]. The reaction of NO_3 with H_2CO also forms OH but with a fairly slow rate constant (5.5×10^{-16} cm^3 $molecule^{-1}$ s^{-1}) [Atkinson et al., 2004]. NO_3 radical is an important intermediate in the nighttime chemistry and quite unusual because it absorbs the red region (620-670 nm) of the visible light spectrum.

$$NO_3 + HO_2 \longrightarrow NO_2 + OH + O_2 \tag{1.9}$$

It was also reported by several research groups that there might be an unknown OH source under low NO condition during the daytime when solar radiation is available. Researchers found it could be compensated by an extra amount of X_{NO}, which behaves like NO, and convert either HO_2 or RO_2 into OH radicals [Lu et al., 2013]; [Yang et al., 2021]. By using around 0.1-1 ppbv of X_{NO}, the modeled OH production rate could be reconciled well with observed production rate. Although X remains to be unknown, there is a high possibility that it is closely related to photolysis procedure.

1.2.2 OH fate; a superstar in the air

OH radicals, as the most reactive species in the air, deciding air compositions in both the troposphere and the stratosphere. Because OH radicals play such a critical role in oxidizing countless trace species, which resulted in air problems under complex mechanism. The description of OH fate will be stated in four aspects from different perspectives.

Firstly, OH radicals initiated oxidants production via HO_x cyclic reactions. As depicted in Figure 1.1, OH converts CO/H_2CO and VOCs into HO_2 and RO_2 radicals, respectively. Those products oxidize NO and produce NO_2. Such reaction processes under the solar radiation increase the oxidative capacity of the air directly via (1.1) and (1.2). This reaction mechanism is responsible for most of the hazardous smog happened in urban areas.

Secondly, the function of OH in atmosphere-biosphere interaction has to be considered. OH is able to oxidize dimethyl sulfate (DMS, CH_3SCH_3), which is emitted from the oceanic biosphere. Their products will cause acid deposition.

$$CH_3SCH_3 + OH \longrightarrow ... \longrightarrow SO_2 + \text{products} \tag{1.10}$$

The emergence of acid deposition, either initiated from sulfur dioxide or nitrogen dioxide, are also forwarded by OH radicals. The acid deposition can be divided into wet deposition and dry deposition. The former including rain, snow, fog, and other precipitation form while the dry deposition refers to the process whereby particles fall down to the ground and get removed from the atmosphere. Also, (1.14) is the most significant termination channel for OH radicals, this will be introduced later.

$$OH + SO_2 + [M] \longrightarrow HSO_3 + [M] \tag{1.11}$$

$$HSO_3 + O_2 \longrightarrow SO_3 + HO_2 \tag{1.12}$$

$$SO_3 + H_2O + [M] \longrightarrow H_2SO_4 + [M] \tag{1.13}$$

$$OH + NO_2 + [M] \longrightarrow HNO_3 + [M] \tag{1.14}$$

The third aspect, let's look up into the stratosphere. Chlorofluorocarbons (CFCs) are quite stable and do not react with OH in the troposphere. Therefore, CFCs are easily to get dispersed to the upper layer. Researchers have found the link of CFCs in the stratosphere with ozone depletion. After photo-dissociation of CFCs, halogen radicals are produced and act as catalyst to consume ozone continuously in the stratosphere.

$$CFC + h\nu \longrightarrow Cl + \text{products} \tag{1.15}$$

$$Cl + O_3 \longrightarrow ClO + O_2 \tag{1.16}$$

$$ClO + O_3 \longrightarrow Cl + 2\,O_2 \tag{1.17}$$

The net reaction of (1.16) and (1.17) leads to decomposition of O_3. As a consequence, ozone in the stratosphere will be consumed and more harmful ultraviolet light can arrive the earth surface. To avoid such ozone depletion, a group of less stable compounds is synthesized to replace CFCs with an extra hydro-atom: hydrochlorofluorocarbons (HCFCs). HCFCs can react with OH in the lower atmosphere, and break down before reaching the ozone layer. The lifetime of HCFCs in the troposphere would be importantly depends on their destruction rates. However, HCFCs contains chlorine which can destruct the stratospheric ozone while HCFCs

have less ozone depletion potential than CFCs. In addition, HCFCs also act as greenhouse gases (GHGs) and cause climate change. Considering both CFCs and HCFCs are ozone-depleting substances (ODSs), hydrofluorocarbons (HFCs) are much safer, which do not hold chlorine and do not damage stratospheric ozone. However, HFCs are extremely powerful GHGs that accelerates climate change. It was reported that HFCs can be hundreds to thousands of times more powerful than carbon dioxide at warming the Earth surface [EPA, 2021]. An international agreement-Kigali Amendment to the Montreal Protocol (the AIM Act's phase down in U.S.EPA) ratified by over 115 countries aim to phase down HFCs, expecting to avoid up to 0.5 °C of global warming by 2100 [Andersen et al., 2018].

$$\mathrm{HFC} + \mathrm{OH} \longrightarrow \mathrm{products} \tag{1.18}$$

$$\mathrm{HCFC} + \mathrm{OH} \longrightarrow \mathrm{products} \tag{1.19}$$

The fourth point is about OH's relationship with GHGs. The reaction of OH radicals with methane is the main termination pathway for methane (1.20). In addition, HCFCs are also recognized as GHGs, and contribute to climate change. By taking reactions with these GHGs, OH radicals can convert or oxidize these GHGs, and make influences to climate change.

$$\mathrm{OH} + \mathrm{CH_4} \longrightarrow \mathrm{H_2O} + \mathrm{CH_3} \tag{1.20}$$

(The four perspectives are firstly adapted from [Kanaya, 1997].)

1.2.3 OH termination

OH is super reactive and gets a tendency to abstract an H-atom when it is possible. Subsection 1.2.2 interpolates most of its reaction pathways according to their different types of influence. The current subsection will focus on the destruction channel which terminates HO_x cycle. One of the main destruction pathway come from NO_2 (1.14), this dominates most of the OH radicals in urban areas or polluted areas.

$$\mathrm{OH} + \mathrm{NO_2} + [\mathrm{M}] \longrightarrow \mathrm{HONO_2\,(nitric\,acid)} + [\mathrm{M}] \tag{1.21}$$

$$OH + NO_2 + [M] \longrightarrow HOONO\,(per-nitrous\,acid) + [M] \tag{1.22}$$

There are two product channels for OH reaction with NO_2, as displayed in (1.21) and (1.22) [Burkholder et al., 2019]. The three body association reaction (1.21) is important throughout the lower atmosphere. [M] refers to N_2 or O_2 in air. Under low pressure condition, only products in (1.21) are stable enough to act as sink of HO_x and NO_x. (1.22) is comparable in the high pressure conditions while re-dissociate rapidly under low pressure conditions such as boundary layer [Mollner et al., 2010].

The production of HONO is both termination and regeneration channels of OH in the air.

1.3 Other members in HO_x cycle: HO_2 and RO_2 radicals

Different to OH radicals in super low concentration, peroxy radicals are in two orders of magnitude higher than OH. Peroxy radicals play an important role in the formation of SOA and also fulfill HO_x cycle reactions. The sources and sinks of peroxy radicals shared several pathways in common, as Figure 1.1 shows. The current section presents the details of HO_2 and RO_2, separately, from the perspectives of their sources and sinks.

1.3.1 Sources and fate of HO_2 radicals

HO_2 source contains primary production (photolysis of H_2CO, photolysis of RCHO, and ozonolysis of alkene) and secondary production (the conversion from OH and RO_2) refer to Figure 1.1.

$$H_2CO + h\nu\,(\lambda < 330\,nm) \longrightarrow H + HCO \tag{1.23}$$

$$H + O_2 + [M] \longrightarrow HO_2 + [M] \tag{1.24}$$

$$HCO + O_2 \longrightarrow HO_2 + CO \tag{1.25}$$

Except (1.23) (1.24) and (1.25), there is another competing H_2CO photodissociation process occurs the same time (1.26), which produces H_2 and CO. Figure 1.3 shows the quantum yield in two channels under atmospheric pressure. Photolysis of H_2CO is one of the most important dominate sources for HO_x production. In several study cases, the fraction of HO_2 production via H_2CO photolysis was reported to be 49% in Mexico city [Volkamer et al., 2010], 23% in a

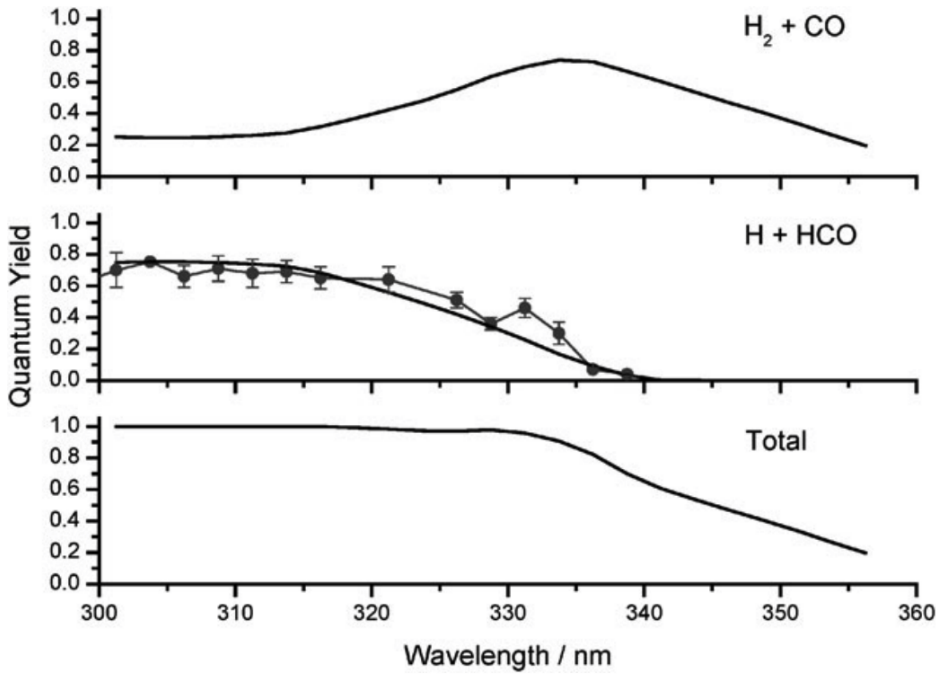

Figure 1.3: Quantum yields for two photo-decomposition channels of formaldehyde in the air under atmospheric pressure with wavelength range from 301-356 nm. Solid lines were recommended from JPL and the filled circles in the middle panel used the data from [Smith et al., 2002]. Figure from [Pope et al., 2005].

suburban area of Chengdu (2019 CHOOSE campaign) [Yang et al., 2021], and 11% in Beijing [Whalley et al., 2021].

$$H_2CO + h\nu\,(\lambda < 360\,nm) \longrightarrow H_2 + CO \tag{1.26}$$

Except H_2CO, higher aldehydes, RCHO, also form HCO from photo-decomposition procedure, as showed in (1.27), and hence generate HO_2. However, aldehydes larger than formaldehyde absorb much shorter light wavelength than formaldehyde [Finlayson-Pitts and Pitts Jr, 1999]. Moreover, the photolysis of H_2CO generates $2HO_2$ compared with higher aldehydes can only produce $1HO_2$. Therefore, photolysis of RCHO was considered as less important at same concentrations as formaldehyde.

$$RCHO + h\nu\,(\lambda < 330\,nm) \longrightarrow HCO + R \tag{1.27}$$

The ozonolysis of alkene is another important channel for HO_2 radicals production. Ozonolysis starts from the step in the reaction in which O_3 addition to the double bond and forms

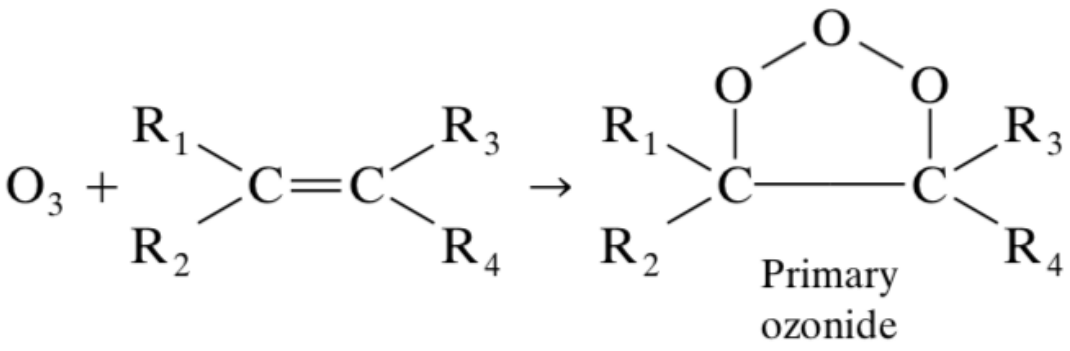

Figure 1.4: Ozonolysis of alkene; the formation of primary ozonide. Figure is adapted from [Finlayson-Pitts and Pitts Jr, 1999].

molozonide (1,2,3-trioxolane), which is also known as a primary ozonide, as exhibited in Figure 1.4. The breakdown of molozonide produce Criegee intermediates, which in the gas phase can be decomposed to radicals depends on the structure and properties of the Criegee intermediates.

HO_2 radicals can be formed from OH or RO_2 conversion through HO_x cycle reaction. Such procedures are concluded as the secondary production routine. Most of the peroxy radicals come from inter-transformation of HO_x cycle. (1.28), (1.29) (1.30), and (1.31) provide the reaction pathway of OH to generate HO_2. The rate constants of (1.28) and (1.29) are at least two orders of magnitude larger than (1.30) and (1.31). Considering the concentration of reactants and the corresponding rate constant, (1.28) is the most important pathway inside of HO_x cycle converting OH into HO_2.

$$OH + CO + O_2 \longrightarrow HO_2 + CO_2 \tag{1.28}$$

$$OH + H_2CO \longrightarrow H_2O + HCO \tag{1.29}$$

$$OH + O_3 \longrightarrow HO_2 + O_2 \tag{1.30}$$

$$OH + H_2 + O_2 \longrightarrow HO_2 + H_2O \tag{1.31}$$

RO_2 radicals also produce HO_2 radicals importantly as a result of the cyclic reactions, as showed in (1.32) and (1.33).

$$RO_2 + NO \longrightarrow RO + NO_2 \tag{1.32}$$

$$RO + O_2 \longrightarrow R_1CHO + HO_2 \tag{1.33}$$

A majority of HO_2 radicals go through the decomposition process to form OH radicals. This channel is of paramount significance especially under high NO conditions in polluted areas. However, because (1.34) reproduces OH radicals, therefore there is no net loss of radicals.

$$HO_2 + NO \longrightarrow OH + NO_2 \tag{1.34}$$

Self-reaction of peroxy radicals is another important pathway in terms of primary HO_2 loss. Briefly, self-reaction contains three type, including HO_2 reaction with HO_2, HO_2 with RO_2, and HO_2 with HO_2-H_2O complex. Their products would be hydrogen peroxides (1.35), hydroperoxides (1.36), and a water complex of HO_2 (1.37), respectively.

$$HO_2 + HO_2 \longrightarrow H_2O_2 + O_2 \tag{1.35}$$

$$HO_2 + RO_2 \longrightarrow ROOH + O_2 \tag{1.36}$$

The production pathway of hydrogen peroxide and hydroperoxide, as displayed in (1.35) and (1.36), affect tropospheric concentration of HO_x species.

$$HO_2 + H_2O \longrightarrow HO_2{-}H_2O \tag{1.37}$$

$$HO_2 + HO_2{-}H_2O \longrightarrow \text{products} \tag{1.38}$$

$$HO_2{-}H_2O + HO_2{-}H_2O \longrightarrow \text{products} \tag{1.39}$$

The self-reaction could be enhanced with the existence of water vapor, NH_3, and CH_3OH. Since the massive presence of water vapor in the air, effects of H_2O are considerable to HO_2 chemistry. It was reported that in the lower troposphere below an altitude of 2 km, more than half of HO_2 would be consumed by (1.37) and (1.38) [Kanno et al., 2006].

1.3.2 Sources and fate of RO_2 radicals

As for RO_2's source, it is quantified as primary production by photolysis of RCHO ((1.27) and subsequently (1.40)), and ozonolysis of alkene (Figure 1.4). Also, RO_2 can be produced by the conversion of OH in HO_x cycle. There is a diversity of RO_2 radicals based on its precursor's

structure, which makes it difficult to detect RO_2 radicals.

$$R + O_2 \longrightarrow RO_2 \tag{1.40}$$

$$OH + RH + O_2 \longrightarrow H_2O + RO_2 \tag{1.41}$$

Like HO_2 radicals, the fate of RO_2 could be reaction with NO and self- and cross-reactions (including with HO_2 radicals). In addition, peroxynitrate also acts as NO_2 reservoir in the air when a third-body collisional gas exist.

$$RO_2 + NO \longrightarrow RO + NO_2 \tag{1.42}$$

Products in reaction (1.42) can further react with oxygen and NO to form HO_2 radicals. This is one of the most important parts to link RO_2 with HO_2 in HO_x cycle.

$$RO_2 + R_1O_2 \longrightarrow RO + R_1O + O_2 \tag{1.43}$$

$$RO_2 + R_1O_2 \longrightarrow ROH + R_1HO + O_2 \tag{1.44}$$

There is a diversity of self- and cross-reactions among peroxy radicals, this pathway could compete with corresponding reactions with NO or HO_2 radicals. (1.43) and (1.44) indicate two of the major products which is accepted currently [Berndt et al., 2018]. The formation of dialkylperoxides is another reaction pathway while at a small yield. Although self- and cross-reactions of RO_2 haven't been understood thoroughly, researchers reckoned such a channel as an effective source for SOA [Berndt et al., 2018].

$$RO_2 + NO_2 + [M] \rightleftharpoons RO_2NO_2 + [M] \tag{1.45}$$

RO_2 radicals also react with NO_2 to form RO_2NO_2 complex in the air. The forward reaction products are quite stable in the upper air. However, since (1.45) is reversible, thermal decomposition would re-produce RO_2 and NO_2 in the troposphere [Kohno et al., 2020].

1.4 OH reactivity; characterize the air quality

OH reactivity, which equals the inverse of OH lifetime, has been investigated worldwide for more than two decades. There are two approaches to attain OH reactivity which including total OH reactivity and calculated OH reactivity. As a top-down assessment, total OH reactivity is a forthright parameter of sophisticated air pollutants and help implement effective mitigation strategies based on a rigorous interpretation of HO_x cycle. The total OH reactivity varies significantly inasmuch as observations came up with varied spatial and temporal scales. Besides, calculated OH reactivity is the sum of the products of measured trace species concentrations [x] and their corresponding bimolecular rate constants with OH radicals (1.46).

$$k'_{cal} = \Sigma k_{x-OH}[x] \tag{1.46}$$

$$k'_{miss} = k'_{total} - k'_{cal} \tag{1.47}$$

In most cases, calculated OH reactivity cannot reconcile with total OH reactivity. The remaining unexplained reactivity, namely missing OH reactivity (1.47), importantly comes from unmeasured or unknown species reactive towards OH radicals. Table 1.1 synthesizes the observation results classified under different locations. Specified in urban areas, Paris obtained the highest total OH reactivity and largest missing ratio when the air mass came from continent [Dolgorouky et al., 2012]. The field observations conducted in Tokyo, London, Beijing and Nashville got similar missing ratio about 30% though varied total OH reactivity [Kovacs et al., 2003]; [Martinez et al., 2003]; [Whalley et al., 2016]; [Yoshino et al., 2012]; [Yoshino et al., 2006]; [Williams et al., 2016]; [Whalley et al., 2021]. In contrast, Both Beijing (in summer 2013) and New York revealed moderate total OH reactivity about 20 s^{-1} with different fraction of missing OH reactivity [Ren et al., 2003a]; [Ren et al., 2003b]; [Ren et al., 2006]; [Williams et al., 2016]; [Yang et al., 2017]. In suburban areas, much higher fraction of missing OH reactivity is ubiquitous compared to urban campaigns. Although with a smaller total OH reactivity in general. Except two of those campaigns (Yufa and Wangdu) conducted in China, other reported at least over 30% of missing OH reactivity. The smallest total OH reactivity which equals 4.9 s^{-1} was claimed by [Ingham et al., 2009] in Weybourne, England. Most of the suburban campaigns obtained a total OH reactivity with a mean value around 20 s^{-1}.

Cases in forested area are quite different owing to active BVOCs in abundant. Ground-based observations in Michigan, the Rocky Mountains, and Wakayama stated the total OH reactivity below 10 s^{-1} [Di Carlo et al., 2004]; [Nakashima et al., 2014]; [Ramasamy et al., 2016]. The field study conducted in the Amazon jungle delineated quite contrasting results from dry season and wet season in which dry season acquired the highest missing OH reactivity as 62 s^{-1} out of which 79% remains to be missing. Wet season's total OH reactivity and missing fraction are close to aforementioned three campaigns'. In addition, the height above the ground also make big differences to the level of missing OH reactivity, as investigated by [Zannoni et al., 2016]. Elevated missing OH reactivity appeared under a higher height, which indicates the varied air mixing in the forested area considering the height. A study observed in the Pacific announced the smallest total OH reactivity as low as 4 s^{-1} [Mao et al., 2009]. Specified in Japan, our group have conducted a series of observations in megacity, suburb, and forest area, where missing OH reactivity was reported to be 31 $\pm$ 3.5%, leading to missing radical propagation in HO_x cycle resulting in uncertainty in evaluation of ozone formation efficiency with a factor of up to 3 [Li et al., 2020]; [Ramasamy et al., 2018]; [Ramasamy et al., 2016]; [Yoshino et al., 2012]. In those areas, sophisticated chemical reactions that accelerated under the solar radiation have been considered as essential sources for air pollutants. Alternatively, in specific coastal industrial region like Yokohama campaign, such in-situ photochemical processes might get partly-eliminated by the wind and quickly-terminated due to high NO_x. More informative paragraphs about the researches conducted in Japan will be discussed in Section 1.7, which depicting the general and challenging situations in relation to OH reactivity measurement in Japan.

1.4.1 Two ways to estimate OH reactivity

There are two types of approaches to assess OH reactivity as aforementioned total OH reactivity and calculated OH reactivity. Total OH reactivity can be obtained either by direct measurement or indirect evaluation via competition species. Direct detection techniques contain laser-pump and laser induced fluorescence (LP-LIF), total OH loss-rate measurement (TOHLM), and chemical ionization mass spectrometry (CIMS). The details of instrumentations will be introduced in Section 1.5 and Section 1.6. Indirect approach is comparative reactivity method (CRM), which measure not OH but a tracer's reactivity to reactive trace gases in the

Table 1.1: Total OH reactivity measurements in urban, suburban, forest, and remote regions.

	Site	Year	Total OH reactivity (s^{-1})	Missing OH reactivity(s^{-1}); (%)	reference
Urban	Nashiville, USA	summer 1999	11.3	4.1;36%	[Kovacs et al., 2003]; [Kovacs and Brune, 2001]; [Martinez et al., 2003]
	New York, USA	summer 2001	20	<10%	[Ren et al., 2006]; [Ren et al., 2003a]; [Ren et al., 2003b]
	Mexico, Mexico	spring 2003	10-120	23%	[Shirley et al., 2006]
	Tokyo, Japan	summer 2003	30	7.8; 26%	[Sadanaga et al., 2005]
	Tokyo, Japan	2003-2004	10-100	30% (5% in winter)	[Yoshino et al., 2006]
	Tokyo, Japan	summer 2007	33.4	9.0; 27%	[Yoshino et al., 2012]
	Tokyo, Japan	autumn 2012	7.4	24.5%	
		summer 2013	11.4	34.1%	[Ramasamy et al., 2018]
	Houston, USA	summer 2006	9-22	agree well	[Mao et al., 2010]
	Paris, France	winter 2010	18.8	2.3; 12%	oceanic air mass [Dolgorouky et al., 2012]
			63.3	46.8; 74%	continental air mass [Dolgorouky et al., 2012]
	London, UK	summer 2012	18.1	6.7; 37%	[Whalley et al., 2016]
	Beijing, China	summer 2013	15-26	25%	[Williams et al., 2016]
	Beijing, China	summer 2017	43	30%	[Whalley et al., 2021]
	PRD, China	autumn 2014	15-80	50%	[Tan et al., 2019]
Suburban	Weybourne, England	spring 2004	4.9	1.9; 39%	[Ingham et al., 2009]; [Lee et al., 2009]
	Yufa, China	summer 2006	6-30	20%	[Lu et al., 2010])
	Backgarden, China	summer 2006	10-120	50%	[Lou et al., 2010]
	Wangdu, China	summer 2014	mostly 10-20	good agreement; median value 0.3 s^{-1}	[Fuchs et al., 2017]
	Brent, USA	summer 2013	16-25.6	17-51%	[Sanchez et al., 2018]
	Tsukuba, Japan	summer 2017	12.9	4.5; 35%	[Li et al., 2020]
Forest	Michigan, USA	summer 2000	7.8	2.6; 33%	[Di Carlo et al., 2004]
	Rocky Mountains, USA	summer 2008	6.7	2.0; 30%	[Nakashima et al., 2014]
	Amazon, Brazil	2012-2013	62	79%	dry season [Nölscher et al., 2016]
			10	49%	wet season [Nölscher et al., 2016]
	Haute Provence, France	summer 2014	26 (2m); 24 (10m)	8% (2m); 21% (10m)	[Zannoni et al., 2016]
	Wakayama, Japan	summer 2014	8.1	2.3; 28.4%	[Ramasamy et al., 2016]
Remote	Pacific	spring 2006	4	2.4; 60%	[Mao et al., 2009]

The missing OH reactivity shown here was determined from the calculated OH reactivity only based on individually identified trace species. The coverages depend on the co-deployed instrumentations and are not necessarily comparable between studies.

air. CRM is described in Section 1.6.

As for calculated OH reactivity, it is necessary to measure the concentration of OH-reactants, i.e., the copious trace species in the air. Calculated OH reactivity can be estimated by (1.46), in which the second order rate constants under experimental conditions (pressure and temperature) can be found from © NIST, IUPAC, or JPL. In addition, it is also quite popular to compose calculated OH reactivity from model which include intermediates or unmeasured trace species. For instance, OVOCs especially these aldehydes, as one of the most important contributors to OH reactivity, are hard to detect. Therefore, prediction via model provides another flexible approach to precisely investigate calculated OH reactivity. Currently MCM is one of the most widely-used model, which is developed by university of Leeds.

1.4.2 Steady state of OH radicals

In the troposphere, free radicals (OH, HO_2, RO_2, halogen, NO, NO_2, NO_3, and so on) are pivotal species especially those who are highly reactive. Among these radicals, NO and NO_2 radicals are comparatively stable therefore not worthy of discussing here. It is well known that O_2 and N_2 are the most massive gases in the air, which takes 20%, and 80% of the air mixing, respectively. Most of the radicals in Table 1.2 can take reactions with O_2 or quenching by O_2 (N_2), Therefore, their lifetime gets extremely short, varies from millisecond to nanosecond. However, OH, HO_2, and RO_2 radicals do not react with O_2 in the air, leading to a corresponding lifetime in the unit of second (refer to Table 1.2). Amongst these three type of radicals, OH plays the most important role since it can react with most trace species in the air and therefore known as "detergent of the atmosphere". OH reacts with NMHCs or CO under a relatively large rate constant, which is over a factor of one to three compared with their reaction with $O(^3P)$ in the same condition. Products from such processes can further take reactions to generate SOA or oxidants in the air. On the other hand, since OH's concentration in the air is super low, in 10^6 molecule cm^{-3} and HO_2 is around 100 times more than OH. When there is NO, HO_2 can be converted into OH very soon.

Because of high reactivity and short lifetime in the air, the balance of production and destruction procedure in HO_x cycle for OH radicals is supposed to be steady-state, the dominate

channels were displayed in (1.48) and (1.49).

$$RH + OH + O_2 \longrightarrow RO_2 + H_2O \tag{1.48}$$

$$HO_2 + NO \longrightarrow OH + NO_2 \tag{1.49}$$

The major degradation (D_{OH}) and production pathways (P_{OH}) of OH in HO_x cycle are exhibited in (1.48) and (1.49). From the assumed simple steady-state, we can obtain a general relationship between them, as showed in (1.50), in which the calculation is explained in detail in (1.51) and (1.52).

$$D_{OH} = P_{OH} \tag{1.50}$$

$$P_{OH} = k_{HO2-NO}[HO_2][NO] \tag{1.51}$$

$$D_{OH} = k_{OH-RH}[OH][RH] \tag{1.52}$$

Although steady-state of radicals comes from a hypothesis, in terms of species like OH, which is super reactive and exist in the air less than 1 second. Such a hypothesis was considered to be acceptable, and this steady-state helps to further estimations on HO_x mechanism and ozone production analysis. Similar to OH radicals, the steady state of all HO_x radicals also make it possible to specify the ozone production sensitivity, as discussed in Chapter 3.

1.5 LP-LIF technique; instrumentation

The current section will introduce radical measurement techniques, focus on Laser-pump and laser induced fluorescence (LP-LIF) spectroscopy, Section 1.5 describes from the very fundament to amplification. Comparatively, Section 1.6 briefly delineates other comparative radicals measurement instruments.

The terminology, *LASER*, comes from the acronym for *light amplification by stimulated emission of radiation*. The instrument LP-LIF for total OH reactivity measurement is a joint-application of two laser system. The first system uses pump pulse to start the photochemical dissociation of ozone, and produce OH free radicals. The second system uses probe pulse to

Table 1.2: Examples of model radicals' information in the air. This table is adapted from [Akimoto et al., 2002].

Radicals	main source	reactants (abundance in the air)	reaction	rate constant (second order)	lifetime (s)	products
$O(^1D)$	$O_3 + h\nu$	N_2 (80%)	$O(^1D) + N_2 \rightarrow O(^3P) + N_2$	2.6×10^{-11}		
		O_2 (20%)	$O(^1D) + O_2 \rightarrow O(^3P) + O_2$	4.0×10^{-11}	1.3×10^{-9}	$O(^3P)$
$O(^3P)$	$NO_2 + h\nu$	O_2 (20%)	$O + O_2 + [M] \rightarrow O_3 + [M]$	1.6×10^{-14} (1 atm)	2.5×10^{-6}	O_3
OH	$O(^1D) + H_2O$	CH_4 (1.9 ppmv)	$CH_4 + OH \rightarrow CH_3 + H_2O$	8.3×10^{-15}	2.4	CH_3O_2
		CO (100 ppbv)	$OH + CO \rightarrow H + CO_2$	2.4×10^{-13} (1 atm)	1.3	HO_2
CH_3O	$CH_3O_2 + NO$	O_2 (20%)	$CH_3O + O_2 \rightarrow CH_2O + HO_2$	2×10^{-15}	1×10^{-4}	HO_2
HO_2	$OH + CO + O_2$	NO (50 pptv)	$HO_2 + NO \rightarrow OH + NO_2$	8.3×10^{-12}	73	OH
	$HCO + O_2$					
CH_3O_2	$CH_3 + O_2$	NO (50 pptv)	$CH_3O_2 + NO \rightarrow CH_3O + NO_2$	1.1×10^{-11}	55	CH_3O
HCO	$RCHO + h\nu$	O_2 (20%)	$HCO + O_2 \rightarrow HO_2 + CO$	5.6×10^{-12}	3×10^{-8}	HO_2
O_3	$O + O_2 + [M]$	NO (50 pptv)	$O_3 + NO \rightarrow O_2 + NO_2$	1.8×10^{-14}	3×10^5	NO_2
NO_3	$NO_2 + O_3$	NO (50 pptv)	$NO_3 + NO \rightarrow N_2O_4$	2.7×10^{-11}	20	N_2O_4

excite OH radical for the detection of fluorescence signal, in which the intensity is proportional to amount of excited OH radicals. There are four subsections in Section 1.5, including pump laser (Subsection 1.5.1) and probe laser (Subsection 1.5.3), and also the dissociation photolysis of ozone discussed in Subsection 1.5.2, finally I concluded these three parts in LP-LIF technique as in Subsection 1.5.4.

1.5.1 Pump laser

Pump laser decides the frequency of radicals generation, in LP-LIF spectroscopy, pump laser, a lamp-pumped, Q-switched neodymium-doped yttrium aluminum garnet laser (Nd:YAG, New Wave Research) produces an infra-red (IR) at the fundamental wavelength of 1064 nm, then the IR beam pass through an angle tuned Potassium Titanyl Phosphate (KTP) crystal to generate second harmonic at 532 nm. After that, the 532 nm second harmonic light passes the Beta-Barium Borate (BBO) crystal to combine two photons and give one photon at 266 nm, which is the fourth harmonic of Nd:YAG. The light at 266 nm is then separated using a pair of dichroic mirrors to select only the vertically polarized fourth harmonic light.

The 266 nm laser pulse (0.5–2 Hz, 3–5 $\mathrm{mJ\,s^{-1}}$) can photolyze ozone into excited singlet oxygen atoms, $O(^1D)$, which then can react with water vapor to generate OH radicals, as displayed in (1.53) and (1.54) [Finlayson-Pitts and Pitts Jr, 1999]. Ozone's photolysis also produce triplet oxygen atoms, $O(^3P)$, which re-forms ozone quickly after reacting with oxygen. In addition, most of the $O(^1D)$ are efficiently de-excited to the ground state, $O(^3P)$, by collisions with N_2 or O_2 molecules ((1.55) & Table 1.2), which are the main air composition.

$$O_3 + h\nu\,(\lambda < 336\,\mathrm{nm}) \longrightarrow O(^1D) + O_2 \tag{1.53}$$

$$O(^1D) + H_2O \longrightarrow 2\,OH \tag{1.54}$$

$$O(^1D) \xrightarrow{N_2,\,O_2} O(^3P) \tag{1.55}$$

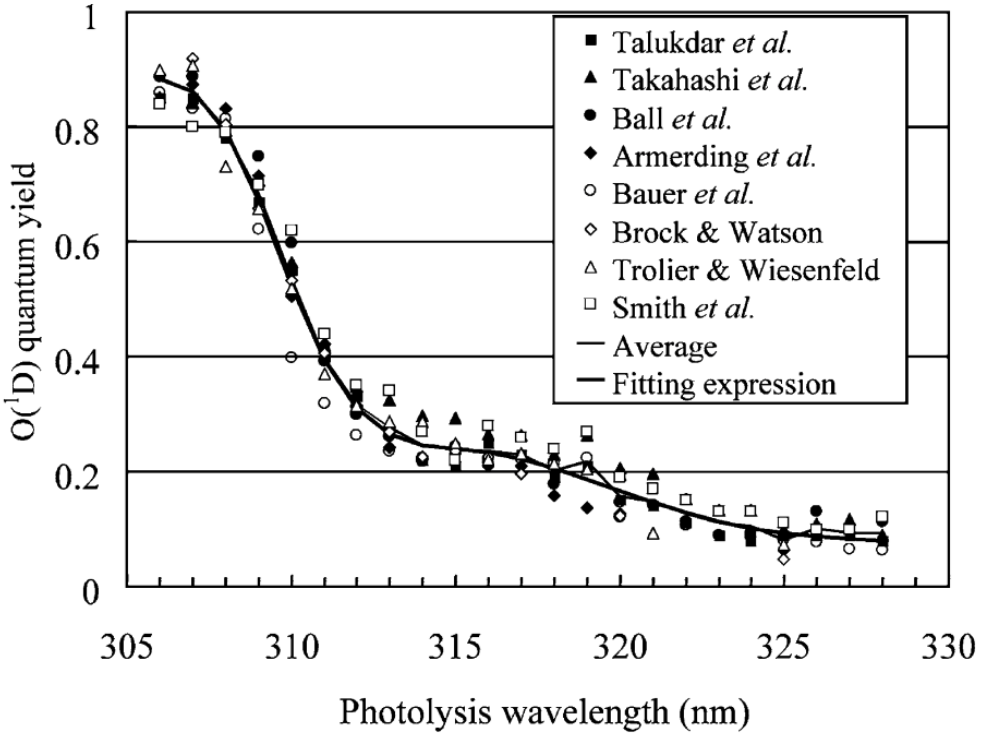

Figure 1.5: Wavelength dependence of the O(^{1}D) quantum yield in the photolysis of ozone at 298 K between 306 nm to 328 nm from eight studies ([Talukdar et al., 1998], [Takahashi et al., 1996], [Ball et al., 1997], [Armerding et al., 1995], [Bauer et al., 2001], [Brock and Watson, 1980], [Trolier and Wiesenfeld, 1988], and [Smith et al., 2000]) [Matsumi and Kawasaki, 2003].

1.5.2 Dissociation photolysis of ozone

Details of ozone photolysis will be discussed here, the near-UV photochemistry of ozone depends on the wavelength, temperature, solar actinic flux, and solar zenith angle. Although $O(^1D)$ is the most important product during the dissociation processes of ozone in the lower atmosphere, the $O(^1D)$ quantum yield, which equals the produced $O(^1D)$ amount divided by the number of absorption photons, varies greatly with photolysis wavelength. Figure 1.5 displays a review of the $O(^1D)$ quantum yield measurements from 306 nm to 328 nm. The production rate has been reported to be 0.9 for the wavelength range 220–305 nm at room temperature, and dropped to 0.08 ± 0.04 between 329–340 nm.

As for temperature dependence, experiments were conducted to examine the temperature dependence of $O(^1D)$ yield at 308 nm, $\Phi(308\,\mathrm{nm,T})$, equation (1.56) shows the linear least-squares fitting relationship [Matsumi and Kawasaki, 2003] which assuming the quantum yield of $O(^1D)$ equals 0.79 at 298K, and the expression was normalized empirically from different temperatures.

$$\Phi(308\,nm,T) = (6.10\times10^{-4})T + 0.608 \tag{1.56}$$

Combining both wavelength and temperature dependence, a fitting expression of $O(^1D)$ yield, containing three Gaussian-like functions, a temperature term, and a constant term, have been proposed [Matsumi and Kawasaki, 2003].

$$\begin{aligned}\Phi(\lambda,T) = {} & (\frac{q_1}{q_1+q_2})\times A_1 \times exp\{-(\frac{X_1-\lambda}{\omega_1})^4\}+ \\ & (\frac{q_2}{q_1+q_2})\times A_2 \times (\frac{T}{300})^2 \times exp\{-(\frac{X_2-\lambda}{\omega_2})^2\}+ \\ & A_3 \times (\frac{T}{300})^{1.5} \times exp\{-(\frac{X_3-\lambda}{\omega_3})^2\} + c\end{aligned} \tag{1.57}$$

$$q_i = exp(-\frac{\nu_i}{RT}) \tag{1.58}$$

The equation (1.57) is the fitting result using a non-linear least-squares method, where X_{1-3}, A_{1-3}, ω_{1-3}, ν_2, and c are fitting parameters, except the variable λ and T, the values of ν_1 and R are 0 (cm^{-1}), and 0.695 ($cm^{-1}\,K^{-1}$), respectively. Figure 1.6 shows the results based on equation (1.58), where region I, region II marked with hatched vertical lines, and region III with hatched slash lines representing different fragmentation pathways in the photolysis of O_3.

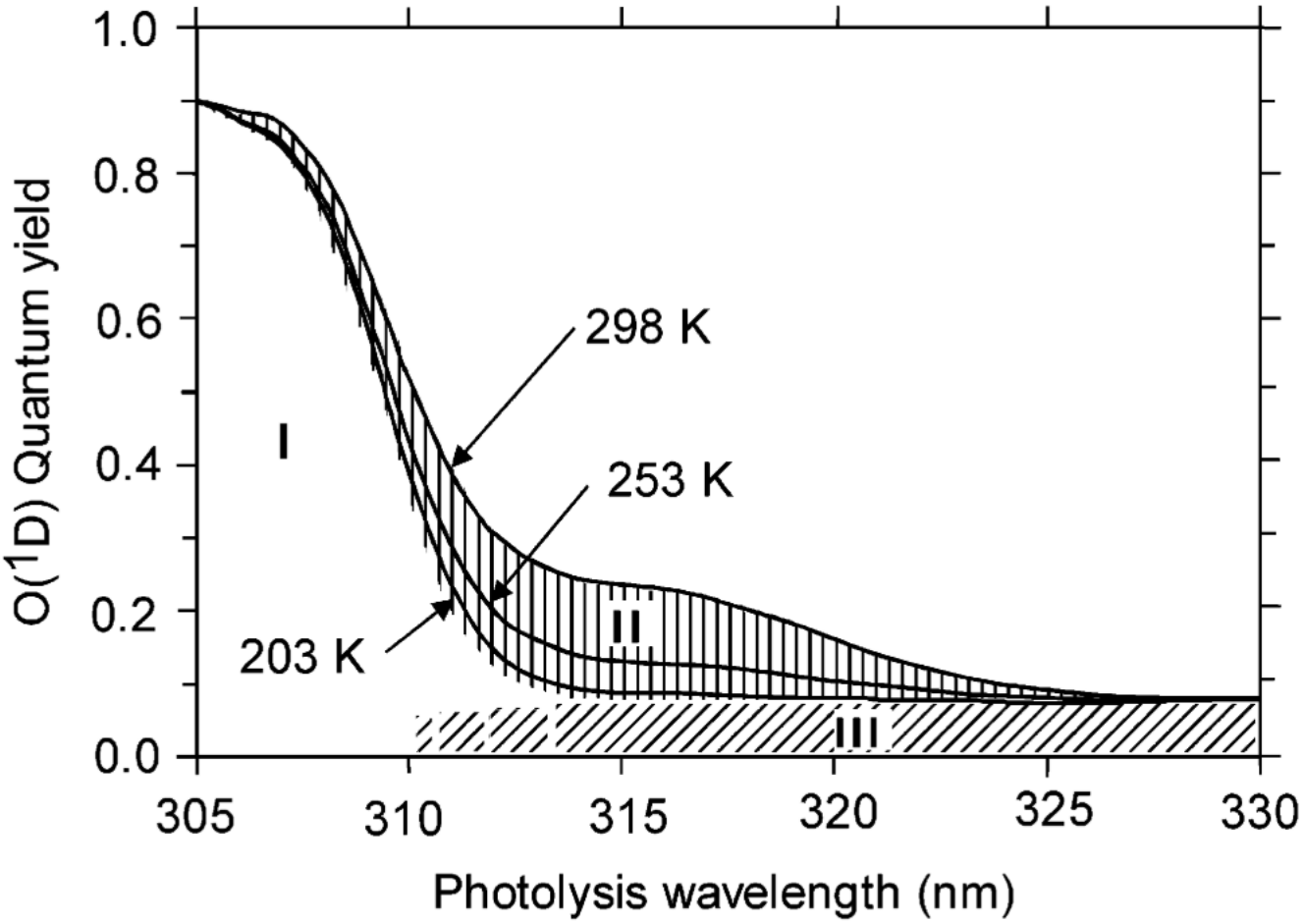

Figure 1.6: Recommended $O(^1D)$ quantum yields estimated from equation (1.57) using fitting parameters from 200K, 253K, and 298K in the wavelength range 306–328 nm [Matsumi and Kawasaki, 2003].

1.5.3 Probe laser

The produced OH radical has an unpaired electron in the outer orbit, probe laser will stimulate the electron. The excited state will return to ground state, and the radiative transition emits fluorescence signal in time scale of 10^{-9} s. The laser beam for electron excitation is orthogonal to the detection axis of the fluorescence signal. To enhance the fluorescence signal for detection, the cell for probe laser is designed as white cell (multi-pass cell) as showed in Figure 1.7 with 5 collecting optics. There are two special treated mirrors used in the white cell, which were compacted with a diameter of 3.8 cm. Although the laser beam encountered multi-pass inside of the detection cell, there were another two mirrors placed before and after the window, which were 45° reflection mirrors. Hence, it would be easy for the alignment via

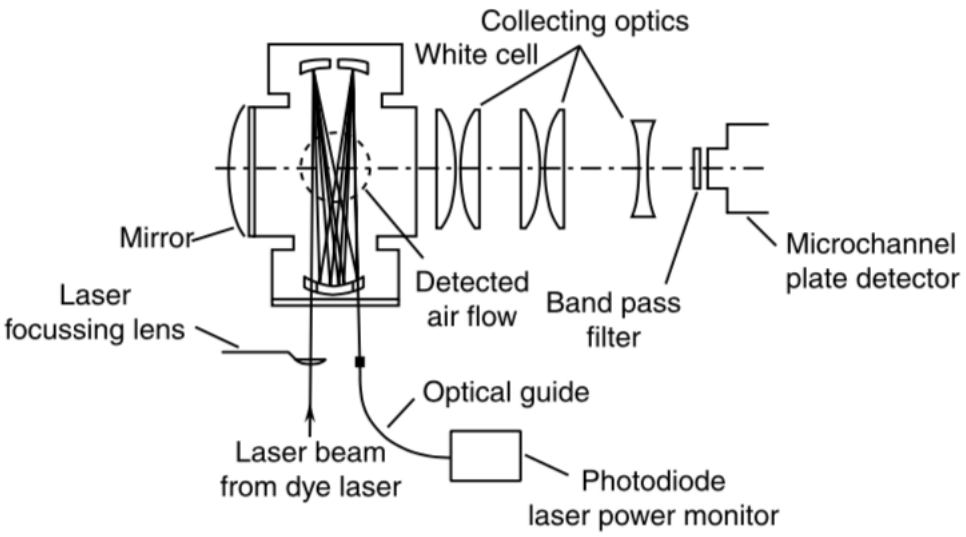

Figure 1.7: The schematic of white multi-pass cell and detection mirror setting system for probe laser [Finlayson-Pitts and Pitts Jr, 1999].

slight adjustment on such mirrors outside of the detection cell.

The laser induced fluorescence cell uses a wavelength of 308 nm, which is provided by a Nd:YVO_4 laser (Sirah Laser PrecisionScan, Spectra Physics) with a repetition rate of 10kHz. Artifact formation of OH radicals under 308 nm was reported to be less severe compared with other wavelengths. Rhodamine 610 (B) and Rhodamine 640 (101) dissolved in 99.9% ethanol solution at a density of 0.255 g L^{-1}, and 0.06 g L^{-1}, respectively. The dye cell will excite the probe laser from 532 nm into 616 nm. Then BBO crystal generate second harmonic at 308 nm, which correspond to A-X(0,0) transition of OH. A dynode-gated photomultiplier tube (PMT; R2256P, Hamamatsu) is used to collect the photon counting intensity signals [Sadanaga et al., 2005]. The dynode gating system helps PMT to distinguish the fluorescence signal from scatter light by a positive transistor-transistor logic (TTL) pulse generated by a delay/pulse generator (DG535, Stanford Research Systems). The DG controls the gate time for photon counting ranged around 100-300 ns after the laser pulse [Kanaya, 1997]; [Sadanaga et al., 2017].

1.5.4 LP-LIF technique

Pump probe spectroscopy is well suited for measuring the lifetime of electronic excitations in femtosecond (10^{-15} s) time resolution. Laser pump and laser induced fluorescence (LP-LIF) technique utilizes pump probe spectroscopy technique and the simplified schematic was showed

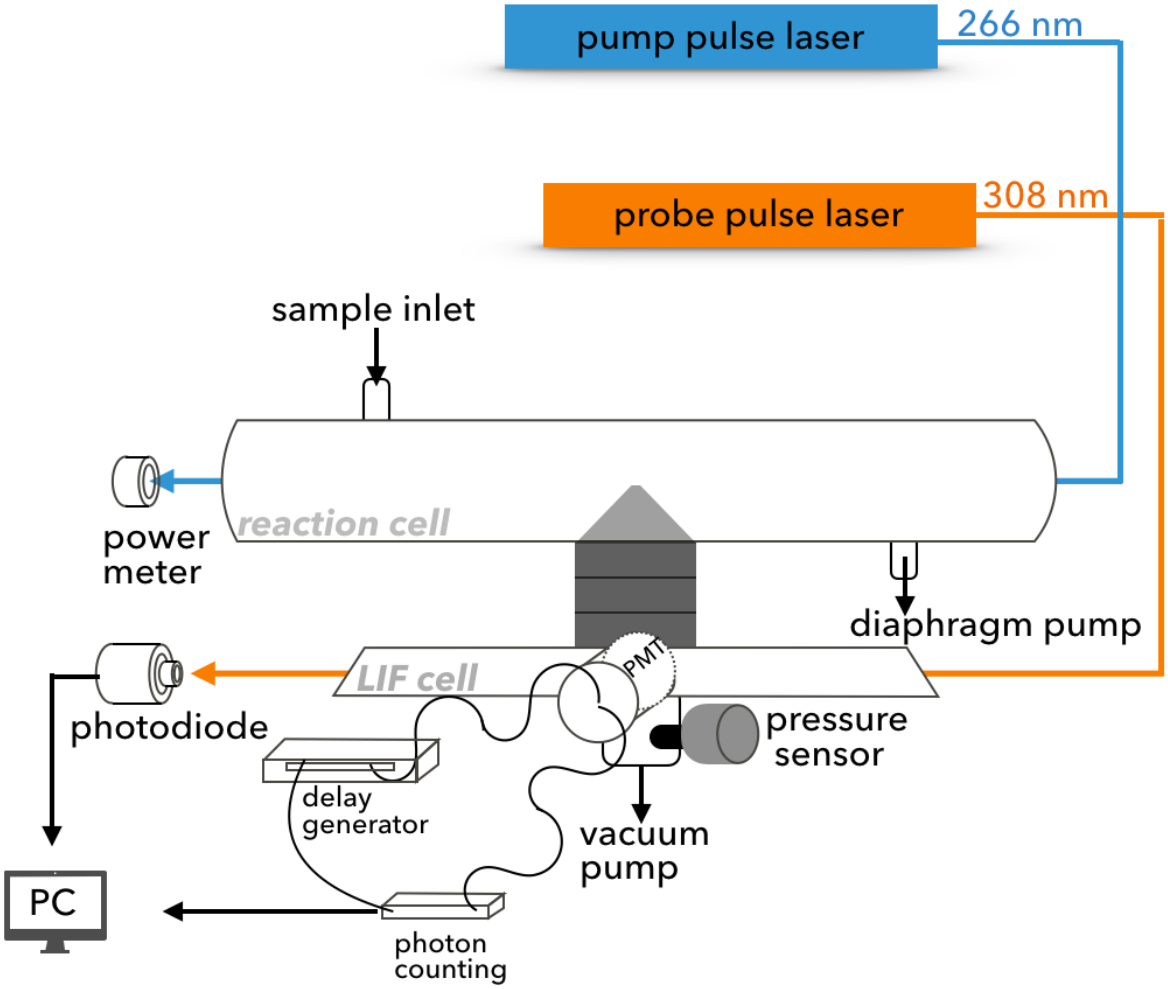

Figure 1.8: Schematic diagram of the LP-LIF technique.

in Figure 1.8. The pump laser is used to dissociate ozone and generate OH radicals (1.53) & (1.54), and probe laser with a weaker beam is used to monitor the changes in the fluorescence signal. Measuring the changes in the fluorescence intensity as a function of time delay between pump initiation and probe pulses yields information about the relaxation of electronic excited radicals. In LP-LIF, pump laser (New wave Research, Tempest 300) is applied in the reaction cell (Figure 1.8), in which artificial OH radicals are produced via the photolysis of ozone and subsequent reaction with water vapor (refer to (1.3). Sampling air can be induced through the inlet, a mass flow controller (MFC, KOFLOC, 3810S) placed after the outlet constrained the total flow rate less than 13 SLM (standard liter per minute at 273K and 1 atm). Pressure inside reaction cell is kept as standard pressure.

A conical inlet with the diameter of 0.1–0.5 mm pinhole linked reaction cell to LIF cell where

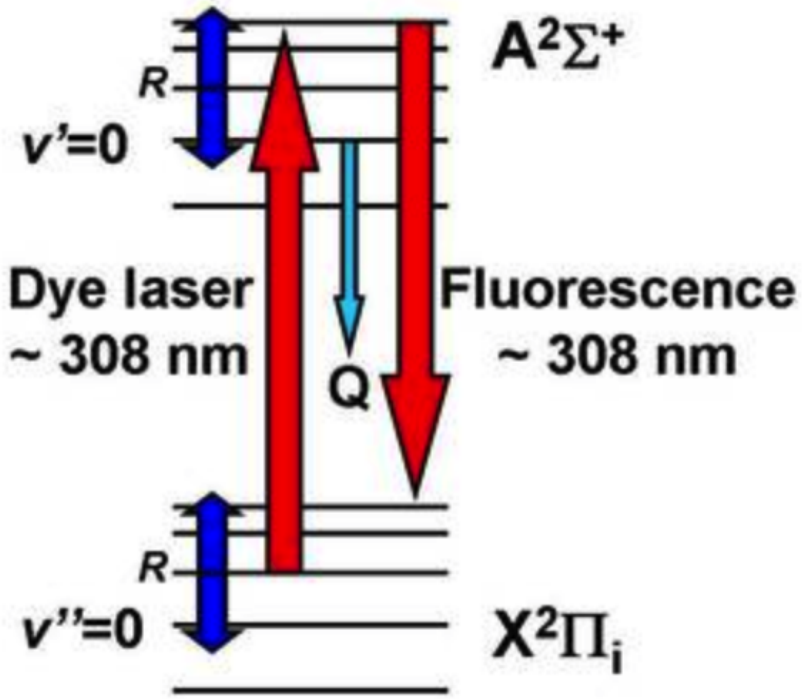

Figure 1.9: On-resonance laser induced fluorescence of OH at 308 nm (figure from website [Heard, 2021]).

probe laser (Sirah Credo, Spectra Physics) is used for detection. In the detection cell, a rotary oil pump (ULVAC, D-950) facilitates the pressure to be less than 2 Torr. Low pressure helps to reduce the collisional quenching of the excited state, increase the quantum yield of fluorescence, and also prolong OH fluorescence lifetime. The LIF signal is gathered by time-gated photomultiplier tube (Hamamatsu Photonics, R2256P), as displayed in Figure 1.8. Wavelength of 308 nm is chosen to detect OH transition over $A^2\Sigma^+(v'=0)$–$X^2\Pi(v''=0)$ band transition (see Figure 1.9). As mentioned before, OH has an unpair electron in the outer orbit, $X^2\Pi(v''=0)$ means the ground state energy level of the electron, and $A^2\Sigma^+(v'=0)$ is the excited first state energy level. Dye laser provides the exact amount of energy to excite the ground state to first state. Conversely, the excited OH can spontaneously emit photons equal to the energy difference to go back to ground state. The intensity of fluorescence signal is proportional to laser intensity, which indicates radicals content. The whole detection system is known as Fluorescence assay by gas expansion-laser induced fluorescence (FAGE-LIF) technique.

Except for radical reactivity measurement, FAGE-LIF is also available for radical concentration measurement, in which OH can be detected directly with the LOD as reported as 6×10^5 molecule cm^{-3}. HO_2 and RO_2 radicals can be measured by chemical conversion to OH with

NO, the LOD is 1×10^6 molecule cm^{-3} [Heard, 2021]. A description of the chemical conversion for HO_2 and RO_2 radicals measurement was provided in appendix.

1.6 Other OH reactivity detection techniques

As introduced in Subsection 1.4.1, there are other technique available for OH reactivity measurement including (semi-)direct measurements refer to TOHLM in Subsection 1.6.1 and CIMS in Subsection 1.6.2, and indirect measurement CRM described in Subsection 1.6.3. An incisive comparison including LP-LIF will be introduced in Subsection 1.6.4, and previous researches conducted by our group in Japan using LP-LIF should be specified in Section 1.7 and further stresses remaining problems based on the situation.

1.6.1 TOHLM

Total OH loss rate method (TOHLM) technique, also known as flow tube-LIF, is comprised by a flow tube, an injector, and a detection system [Kovacs and Brune, 2001]. As showed in Figure 1.10, the detection system consists of a tunable laser, flow tube, detection cell, a microchannel plate (MCP) detector, and a vacuum pump. The flow tube consists a small movable tube in which OH is produced via photolysis of water vapor (1.59). Sampling air and artificial OH comprised the air in the flow tube. The injector connected to the flow tube and transport N_2 mixed with water vapor to the mercury lamp. The generation of OH by photolysis of water vapor is showed in (1.59), the photolysis also produces equal amount of HO_2 radicals (1.60. This would bring interference to OH result when NO mixing ratio is larger than 1 ppbv because NO will react with HO_2 and regenerate OH radicals.

$$H_2O + h\nu \longrightarrow H + OH \tag{1.59}$$

$$H + O_2 \longrightarrow HO_2 \tag{1.60}$$

The injector located only at the final 40 cm of the flow tube based on the method described by [Kovacs and Brune, 2001] and the place can be changed to alter the reaction time. Because

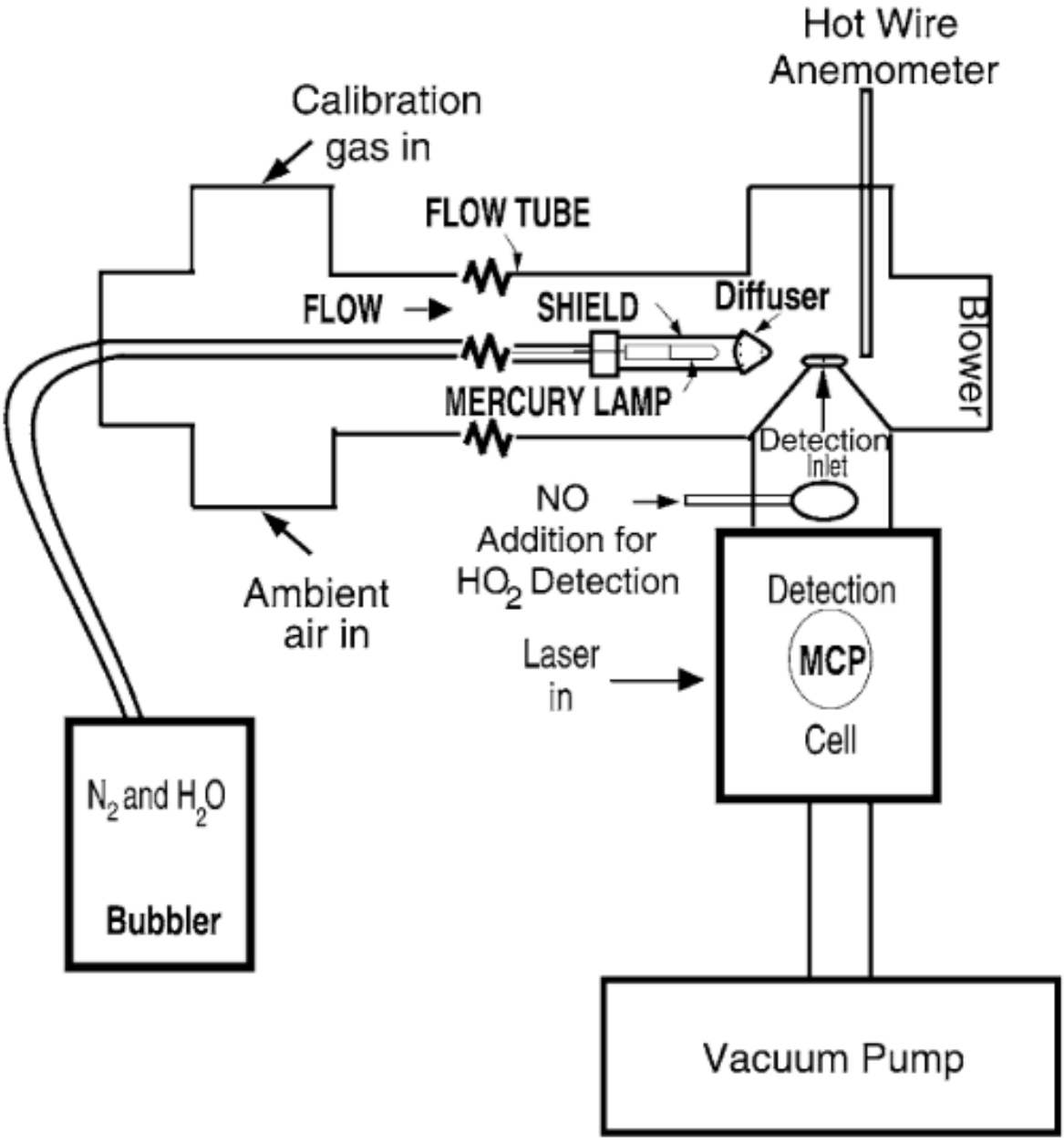

Figure 1.10: Schematic of the TOHLM instrument showing the main flow tube, injector, and detection system [Kovacs and Brune, 2001].

the artificial OH concentration in the flow tube is much less than ambient VOCs, generally three orders of magnitude smaller. Therefore the loss of OH as a function of reaction time can be expressed as a first-order exponential decay. The total OH reactivity, gives:

$$k_{OH} = \frac{-d(ln[OH])}{dt} - k_{base} \tag{1.61}$$

In (1.61), ln[OH] is the OH fluorescence signal, which is proportional to the OH concentration, and therefore, ln[OH] over the reaction time is the measured OH reactivity value. k_{base} is the decay rate from zero gas measurement.

1.6.2 CIMS

Chemical ionization mass spectrometry (CIMS) technique for OH reactivity measurement is based on the logarithmic relation of any two points of OH concentration at time t_1 and time t_2 on the decay curve, from which OH reactivity can be estimated. This technique is a semi-direct measurement for OH reactivity.

$$k_{OH} = ln(\frac{[OH]_{t_1}}{[OH]_{t_2}}) \times \frac{1}{t_2 - t_1} - k_w \tag{1.62}$$

In (1.62) (adapted from [Muller et al., 2018]), the total OH loss rate as measured by CIMS includes the loss by chemical reactions (k_{OH}) and loss onto flow tube walls (k_w). The wall lose rate can be determined by injecting zero gas into CIMS tube. The scaling rate of time difference $\frac{1}{t_2 - t_1}$ in s^{-1} can be quantified under synthetic conditions when a known amount of OH reactivity is delivered to the instrument. The schematic of CIMS for OH reactivity measurement is displayed in Figure 1.11, in which P presents OH production from water vapor photolysis. F1 and F2 is the injection point of SO_2 for the first and second titration zone to produce H_2SO_4 from OH titration. R1 and R2 is where propane is added to stop H_2SO_4 production from recycled OH. The concentration of OH radicals was measured by addition of SO_2 which convert OH into H_2SO_4. The H_2SO_4 is then ionized by charging negative chemical ionization transferred from NO_3^- reactant ions. Finally, both HSO_4^- and NO_3^- can be detected by quadrupole mass spectrometry to decide the concentration [Muller et al., 2018].

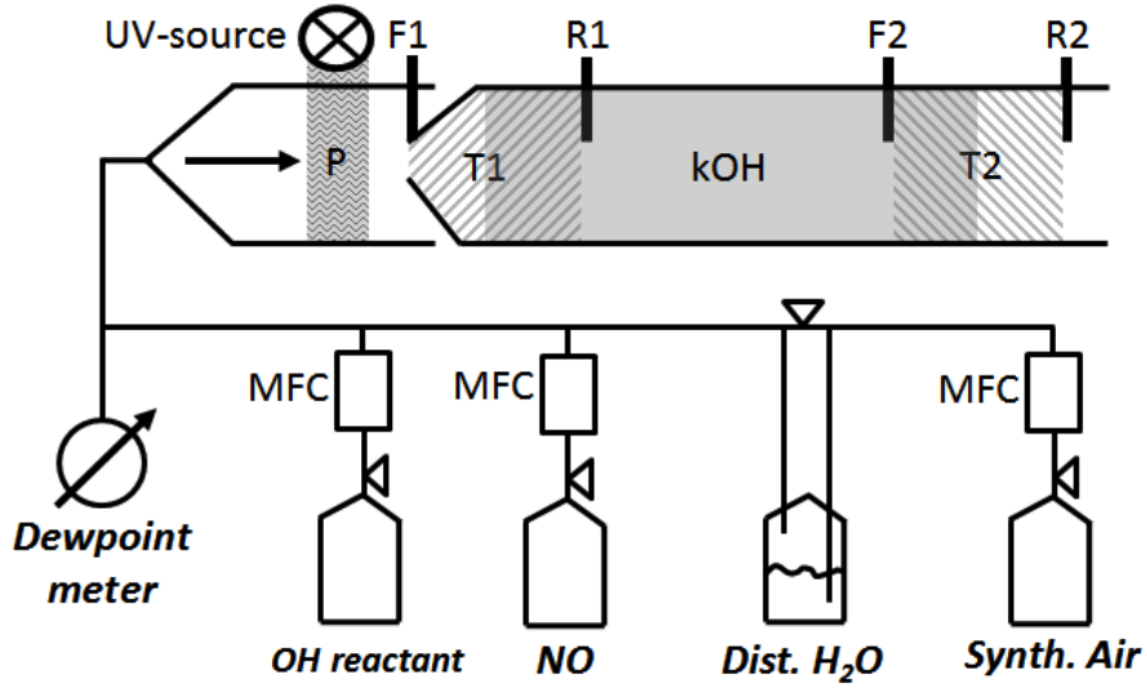

Figure 1.11: Schematic of CIMS flow tube with two titration zones for OH reactivity measurement [Muller et al., 2018]. For CIMS, I only introduced the OH reactivity detecting flow tube part.

1.6.3 CRM

As the indirect measurement technique, comparative reactivity method (CRM) is based on the competition of a tracer molecule for reaction with OH [Hansen et al., 2015]. The specific tracer is typically pyrrole because three reasons as follows: (1)it reacts fast enough with OH ($k_p = 1.28 \times 10^{-10}$ $cm^3 molecule^{-1} s^{-1}$), (2)negligible ambient concentration of pyrrole in the air, and (3)it reacts fast enough to compete with other trace gases that can react with OH [Sinha et al., 2008].

The CRM measurement sequence including three distinct steps as colored differently in Figure 1.12. C1 mode means pyrrole and dry zero air are induced into reactor together with dry nitrogen. In the absence of water vapor, OH cannot be produced. Hence C1 is the baseline concentration. In C2, humid zero air and humid nitrogen are induced. Both OH and HO_2 are produced. Pyrrole then reacts with OH and leads to a lowering concentration of pyrrole in the reactor to C2. During C3 step, ambient air replaced zero air in the reactor, keeping the same flow of humid nitrogen. Trace gases present in the ambient air compete with pyrrole and consume OH radicals. The decrease of pyrrole between C1 and C2 is offset by the reaction of

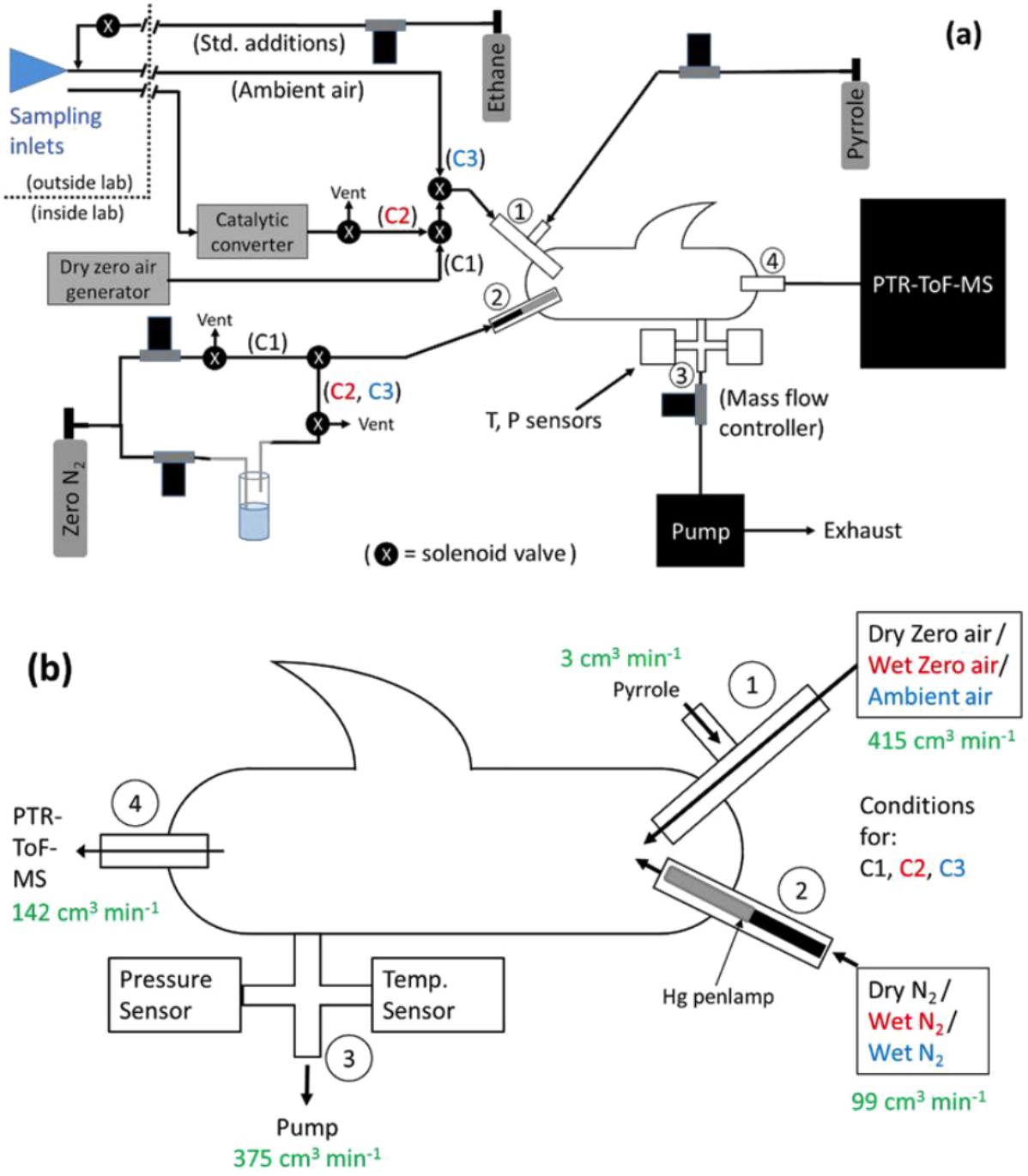

Figure 1.12: One example of the schematic of CRM instrument in graph (a) and reactor in (b) [Hansen et al., 2015].

OH with trace species in the ambient air, which leads to a increase from C2 to C3. Another step C0 is defined as the pyrrole concentration inside the reactor when mercury lamp is off. The difference between C0 and C1 is used to assess the lost of pyrrole due to the photolysis.

$$k_{OH} = \frac{(C3 - C2)}{(C1 - C3)} k_p C1 \tag{1.63}$$

(1.63) was extrapolated based on pseudo first-order assumptions in which pyrrole concentration is much larger than OH. [Sinha et al., 2008] and [Dolgorouky et al., 2012] found that humidity variations change the OH production in step C2 and C3. Such an artifact requires humidity sensitivity analysis to calibrate C2 and match humidity levels to C3 as observed.

1.6.4 A review on these techniques

The TOHLM technique is susceptible to measurement artifacts from ambient NO due to HO_2 + NO reaction. Although this could be solved by a correction procedure developed by [Shirley et al., 2006], utilizing continuously measurements of ambient NO and HO_2 in the reactor. Actually, not only TOHLM, but also all other techniques suffer from high NO conditions. Therefore, dilution of the sampling air has to be conducted considering NO recycles peroxy radicals and slow down OH reactivity.

Intercomparisons between different OH reactivity measurement techniques have been conducted by several groups. [Hansen et al., 2015] reported a comparison between CRM and LP-LIF observed in 2012. Both instruments may underestimate the total OH reactivity. The uncertainty of around 20% from CRM was caused by the photolysis of VOCs in the sampling reactor, which firmly depends on the position of the lamp. As for LP-LIF, the bias was risen by the measurement of zero air, although the uncertainty varies with the experimental conditions, as high as approximately 2 s^{-1} of uncertainty may exist due to the impurity of zero air [Hansen et al., 2015].

A chamber study SAPHIR compared the performance of all aforementioned instrumentations including TOHLM, CIMS, CRM and LP-LIF conducted in 2015 and 2016 [Fuchs et al., 2017]. As summed in Table 1.3, the general characteristics of each technique was compared. From the chamber experiment in the presence of OH-reactants, LP-LIF was considered as the optimal technique for OH reactivity measurement compared to CRM which showed biggest difference

Table 1.3: Specification of techniques parameters of OH reactivity measurements.

Techniques	Time resolution (s)	LOD $1\sigma(s^{-1})$	accuracy 1σ	Reference
LP-LIF	30-60	≤ 0.4	$\leq 10\%$	[Parker et al., 2011]
TOHLM	30	0.5	7%-23%*	[Kovacs and Brune, 2001]; [Mao et al., 2009]
CIMS	60	0.5	1 s^{-1}-2 s^{-1}	[Berresheim et al., 2000]
CRM	600	1	20%	[Michoud et al., 2015]

*Depends on the total OH reactivity level

to calculated OH reactivity [Fuchs et al., 2017].

LP-LIF, TOHLM, and CIMS share principles in common, which produce high concentration of artificial OH radicals in the apparatus, and detect the decay rate of OH radicals after it reacting with sampling air. However, the details are distinct from each other, like TOHLM and CIMS photolysis water vapor to generate OH radicals compare to LP-LIF photo-dissociates O_3. In TOHLM and LP-LIF, the detection system are same, both utilize LIF spectroscopy technique. The main difference in two instruments depends on the way to control OH remaining time in the reaction tube. TOHLM changes the reaction time of OH by altering the injection place of water vapor embedded in the flow tube. LP-LIF technique makes use of pump laser to generate OH in each pulse. CIMS modifies OH concentration by the addition of SO_2, and detect the decay rate of OH at two locations from the concentration of products measured by CIMS. CRM detects OH radicals indirectly by using pyrrole. Except these limitations mention before, there is extra regard on the ratio of pyrrole over OH (from 1.7:1-5:1) during the detection. Moreover, calibration is required for CRM while the precision of such calibration should be further tested.

Simply put, LP-LIF, TOHLM, and CIMS have much shorter time resolution than CRM, as compared in Table 1.3. Under complex atmospheric chemistry conditions, the accuracy of LP-LIF is much better than TOHLM and CIMS. The later is suitable for relatively clean conditions with low NO_x. Therefore, LP-LIF was considered as the optimal technique for OH reactivity detection under different atmosphere conditions based on its time resolution, LOD, and accuracy.

1.7 Situation of the field studies utilizing LP-LIF in Japan

Since the first ambient observation of total OH reactivity measured by LP-LIF conducted in Japan in 2003 by [Sadanaga et al., 2004], a series of field studies in terms of OH reactivity have been practiced from then on. Table 1.1 summaries total OH reactivity measurements in different type of locations, specified in Japan, most of the previous observations were conducted in the megacity Tokyo, either in the central area [Yoshino et al., 2012] or in its suburbs [Sadanaga et al., 2004]; [Sadanaga et al., 2005]; [Yoshino et al., 2006]; [Ramasamy et al., 2018]. Only one exception was conducted outside of the great Tokyo area which observed in a BVOCs dominated temperate forest [Ramasamy et al., 2016]. Note that another campaign conducted in Rocky Mountains in USA [Nakashima et al., 2014] also utilized our LP-LIF instrument. In these campaigns, it is clear that out of 5% - 35% of total OH reactivity came from unknown VOCs, however, do those missing reactants stay inside of the HO_x cycle or cause termination of radicals require for further study. On the other hand, ozone production analyses were conducted in some of these locations limitedly. The extent of unknown trace species, missing OH reactivity attribution, and heterogeneous effects of particles remain unknown in different types of urban areas. Thorough measurements on trace species combine with total OH reactivity detection should be critical to explore aforementioned aspects as well as oxidants (mainly ozone) production spatiotemporally.

Long term temporal variations of OH reactivity in the Tokyo area indicating a decrease from 2003 to 2013 due to the stringent regulations for environmental protection and advanced technique on vehicle emissions. Although the total OH reactivity declined greatly, the fraction of missing OH reactivity kept stable at ca. 30% in summer, and slightly varied in seasons. Basically, a relative higher level of portion for missing OH reactivity existed during the summer compared with lower level in autumn and the lowest in winter. Total OH reactivity measurements diagnose air quality as a whole, and give the information on unknown trace species in the air. Furthermore, oxidative capacity analysis derived from HO_x cycle reactions provides indispensable information for ozone production, which directly threats the human health, vegetation, and ecosystem in the troposphere.

The previous researches pointed to limitations in our understanding of the air quality considering HO_x cycle-involving reactants and photochemical processes in a diversity of places

except for megacity. It seems likely that the measurement site of Tokyo and in its vicinity contains sophisticated chemical reactions that boost the active total OH reactivity and secondary products formation. However, field studies efforts can examine OH reactivity from comparable contrasting places. Investigations on a diversity of locations may provide thorough information in identifying the typical air quality, exploring unknown trace species, investigating missing OH reactivity and estimating oxidants formation. Such studies can indicate a geographically diverse "map" of the air quality, providing quantitative understandings of the OH reactants, and can guide ozone mitigation scientifically, therefore is urgently required.

1.8 Motivation

Based on the facts that reactions occur in the air are changing the air composition indeed and causing secondary products. This work focused on answering questions like regardless of the great amount of trace species in the air, how to find unknown VOCs. And questions when considering the formation of secondary products (ozone) which process/parameter affect it mostly, and how to achieve mitigation effectively. Hence, here comes the motivation of this research which including three aspects as follows:

(1) Explore the total OH reactivity, quantify the missing OH reactivity, and extrapolate information on unknown species in urban areas;

(2) Get highly sensitive analysis of ozone production regime in terms of VOC-limited or NO_x-limited, to reduce ozone effectively;

(3) Investigate the contribution of missing OH reactivity and aerosol uptake effects to ozone production potential and their influence on ozone production regime.

Therefore, three different model places were chosen for field studies, in which the chemical reaction in abundance was quantitatively evaluated by measuring total OH reactivity and other trace species. The first location is a suburban area in Tsukuba, second is a coastal industrial region in Yokohama, and the third one in a "clean city" (Kyoto). Through such comprehensive field measurements, the existence of missing trace species could be handled via OH reactivity measurement and analysis. On the other hand, unknown reaction pathway and their oxidative capacity could be assessed and compared. Ozone, as one of the most important oxidants (secondary products) in the air, was thoroughly inspected, and the ozone production potential

and ozone production sensitivity related to its precursors-involved reactions were investigated under different conditions. Missing OH reactivity's influence to HO_x cycle was assessed as a upper limit regarding ozone production potential. The heterogenous effects of hydroperoxy radicals uptake with respect to ozone production potential and ozone sensitivity were discussed in this work. The mechanism of ozone production in different locations could provide more information on the oxidative capacity of the air.

In addition, Appendix introduced laboratory work focused on the development of our technique to detect other peroxy radicals. Kinetic studies have been conducted to explore the rate constants between simple peroxy radicals and NO_x under atmospheric conditions.

1.9 Structure of this thesis

Followed by the motivation, here states the whole structure of this document. Chapter 1 provides an overview of the background related to radicals, which is crucial to convert primary pollutants into secondary pollutants in the air. The whole contents focus on the generation, propagation, and termination of three types of radicals (OH, HO_2, and RO_2) in HO_x cycle. The second half of Chapter 1 introduces the set of instrumentation applied in field campaigns. Section 1.5 describes the instrument for radicals detection used in our lab. This section firstly depicts two laser techniques separately and then combines them together to give the panorama. Section 1.6 explains other comparative OH reactivity detection techniques. Then a review conveys a brief comparison on OH reactivity techniques used in the field studies. Finally the situation of OH reactivity measurement was stressed in Japan and remaining problems were specified in Section 1.7 followed by the motivation of this work in Section 1.8.

Chapter 2 explains the details of three field measurements conducted in Tsukuba, Yokohama, and Kyoto. Each section firstly grasped the characteristics of measurement site, and then describes in-situ observation from the perspective of trace species concentrations and total OH reactivity. Unknown trace species was described in the form of missing OH reactivity. Furthermore, information on the source of missing OH reactivity was characterized at each site. The last section in Chapter 2 synthesizes all campaigns' results.

Chapter 3 explores ozone production analysis based on the results from three field studies. As the main by-products of HO_x cycle, ozone's relationship with its precursors (VOCs and NO_x)

and HO_x radicals was reported to be non-linear and complex. Mitigation of main precursors in the air cannot bring same reduction of ozone. Therefore, this chapter examined the mechanism of ozone production potential in different air conditions, quantified unknown trace species' contribution to oxidants generation, and further investigated the change of ozone production from heterogeneous effects, i.e. ozone reduction caused by the radicals loss via aerosol uptake.

The second part of Chapter 3 explaines the results of ozone regime in the consideration of missing OH reactivity and aerosol uptake effects. VOC-limited regime was converted into NO_x-limited regime after taking the missing OH reactivity into account. Moreover, heterogeneous effects indicated identical transitional shift on the regime with missing OH reactivity. When making stringent policies to control ozone, the consideration of influence from missing OH reactivity and heterogeneous effects would be necessary.

Chapter 4 summarizes the major findings obtained from this study, proposes problems need to be considered in future for field studies, gives suggestions to solve air pollution problems, and achieves ozone mitigation effectively.

Appendix lies on the laboratory application of LP-LIF technique. The system was developed to measure some type of RO_2 radicals successfully by oxygen addition into the detection cell under low pressure. The kinetic reactions between three representative RO_2 radicals with NO_x under atmospheric conditions were discussed.

Chapter 2

Field measurements

Three different types of field studies were conducted in Japan in summer, where the strong solar radiation accelerates gaseous reactions in the air. The sites in Section 2.1 and Section 2.2 are not far away from the megacity Tokyo, however, with varied local circumstances. Transported air pollutants and local air emissions should be studied from such two measurements. Section 2.3 interpreted a relatively clean city air quality in Japan, the observation was conducted during the COVID-19 pandemic, from which constrained the anthropogenic activities, while can somehow predict a future quasi-zero emission society. Total OH reactivity in all three studies were continuously measured, concurrently with trace species detecting. A comparison among these observations and other campaigns can help to diagnose local air quality.

2.1 Suburban area; the case study in Tsukuba in 2017 summer

The first field measurement was chosen at Tsukuba, a suburban area in Japan, Transported air pollutions from the Tokyo area, surrounding vegetation, and local anthropogenic emissions such as traffic exhaust were supposed to be the main pollutants.

2.1.1 Description of the measurement location

We conducted a summer campaign in August 2017 at the National Institute for Environmental Studies (NIES; 36°03′N, 140°07′E), located in the suburban area of Tsukuba city, Ibaraki Prefecture, Japan. The observation site (see Figure 2.1) is located roughly 50 km northeast of Tokyo, 9 km west of Kasumigaura (the second largest lake in Japan), and 12 km south of

Figure 2.1: Map information of Tsukuba campaign.

Tsukuba Mountain. Moreover, the observation site is surrounded by large industrial regions: North Kanto industrial region to the west, Keihin industrial area to the southwest, Keiyo industrial region to the south, and coastal industrial areas facing the Pacific Ocean, from southeast to northeast. Tsukuba does not have significant local emission sources; rather, it receives air masses transported from Tokyo, from industrial regions, and possibly from natural surroundings ([Chatani et al., 2018]; [Kondo et al., 2008]; [Matsui et al., 2009]; [Morino et al., 2011]) that may influence the atmospheric environment in situ. Vegetation around observation site mainly distributed at parks and pedestrian streets which may be local BVOCs source. Agricultural fields which are decentralized across the whole city may also have a contribution. The observation was conducted from August 22 (partly from August 21) to August 28. It should be noted that since August 26 and 27 comprised a weekend, fewer emissions from local and upwind areas were expected.

2.1.2 Methodology in the field study

Along with OH reactivity, concentrations of 54 trace species were simultaneously measured, where CO, SO_2, NO_x, and O_3 were monitored using commercially available analyzers (Thermo Scientific, Model 48i-TLE for CO; Thermo Scientific, Model 43i-TLE for SO_2; Thermo Scientific,

Model 42i-TL for NO_x; and Dylec, Model 1150 for O_3). Both CO and SO_2 were monitored using a time resolution of 1 min at a sixth-floor height; NO_x and O_3 were monitored at ground level with 1-min, and 10-s time resolution, respectively.

The 46 NMHCs of C2-C10, including 22 alkanes, 11 alkenes, one alkyne, three BVOCs (isoprene, α-, and β-pinene), and 9 aromatics, were measured with 1-hour intervals via online gas chromatograph (GC; Agilent 6890) with a flame ionization detector (FID). For the calibration of NMHCs, standard gases (1 ppm, PAMSJ58; Sumitomo Seika Chemicals, Japan; 1 ppbv; Taiyo Nippon Sanso Corporation, Japan) were utilized.

In the oxygenated VOC group, formaldehyde (HCHO) and glyoxal (OCHCHO) were measured on the fourth floor of the laboratory building. Formaldehyde was measured by automatic analyzer (AL4021, Aero-Laser GmbH, Germany). The HCHO monitor measured atmospheric HCHO by transferring the gas phase into the liquid phase, based on the Hantzsch technique, with a 1-min time resolution [Junkermann and Burger, 2006]. Glyoxal was measured by incoherent broadband cavity-enhanced absorption spectroscopy (IBBCEAS). To achieve simultaneous concentrations of OCHCHO, the derived absorption spectra were retrieved using DOASIS software v3.2.3505 (Institute of Environmental Physics at Heidelberg University, Germany) and a wavelength range of 450-460 nm. Absorption cross section for OCHCHO as reported by [Volkamer et al., 2005] was used.

Weather conditions were also recorded on-site by the air quality research station in NIES. Parameters including hourly wind direction (WD), wind speed (WS), ambient temperature, relative humidity (RH), and $PM_{2.5}$ (fine particles with a diameter of 2.5 um or less) were measured. Solar radiation of total sunlight and ultra-violent A were recorded for meteorological reference. The station also provided hourly methane concentrations during this campaign.

2.1.3 Meteorological conditions and trace species

The air mass (refer to the bottom graph in Figure 2.2) that originated from southwest–northwest between August 22 and 25, and which passed through the metropolis of Tokyo and/or large surrounding industrial areas, may have brought polluted mainland air to the observation site. On August 27 and 28, northerly–easterly winds brought relatively clean air masses from the Pacific Ocean through Mt. Tsukuba and Lake Kasumigaura. On August 26, even though air

direction was east/northeast, wind passed the North Kanto industrial area inland and returned without moving out to the Pacific Ocean. As such, the measurement site received not only local emissions but also air masses from urban anthropogenic and partly rural biogenic emissions. Typical wind speed was 2–3 m/s with which the air masses could cross 40–50 km in 5 h, i.e., they could transport from Tokyo in ca.5 h to observation site. Backward trajectories are provided in the Figure 2.3. The time series of inorganic species $SO_2, CO, PM_{2.5}, O_3$, and NO_x are shown in Figure 2.2 alongside weather conditions (RH, solar radiation, and temperature).

The maximum temperature was observed at 14:00 during the daytime and exceeded 34°C. On August 26 and 27, the highest temperature was below 30°C. The peak solar radiation demonstrated a similar trend to temperature. On August 25 and 26, radiation was weaker than on other days. The RH was influenced by both temperature and solar radiation and showed an opposite trend while varied from 43% to 93%.

Futhermore, SO_2 was observed in the range of 0–4 ppbv, and the highest concentration of up to 4 ppbv occurred on August 28. The period from August 26 to 28 with a northerly–easterly wind direction had a larger SO_2 concentration. This may suggest the presence of SO_2 emissions from coastal areas. There were large peaks in the afternoon/night on August 22, 24, 26, and 28, when CO, NO_x, and selected anthropogenic VOCs (alkanes and alkenes) also had concurrent peaks, indicating the existence of specific pollutant emissions sources. No clear evidence of a specific source was found; however, oceanic vessels that burn bunker oil for diesel engines may be a possible explanation.

The CO was present in much larger concentrations and maintained above 250 ppbv from August 22 to 26, when air masses from Tokyo or other industrial areas passed the observation site. Contrastingly, concentrations declined and exhibited lower values on August 27 and 28, when northeasterly and easterly winds brought relatively clean air from the Pacific Ocean. Since August 27 was a Sunday (part of a weekend), the concentration on that day should represent local background levels. An increase of CO in the afternoon was measured from August 28 (start of the week). Meanwhile, $PM_{2.5}$ depicted a similar tendency to CO, i.e., a larger concentration from August 22 to 26 and a decline on August 27 and 28. The trends for CO and $PM_{2.5}$ showed that the Tsukuba air quality was influenced by wind direction, which transported pollutants to the campaign site from surrounding areas. The average hourly concentration of $PM_{2.5}$ was 13.5

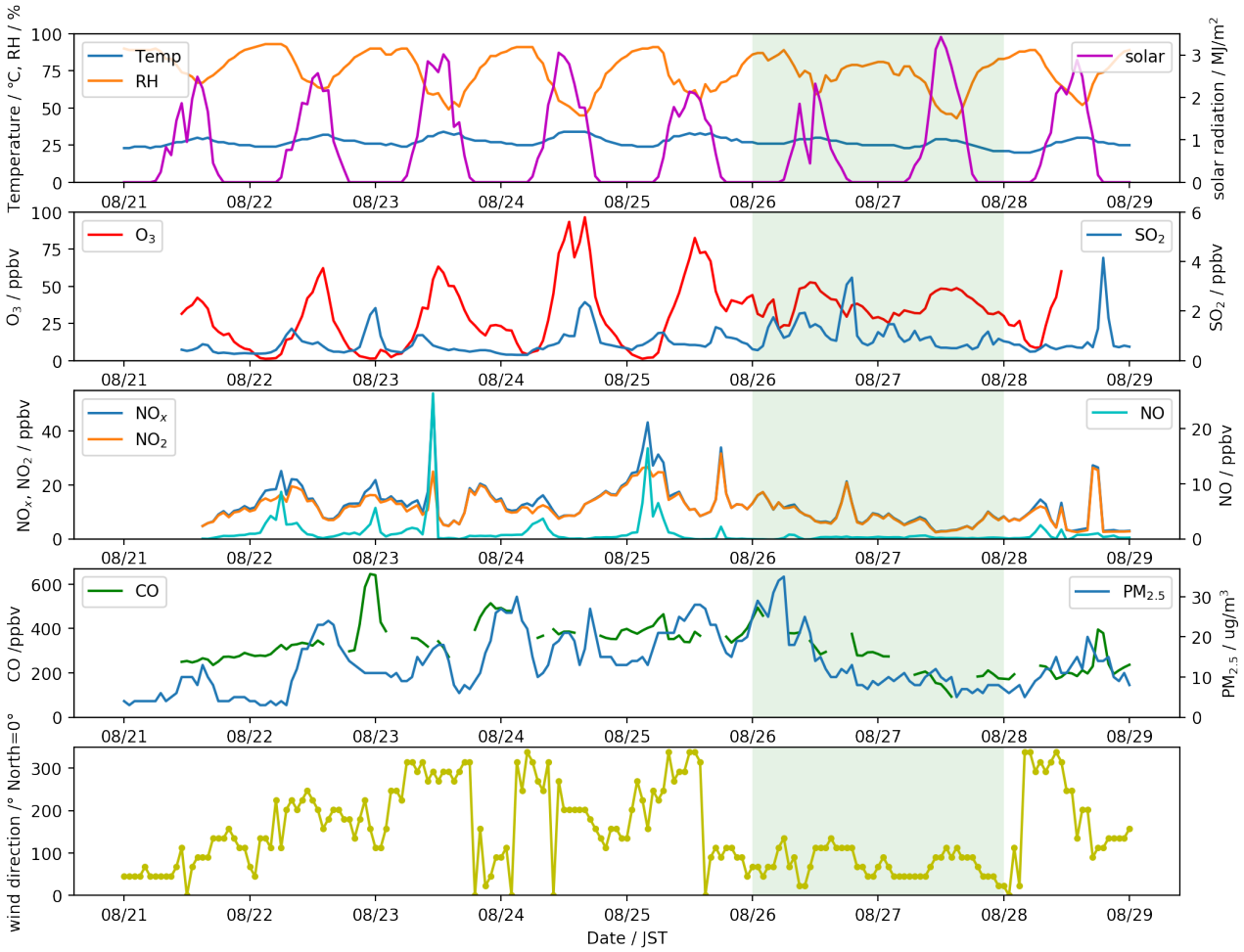

Figure 2.2: Graphs from the top to bottom are time series of weather conditions (including Temperature, RH, and solar radiation), $O_3, SO_2, NO_x\,(NO_x = NO_2 + NO), CO, PM_{2.5}$, and wind directions during the summer campaign. The wind directions were plotted in degrees clockwise from north as zero degree. The weekend (August 26 and 27) is highlighted in light green shaded area.

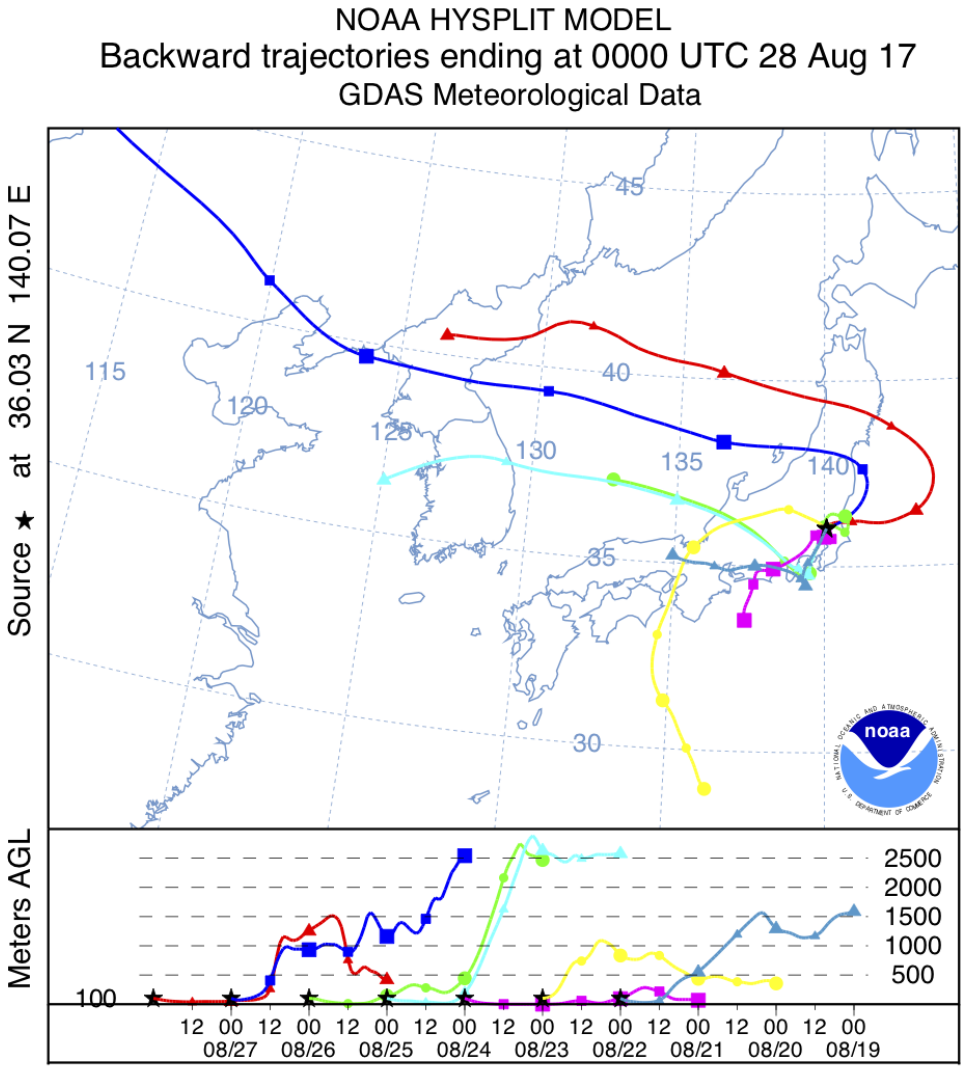

Figure 2.3: Backward trajectory analysis (morning time [UTC+9]) at 100 m height. The air mass was traced within 72 hrs, air mass on the first day of August 22 was plotted since 19^{th}. From 22^{nd} to 26^{th}, the air masses passed from urban site such as Tokyo. On 27 and 28, the wind flowed from the Pacific Ocean.

ug cm^{-3}. Diurnal variations of $PM_{2.5}$ indicates the daily peak to be at noon and a minimum during nighttime, revealing secondary formation in addition to primary emissions during the day.

Similar to CO and $PM_{2.5}$, higher NO_x concentrations were observed from August 22 to 26 and lower values on August 27 and 28, indicating a significant contribution of transported pollutants between August 22 and 26. Since August 26 and 27 was a weekend, when traffic flow was scattered throughout the day and NO concentrations were < 0.8 ppbv during these two days. On August 28 morning, NO showed a small peak of 2.5 ppbv. Generally, NO_x was present due to on-road vehicles and fuel combustion. This peak can be explained by rush-hour emissions, which were assumed to reflect the impact of local emissions.

Higher ozone values were recorded during daytime when photochemical reactions were active and reached a maximum in the afternoon. Lower concentrations were observed at night, due to the lack of photochemical production and the deposition processes driven by shallower boundary layers. In addition, there was significant NO (hourly average: 1.22 ppbv) at night from August 22 to 26, which was emitted from local source and may significantly titrate ozone. The highest ozone concentration (above 100 ppbv) was observed on August 24. Following on, we found that ozone was not significantly consumed during nighttime on August 26 and 27, which may have been due to the low level of NO with an average concentration of 0.15 ppbv during the weekend. Additionally, even though about 40 ppbv O_3 during the weekend could produce radicals along with other sources such as HONO and OVOC which initiated HO_x cycle, the overall ozone production during the daytime was undersized. The lack of NO on weekend made the HO_x cycle propagation less effective and led to less ozone production during the daytime.

Figure 2.4 provides the time series and diurnal profiles of NMVOCs in groups during the observation period. The concentration of alkanes represented almost half of the measured NMVOCs, where OVOCs takes 19% (only contains H_2CO and glyoxal), aromatics 13%, alkenes 9%, alkynes 5% (acetylene), and BVOCs 3% (isoprene and monoterpene). The most abundant species (in ppbv) was propane (2.77 ± 2.32), followed by ethane (1.79 ± 0.82), n-butane (1.01 ± 0.77), i-butane (0.68 ± 0.57), and i-pentane (0.67 ± 0.63) in alkanes (except methane). In alkenes, these were ethene (0.95 ± 0.72), followed by propene (0.17 ± 0.18), 1,3-butadiene (0.09 ± 0.02), and i-butene (0.07 ± 0.04). In aromatics, these were toluene (1.21 ± 0.98), followed

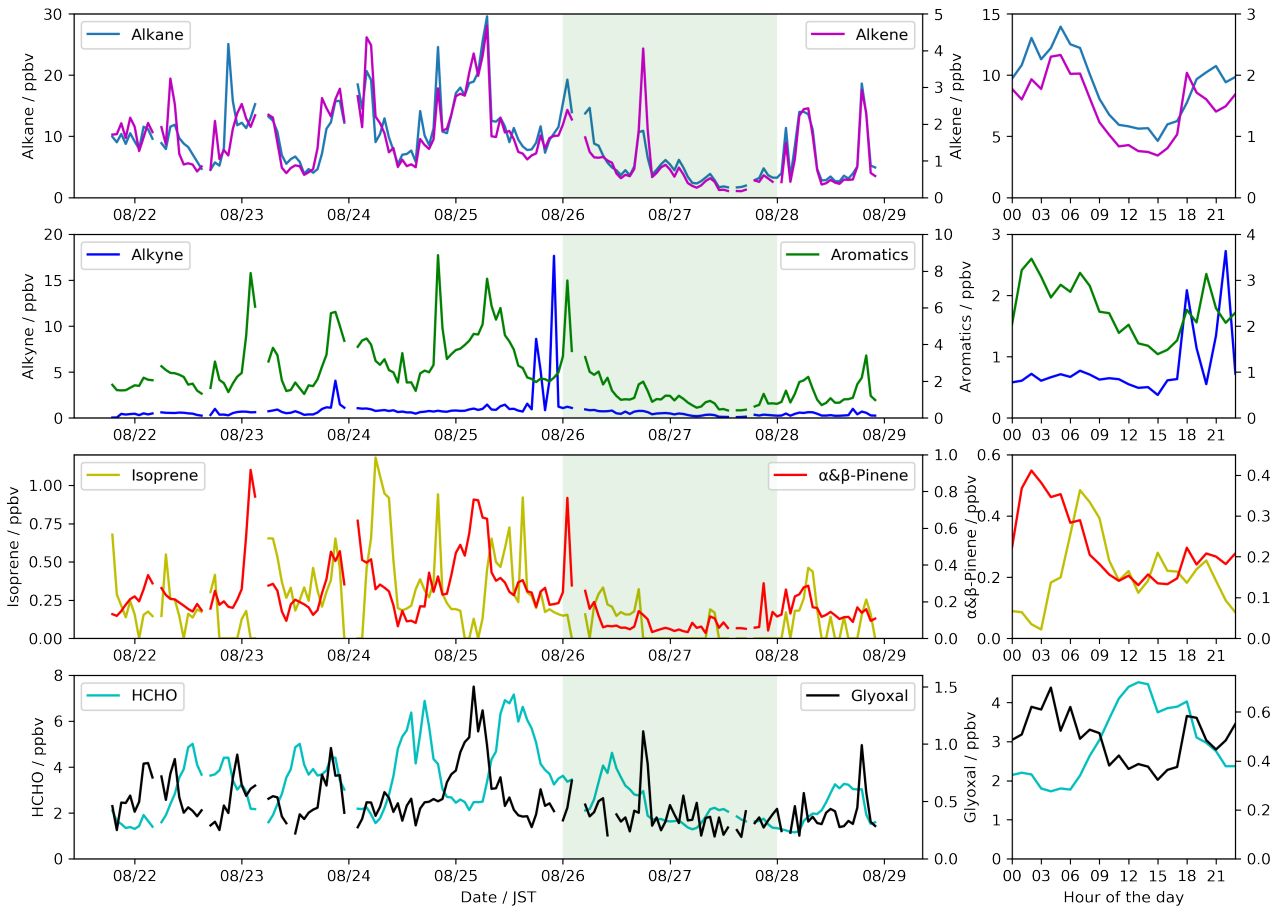

Figure 2.4: The time series (left side) and diurnal profiles (right side) of anthropogenic and biogenic VOCs. August 26 and 27 (on weekend) are highlighted in light green area. The diurnal profiles are using the same y-axis orders as time series, in which legends were set at corresponding side.

by benzene (0.29 ± 0.14), ethylbenzene (0.28 ± 0.31), and m,p-xylene (0.21 ± 0.20).

Anthropogenic VOCs (AVOCs), including alkanes, alkenes, alkynes, and aromatics, together with BVOCs, essentially exhibited similar trends to $\mathbf{CO}, \mathbf{PM}_{2.5}$, and $\mathbf{NO}_x$, i.e., larger concentrations from August 22 to 26 and lower values on August 27 and 28. This indicates that they had been transported importantly from surrounding areas between August 22 and 26. The movement primarily occurred at night since the lifetime of reactive species such as isoprene is few hours during the daytime. A morning peak on August 28 depicted contributions from local emissions. Isoprene and $\alpha-$ and $\beta-$pinene were measured as BVOCs and represented typical emissions from trees and shrubs ([Altshuller, 1983], [Tanner and Zielinska, 1994], [Watson et al., 2001]); these also delineated temperature dependence, where lower concentrations were evident on cooler days. The diel profiles of AVOCs and BVOCs were basically similar. The change of boundary layer from 300 m at night to 1000 m at noon in summer in Tsukuba [Chen et al., 2001] and consumption by photochemical reactions explain this phe-

nomenon. Acetylene as alkynes had a strong emission event on August 25 night which affects average diel profile. $\alpha-$Pinene and $\beta-$pinene showed similar trends while isoprene depicted the depletion during the night. This is because isoprene production requires solar radiation and thus emission at night is negligible.

From aforementioned note, the alkane and alkene spikes in the afternoon/night on August 22, 24, 26, and 28 may have been derived from specific pollutant emissions that we were unable to identify. Marine diesel engines are possible sources of these peaks. The NO_x, SO_2, and AVOCs such as propane and butane may be representative of species emitted from waterborne transportation and navigation [Jun et al., 2000].

The source of H_2CO included primary emissions and secondary photochemical formation [Lui et al., 2017]. H_2CO displayed a mimic tendency to ozone, i.e., a maximum concentration during daytime and low concentration at night. This indicates that H_2CO might have been from the photochemical reaction process, corresponding with a previous report stating that NMVOCs are the dominant precursors of H_2CO over continental areas [Stavrakou et al., 2009b]. The high level of H_2CO evident from August 22 to 26 may have been caused by the large-scale transportation of precursor pollutants from inland areas.

It has been reported that BVOCs' oxidation process can explain ca. 55%–70% of the global glyoxal ([Myriokefalitakis et al., 2008]; [Stavrakou et al., 2009a]). We also found that the peaks of glyoxal appeared after those of H_2CO, which might reflect differences in formation processes between them. Direct anthropogenic emissions in urban region might also make the difference ([Stavrakou et al., 2009a]; [Zhang et al., 2016]).

2.1.4 Total OH reactivity and missing OH reactivity analysis

Figure 3.5 shows the time series of total OH reactivity and missing OH reactivity. Note that some trace species had missing parts such as CO missing due to baseline measurements as shown in Figure 3.2, these gaps were fulfilled by linear interpolation. Although this could make potential error in calculated OH reactivity, its effect is limited because of their relative small fraction to total OH reactivity.

Total OH reactivity displayed an identical trend to the observed trace species as expected. There were larger total OH reactivity from August 22 to 26 and lower values on August 27

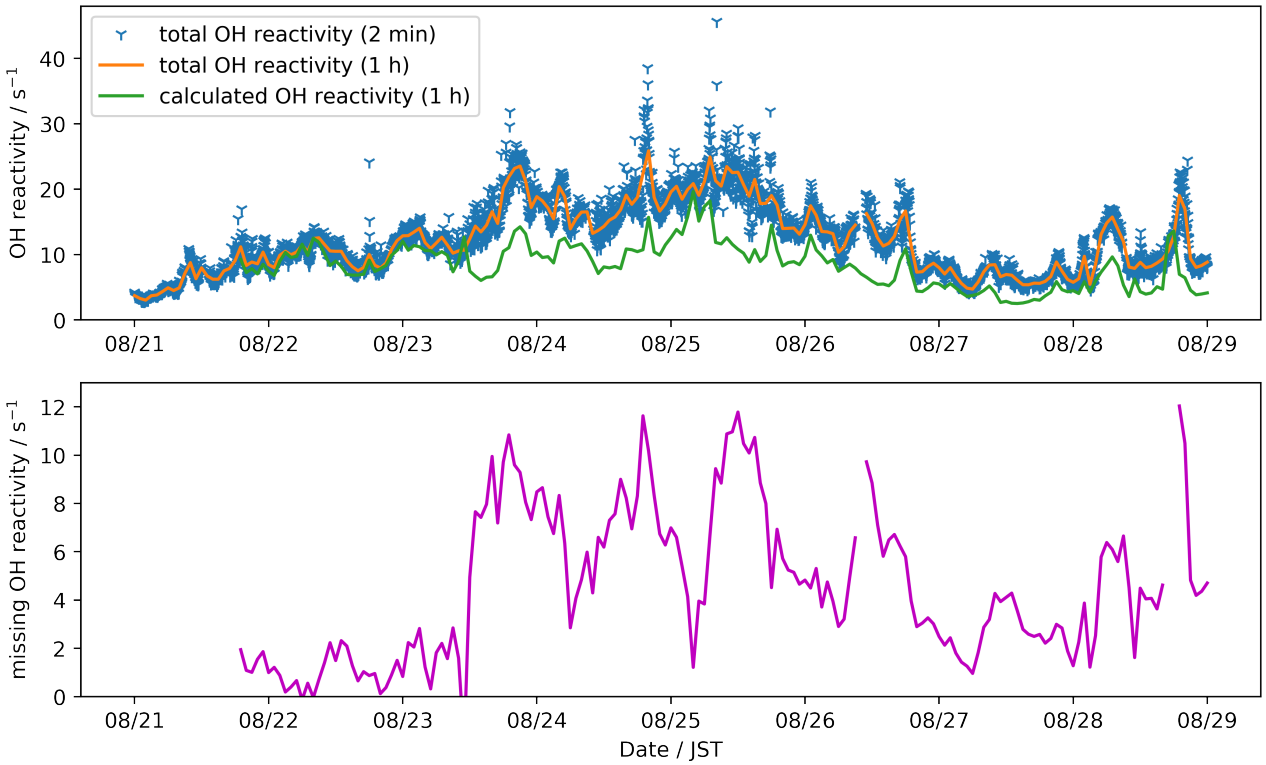

Figure 2.5: Time series of total OH reactivity (upper graph) compared with calculated OH reactivity (bottom graph).

and 28. Diurnal spikes appeared in the early morning and late afternoon throughout the entire period, which may reflect the contribution from local emission, e.g. from transportation. Average total OH reactivity over the entire period was 12.9 s^{-1}. Hourly mean values ranged from 5 to 26 s^{-1}. Figure 2.5 also shows the calculated OH reactivity from detected trace species, which is close in appearance to total OH reactivity, but with lower rates. This discrepancy occurred due to missing OH reactivity from unmeasured/unknown species, as showed in the bottom graph of Figure 2.5. Missing OH reactivity accounted for 35.3% of the total OH reactivity on average over the entire period and increased up to 11.8 s^{-1}. On 22^{nd} and 23^{rd}, lower missing reactivity was anonymously obtained. However, we cannot find a big difference in wind direction and backward trajectory analysis from other polluted periods other than that the air masses on the two days came from a height above 500 m. Distribution of compositions was also same as other polluted days except for lower level of aromatics and BVOCs. Several peaks were observed on August 23, 24, 25, and 26. Following on, missing OH reactivity decreased on August 27 and 28.

Figure 2.6 shows the fractions of trace species (in groups) to OH reactivity and their diel variations. Among the observed species, the most significant contributors to total OH reactivity

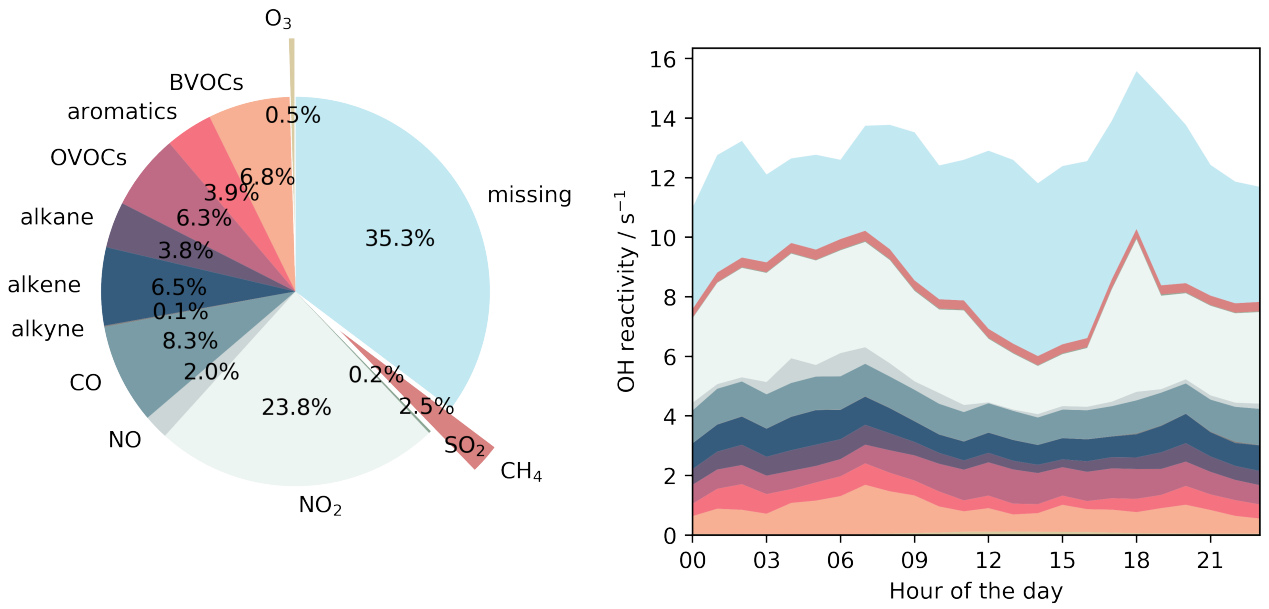

Figure 2.6: The fractions of trace species in the total OH reactivity (left side) and the hourly diel averages of total OH reactivity (right side).

were inorganics NO_2 (23.8%) and CO (8.3%), followed by organic groups, i.e., BVOCs (6.8%), alkenes (6.5%), OVOCs (6.3%), aromatics (3.9%), and alkanes (3.8%). The added BVOCs' reactivity began to increasing during the early morning when solar radiation became available which reflects mainly the isoprene profile. Subsequently it decreased at noon due to active photochemical reactions and expansion of boundary height. After that, the concentration was almost constant. The added reactivities of aromatics, alkanes, alkenes, and NO_x displayed similar trends: accumulation at night and a decrease in the daytime. However, the added reactivity of AVOCs did not show a marked increase during traffic rush-hour, when vehicles were expected to emit pollutants intensively. This indicates that the contribution of local emissions might not be dominant compared to transported pollutants. The reactivity of OVOCs and O_3 exhibited close relationships based on the photochemical process, where largest concentrations were observed at noon. Regardless, there was only a small discrepancy: O_3 only appeared during the daytime when solar radiation drove photochemical reactions with the exception of the weekend, while OVOCs showed a long tail after sunset.

Missing OH reactivity during the daytime was higher than at night, which was similar to O_3 and OVOCs. This may reflect the existence of additional unmeasured species generated during the daytime. Unknown primary biogenic species and OVOCs in this campaign also likely contributed to missing OH reactivity [Di Carlo et al., 2004]. [Ramasamy et al., 2016] found

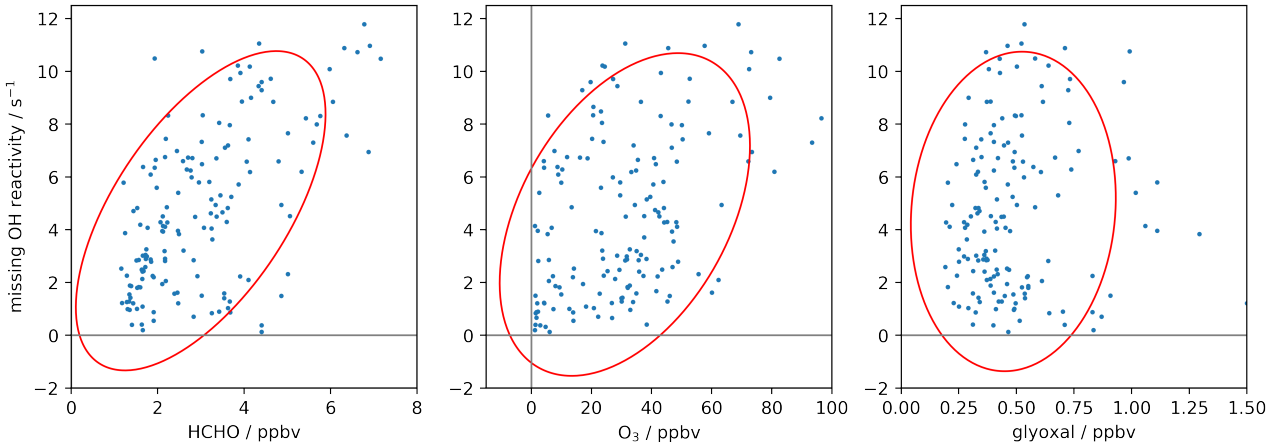

Figure 2.7: Correlation analysis of H_2CO (left graph), ozone (middle graph), and glyoxal (right graph) with missing OH reactivity. A 95% confidence ellipse of the covariance was plotted in each graph to visually compare the correlation (standard deviation equals 2).

that missing OH reactivity and photochemical activities are positively related. Therefore, the relationship between missing OH reactivity and OVOCs (including O_3) was explored, and Figure 2.7 depicts the result.

A rank-correlation test confirmed that H_2CO had a moderate correlation with missing OH reactivity, where R_s (Spearman's rank correlation coefficient) equals 0.51. Glyoxal exhibited the weakest correlation with missing OH reactivity, where R_s equals 0.14 and R_s from ozone is 0.43.

Formaldehyde was high at noon, which implies that H_2CO was mainly formed through photochemical oxidation processes. The moderate correlation between H_2CO and missing OH reactivity suggesting missing OH reactivity could also be originated from secondary photochemical products. As for the source of oxygenated products, H_2CO is generated from both AVOCs and BVOCs, while glyoxal is mainly from BVOCs oxidation. This could explain the weakest relationship with glyoxal and indicate missing OH reactivity was originated from both AVOCs and BVOCs.

In Tsukuba field study, acetaldehyde was not available although it may become a significant reason for missing OH reactivity. Considering the case of London, where H_2CO and CH_3CHO account for 94% of carbonyls' reactivity [Whalley et al., 2016], hereinafter, the ratio ($[CH_3CHO]/[H_2CO] = 4.79/6.26$ ppbv ppbv^{-1}) was used to estimate CH_3CHO from time series of H_2CO. The relationship is similar to other observations conducted in urban and suburban areas [Yoshino et al., 2012];[Jiang et al., 2019]. As Figure 2.8 shows, CH_3CHO can only explain

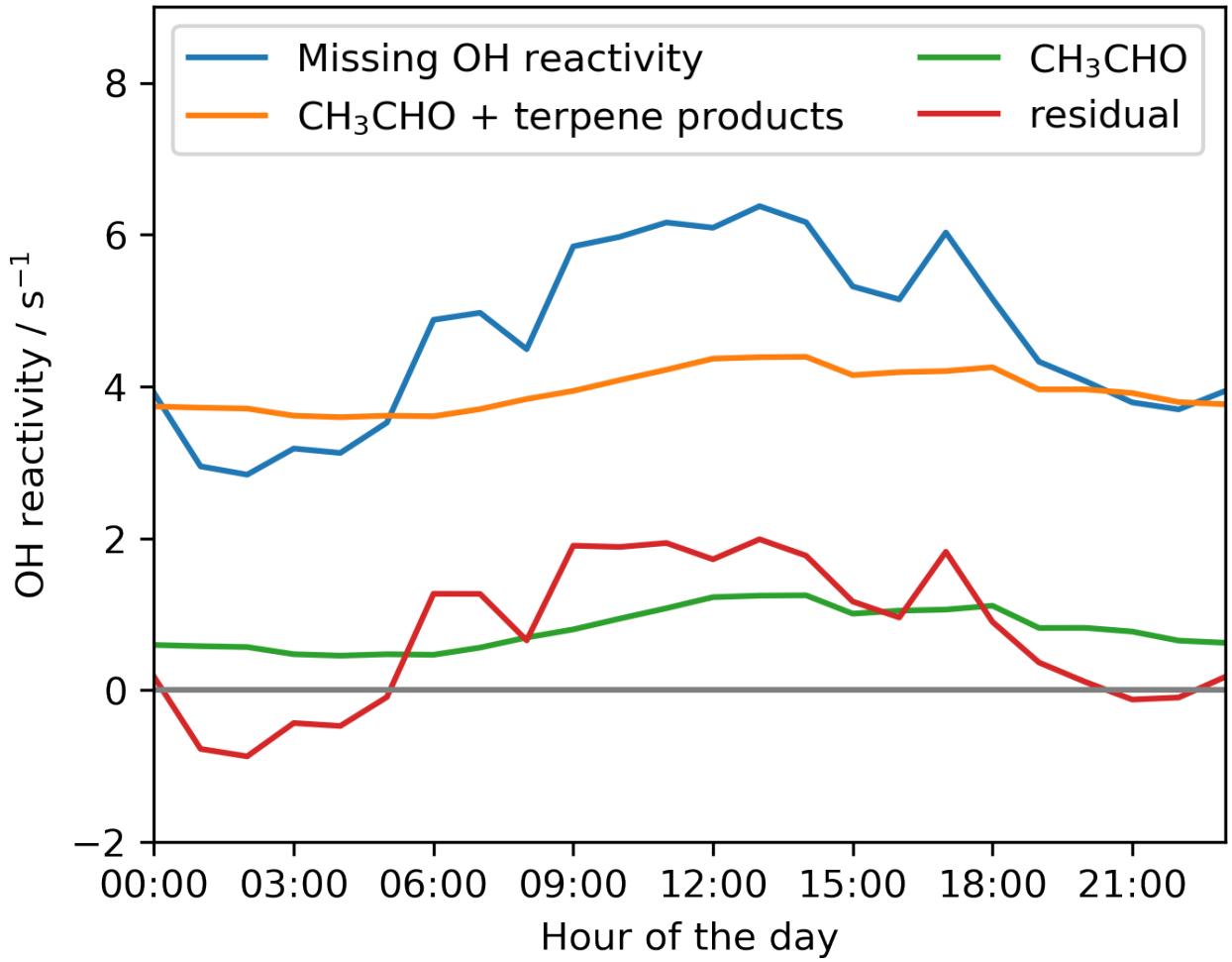

Figure 2.8: Hourly diurnal averages of missing OH reactivity (blue line) along with estimated reactivity of secondary products from both terpenes and CH_3CHO (orange line), and estimated reactivity of CH_3CHO (green line). Residual in red line indicates the difference between missing OH reactivity and estimated reactivity.

a limited part of missing OH reactivity and require us to consider intermediate species which are unmeasurable or hard to detect.

[Whalley et al., 2016] investigated contributions of secondary oxidation products to OH reactivity combined with MCM model calculation in central London and reported that primary terpenes themselves have a small contribution to total OH reactivity (1.4%) while intermediate species from their oxidation such as pinonaldehyde could account for a larger fraction (12%). Using the relationship between the reactivity of parent BVOCs and that of their oxidation products in London case, it was reckoned that the contribution of secondary products from terpenes to be 3.1 s^{-1} compared with observed terpenes reactivity of 0.36 s^{-1} on average. As MCM calculation for London case showed that reactivity from secondary products of terpenes did not have a strong diel trend, therefore it was assumed the contribution of secondary prod-

ucts from terpenes to be constant. In Figure 2.8, combining with CH_3CHO reactivity, the estimated reactivities may explain nocturnal missing OH reactivity and two-thirds of daytime missing reactivity. However, note that this estimation may be too rough to predict the exact contribution. The results should be somewhat overestimated since residual manifested negative values.

The remaining one-third of missing OH reactivity in Figure 2.8 remained as residual during the daytime. It was reported in chamber experiments that photochemical oxidation of aromatics can produce secondary products which increase total OH reactivity [Sato et al., 2017]. This is because, the oxidation products are unsaturated multifunctional products such as epoxy-dicarbonyls and furanones, which have higher OH reactivity than the parent [Sato et al., 2017]. In the case of toluene, missing OH reactivity was up to 3 times larger than the reactivity of consumed reactants. In our campaign, up to 8 ppbv of aromatics, which is equivalent to ca. 5 s^{-1} reactivity, were observed in the morning from August 23 to 26. The consumption of those high levels of aromatics can produce substantial secondary OVOCs, and may explain the increase of missing OH reactivity in the daytime. On August 22, H_2CO increased during the daytime, while missing OH reactivity was kept small. Alkanes and alkenes had significant values on the morning of August 22, when photochemical reactions may bring H_2CO formation at noon. However, these processes could not link secondary products to the missing OH reactivity. In contrast, aromatics evidenced small concentrations on the morning of August 22 and increased from August 23 to 26, when high missing OH reactivity was observed. This supports that secondary products from aromatics may have been one reason for the missing OH reactivity. In London case, missing OH reactivity exhibited smaller diel variation, while in Tsukuba case higher values were appeared during the daytime. Furthermore, this observation observed elevated aromatics which is equivalent to 1.4 s^{-1} on average compared to the London case of 0.24 s^{-1} [Whalley et al., 2016]. This difference in aromatics concentration may cause different diel variations of total OH reactivity.

Unmeasured primary BVOCs and AVOCs may also have contributed to missing OH reactivity. Two peaks were recorded from missing OH reactivity on August 28 which were larger than 6 s^{-1} (see Figure 2.5). The peaks are attributed to primary missing OH reactivity from anthropogenic sources since we observed concurrent peaks of total OH reactivity and other

trace species. A research reported around 17% missing OH reactivity has been related to vehicle exhaust gases [Nakashima et al., 2010], which may explain the peak observed in the morning on August 28. The peak in the afternoon was attributed to a special source emitting SO_2, possibly oceanic vessels that burn bunker oil, as noted earlier. These two peaks might represent considerable contributions of primary unmeasured emissions to missing OH reactivity. Total OH reactivity in Figure 2.5 shows peaks not only on the 28^{th} but also other days which appeared in the morning and evening and may reflect the contribution of local emission from transportation. These primary emissions may partly cause missing OH reactivity in the morning and evening in Figure 2.8.

(The result of Tsukuba campaign was published in [Li et al., 2020].)

2.2 Seaside industrial area; the case study in Yokohama in 2019 summer

The second campaign's location was selected to be Yokohama, in a coastal industrial area in Japan. Oceanic air masses from the Pacific were supposed to fresh local air frequently during the summer. Emissions from surrounding manufactories, petroleum solvent, and traffic vehicles were the dominate pollutants' sources.

2.2.1 Description of the measurement location

An intensive field observation was conducted in summer 2019, at Yokohama Environmental Science research institute (YES; 35°28′53″N, 139°39′30″E) in Yokohama city of Japan. Figure 2.9 exhibits the relevant geographical information. The chosen location is situated in Keihin coastal industrial area that faces the Yokohama Port (ca. 4 km) in the southerly direction, Haneda airport (ca. 12 km) and Tokyo Port (ca. 20 km) in the northeasterly direction. The YES institute is largely surrounded by various factories and several chemical industrial, demolition and construction sites including a brewery factory, fossil fuel power station, motor manufacturing plant, and food industry in the vicinity. In addition, since the given location is a curbside site, emissions from main road and container port often encounter the observation site. [McDonald et al., 2018] have found that the use of volatile chemical products (VCPs)

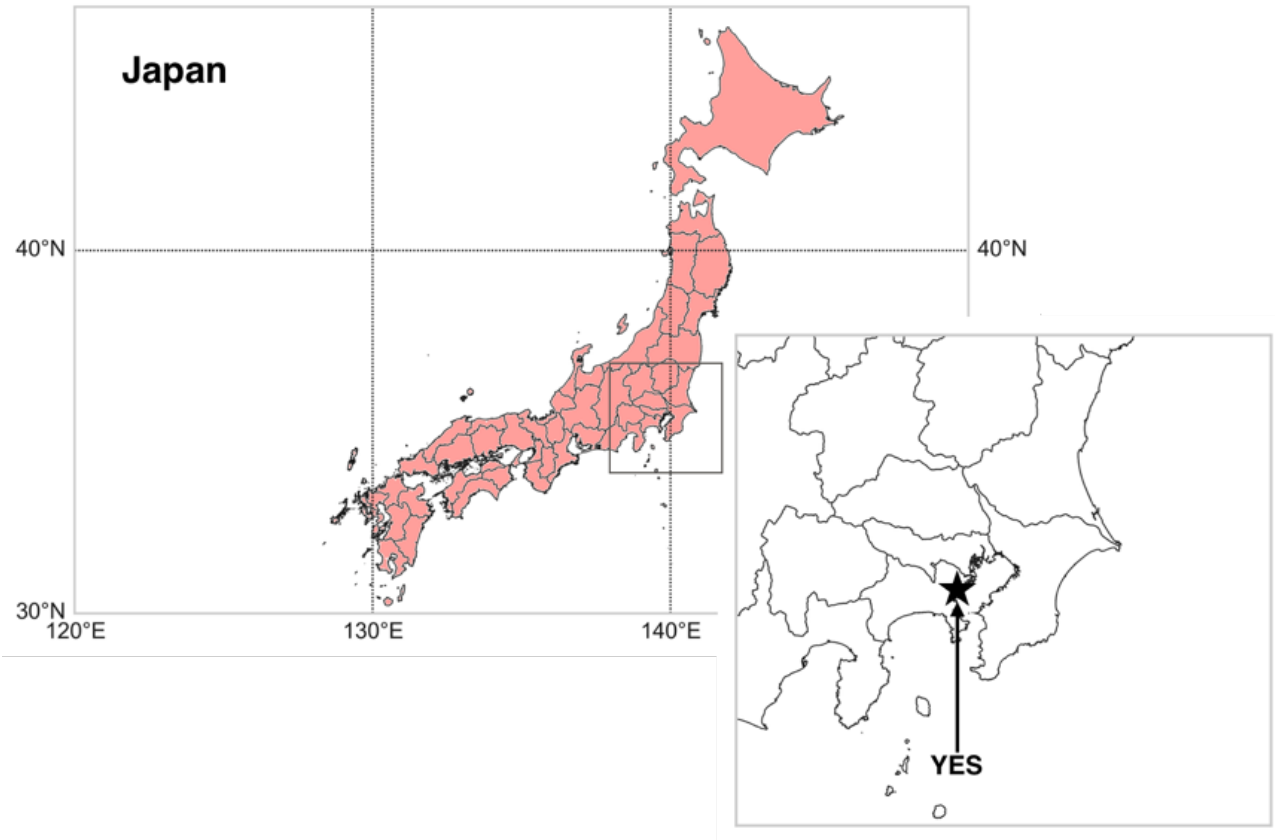

Figure 2.9: Map of Japan and the site of YES as marked with the black star.

constitute half of the petrochemical emissions in industrialized areas. Yokohama coastal industrial area has been reported to receive major emissions from petrochemical storage facilities [Tiwari et al., 2010]. Therefore, in terms of the YES institute, VCPs from surrounding assembly factories, chemical industries, and disposal facilities, mixed with traffic emissions are supposed to be main air pollutants. The observational period started from 25 July to 4 August in 2019. Yokohama is characterized by a temperate climate and affected by monsoon circulation. The predominant wind sector (Figure 2.10), based on hourly wind direction measurements from Japan Meteorological Agency during the observational period, was southerly to southwesterly (from the ocean -78%), followed by northerly (from Tokyo and the surrounding areas -10%) and southeasterly (from the ocean -10%).

2.2.2 Instrumentations used in Yokohama campaign

The composition of the inorganic species was monitored separately by sampling from inlets as showed in Figure 2.11 through 6.35 mm O.D. PFA (perfluoroalkoxy) lines with instruments as follow: O_3 Monitor (UV absorption, Model 1150, Dylec, 10 s time resolution), NO-NO_2-

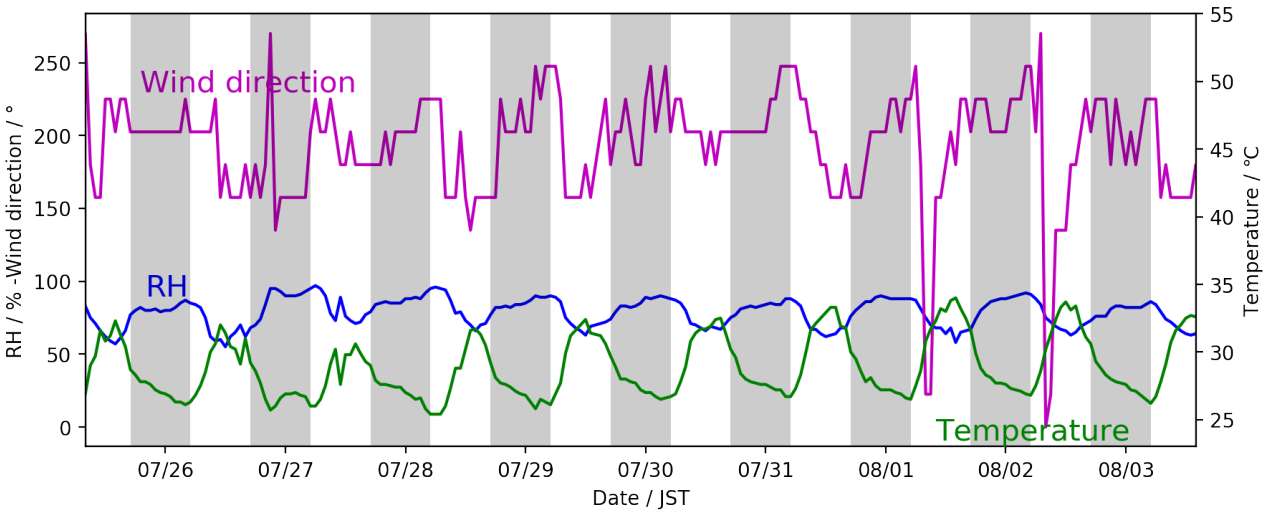

Figure 2.10: Meteorological information of wind direction, RH, and temperature during the observation period. Wind direction starts from the north direction and proceeds in clockwise motion.

NO_x analyzer (Chemiluminescence, Model 42i-TL, Thermo Scientific, 1 min time resolution), Cavity Attenuated Phase Shift for NO_2 (CAPS, Aerodyne Research, 1 s time resolution), and CO Monitor (Model 48i-TLE, Thermo Scientific, 10 s time resolution). Two CAPS devices were used to measure NO_2 from the ambient air (NO_{2aa}) and the reaction cell (NO_{2rc}), respectively. The detection limits (LOD) of some of these species are reported to be several tens of parts per trillion by volume (pptv), which is three orders of magnitude lower than the level measured during AQUAS-Yokohama. The details of each instrument can be found in Table 2.1. In addition, off-line measurement of hydrogen via Reduction Gas Detector (RGD, SRI instruments Europe GmbH) has been conducted in conjunction with ambient observations. Two samples were taken every day in the morning and afternoon, separately.

NMVOCs except aldehyde species were measured by GC-MS and GC-FID. GC-FID (Nexis GC2030, Shimadzu) accompanied with a C2-C5 components concentrator (GL Science) was applied for the detection of short-chain hydrocarbons. All other long-chain hydrocarbons were measured by GC-MS (GCMS-QP2020, Shimadzu) assembly of a pre-concentrator (CC2110, GL Science). Standard gas (HAPs-J44+F7, Sumitomo Seika Chemicals, Japan; PAMs-J58, HAPs-Z, alkenes, Takachiho Chemical Industrial, Japan) was used for calibration. For sampling, 8-min ambient air was drawn into a canister at the flow rate of 25 mL min^{-1} during each even hour coordinated with the centric period of OH measurement. Then the pre-concentrator facilitated 200 mL sampling gas to scrub water vapor and carbon dioxide out. After that, the condensed sampling air will be separated in GC and subsequently detected by MS and FID.

Figure 2.11: Scenery outside the sampling window in Yokohama campaign.

Table 2.1: Species in class and their corresponding detection method deployed in the campaign, time resolution, instrumental uncertainty in percentage, and the contribution of each class to OH reactivity are provided here. Limit of detection (LOD) and the fraction to total OH reactivity is given in parentheses.

Species in class	Instrument	Time resolution	Uncertainty (LOD)	Contribution to OH reactivity in s^{-1} (%)
O_3	UV absorption O_3 monitor	10 sec	0.5% (1 ppbv)	0.02 (0.2)
NO	chemiluminescence	1 min	1% (50 pptv)	1.40 (12.3)
NO_2	CAPS	1 sec	<1% (20 pptv)	4.66 (40.9)
CO	CO monitor	10 sec	1% (1 ppbv)	0.68 (6.0)
H_2	RGD	1 day	2% (20 ppbv)	0.09 (0.8)
C2-C5 NMHCs	GC-FID	2 hour	10%[a]	1.37 (12.0)
Other NMVOCs	GC-MS			
H_2CO, CH_3CHO	HPLC			
H_2CO	Aerolaser HCHO analyser	1 min	2% (100 pptv)	0.31 (2.7)
CH_3CHO	PTR-MS	10 min	<1% (1 pptv)	1.63 (14.3)
glyoxal	IBBCEAS	4 min	<1% (30 pptv)	0.05 (0.4)

[a]From the calibration experiment compared with LP-LIF result.

Except off-line method, Proton Transfer Reaction-Mass Spectrometry (PTR-MS; PTR-QMS 500, Ionicon Analytik, Austria) concurrently measured part of NMVOCs during the observation period. Real-time concentrations of acetaldehyde, acetone, isoprene, benzene, the group of C8-benzene, C9-benzene, and monoterpene were detected by PTR-MS with 10 min intervals. The detailed information has been summarized in the Table 2.2.

Table 2.2: Average concentrations of each measured trace species and their instrumentation information.

groups	species	concentration ± standard deviation 1 σ (in ppbv)	reference
NMHCs			
	n-butane	1.09 ± 1.40	GC-FID
	i-butane	0.572 ± 0.640	GC-FID
	propane	1.36 ± 1.57	GC-FID
	ethane	0.939 ± 0.424	GC-FID
	n-undecane	0.00902 ± 0.00750	GC-MS
	n-decane	0.0135 ± 0.0335	GC-MS
	n-nonane	0.0154 ± 0.0505	GC-MS
	n-octane	0.00885 ± 0.00650	GC-MS
	methylcyclohexane	0.0256 ± 0.0288	GC-MS
	3-methylheptane	0.00465 ± 0.00336	GC-MS
	2-methylheptane	0.00585 ± 0.00447	GC-MS
	2,3-dimethylpentane	0.00784 ± 0.00748	GC-MS
	cyclohexane	0.0367 ± 0.0342	GC-MS
	2-methylhexane	0.0202 ± 0.0166	GC-MS
	n-heptane	0.0236 ± 0.0251	GC-MS
	2,3,4-trimethylpentane	0.00293 ± 0.00110	GC-MS
	2,2,4-trimethylpentane	0.00231 ± 0.00250	GC-MS

3-methylhexane	0.0233 ± 0.0189	GC-MS
2,3-dimethylbutane	0.0395 ± 0.0524	GC-MS
methylcyclopentane	0.124 ± 0.147	GC-MS
n-hexane	0.421 ± 0.499	GC-MS
3-methylpentane	0.159 ± 0.167	GC-MS
2-methylpentane	0.189 ± 0.214	GC-MS
cyclopentane	0.0283 ± 0.0357	GC-MS
2,4-dimethylpentane	0.00527 ± 0.00532	GC-MS
n-pentane	0.506 ± 0.746	GC-MS
i-pentane	1.09 ± 1.40	GC-MS
2,2-dimethylbutane	0.0270 ± 0.0649	GC-MS
1,3-butadiene	0.00914 ± 0.00795	GC-FID
i-butene	0.0289 ± 0.0315	GC-FID
1-butene	0.0385 ± 0.0943	GC-FID
propylene	0.0972 ± 0.0749	GC-FID
ethylene	0.306 ± 0.199	GC-FID
trans-1,3-pentadiene	0.00237 ± 0.00127	GC-MS
cis-1,3-pentadiene	0.00361 ± NaN	GC-MS
trans-3-methyl-2-pentene	0.00288 ± 0.00335	GC-MS
cis-3-methyl-2-pentene	0.00220 ± 0.00259	GC-MS
2-methyl-2-butene	0.0303 ± 0.0401	GC-MS
trans-2-pentene	0.0262 ± 0.0290	GC-MS
cis-2-hexene	0.00422 ± 0.00421	GC-MS
trans-2-hexene	0.00423 ± 0.00361	GC-MS
cis-3-hexene	0.00285 ± 0.00159	GC-MS
cis-2-pentene	0.0155 ± 0.0166	GC-MS
trans-2-butene	0.0387 ± 0.0460	GC-MS
2-methyl-1-pentene	0.00469 ± 0.00408	GC-MS

	2-methyl-1-butene	0.0348 ± 0.0356	GC-MS
	cis-2-butene	0.0324 ± 0.0383	GC-MS
	1-heptene	0.00494 ± 0.00299	GC-MS
	1-hexene	0.00725 ± 0.00506	GC-MS
	1-pentene	0.0209 ± 0.0176	GC-MS
	3-methyl-1-butene	0.0102 ± 0.00997	GC-MS
Aromatics			
	styrene	0.00467 ± 0.00452	GC-MS
	1,3,5-trimethylbenzene	0.00644 ± 0.0247	GC-MS, PTR-MS¶
	1,2,3-trimethylbenzene	0.00383± 0.0107	GC-MS, PTR-MS¶
	1,2,4-trimethylbenzene	0.0164± 0.0560	GC-MS, PTR-MS¶
	m-diethylbenzene	0.000926± 0.000936	GC-MS
	m-xylene	0.0288 ± 0.0254	GC-MS, PTR-MS*
	p-xylene	0.0103 ± 0.00876	GC-MS, PTR-MS*
	o-xylene	0.0133±0.0123	GC-MS, PTR-MS*
	p-diethylbenzene	0.00244± 0.00414	GC-MS
	m-ethyltoluene	0.00895 ± 0.0332	GC-MS, PTR-MS¶
	p-ethyltoluene	0.00477 ± 0.0172	GC-MS, PTR-MS¶
	o-ethyltoluene	0.00464± 0.0157	GC-MS, PTR-MS¶
	ethylbenzene	0.0636 ± 0.0621	GC-MS, PTR-MS*
	i-propylbenzene	0.00190± 0.00451	GC-MS, PTR-MS¶
	n-propylbenzene	0.00289 ± 0.00954	GC-MS, PTR-MS¶
	toluene	0.226 ± 0.243	GC-MS
	benzene	0.0462 ± 0.0389	GC-MS
	2-ethyl-p-xylene	0.00105 ± 0.000406	GC-MS
	4-ethyl-m-xylene	0.00168 ± 0.000603	GC-MS

	1,2,3,5-tetramethylbenzene	0.00152± 0.000374	GC-MS
Biogenic VOCs			
	isoprene	0.0624 ± 0.0536	GC-MS, PTR-MS‡
	α-pinene	0.0160 ± 0.0180	GC-MS, PTR-MS†
	β-pinene	0.00380 ± 0.00338	GC-MS, PTR-MS†
OVOCs			
	isobutanol	0.0434± 0.0451	GC-MS
	ethyl-t-buthylether	0.0352 ± 0.0356	GC-MS
	n-butanol	0.281 ± 0.274	GC-MS
	n-propanol	0.0181 ±0.0170	GC-MS
	isopropanol	0.515 ± 0.442	GC-MS
	buthylacetate	0.0175 ± 0.0161	GC-MS
	methyl-t-buthylether	0.00212 ± NaN	GC-MS
	ethylacetate	0.296± 0.501	GC-MS
	methylacetate	0.0191 ± 0.0115	GC-MS
Aldehydes			
	formaldehyde	1.38± 1.03	HPLC,AL2041
	acetaldehyde	4.41± 1.41	HPLC,PTR-MS
	glyoxal	0.191± 0.0951	IBBCEAS
Ketone			
	methyl-iso-buthylketone	0.0216± 0.0164	GC-MS
	methylethylketone	0.253± 0.241	GC-MS
	acetone	3.60 ± 3.03	GC-MS
Others			
	acrylonitrile	0.0614± 0.0842	GC-MS
	acetylene	0.152± 0.134	GC-FID
Inorganics			

NO	7.84 ± 9.74	Chemiluminescence
NO_2	17.6 ± 13.3	CAPS
O_3	15.5± 12.4	O_3 monitor
CO	119 ± 52.4	CO monitor
H_2	615 ± 148	RGD
CH_4	2000	assumption

¶These species were measured together as C9-benzene by PTR-MS.

*These species were measured together as C8-benzene by PTR-MS.

‡Including isoprene, t-1,3-pentadiene, and c-1,3-pentadiene measured by PTR-MS.

†The two species were measured together as monoterpene by PTR-MS.

Aldehyde group was measured by four different apparatuses. High-Performance Liquid Chromatography (HPLC, Agilent Technologies, Inc.) was utilized for the determination of formaldehyde and acetaldehyde. A separate collection system of HPLC was applied in which inlets went first through ozone scrubber and 2,4-dinitrophenylhydrazine (DNPH) cartridge at the flow rate of 500 mL min^{-1}. After the derivatization of carbonyls, the solvent of acetonitrile collected the products and got further quantified by HPLC. Following this, acetaldehyde was also measured by PTR-MS as mentioned before. We failed to get valid data for the whole period from one device alone, therefore both dataset were adopted and the average value was used when there is an overlap of two instruments. Formaldehyde analyzer (AL4021, Aero-Laser GmbH, Germany) monitored gaseous H_2CO continuously and automatically with 1 min time intervals via hantzsch-reaction [Nash, 1953], which transfers gaseous H_2CO into liquid phase and measures with the fluorescence of 3,5-diacetyl-1,4-dihydrolutidine at 510 nm. The concentrations of H_2CO from both instruments have been synthesized and average value was also applied for the overlap period. An extensive inter-comparison has been conducted for CH_3CHO and H_2CO from different instruments in the Figure 2.12. The relationship between H_2CO and CH_3CHO was fitted via linear regression analysis, where all dots in y-axis ranged from 2 to 8 ppbv states a stable source for CH_3CHO exist, and in x-axis ranged from 0 to 5 ppbv for H_2CO, as showed in Figure 2.12. H_2CO should be produced and consumed quickly,

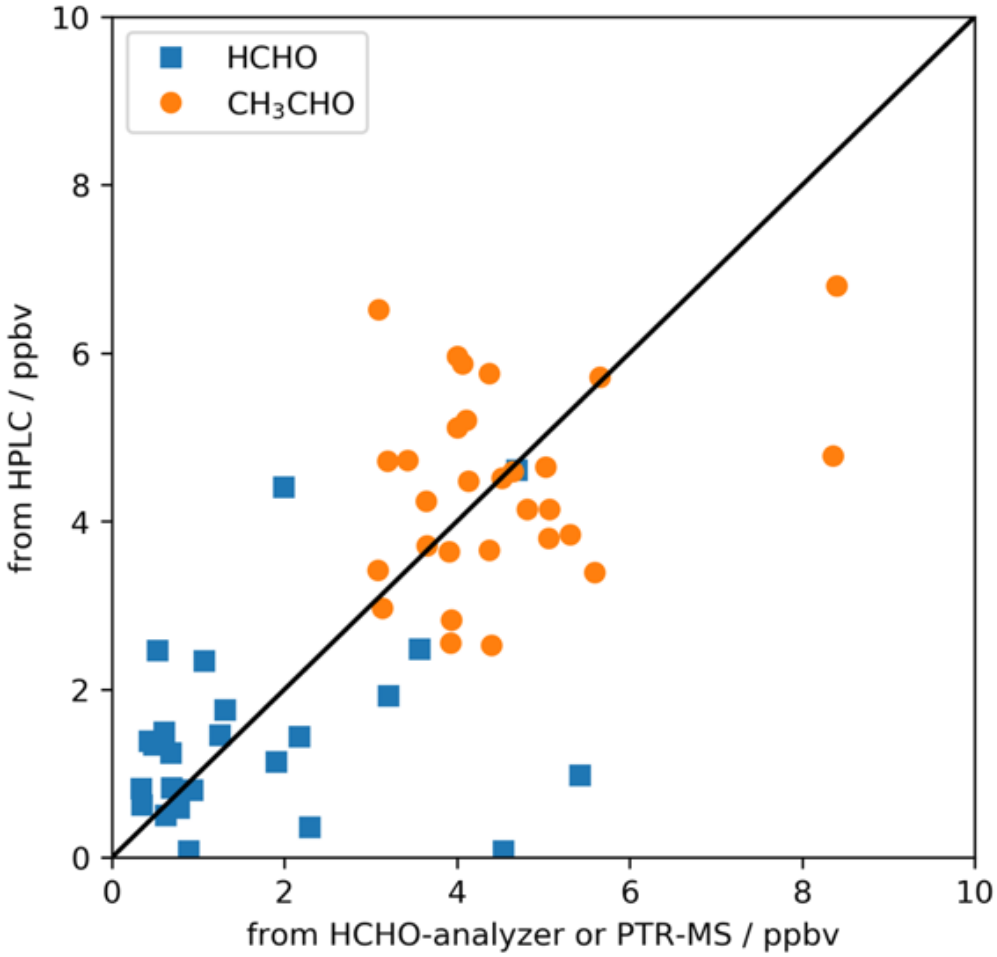

Figure 2.12: Inter-comparison of H_2CO and CH_3CHO concentrations between different apparatuses.

and a distinct source for CH_3CHO present in Yokohama. Therefore, a linear regression with intercept was used to predict the blank data of H_2CO, which can help to estimate the H_2CO concentration from CH_3CHO.

Although instrumental uncertainty leads the fluctuations to two dataset, the limited data samples still prove both instruments are in good agreement. Online measurement of glyoxal via incoherent broadband cavity enhanced absorption spectroscopy (IBBCEAS) was also conducted with 4 min intervals. Each 4 min cycle contains four steps as 1)one minute of ambient air measurement; 2)one minute of zero air flush; 3) one minute of zero air measurement; and 4)one minute of ambient air flush. The details of IBBCEAS was described by [Nakashima and Sadanaga, 2017] .

Calculated OH reactivity was estimated from either measured or assumed concentrations of trace gases during the intermittent observations. A gap of H_2CO (from July 27 to 29) was predicted from acetaldehyde, where $[CH_3CHO] = 3.3 + 0.89 \times [H_2CO]$; the regression

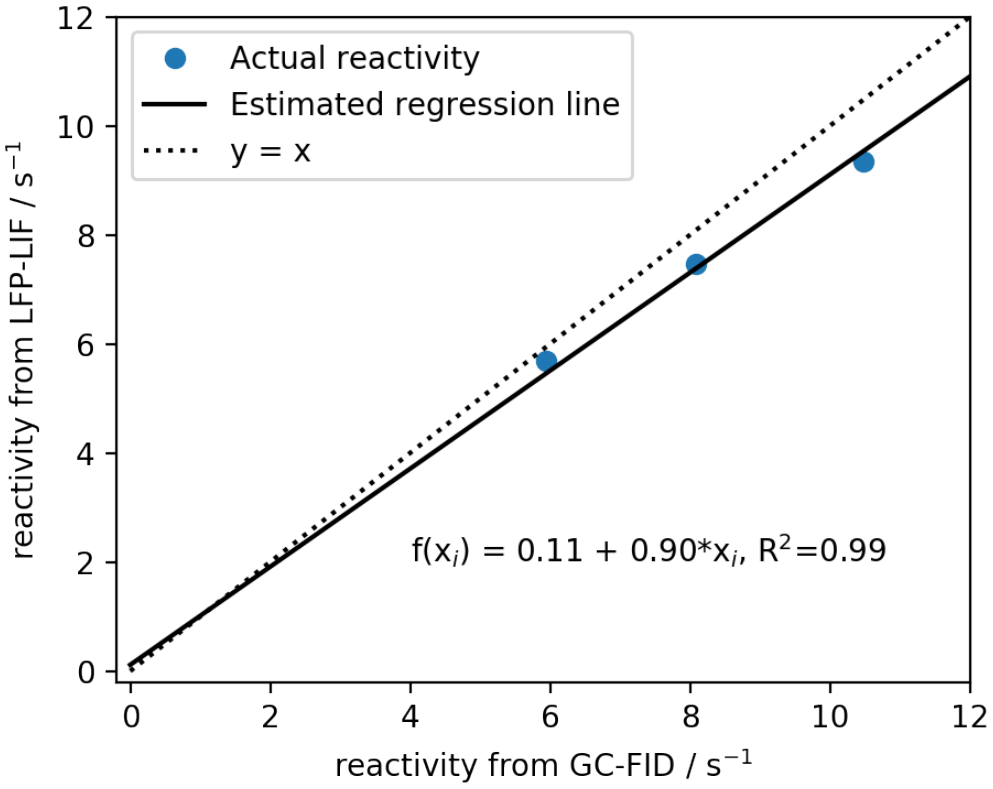

Figure 2.13: Calibration results and regression analysis from the injection of propylene.

result will be discussed later for a detailed description. Gaps of other NMVOCs were obtained by linear interpolation. According to a calibration experiment based on a propylene cylinder (9.82 ppm, Teisan Kyoto co.,) connected with both LP-LIF and GC-FID conducted after the campaign, all GC-MS & GC-FID measured NMVOCs' contributions to OH reactivity applied an effective factor of 0.90, Figure 2.13 shows the details.

A propylene cylinder (9.82 ppm, Teisan Kyoto co.,) was connected to the sampling line through a MFC (KOFLOC, 3660) of full-scale 50 sccm. The sampling line was linked with GC-FID and LFP-LIF via a T-valve for concurrent detection. Three different flow rates of propylene have been set and each group was recorded continually for at least 15 min. The rate constant–k = $2.5*10^{-11}$cm^3 molecule^{-1} s^{-1}– recommended by JPL Publication 19-5 [Burkholder et al., 2019] under standard pressure and room temperature has been applied to estimate the reactivity from GC-FID. A comparison between the average results from GC-FID and LP-LIF is displayed in Figure 2.13. From the regression analysis a calibration factor equals 0.9 was discovered, which indicates a slight overestimate of GC-FID to LP-LIF.

Aforementioned information of hourly wind direction, concomitant wind velocity, relative humidity (RH), and temperature are downloaded from the site of Japan Meteorological Agency

(https://www.jma.go.jp/jma/indexe.html).

2.2.3 Total OH reactivity and trace species

Total OH reactivity was measured by LP-LIF as introduced in Section 1.7. In Yokohama campaign, total HO_2 reactivity was also alternately measured with same one system, but such details won't be introduced in the thesis. Total HO_2 reactivity results in Yokohama campaign can refer to [Zhou et al., 2021]. The measurement modes between OH and HO_2 reactivity were switched automatically by the computer program configured with a three-way solenoid valve (Koganei, 062E1), by operations scheduling where one measurement cycle consisted of 20 mins for OH reactivity and 100 mins for HO_2 reactivity. The timing and length of total OH reactivity measurement was fixed with those of NMVOCs. Before each OH measurement, the system was shortly flushed with zero air and initial three data points of OH reactivity were discarded to avoid interference from CO and NO addition in HO_2 reactivity measurement.

As Figure 2.11 shows, the inlets covered with rainproof materials were set outside the window of YES, on the fifth floor ca. 25 m above the ground. Ambient air was pumped through ca. 5 m long and 12.7 mm O.D. PFA tubes. Mass flow controllers (MFC, KOFLOC, 3810S) constrained the total flow of the sampling gas at 11 SLM. In the OH reactivity measurement, to avoid interferences in the environment with copious NO_x which recycles HO_2/RO_2 and slows OH decay, ambient air was diluted by purified air before measurement. The flow rate of dilution gas was manually operated according to the ambient level of NO_x, varied between 3-8 SLM in total flow rate of 11 SLM. The residence time of trace species in the sampling line was estimated to be 4-11 s with dilution.

The measured OH reactivity in reaction cell k'_{obs} was diluted by zero air and need to be converted from the dilution rate. Additionally, ambient NO_2 and reaction cell NO_2 concentrations exhibited distinct differences because of interconversion of NO to NO_2 during the sampling procedure. The ambient total OH reactivity k'_{amb} was estimated considering both dilution and the NO_x conversion effects.

$$k'_{amb} = k'_{obs} \times \sigma + ([NO_2]_{aa} - [NO_2]_{rc} \times \sigma)(k_{NO2-OH} - k_{NO-OH}) \tag{2.1}$$

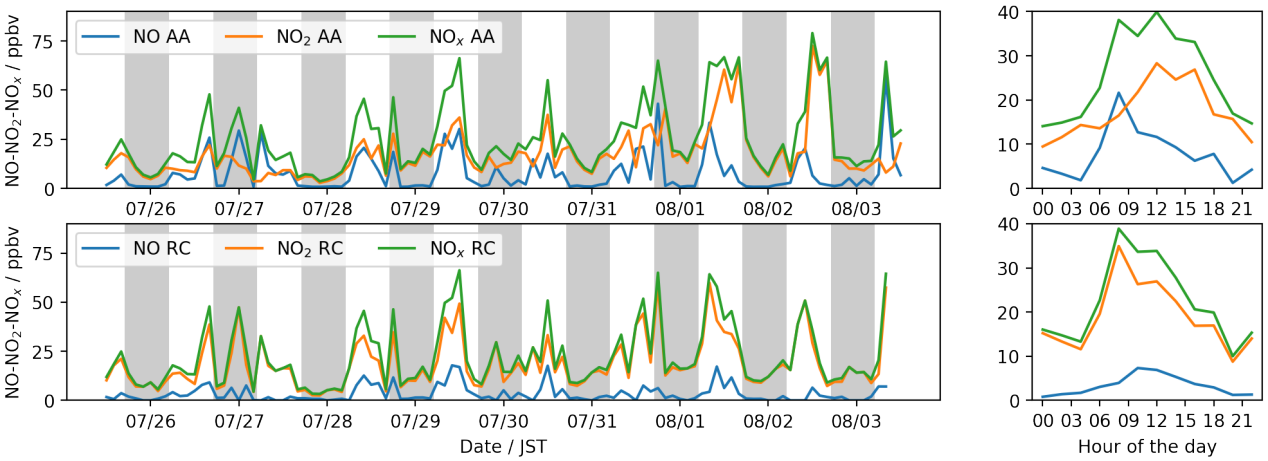

Figure 2.14: Time series and diel variations of NO_x during the whole campaign. The upper graphs are concentrations measured from ambient air, bottom graphs are measured/estimated concentrations in reaction cell after converting from the dilution rate.

$$\sigma = \frac{Total\,flowrate}{Total\,flowrate - dilutiongas\,flowrate} \tag{2.2}$$

As equation (2.1) shows, the real ambient OH reactivity k'_{amb} was calculated from the diluted rate σ, which is interpreted in (2.2), ambient NO_2 concentration $[NO_2]_{aa}$, reaction cell NO_2 concentration $[NO_2]_{rc}$, and rate constant of NO_2 and NO with OH radicals. The measured NO_2 concentration in reaction cell was also corrected from σ, since it also got diluted inside the reaction cell. The change of NO concentration during the sampling procedure was supposed to be equivalent to that of NO_2 concentration, taking the oxidation of NO as the only source for extra NO_2 into account.

The comparison between ambient NO_x and reaction cell NO_x is provided in Figure 2.14. NO_{2rc} after converting from dilution rate, displays similar tendency as ambient NO rather than that of NO_2. In sufficient NO_x circumstance, i.e. polluted area, the oxidation reaction of NO has to be considered since it leads to production of NO_2, which occurs in two dozen of seconds in the sampling process. Considering this, NO_{2rc} was used for the chemical analysis of directly measured OH reactivity (see Figure 2.15) due to the short-term interconversion of NO to NO_2. Furthermore, abated NO in the reaction cell was indirectly evaluated for calculated OH reactivity from the change of NO_{2aa} to NO_{2rc}.

OH reactivity in the reaction cell

The average measured OH reactivity is 10.7 s^{-1}, compared with a 9.8 s^{-1} calculated OH

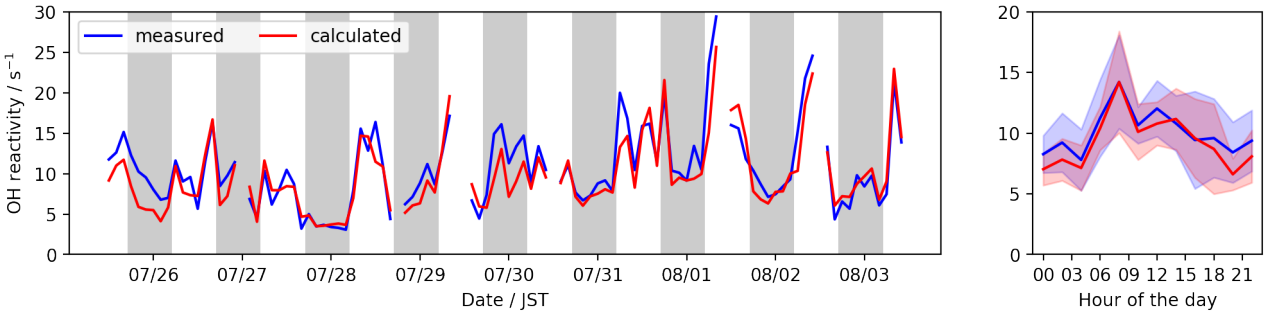

Figure 2.15: Time series and diel variations of measured OH reactivity (in blue) and calculated OH reactivity (in red) inside reaction cell. The diel variations were calculated excluding Aug 1^{st} and 2^{nd} and shaded areas indicate the 95% confidence interval.

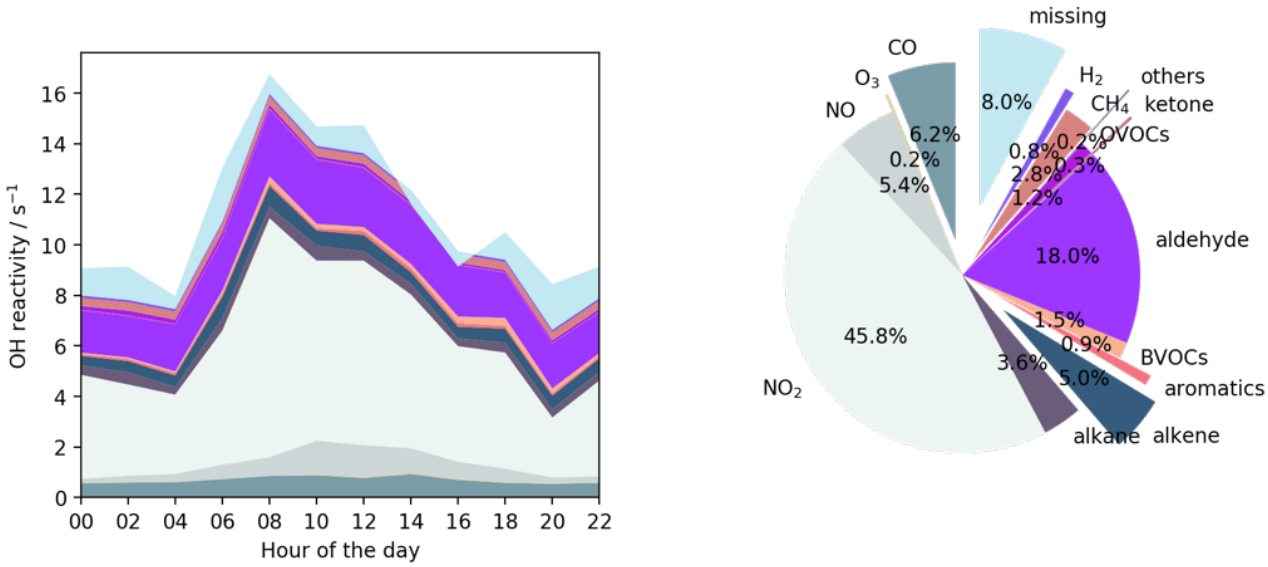

Figure 2.16: Stack of diel profiles of reactivities from all measured OH reactants compared to the measured OH reactivity in reaction cell. Pie plot of each groups' contribution to total OH reactivity.

reactivity in reaction cell. Breakdowns of measured OH reactivity inside reaction cell were explored in Figure 2.16, where NO_x dominates the diel variations. The diurnal peak appeared in the early morning due to the elevated NO_2 in reaction cell. Ambient total OH reactivity and calculated OH reactivity will also be introduced later, which allows to a better understanding of sampling.

Although directly measured total OH reactivity is meaningful considering the effects of an in-situ sampling in polluted area, the purpose of field studies should focus on real ambient air situation. Hence, discussion will give a priority to ambient total OH reactivity.

Ambient OH reactivity and trace species

k'_{amb} ranges from 3 to 29 s^{-1} during the Yokohama campaign, as shown in Figure 2.15.

In general, k'_{amb} were higher during the daytime than at night due to abundant emissions of diurnal NO_x. Calculated OH reactivity showed in consistent with k'_{amb}. Although k'_{amb} was continuously obtained during the whole period, when there was elevated NO in the reaction cell i.e. over 10 ppbv after the dilution, k'_{obs} should be underestimated because of fast OH regeneration in the reaction cell through HO_x cyclic reactions, and thus excepted from analysis, shown as gaps in Figure 2.17. All species of interest depicted in Figure 2.17 were calculated based on the initial 20 min measurement results out of every two hours. The data point is concurrent with that of k'_{amb}. Almost all trace species' abundances were on August 1 and 2 when northerly wind transferred aged and contaminated air masses from Tokyo area in the morning as shown in Figure 2.10. k'_{amb} also exhibited an increasing trend on these two days. To represent the condition in coastal regions, Figure 2.17 summed the diel variations excluding August 1 and 2 of high concentrations.

Generally, NO_x concentrations were high during the daytime as mentioned before. NO was elevated in the early morning around 8 am at the rush hour up to 20 ppbv on average and kept around 10 ppbv during the daytime. The values on August 1 and 2 were not higher than other days, revealing that NO is mainly triggered by the local emissions. NO_2 did not have a morning peak and increased till noon up to 20 ppbv on average. The highest concentration of NO_2 appeared to be 70 ppbv on August 1 and 2 due to transportation by northern wind. As for O_3, the general level of O_3 was not high over the whole campaign due to copious NO_x, the latter acts as termination of OH radicals and lead to inert HO_x cycle reactions. Diurnal peak of O_3 appeared around 2 pm with mean concentration of 20 ppbv except for August 1 and 2 when the values increased up to 60 ppbv.

Three aldehyde species and O_z ($O_z = O_3 + NO_2$) were plotted in middle graphs in Figure 2.15. O_z was added here because both ozone and NO_2 are important oxidant gases, the photolysis of NO_2 is the most important source for tropospheric ozone. Furthermore, O_z exposure has been reported to cause biological oxidative stress which is arisen from the high reactivity of the two oxidant gases and their secondary reaction products [Last et al., 1994]. As a result, O_z showed quite similar tendency as glyoxal, which indicates similar pathways in source and sink. The aldehyde group together with O_z were further explored during daytime and night-time. The concentrations during the daytime were higher than night, with dispersed

distribution (see Figure 2.18). However, the averaged level of diurnal and nocturnal ozone (day:night = 20:11 ppbv ppbv^{-1}), glyoxal (day:night = 0.23:0.15 ppbv ppbv^{-1}), and H_2CO (day:night = 1.81:0.94 ppbv ppbv^{-1}) were fairly close in both groups. Meanwhile, acetaldehyde (day:night = 4.9:3.9 ppbv ppbv^{-1}) showed smallest discrepancy. The ratio of H_2CO to CH_3CHO in the current work ([H_2CO]:[CH_3CHO] = 1.38:4.40 ppbv ppbv^{-1}) is smaller than unity, which is contradictory to reported results in London ([H_2CO]:[CH_3CHO] = 5.99:5.00 ppbv ppbv^{-1}) and Tokyo ([H_2CO]:[CH_3CHO] = 6.26:4.79 ppbv ppbv^{-1}) [Whalley et al., 2016]; [Yoshino et al., 2012]. A difference in concentration of precursors could be one explanation. H_2CO has been reported to be higher in suburban site than urban area during the summer [Qian et al., 2019]; [Yang et al., 2018], which could be explained by the fact that suburbs tend to have more vegetation and H_2CO are produced primarily via the oxidation of biogenic precursors. Also, acetaldehyde concentrations should be more influenced by alkanes while H_2CO is less sensitive to alkanes [Luecken et al., 2018]. In this observation, low concentrations of BVOCs and high levels of alkanes should have resulted in less H_2CO compared with CH_3CHO. Additionally, as shown in Figure 2.19, a regression line of CH_3CHO on H_2CO has an intercept, which would represent the presence of local emission for CH_3CHO.

The relationship between H_2CO and CH_3CHO was fitted via linear regression analysis, where all dots in y-axis ranged from 2 to 8 ppbv states a stable source for CH_3CHO exist, and in x-axis ranged from 0 to 5 ppbv for H_2CO, as showed in Figure 2.19. H_2CO should be produced and consumed quickly, and a distinct source for CH_3CHO present in Yokohama. Therefore, a linear regression with intercept was used to predict the blank data of H_2CO, which can help to estimate the H_2CO concentration from CH_3CHO.

Alkane, alkene, and aromatics groups in Figure 2.17 basically depict similar tendency indicating they are possibly originated from same sources. They have been reported to receive the main contributions from traffic emissions, followed by combustion process and petroleum products [Hellen et al., 2006]. Meanwhile, some extent of peaks at different time stating aforementioned sources should contribute differently to the three groups and occasional additional sources also presented. For example, the largest concentration of both alkane groups (39.1 ppbv) and alkene groups (2.4 ppbv) appeared on August 3, however, with alkane's peak came behind alkene's. Considering one of the major sources of alkane is petrochemicals, the surrounding cir-

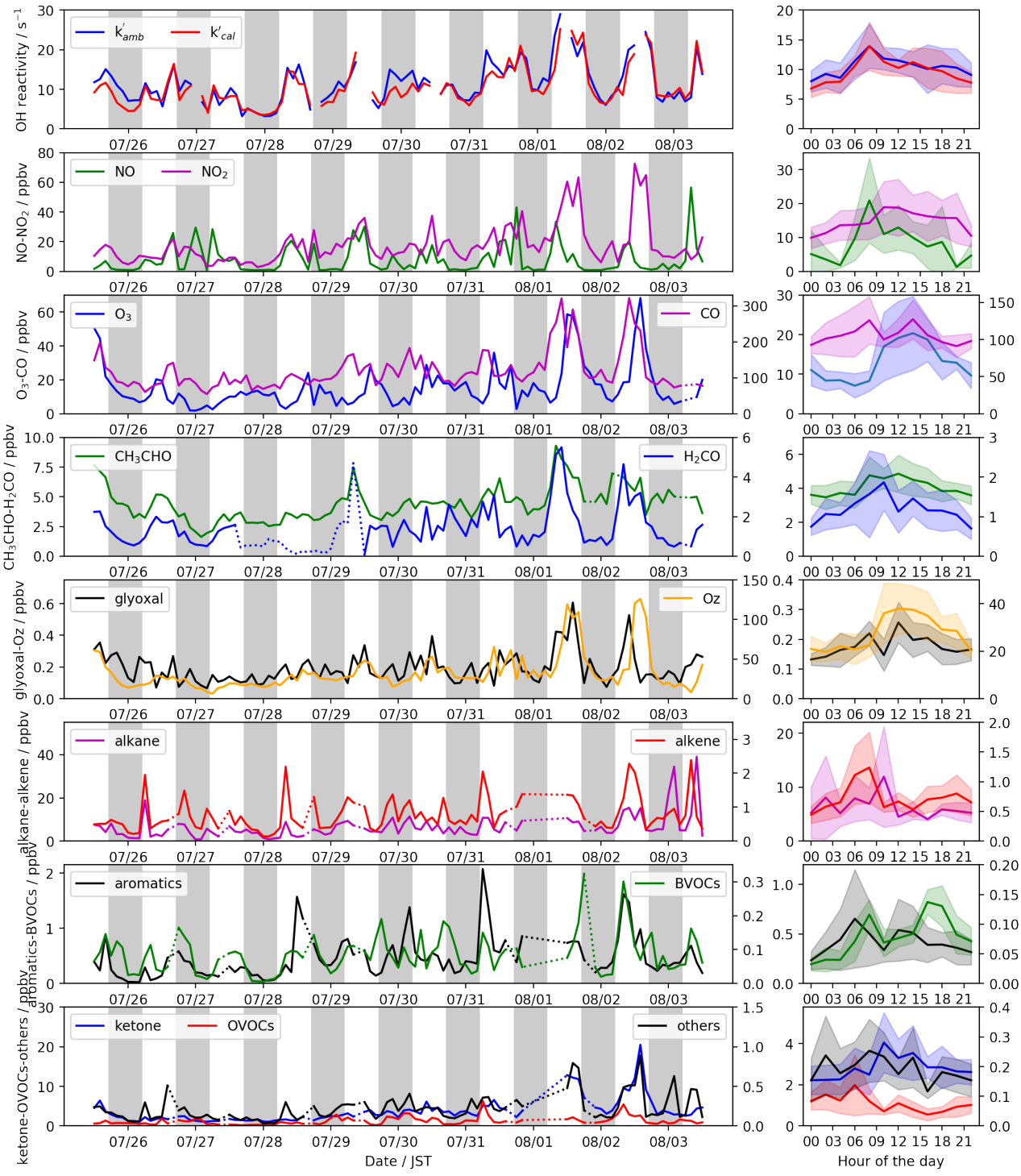

Figure 2.17: Time series of k'_{amb} and k'_{obs} exhibit in the left panel, together with their diel variations excluding Aug 1^{st} and 2^{nd} depict at the right panel. Shaded areas indicate the 95% confidence interval. Lower graphs give same time series and diel variations of ambient trace species concentrations. In every time series graph, vertical grey areas indicate night-time (17:00-05:00) period and dash lines interpret the missing concentrations.

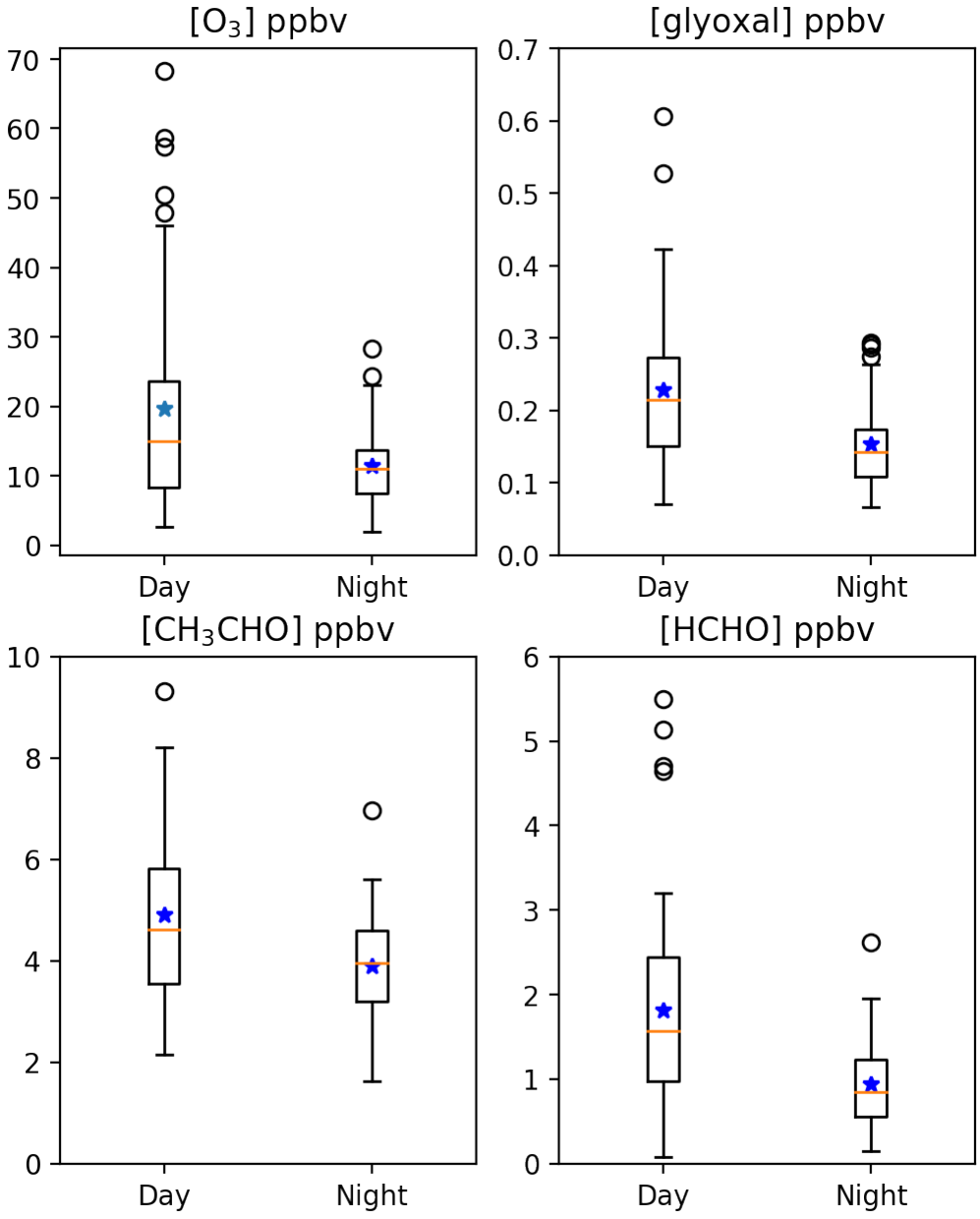

Figure 2.18: Comparison of ozone and aldehyde species mixing ratios during the daytime and nighttime in tukey-box plots. The middle ”box“ in each graph represents the inter-quartile range, each pink line marks the individual median value, and the upper and lower whiskers represent concentrations outside the middle 50%. Black circles imply the outliers and blue stars are the average values.

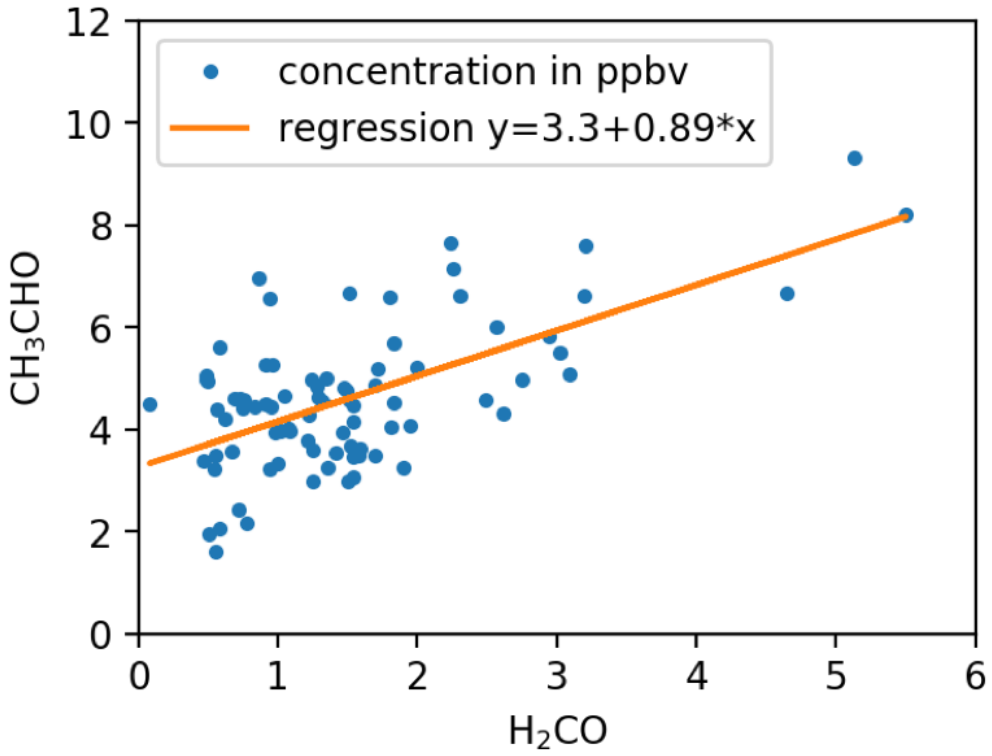

Figure 2.19: Linear regression analysis of H_2CO and CH_3CHO concentrations. The equation as shown in the legend box was utilized to predict H_2CO.

cumstance might have caused elevated concentrations of alkanes, especially amongst long-chain hydrocarbons.

As the representative species of anthropogenic and biogenic emissions, aromatics and biogenic VOCs were pretty low with regard to reported urban/suburban observations [Li et al., 2020]; [Whalley et al., 2016]. This is because the location at coastal area where most of the time during the campaign clean air from the Pacific ocean refreshed local air. On August 2 morning, peaks of aromatics and BVOCs appeared together with CO, aldehyde groups, and alkenes, when the air mass mainly came from continental region. Moreover, the concentration of OVOCs (excluding aldehyde and ketone), ketone and others (acetylene and acrylonitrile) generally display similar tendency: lower concentrations with oceanic air masses, and erupted peaks on August 1 and 2. In this case, peaks appeared in the afternoon instead of morning time, owing to photochemical reactions of transported species.

2.2.4 Missing OH reactivity analysis

Breakdowns of the diel reactivities based on measured reactants were depicted in Figure

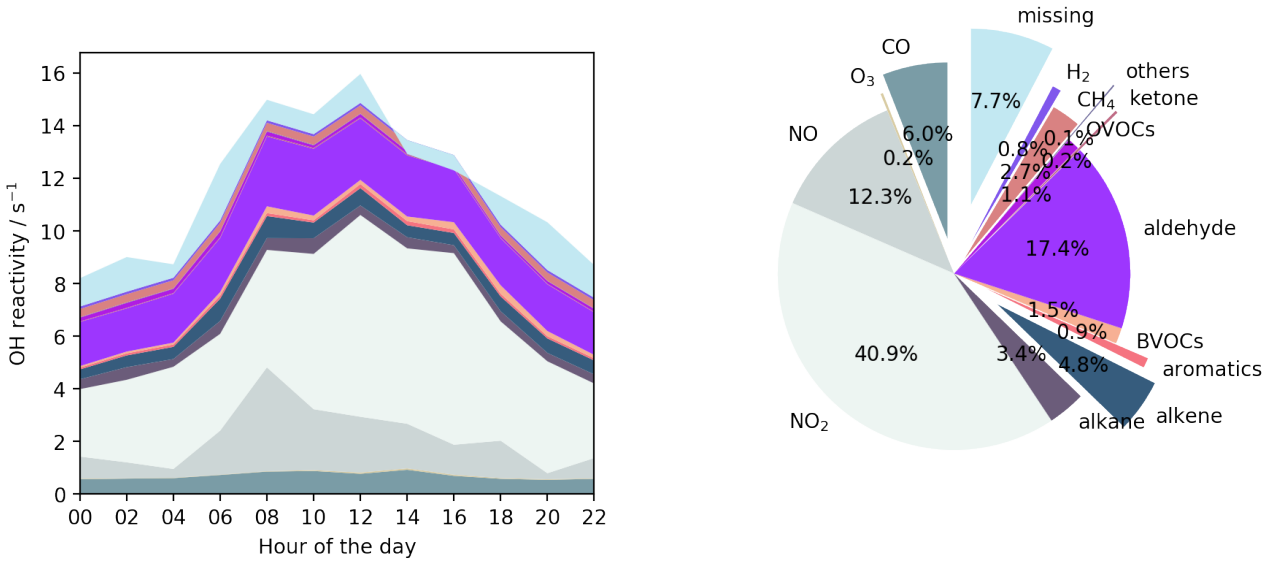

Figure 2.20: Stack of diel profiles of reactivities from all measured OH reactants compared to the k'_{amb} (left graph). Pie plot of each group's contribution to k'_{amb}.

2.20. Generally, total OH reactivity, k'_{amb}, was higher during the daytime than at night. NOx accounts for over half of the total OH reactivity, amongst which NO_2 takes up 40.9% and NO 12.3%, and determines the diel profile of k'_{amb}. The second biggest contributor is aldehyde group (17.4%) including formaldehyde (2.7%), acetaldehyde (14.3%), and glyoxal (0.4%). Unlike previous studies such as in Tsukuba, BVOCs and aromatics in the current study only have few contributions to total OH reactivity, both are less than 2%. Although methane was not detected, a constant level of methane was postulated to be 2 ppmv, which is 2.7% of the total OH reactivity in Yokohama. Missing OH reactivity, k'_{amb}-k'_{cal}, in total takes up 7.7%.

Figure 2.21 shows time series and diel variations of missing reactivity. The missing OH reactivity was sometime smaller than zero, which could be explained by potential uncertainty mainly involved in k'_{bkg} (as indicated in dashed-line with $\pm$ 0.5 s^{-1}) as well as those in k'_{cal}. Missing reactivity kept low having about 0.9 s^{-1} on average, while occasionally increased. The largest missing reactivity (8.5 s^{-1}) appeared on August 1 morning as showed in Figure 2.21A when the polluted air masses started blowing. Diel missing OH reactivity exhibited larger values at night (on average 1.17 s^{-1}) and disappeared in the afternoon (on average 0.57 s^{-1}), so that a better corresponding relation between k'_{amb} and k'_{cal}, was found during the daytime, as showed in Figure 2.21C. The general distribution of OH reactivity at night was concentrated slightly below the diagonal line, compared to the diurnal results distributed over the diagonal line.

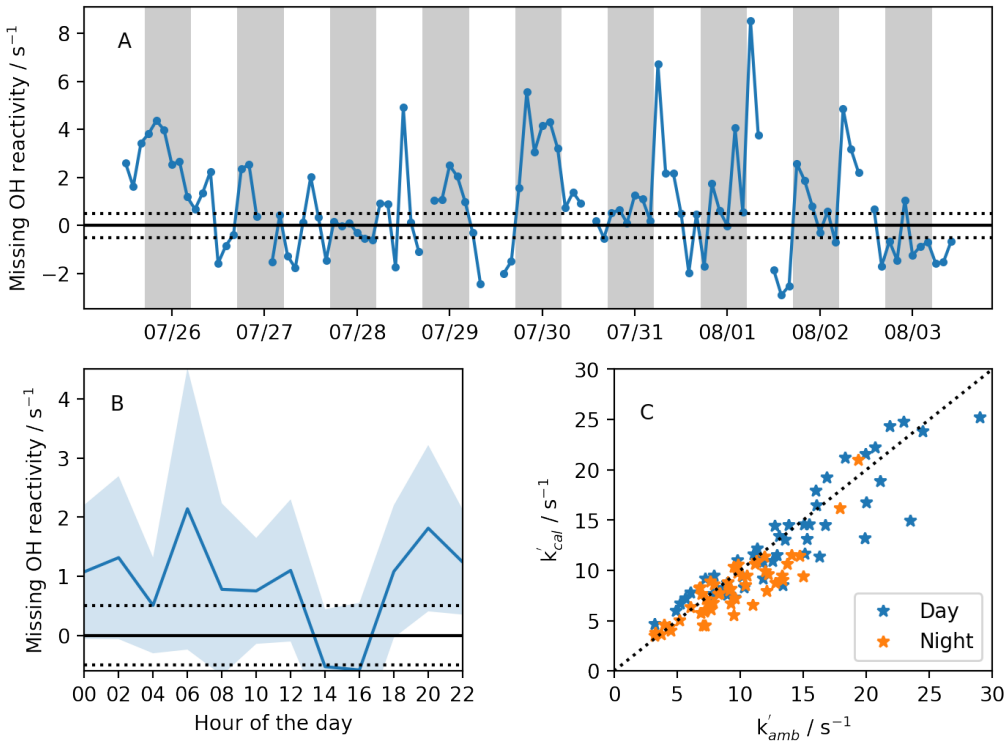

Figure 2.21: Time series (A) and diel variations (B) of missing OH reactivity.

2.3 “Clean urban” area; the case study in Kyoto in 2020 summer

In 2020, during the COVID-19 pandemic, a comprehensive field campaign was conducted in Kyoto. This observation provides a good chance to investigate anthropogenic emissions influence and also helps to foresee air composition change in a low-emission society.

2.3.1 Description of the measurement location

The third observation was conducted in summer 2020 at Kyoto University Yoshida campus (KU; 35°01′N,135°46′E), Kyoto, Japan. All instruments were mounted beside the window on the 3^{rd} floor, ca. 10 m above the ground, in the Yoshida-South Campus Academic Center Bldg. Figure 2.22 depicted the map information of KU inset with the wind-rose map . The megacity Osaka is located 40 km in the southwestern direction as marked in the map, hence, the southwestern wind is considered as polluted air masses. The observation period started on September 5 and ended on September 15 in 2020.

2.3.2 Instrumentations information

The OH reactivity was measured by LP-LIF as introduced before. Because there is no

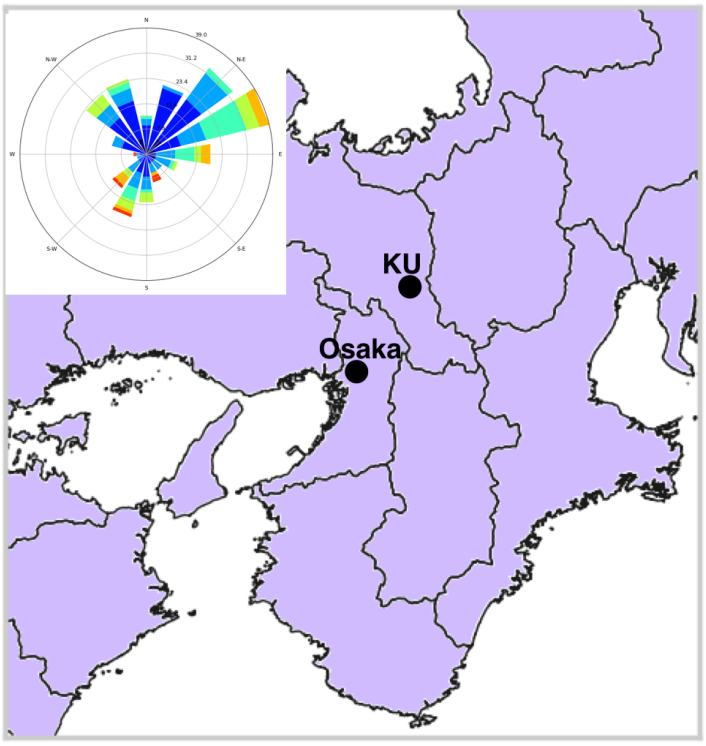

Figure 2.22: Map information of the Kyoto campaign, a wind-rose map indicating the wind direction information was inserted in the upper left.

important manufactories in Kyoto, and also according to a campaign conducted in the same place in 2018, OH reactivity measurement does not need dilution in Kyoto's case considering NO concentration is not that high (refer to Figure 2.23).

The concentration of trace species were monitored by commercial instruments, similar as Table 2.1 indicated as follows: Cavity attenuated phase shift (CAPS) for NO_2 (Aerodyne Research, 1 s time resolution). NO_xbox (Thermo Model 42i-TL, 1 min time resolution). CO monitor (Thermo Model 48i-TLE, 10 s time resolution). UV absorption O_3 monitor (Dylec Model 1150, 10 s time resolution). Over 60 NMVOCs were also measured by gas chromatograph-flame ionization detector (GC-FID) and proton transfer reaction mass spectrometer (PTR-MS). A constant concentration of methane was assumed as that in Yokohama as 2 ppmv. Since the details of trace species measurement were quite similar as introduced before, here will skip the description.

2.3.3 Total OH reactivity and trace species

The temporal and diurnal variations of OH reactivity and trace species are compared in

Figure 2.23. Total OH reactivity, calculated OH reactivity, and missing OH reactivity were plotted in the top graphs. There are gaps of total OH reactivity and calculated OH reactivity, which were because of the instrumental calibration, i.e., the baseline measurement of LP-LIF or standard gases calibration on GC-FID. Such periodic results were deleted accordingly. The maxima total OH reactivity appeared on 9^{th}, accompanied with the maxima missing OH reactivity. The lowest total OH reactivity showed up on beginning of 7^{th}, which might be caused by the heavy precipitation that can remove air pollutants from the air [Shukla et al., 2008]. The diurnal variations of OH reactivity was plotted at the right side in which total OH reactivity, calculated OH reactivity, and missing OH reactivity exhibited quite similar tendency during the day, while a relative low level at night and an increase from noon. The breakdown of diel total OH reactivity was explained in Figure 2.26.

Time series of NO_x (NO and NO_2) were also exhibited in the second graph in Figure 2.23. Generally, NO_x concentrations were much lower on weekend (shaded in green) compared with weekdays (shaded in light black). NO exhibited elevated tendency on three days as: 7^{th}, 8^{th}, and 11^{th}. It is noteworthy to mention that road construction beside KU was conducted since September 7^{th}, which located less than 100 meters away from observational site. Therefore, emissions of NO_x in quantity were expected. The lowest NO_x concentration appeared during the heavy rain period, highest NO_x level on 7^{th} and 8^{th} was considered to be transported from Osaka, combined with Figure 2.25. Several spikes between NO_2 and total OH reactivity share their shapes in common, which states the importance of NO_2 that contribute to total OH reactivity. Diel variations of NO and NO_2 indicated quite distinct behaviors while NO exhibited an increase during the daytime from 6 am to 6 pm, this could be explained by the anthropogenic activities such as road construction. On the other hand, NO_2 was quite different in which a general background as high as 2 ppbv existed all the day. Although NO_2 started to increase from the early morning, an accumulated effect continued until 9 pm. Note that the photochemical reactions should consume NO_2 at noon importantly.

According to the meteorological conditions as summed in Figure 2.24 and Figure 2.25, on 7^{th}, wind masses originated from Osaka brought polluted air from the afternoon. Even though heavy precipitation flushed KU on 6^{th}'s night and 7^{th}'s morning, considering gas-phase pollutants can be absorbed by raindrops during the precipitation and construction emissions

started from the morning together with transported pollutants, air condition on 7^{th} might be both fresh and polluted.

As for CO and hydrogen, CO in abundance showed up since the night on 8^{th} and increased to the maximal on 9^{th}, same time as maxima total/missing OH reactivity, which indicates a missing/unknown anthropogenic emissions might have caused elevated OH reactivity on site. Hydrogen is quite stable in the air and exhibited different daily variations compared to CO. Although researchers have reported corresponding relationship between CO and hydrogen considering their common dominate sources like biomass burning and anthropogenic emissions. However, such a correlation is quite weak in Kyoto's case. The diel variations of H_2 and CO showed a comparative stable tendency, while CO contained several fluctuations over time.

O_3 and OVOCs, as the oxidants, displayed mimicking trends in general. The highest level of both O_3 and OVOCs showed up on 8^{th} and 9^{th}. Oxidants were importantly produced during the daytime when solar radiation accelerates photolysis procedure. However, even O_3 is quite active in the air, it was not totally consumed during the nighttime. Except the boundary layer change effects at night condensed pollutants concentration, a relative low concentration of NO should also be responsible for these remained O_3. As for the diel variations, both O_3 and OVOCs indicated a spike at noon and a decrease from afternoon. Note that during the time period from 0 am to 6 am, the level was quite stable for oxidants.

For the main components of NMHCs, alkanes, alkenes, and alkynes were concluded in the same graph in Figure 2.23. Alkyne data is only available during the second half of observation. Both highest and lowest concentration of alkanes and alkenes showed up on weekend, while the highest level on 13^{th}, with pollute air masses blew from Osaka. On 7^{th} night, the lowest concentration of NMHCs can be explained as weekend effects plus rainfall absorption removal [Shukla et al., 2008]. Because every middle night (23:00-01:00) there was a calibration on GC-FID, hence the lowest level should be disregarded. There was a decrease for alkane and alkene during the daytime which can be resulted by the reactions with OH radicals. Only acetylene was measured for the group of alkyne, therefore the concentration of alkyne was much lower than other two groups and also showed a decrease during the afternoon.

BVOCs indicated the largest peak on 5^{th}, which showed up together with the warmest weather (as high as 35.8 degrees Celsius). This phenomenon is in consistent with the hypothe-

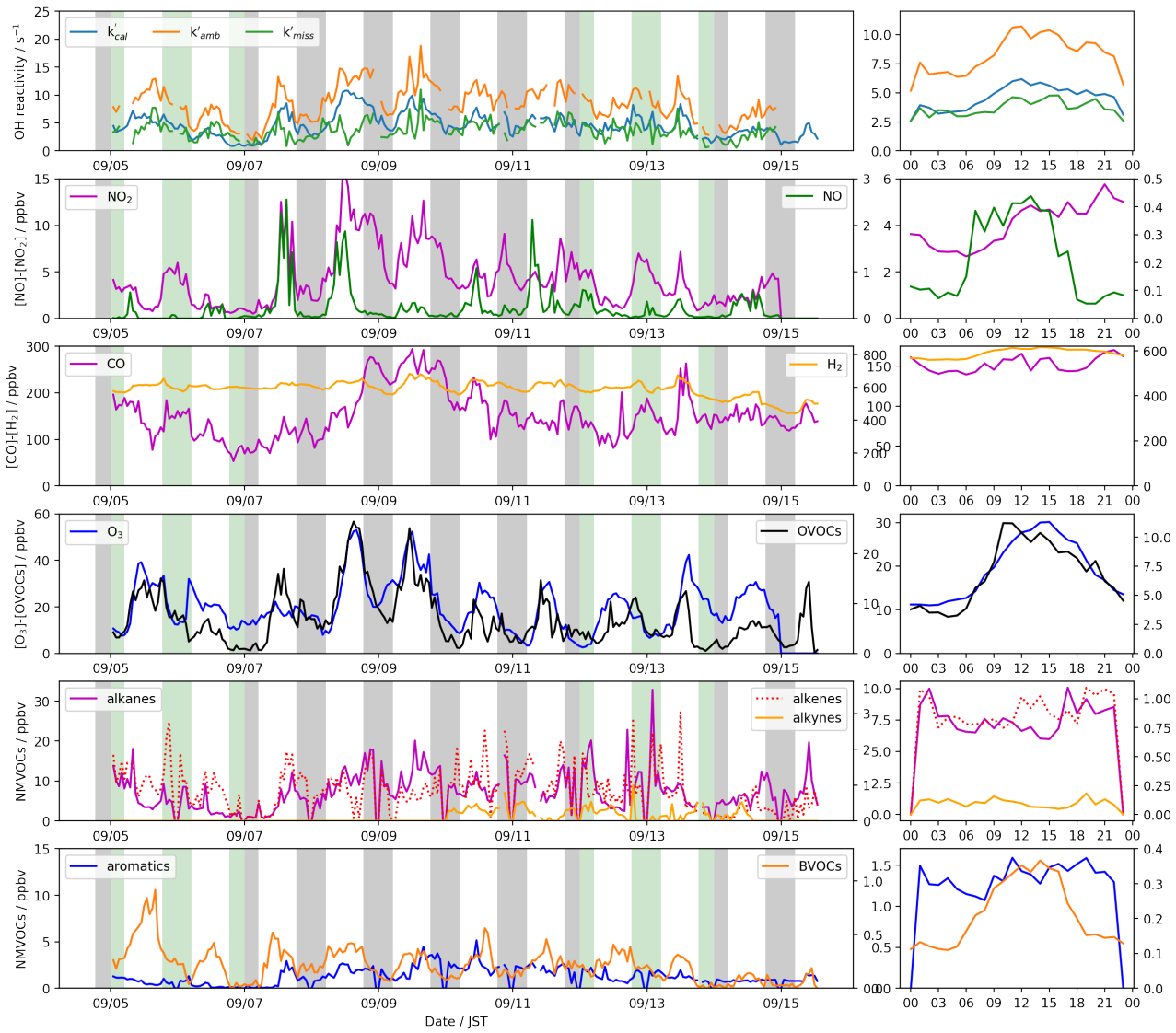

Figure 2.23: Time series of total OH reactivity, calculated OH reactivity (top graph) and concentrations of measured trace species in group (bottom graphs). Shaded areas mean the night-time (18:30-05:00), in which green highlighted the weekend.

sis that the increase of temperature can stimulate the exhaust of BVOCs, as high temperature may act as thermal stress on vegetation [Kleist et al., 2012]. The diurnal variations of BVOCs with a peak at noon also confirmed the heat impacts on BVOCs emissions from plants. Aromatic concentration was quite low during the weekend on 5^{th} and 6^{th} and started to raise after that. The highest level of over 5 ppbv appeared on 10^{th} when the wind came from north to east direction. Although aromatics decreased again on the second weekend, much lower concentrations continued even after weekend such as 14^{th} and 15^{th}, the reason is unclear.

Figure 2.26 showed the breakdowns of diel total OH reactivity compared with each groups' fraction to total OH reactivity. There were two peaks for diurnal total OH reactivity, one before noon and another around 14:00. According to reactants' behavior in Figure 2.23, it was found

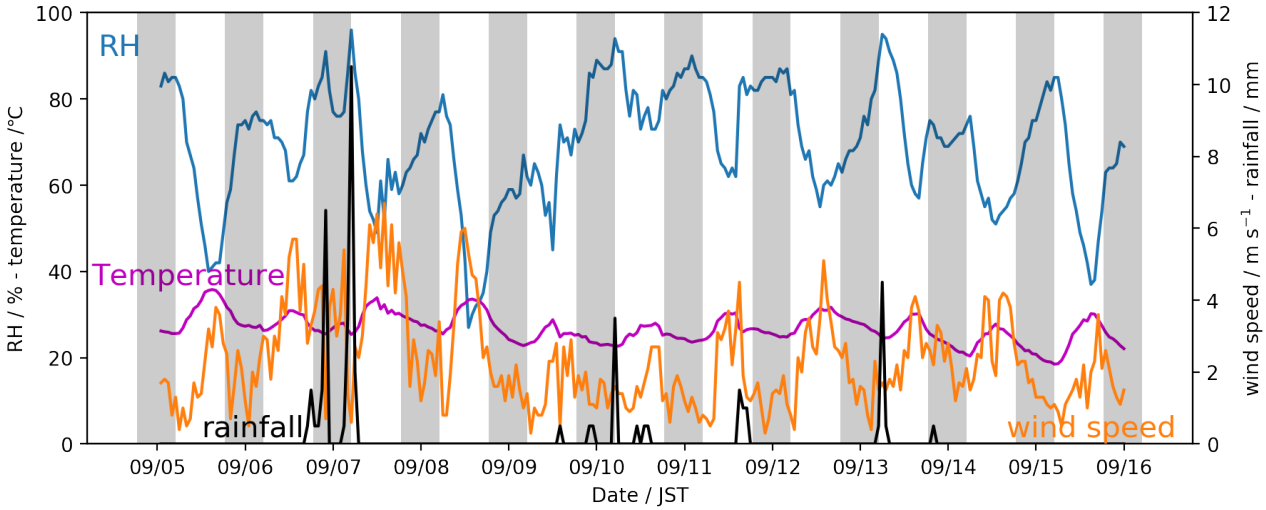

Figure 2.24: Time series of meteorological conditions including RH, temperature and wind speed.

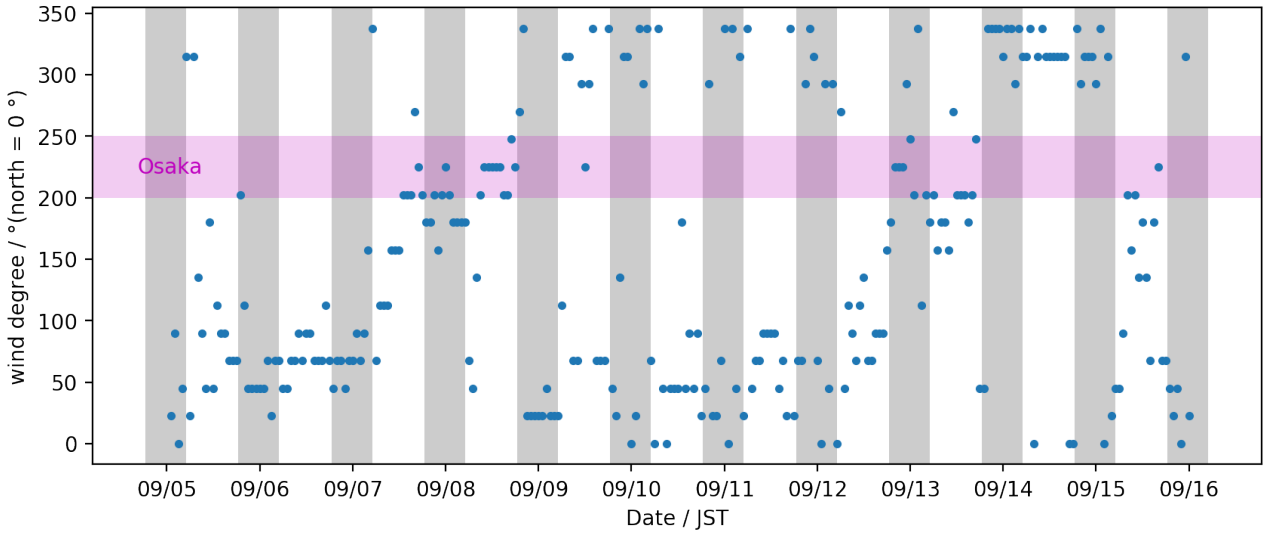

Figure 2.25: Temporal variations of wind direction, which proceeds in clockwise motion. Pink shaded areas represent these periods when air masses came from Osaka.

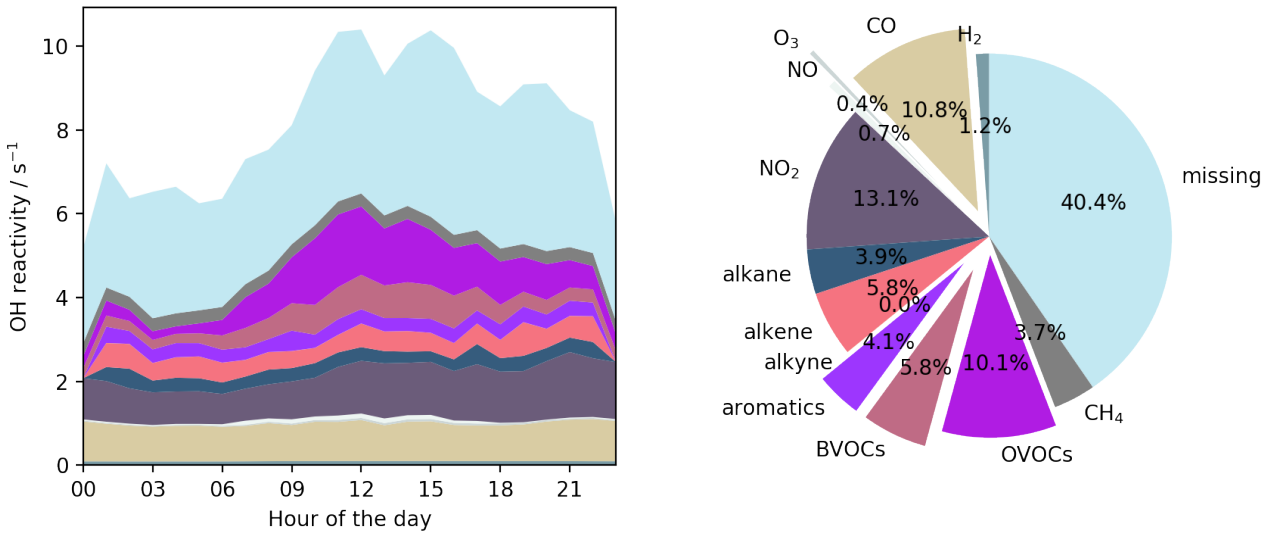

Figure 2.26: Left graph: stack of diel profiles of reactivities from all measured OH reactants compared to the total OH reactivity; right graph: pie plot of each group’s contribution to total OH reactivity.

that the first peak is mainly from primary emissions such as alkane, alkene, aromatics, and BVOCs. OVOCs and the missing also contributed to the first peak while not as much as the second one. The second peak is importantly from missing OH reactivity and OVOCs. Averaged total OH reactivity is 8.5 s^{-1}, among which 40.4% remains as missing OH reactivity. Since Kyoto is a quite clean place, in which CO, as representative of transported pollutants, takes 10.8%. NO_x concentration was quite low in-situ, NO_2 only takes 13.1% of total OH reactivity while NO accounts for 0.7%. The biggest organic contributor came from OVOCs, as high as 10.1%. BVOCs and alkenes takes same fraction of total, both are 5.8%.

2.3.4 Missing OH reactivity analysis

Missing OH reactivity, as showed in Figure 2.23, presented the highest level from 15:00 to 16:00, which equals around 4.5 s^{-1}. Although from 10:00, missing OH reactivity intended to increase except a drop at 13:00. As discussed before, double spikes during the daytime may indicate different missing sources dominate considering the diurnal tendency of measured reactants. The third spike presented at night around 8 pm. Missing OH reactivity was generally higher during the daytime than nighttime with an average value of 3.4 s^{-1}. Because there was always calibration on GC-FID during the mid-night (23:00-01:00) except only one day, missing OH reactivity results were accordingly disregarded.

Corresponding analysis between missing OH reactivity and trace species in groups was

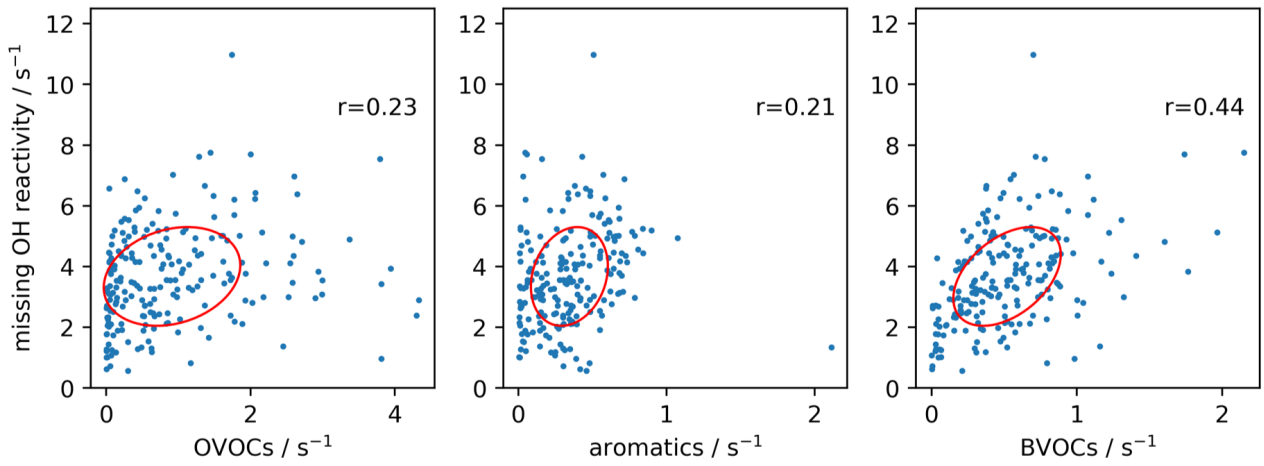

Figure 2.27: Corresponding relationship of missing OH reactivity with the group of OVOCs, aromatics, and BVOCs.A 68% confidence ellipse of the covariance was plotted in each graph to visually compare the correlation (standard deviation equals 1).

conducted, and Figure 2.27 shows the result. Unlike the correlation in Tsukuba, in which OVOCs displayed a moderate corresponding relationship with missing OH reactivity. There was much weaker correlation between missing OH reactivity and OVOCs in Kyoto campaign, in which the pearson r equals 0.23 in the group of OVOCs, and 0.21 in the group of aromatics. In Figure 2.27, BVOCs especially isoprene showed a moderate correlation with missing OH reactivity, in which r equals 0.44. Unknown BVOCs and BVOCs derived secondary products might be quite important to explain missing OH reactivity in Kyoto.

2.4 A comparative analysis on OH reactivity in the three campaigns

Aforementioned Table 1.1 listed the total OH reactivity over Japan and worldwide based on the location type. In this section, specifically, the characteristics of OH reactivity in Tsukuba, Yokohama, and Kyoto in Japan will be compared (geographical information refer to Figure 2.28). Each group of trace species in Tsukuba, Yokohama, and Kyoto were compared in Figure 2.29, the highest level of NO_x was observed in Yokohama together with the lowest of ozone. Ozone and CO were much higher in Tsukuba, in which most of VOCs were also higher in Tsukuba than Yokohama and Kyoto. As for the analysis of OH reactivity, the highest averaged total OH reactivity was obtained in Tsukuba, which is 12.9 s^{-1}, followed by Yokohama as 11.4

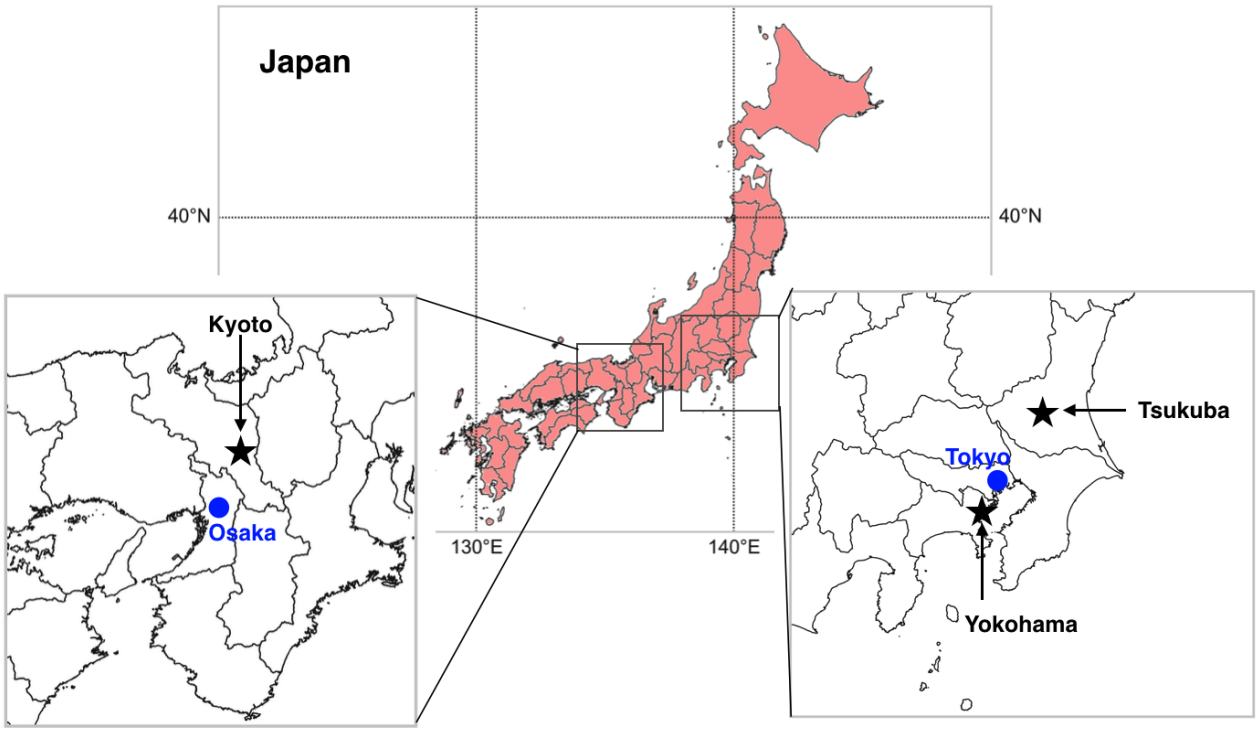

Figure 2.28: Geographical information of the three field studies compared in the map.

s^{-1}, and the smallest of 8.5 s^{-1} in Kyoto (Figure 2.30). The general level of total OH reactivity is quite reasonable in the location as Tsukuba campaign, most of the period experienced transported air pollutions from Tokyo and surrounding areas. Then Yokohama, although it belongs to Keihin industrial area, fresh air from the Pacific Ocean frequently came to the measurement site during the observational period, therefore, most of the total OH reactivity got explained by the primary emissions and aging process of the pollutants was suppressed. In Yokohama, NO_x was extremely high and accounted for over half of the total OH reactivity. Last in the case of Kyoto, which is expected as the cleanest place amongst the three locations, should possess less anthropogenic emissions, and more influenced by biogenic emissions. This can be explained by the moderate correlation between missing OH reactivity and BVOCs as defined in Figure 2.27. Note that the instrument for OH reactivity measurement used in all the three campaigns was totally same, only in Yokohama campaign, because of relative high NO concentration, an extra dilution pretreatment was practiced.

The comparison of calculated OH reactivity was provided in the middle panel in Figure 2.30. Note that the calculated OH reactivity should firmly depend on the co-deployed instrumentations of trace species. Basically, the more trace species measured, the higher level of calculated

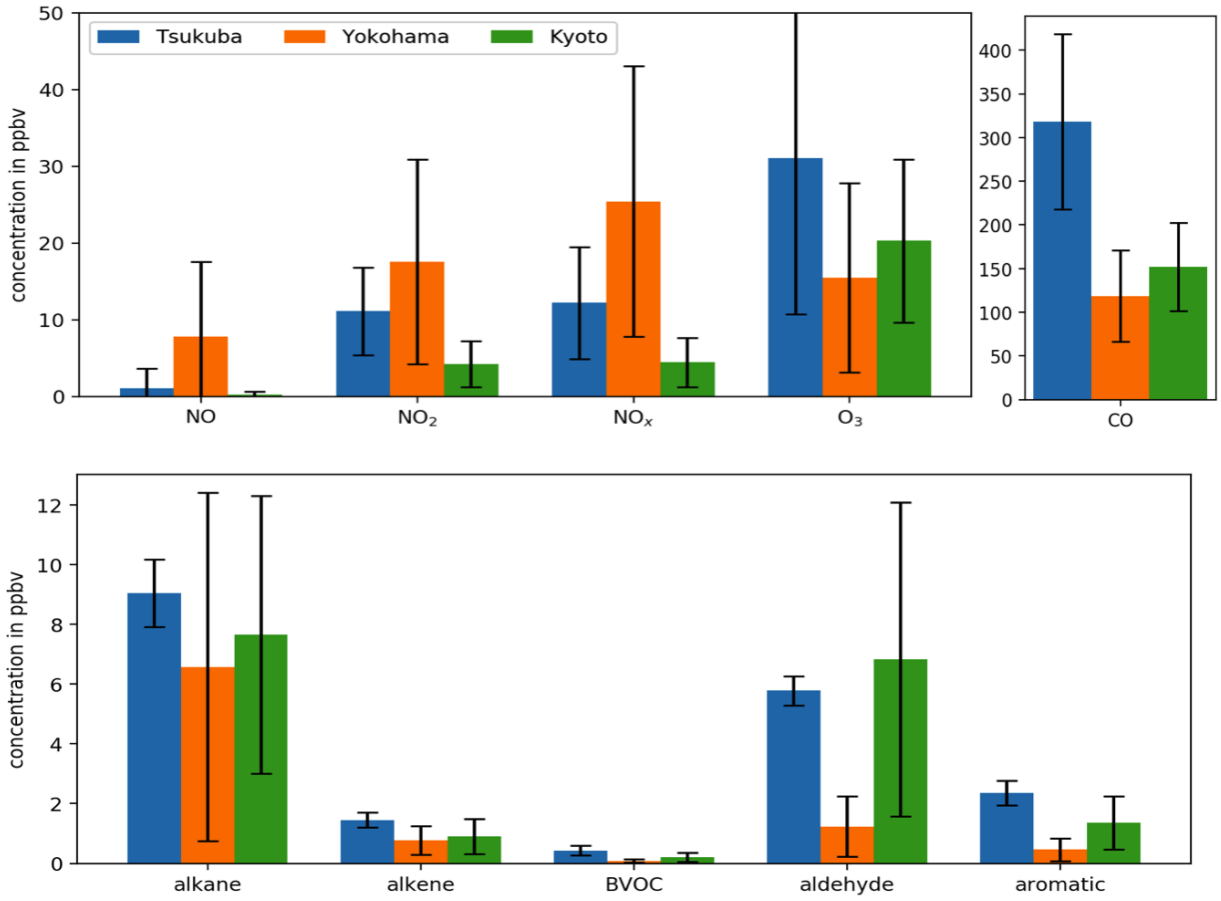

Figure 2.29: Comparison of the concentrations of trace species among three campaigns. Note that acetaldehyde in the group of aldehyde in Tsukuba was not measured therefore an assumption were used for a fair comparison.

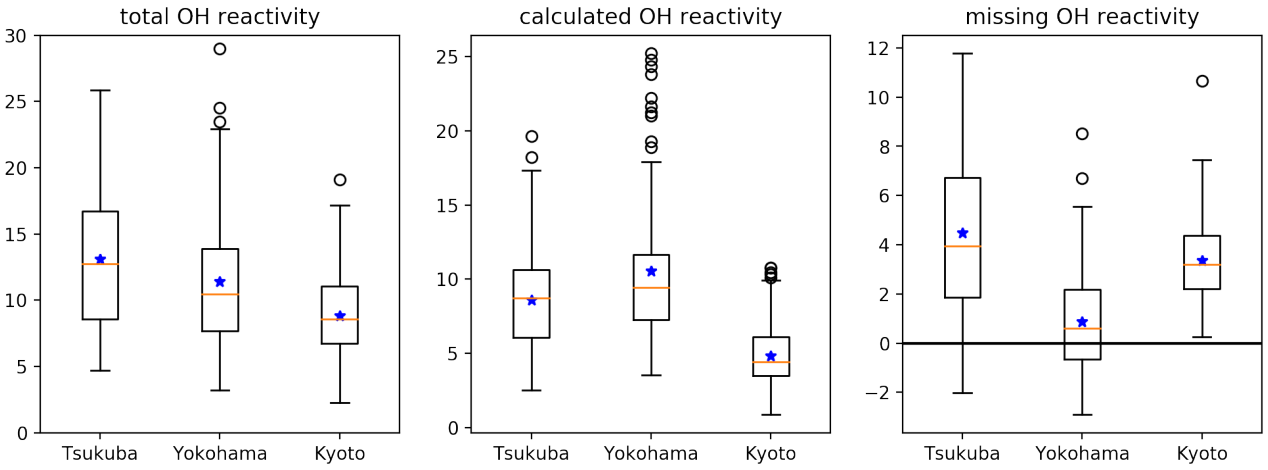

Figure 2.30: Boxplot of hourly total OH reactivity (left panel), calculated OH reactivity (middle panel), and missing OH reactivity (right panel) in three campaigns. Blue stars mean the average value of each group. Orange lines are the median.

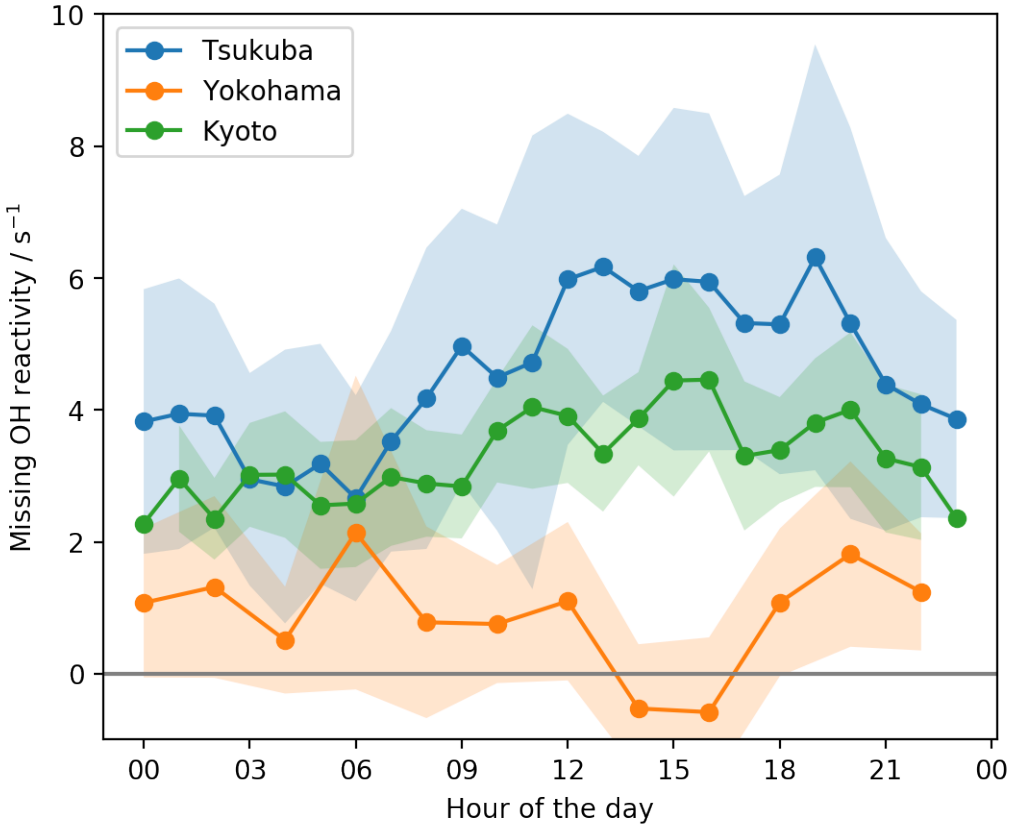

Figure 2.31: Diel variations of missing OH reactivity indicated with 95% confidence interval in Tsukuba, Yokohama, and Kyoto.

OH reactivity might be. This explained the case in Yokohama while over 90 gas phase reactants were measured. However, in Kyoto there were over 60 trace species detected compared to over 50 in Tsukuba. The calculated OH reactivity was higher in Tsukuba compared to that in Kyoto, such difference was mainly caused by the distinct content of inorganic.

As for missing OH reactivity as showed in Figure 2.30 and Figure 2.31, the lowest missing OH reactivity was acquired in Yokohama, which is less than 8% (0.88 s^{-1}). Most of the OH reactivity could be assigned to measured primary emissions, and the analysis in Chapter 3 confirmed that oxidation process in Yokohama was constrained because of high NO_x. The second highest missing OH reactivity fraction was found in Kyoto, which is 3.4 s^{-1} at the fraction of 40.4%, which is over a factor of five higher than that in Yokohama. Because only three species of BVOCs were measured, and there are more than hundreds of BVOCs in the air. The moderate correlation between BVOCs and missing OH reactivity indicates that missing OH reactivity in Kyoto might importantly came from unknown/unmeasured BVOCs. Although OVOCs in Kyoto didn't show same correlation with missing, this might be caused by the low

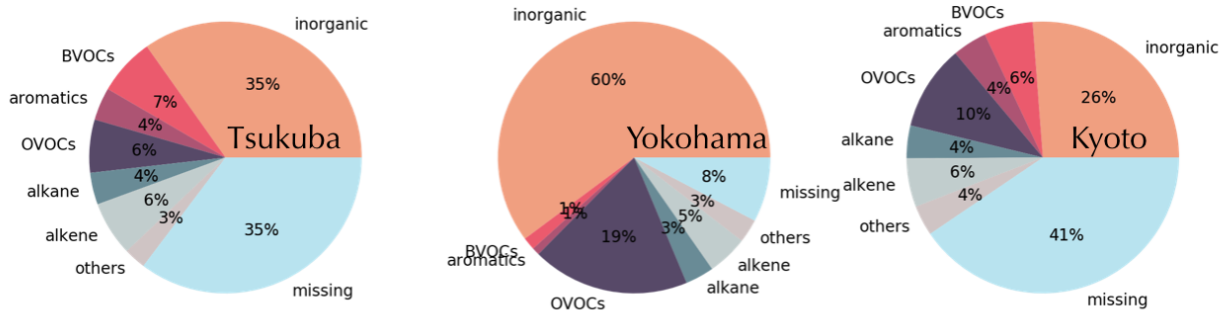

Figure 2.32: Fractions of each group of trace species in total OH reactivity in Tsukuba, Yokohama, and Kyoto. The group of others contains methane and acetylene. The percentage is adapted to the pie plot and might surpass 1.

level of AVOCs, which is also vital to the formation of OVOCs. Tsukuba reported 35% of missing OH reactivity as the highest level of 4.6 s^{-1}. In Tsukuba, OVOCs exhibited a moderate correlation with missing OH reactivity. Because both AVOCs and BVOCs are important parent species for OVOCs, therefore, BVOCs and AVOCs are considered as important sources for the oxidation procedure in Tsukuba. According to the ozone production analysis in Chapter 3, Tsukuba contains the most active oxidative atmosphere compared with Yokohama and Kyoto.

Figure 2.32 compared the fraction of each group in total OH reactivity in all three locations in the same color map. Among all these groups, inorganic took the largest contributions to total OH reactivity especially in Yokohama which mainly came from NO_x. As for organic contributor, OVOCs were the most important species to total OH reactivity in Yokohama and Kyoto, while BVOCs were more crucial in Tsukuba. Missing OH reactivity in Tsukuba and Kyoto were quite close to each other in which BVOCs and aromatics also took similar fractions to total OH reactivity. This indicated that missing OH reactivity might somehow due to unknown reactants related to BVOCs and aromatics.

To put it simply, the air composition in the three sites were totally different, in which Tsukuba experienced with the most active aging procedure initiated from AVOCs and BVOCs. While Kyoto obtained a slightly lower missing OH reactivity level, the relatively low level of AVOCs and primary emissions indicating that BVOCs should be important in Kyoto. Yokohama, different from the other two locations, primary emissions acted as the majority of air pollu-

tants. Furthermore, coastal geographical conditions suppressed the production of secondary pollutants. Therefore, local mitigation policy should vary from place to place to achieve air quality improvement effectively.

Chapter 3

Ozone production sensitivity

Tropospheric ozone is a major photochemical oxidant affecting wide-ranging environmental problems regarding human health, vegetation, ecosystems and climate change [Fuhrer et al., 2016]; [Krupa et al., 2001]; [Monks et al., 2015]; [Nuvolone et al., 2018]; [Van Dingenen et al., 2009]. On the one hand, ozone itself is highly reactive and hazardous in the lower air. On the other hand, ozone absorbs infrared and ultraviolet light, contributing to the "greenhouse effect" in the troposphere and also providing protection from damaging ultraviolet in the stratosphere [Finlayson-Pitts and Pitts Jr, 1999]. The photochemical oxidation procedure of hydrocarbons is responsible for the generation of ozone. As introduced in Chapter 1, the most important source of ozone is NO_2 photolysis in the troposphere, which comes from the by-products of OH initiated cyclic reactions. Hence, evaluating ozone production sensitivity is of paramount importance to explore the HO_x cycle influence. In addition, handling such sensitivity helps to mitigate ozone and improve air quality effectively and scientifically.

This chapter focuses on ozone production sensitivity, and contains three aspects in detail. Firstly, a quantitative approach was proposed to evaluate the number of times that HO_x cyclic reactions could occur in Section 3.1. The indicator is known as **Chain Length**, with an arbitrary unit. Secondly, the maximal amount of ozone (**Ozone production potential**) that could be produced from each OH radical is determined. The details will be described in Section 3.2. Last but not least, **ozone production sensitivity** in terms of VOC-, or NO_x- regime is discussed in three field campaigns Section 3.3. Both gas-phase and heterogenous reactions effects were considered in ozone formation procedure.

3.1 Chain length

Chain length has been defined as the number of times that OH radicals can be recycled [Sheehy et al., 2010] via HO_x cycle (Figure 1.1), which is an indicator of the effectiveness of the fuel (i.e. VOCs) and accelerant (i.e. NO_x) on HO_x cycle rotation.

Theoretically, the chain length can only be quantified after deciding both the initiation and termination point. The initiation perspective considers newly propagated radicals as displayed in blue in Figure 1.1. However, since neither the concentration of HO_x radicals nor the photolysis frequencies were measured in this study, which make it impossible to assess the chain length from the initiation side. Only the chain length from the termination perspective has been analyzed here. The chain length is represented by the term ω proposed by [Sheehy et al., 2010] as shown in equation (3.1).

$$\omega = -[ln\gamma_{HOx}]^{-1} \tag{3.1}$$

$$\gamma_{HOx} = \gamma_{OH\rightarrow RO2}\gamma_{RO2}\gamma_{RO}\gamma_{HO2} + \gamma_{OH\rightarrow HO2}\gamma_{HO2} \tag{3.2}$$

The parameter of γ_x represent x's cyclic proportion to its total loss, as indicated in (3.3)-(3.6). γ_{RO} was assumed to be unity even though the reaction of RO, especially simple RO with oxygen is not fast [Kohno et al., 2020]. Depending on the structure of RO and temperature, dissociation and isomerization might also be important fates. Interestingly, the dissociation of RO generates carbonyl and alkyl fragment, while isomerization produces hydroxyl-substituted alkyl radical, both pathways can reform RO_2 after alkyl react with oxygen [Orlando et al., 2003]. Alternatively, RO can also react with NO and NO_2, which is less important under most atmospheric conditions [Finlayson-Pitts and Pitts Jr, 1999]. Considering an excess existence of O_2 in real ambient condition, the reaction of RO with O_2 is always predominant. Therefore, γ_{RO} equals unity here is acceptable.

$$\gamma_{OH\rightarrow RO2} = \frac{(OH \rightarrow RO_2)}{totalOHreactivity} \tag{3.3}$$

$$\gamma_{OH\rightarrow HO2} = \frac{(OH \rightarrow HO_2)}{totalOHreactivity} \tag{3.4}$$

$$\gamma_{RO2} = \frac{(RO_2 \rightarrow RO)}{totalRO_2reactivity} \tag{3.5}$$

$$\gamma_{HO2} = \frac{(HO_2 \rightarrow OH)}{totalHO_2 reactivity} \tag{3.6}$$

Different quantitative measure of chain length has been proposed before. Depending on the evaluating approach, chain length might get notable discrepancies. Same from termination perspective, [Martinez et al., 2003] used the ratio of HO_x cycle reactions rate to HO_x termination to determine chain length in the southern oxidants study (SOS) as follows:

$$\omega_{SOS} = \frac{[OH]k_{OH} - L(HO_x)}{L(HO_x)} \tag{3.7}$$

The term L(HO_x) is HO_x terminal loss, which including the reaction of OH + NO_2, OH + HO_2, HO_2 + RO_2, and HO_2/RO_2 self-reactions. [Mao et al., 2010] adapted equation (3.7) to estimate OH chain length, where the OH terminal loss is only from the reaction of OH with NO_2. By using this estimation approach, [Martinez et al., 2003] and [Mao et al., 2010] found a general larger chain length, and longer chain length during the daytime than night, which could be due to relatively low levels of NO_x during the daytime, and hence smaller sinks of OH + NO_2 together with a high level of OH concentration.

3.1.1 Chain length in Tsukuba-campaign

Diurnal variations of chain length analyzed in Tsukuba was presented in Figure 3.1. Because the chain length was evaluated only from the termination perspective, therefore nighttime chain length should also be meaningful without considering the photolysis production effects. ω from total OH reactivity varies from 2 to 4 with an average of 2.9, and a higher level appeared during the daytime at noon. Calculated derived chain length also showed a similar tendency as that from the total OH reactivity while generally at much lower level. Missing OH reactivity contributes ca. 1 ration of chain length throughout the day, with longer chain length at noon. Even missing OH reactivity takes only 35% of the total OH reactivity, it contributed importantly to the cyclic reactions, i.e., the oxidation processes. Although the calculation methods are different, chain length in Tsukuba also indicated negative correlations with NO_x like SOS campaign [Mao et al., 2010]; [Martinez et al., 2003] because NO_x acts as radical killer and terminate cyclic reactions efficiently.

A moderate strong positive correlation between ω and the ratio (δ) of NO to NO_2 was

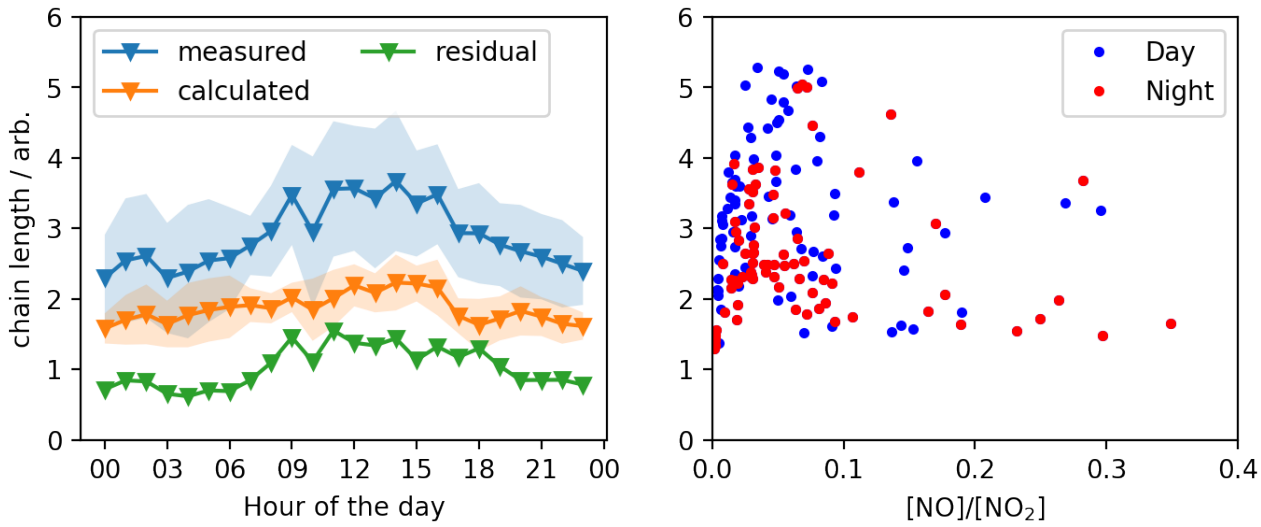

Figure 3.1: Left graph: diurnal variations of chain length estimated from total OH reactivity, calculated OH reactivity, and missing OH reactivity (residual) in Tsukuba campaign; right graph: chain length versus the ratio of NO to NO_2 in daytime and night in Tsukuba.

found in previous campaigns. Researchers have proposed (ω = 15.1×δ + 0.63, r=0.94) and (ω = 14.9×δ + 1.29, r=0.59), in TORCH 2003 [Emmerson et al., 2007] and CHOOSE 2019 [Yang et al., 2021] campaigns, respectively. To investigate the relationship between ω and δ, correlations for the current study were also explored, as indicated in the right graph of Figure 3.1. δ is an indicator for air quality while larger ratio means fresh air mass and it was reported to ascend with a drop in ozone concentration due to the reduction of NO titrate by ozone [Kimbrough et al., 2017]. The results separated in daytime and nighttime were compared. In Tsukuba's case, the overall chain length distributed between 1 to ca. 5 rations both in daytime and night. The difference in daytime and night was not obvious while ω did increase under low δ when smaller than 0.1. After that, the chain length kept stable with elevated NO to NO_2 ratio. Although quite similar δ range was acquired in Tsukuba and CHOOSE campaign (δ: 0-0.3), it is hard to find a linear corresponding relationship between ω and δ in Tsukuba.

3.1.2 Chain length in Yokohama-campaign

Via (3.1) and (3.2), ω was estimated using total OH reactivity, calculated OH reactivity, and their residual (missing OH reactivity) obtained from Yokohama-campaign. The results as showed in Figure 3.2. Chain length as displayed in graph (a) from total OH reactivity mostly distributed from 1 to 3, and was shorter during the daytime than night when more radicals were

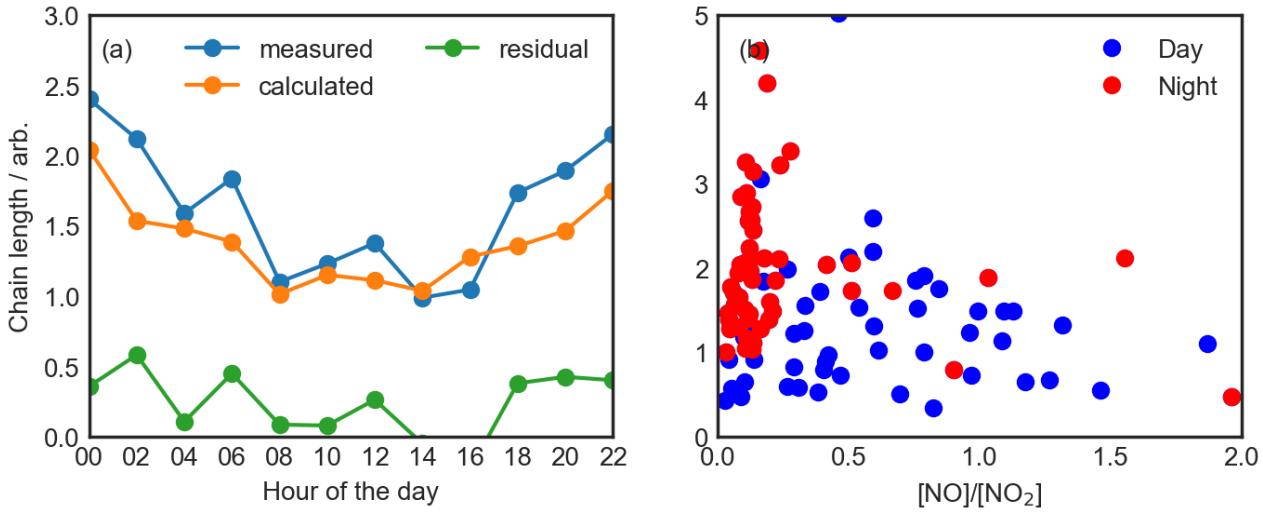

Figure 3.2: Graph (a): diel variations of chain length ω from k'_{amb}, k'_{cal}, and residual (missing OH reactivity); (b): chain length versus the ratio of [NO] to [NO_2] compared in daytime and night in Yokohama. Black line is a horizontal reference line.

lost via termination reactions with NO_2. This is in consistence with the result of Mexico case [Sheehy et al., 2010]. Residual had higher values at night indicating that missing OH reactivity contributes to nocturnal chain length importantly. Simply put, the oxidative chain length in Yokohama is very limited and HO_x cycle is quickly expired during the daytime.

As Figure 3.2(b) shows, generally a lower level of chain length appeared during the daytime followed by relatively high NO to NO_2 ratios. NO mixing ratio was low during nighttime because of NO titration by ozone, which leads to small δ. ω and δ showed no correlation in contrast to previous studies in which ω distribution scattered under low δ range, and stayed below 3 rations with elevated δ. In this case, larger δ means there is more NO compared to NO_2, which makes it easier to terminate cyclic reactions through the formation of HONO, PAN and other nitrates. In TORCH 2003 and CHOOSE 2019 campaigns, the ratio of NO to NO_2 varied from 0 to 0.6, and 0 to 0.3, differently. Relatively low ratio in these cases disclose the positive correlation between ω and δ. However, the current study got NO/NO_2 ratio as high as 2, such anomaly unveil new relationship of ω and δ. When considering chain length efficiency, there might be different mechanism dominate according to the ratio range of NO/NO_2.

3.1.3 Chain length in Kyoto-campaign

Using same method, chain length in Kyoto campaign was also investigated. The ω ranges from 1 to 9 ration in Kyoto with an average value of 3.8 when calculated with the total OH

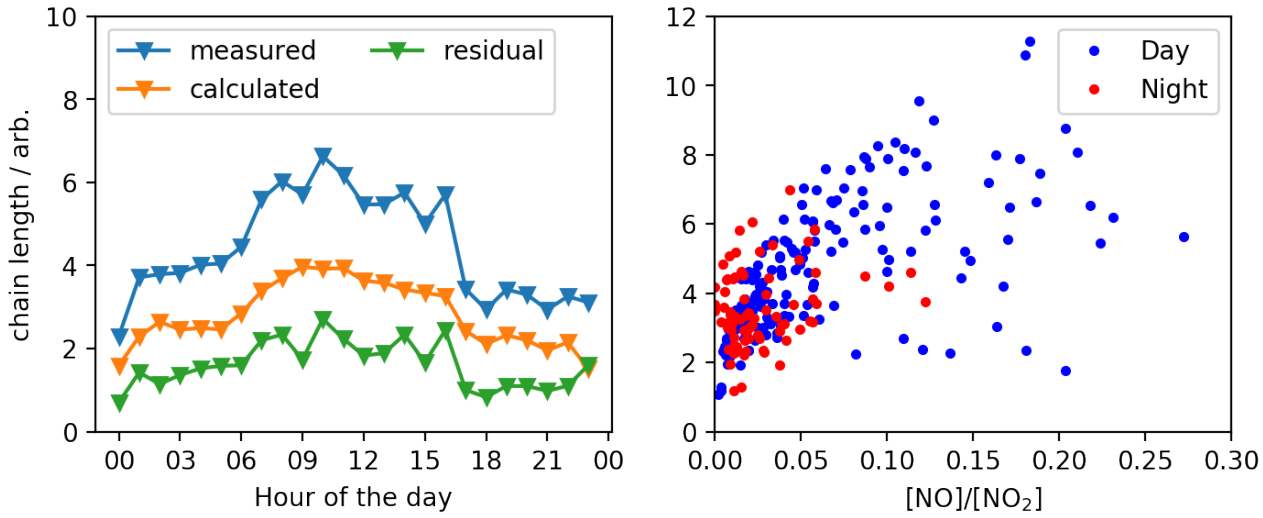

Figure 3.3: Left graph: diel variations of the chain length estimated from k'_{amb}, k'_{cal}, and residual; right graph: chain length versus the ratio of [NO] to [NO_2] in Kyoto campaign.

reactivity. Kyoto's result was similar to Tsukuba's in which much longer chain length appeared during the daytime compared to night. Calculated OH reactivity derived chain length showed a similar trend while varies from 1 to 5 ration with a mean value of 2.5. The residual in Figure 3.3 states the chain length contribution from missing OH reactivity in which varies from 0 to 4 ration. During the daytime, there were fluctuations of chain length from measured and residual as showed in the left graph in Figure 3.3. However, such changes didn't show up in the calculated reactivity estimated ω, which indicates different nature between missing species and detected trace species.

The result of ω in relation to δ in Kyoto campaign was displayed in the right graph in Figure 3.3. A relative longer chain length was obtained here and specific in the group of daytime. NO to NO_2 ratio in Kyoto was reportedly the smallest level which were below 0.3, same as CHOOSE campaign. Initially, ω increased with δ and somehow in a linear mode while the ratio was below 0.1. Most of the dots estimated in the night group also distributed over that range. However, once the ratio got larger than 0.1, the chain length exhibited a dispersed distribution from 1 to 12 rations especially in the day group.

3.1.4 A comparison over these campaigns

An estimation approach from the termination perspective was utilized to analyze the chain length in three contrasting locations, varies from suburban (Tsukuba), coastal industrial (Yoko-

hama), and clean urban (Kyoto) areas. Among these three locations, the longest chain length, which represents the most active HO_x cycle reactions, was obtained from Kyoto with lowest NO_x concentrations. Kyoto and Tsukuba exhibited similar diurnal tendency with an increasing trend during the daytime and declined at night. However, Yokohama displayed an opposite pattern and acquired with the shortest chain length. Such diurnal variations were caused by NO_x abundance, and Yokohama contains much higher concentration of NO_x during the daytime than night. This certificates that NO_x, especially NO_2, is of paramount importance in terms of radicals termination.

3.2 Ozone production analysis

This section will introduce the method for analyzing ozone production including ozone production potential Subsection 3.2.1 and ozone production rate Subsection 3.2.3. Since radical concentration is not available during the field studies, a calculation to figure out radical concentration based on the steady-state of HO_x cycle was explained in Subsection 3.2.2. The second half of this section will describe each field campaigns' ozone production sensitivity in detail in terms of ozone production potential and ozone production rate.

3.2.1 calculation of ozone production potential

Ozone production potential, in short Φ, is defined as the expected value of ozone production per OH radical formation and thus indicates the effectiveness of ozone production [Li et al., 2020]; [Yoshino et al., 2012]. Φ can be estimated by calculating the total accumulated NO_2 from the HO_x cycle prior to the initial consumed OH radicals, as showed in (3.8).

$$\Phi = \frac{\int_0^\infty P(O_3)dt}{[OH]_0} = \frac{\sum \Delta[NO_2]_n}{[OH]_0} \tag{3.8}$$

Where, $\Delta[NO_2]_n$ can be calculated as showed in (3.9). n is the rotation number of HO_x cycles until OH concentration reaches zero. $[OH]_0$ in (3.8) and (3.9) canceled each other out in the calculation. φ_{round} is the ratio of OH radical concentrations before and after one time of rotation in HO_x cycle, as showed in (3.10). φ_{A-B} is the branching ratio of the products

generated from A to B. The details are provided as follows, from (3.11) to (3.14).

$$\Delta[NO_2]_n = [OH]_0(\varphi_{round} + \varphi_{OH-RO2}\varphi_{RO2-HO2})\varphi_{round}^{n-1} \tag{3.9}$$

$$\varphi_{round} = \frac{[OH]_{n+1}}{[OH]_n} = (\varphi_{OH-RO_2}\varphi_{RO_2-HO_2} + \varphi_{OH-HO_2})\varphi_{HO_2-OH} \tag{3.10}$$

$$\varphi_{OH-RO_2} = \frac{\sum k_i[VOC]_i}{k'_{OH}} \tag{3.11}$$

$$\varphi_{OH-HO_2} = \frac{k_{OH+CO}[CO] + k_{OH+HCHO}[HCHO]}{k'_{OH}} \tag{3.12}$$

$$\varphi_{RO_2-HO_2} = \frac{k_{RO_2+NO}[NO]}{k_{RO_2+NO}[NO] + k_{RO_2+HO_2}[HO_2] + k_{p\_RO_2}} \tag{3.13}$$

$$\varphi_{HO_2-OH} = \frac{k_{HO_2+NO}[NO]}{k_{HO_2+NO}[NO] + k_{HO_2+HO_2H_2O}[HO_2] + k_{HO_2+RO_2}[RO_2] + k_{p\_HO_2}} \tag{3.14}$$

k_i is the rate constant of VOC_i with OH radicals and k'_{OH} is the total OH reactivity. $k_{R_1+R_2}$ is the bimolecular reaction rate coefficient of the reaction between R_1 and R_2. $k_{p\_RO_2}$ and $k_{p\_HO_2}$ are the uptake rates of corresponding peroxy radicals into the aerosols.

In the calculation, the formation of alkyl nitrate by NO and PAN by NO_2 were not considered, since such procedures should only take a small fraction of the peroxy radicals.

3.2.2 Derivation of peroxy radicals concentration

Because radicals concentrations were not measured during the field campaigns, therefore the concentration was estimated from the steady-state of radicals. The quasi-steady state of OH radicals makes the OH propagation rate equals OH termination rate, as showed in (3.15).

$$k_{OH-VOC}[OH][VOC] = k_{HO_2-NO}[HO_2][NO] \tag{3.15}$$

From (3.15), OH concentration can be extrapolated, as follows,

$$[OH] = \frac{k_{HO_2-NO}[HO_2][NO]}{k_{OH-VOC}[VOC]} \tag{3.16}$$

Similar to that, it was postulated for all HO_x radicals with a quasi-steady state in which the

production rate of HO_x radicals P(HO_x) equals the sum of termination rate of HO_x radicals.

$$P(HO_x) = 2k_{HO_2-HO_2}[HO_2]^2 + 2k_{HO_2-RO_2}[HO_2][RO_2] + k_{OH-NO_2}[OH][NO_2] \tag{3.17}$$

Combining (3.16) and (3.17), assuming [RO_2] equals α-times amount of [HO_2] and replacing [NO] and [NO_2] by [NO_x] multiplied by their corresponding ratios (β; 1-β).

$$(2k_{HO_2-HO_2} + 2k_{HO_2-RO_2}\alpha)[HO_2]^2 + \frac{k_{OH-NO_2}k_{HO_2-NO}\beta(1-\beta)[NO_x]^2}{k_{OH-VOC}[VOC]}[HO_2] - P(HO_x) = 0 \tag{3.18}$$

From (3.18), [HO_2] can be quantified as follows,

$$[HO_2] = \frac{\frac{k_{OH-NO_2}k_{HO_2-NO}\beta(1-\beta)[NO_x]^2}{k_{OH-VOC}[VOC]} + \sqrt{(\frac{k_{OH-NO_2}k_{HO_2-NO}\beta(1-\beta)[NO_x]^2}{k_{OH-VOC}[VOC]})^2 + (8k_{HO_2-HO_2} + 8k_{HO_2-RO_2}\alpha)P(HO_x)}}{4k_{HO_2-HO_2} + 4k_{HO_2-RO_2}\alpha} \tag{3.19}$$

In equation (3.19), k_{OH-NO_2}, and k_{HO_2-NO} are recommended by JPL Publication 19-5 [Burkholder et al., 2019]. α equals 0.5, and β comes from the average ratio of NO to NO_x. $k_{HO_2-HO_2}$ and $k_{HO_2-RO_2}$ are supposed to be same, the value is fixed to be 8×10^{12} cm^3 molecule^{-1} s^{-1} [Sakamoto et al., 2019].

$$P(HO_x) = 2J_{O_3\rightarrow O^1D}[O_3]\frac{k_{O^1D-H_2O}[H_2O]}{k_{O^1D-H_2O}[H_2O] + k_{O^1D-(N_2+O_2)}[N_2+O_2]} + 2J_{HCHO}[HCHO] \tag{3.20}$$

The production rate P(HO_x) depends on the photolysis rate of ozone and formaldehyde as showed in (3.20). $k_{O^1D-H_2O}$ is the rate constant of reaction O(^{1}D) with water vapor, and $k_{O^1D-(N_2+O_2)}$ is the rate constant of the third body collisional reaction. $J_{O_3\rightarrow O(1D)}$ and J_{HCHO} are the photolysis rate constants of O_3 and HCHO, respectively, which should be derived from solar actinic flux measurements. Because such measurements were not available, a moderate empirical value measured in summer was borrowed from [Thornton et al., 2002], where P(HO_x) equals 0.9 ppbv hr^{-1}. A diversity of P(HO_x) varied from 0.2-2 ppbv hr^{-1} was tested, in which the conclusion is virtually unchangeable.

3.2.3 Estimation of ozone production rate

Ozone production rate, as expressed in (3.21), is quantified from the reaction of XO_2 (= HO_2 + RO_2) with NO. The rate constant of k_t depends on the ratio of HO_2 to XO_2, RO_2 to XO_2 and their individual second-order bimolecular rate constants with NO. The current calculation postulated HO_2 concentration equals double amount of RO_2, and approximately k_{RO_2-NO} equals k_{HO_2-NO}. The temperature dependent Arrhenius expression reported in JPL Publication 19-5 [Burkholder et al., 2019] has been utilized for k_{HO_2-NO}. The details of determination on $[XO_2]$ as discussed in Subsection 3.2.2 was utilized.

$$P(O_3) = k_t[XO_2][NO] \tag{3.21}$$

$$k_t = k_{HO_2-NO}\frac{[HO_2]}{[XO_2]} + k_{RO_2-NO}\frac{[RO_2]}{[XO_2]} \tag{3.22}$$

3.2.4 Ozone production analysis in Tsukuba

The time series of ozone production potential were displayed in Figure 3.4, in which only daytime results are available because photochemical reaction won't occur at night. The calculation method for Φ as explained in (3.8)-(3.14) was used in which real-time NO concentration was replaced by a constant ratio of NO/NO_x multiplied with real-time NO_x concentration. This is to avoid locally and temporally emitted NO or NO_2 influence on photochemical steady state equilibrium of NO_x. Therefore, the average ratio observed from Tsukuba-campaign was applied to remove short-term emission of NO from curbside. The aerosol uptake loss effects combine gas-phase diffusion and reaction processes. As (3.23) showed, k_{p_XO2} represents the loss rate of XO_2 radicals by aerosol, which equals the effective uptake coefficient γ_{eff} times thermal mean velocity, ω_i, and particle surface area concentration, S, divides 4 [Pöschl et al., 2007]; [Sakamoto et al., 2019]. γ_{eff} can be obtained from the gas-phase diffusion (τ) and reaction processes loss (γ considering both aerosol surface and in bulk) (3.24). Because γ_{eff} was not detected directly in Tsukuba campaign, therefore a model value of 0.2 was used to figure out k_{p_XO2} [Sakamoto et al., 2019]. [Zhou et al., 2020] reported an average value of γ equals 0.24 with k_{p_HO2} of 0.0017 according to real-time measurement of HO_2 uptake kinetics onto ambient aerosols. Considering that there is no measurement on k_{p_RO2}, therefore the value of k_{p_RO2}

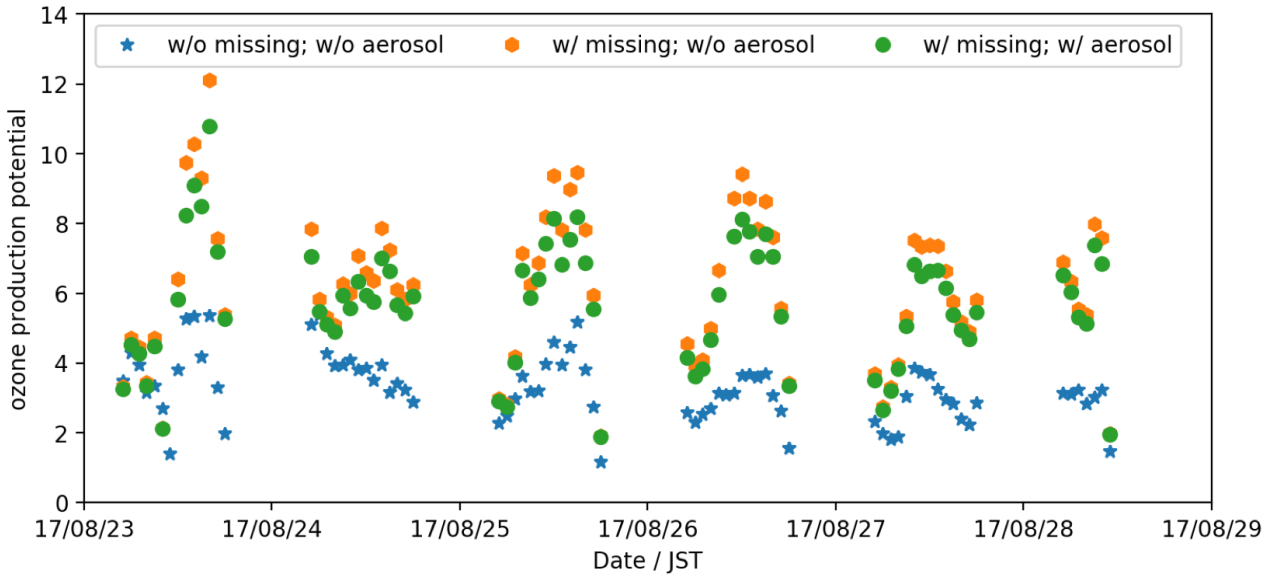

Figure 3.4: Temporal variations of ozone production potential estimated only from calculated OH reactivity (in blue star); from total OH reactivity without considering aerosol uptake effects (in orange hexagon); and from total OH reactivity with aerosol uptake effects (in green circle) in **Tsukuba – campaign**. The results were calculated based on daytime collected data from 05:00-18:00.

was set as zero in the calculation although such a hypothesis must cause overestimate on ozone production potential.

$$k_{p\_XO2} = \gamma_{eff} \times \frac{\omega_i S}{4} \tag{3.23}$$

$$\frac{1}{\gamma_{eff}} = \frac{1}{\tau_g} + \frac{1}{\gamma} \tag{3.24}$$

The green circle in Figure 3.4 came from total OH reactivity with aerosol uptake effects, compared with orange hexagon which also came from total OH reactivity but without considering aerosol effects. It's quite obvious that the aerosol uptake leads to a decrease on ozone production potential to some extent. Except on August 24^{th}, the discrepancy was smaller in the early morning and late afternoon while larger difference appeared at noon. Quite big differences also showed up on 24^{th} morning which might due to contemporarily increased aerosol surface area (see Figure 2.2). When taking the influence of missing OH reactivity into account, it is easily to find that missing OH reactivity importantly rose ozone production potential, as high as 40% [Li et al., 2020] on average.

Figure 3.5 compares the ozone production potential versus NO_x in three conditions as Figure 3.4. The aerosol uptake effects were constrained under high NO_x conditions when NO_x is larger than 20 ppbv. This should be explained as most of the OH radicals got removed by

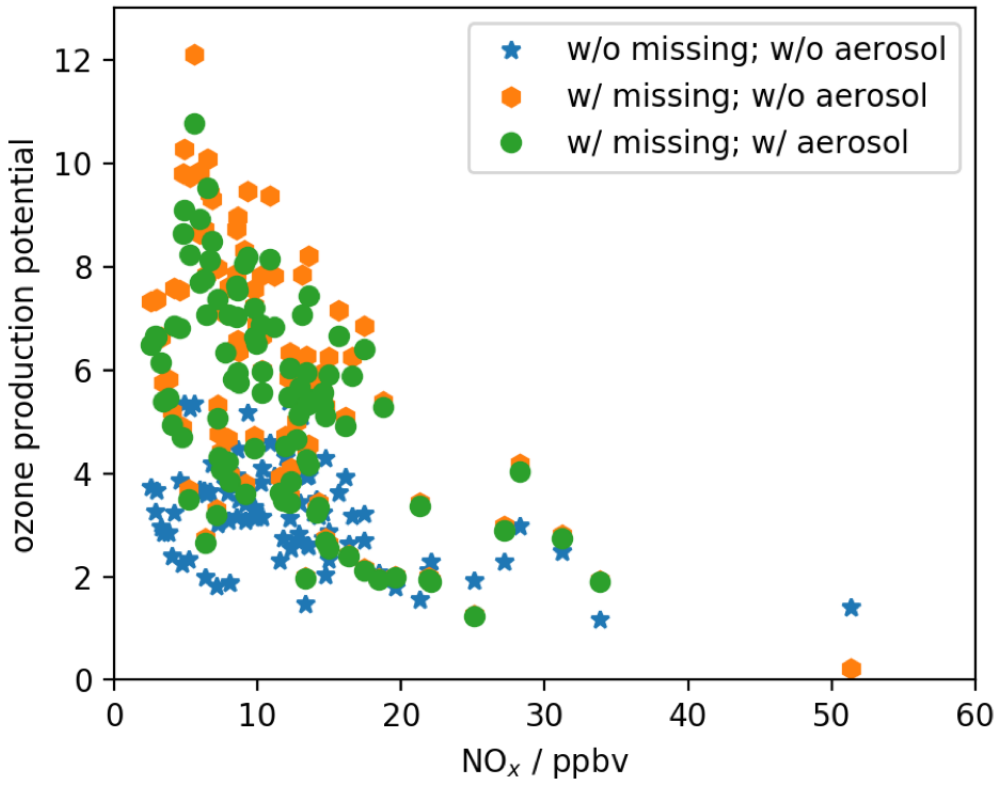

Figure 3.5: Ozone production potential only from calculated OH reactivity (in blue star); from total OH reactivity without considering aerosol uptake effects (in orange hexagon); and from total OH reactivity with aerosol uptake effects (in green circle) versus NO_x concentration in **Tsukuba – campaign**.

NO_2 termination pathways, as a result, leads to limited ozone production potential. On the other hand, it was found that the larger ozone production potential it is, the more important aerosol uptake kinetics should be. Especially when ozone production potential exceeds 6 ration, the contribution from aerosol uptake processes got quite noticeable. Similar conclusions suit with missing OH reactivity, as displayed in orange stars in Figure 3.5, in which missing OH reactivity boosted ozone production potential with low NO_x. When NO_x was too high, missing OH reactivity indicates minus effects on ozone production potential, this might come from the slow down of detected total OH reactivity as NO recycled OH radicals.

3.2.5 Ozone production analysis in Yokohama

Same calculation method on ozone production potential was conducted in Yokohama campaign, because the real-time loss coefficient of HO_2 by ambient particles was detected concurrently, therefore the directly measured k_{p_HO2} from [Zhou et al., 2021] was used. Because of extremely high NO_x concentration in Yokohama campaign, the real-time ambient NO_x con-

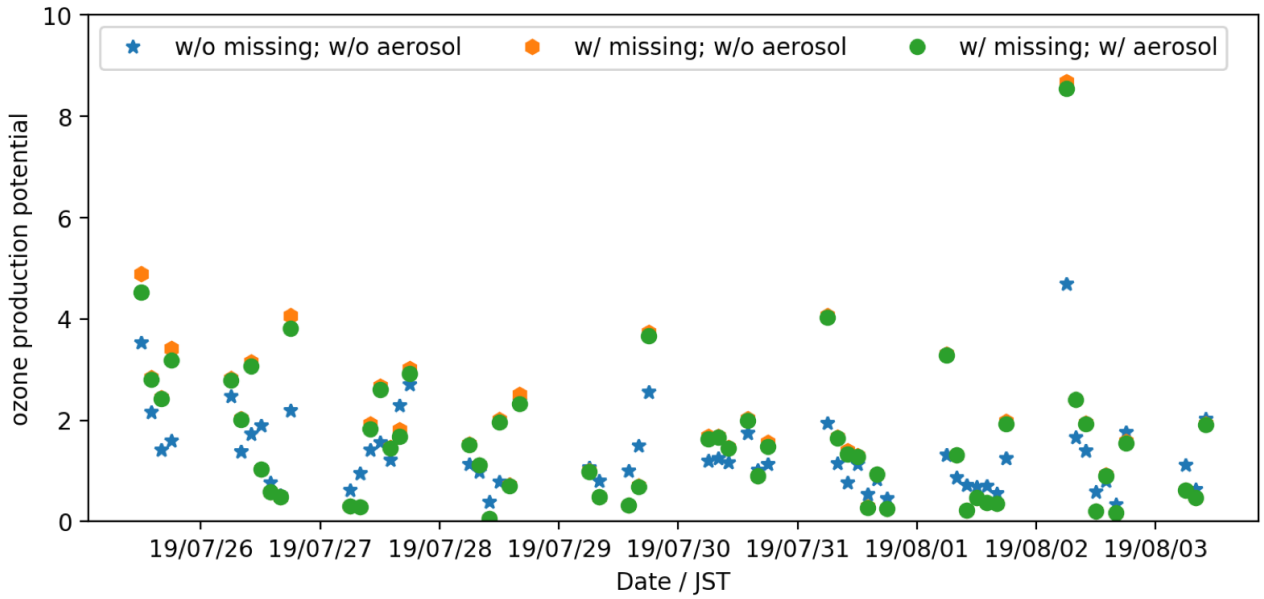

Figure 3.6: Temporal variations of the daytime (06:00-18:00) ozone production potential estimated only from calculated OH reactivity (in blue star); from total OH reactivity without considering aerosol uptake effects (in orange hexagon); and from total OH reactivity with aerosol uptake effects (in green circle) in **Yokohama – campaign**.

centrations were utilized for calculation and HO_x cycle reactions ceased quickly which lead to mitigating oxidative capacity. Therefore, the general ozone production potential in Figure 3.6 was distributed pretty low with maximal around 8 ration and most of the values were below 5 ration. Also, considering the limited active cyclic reactions, the influences from both missing OH reactivity and from uptake by particles were less important than that in Tsukuba. Especially the aerosol consideration condition almost make no difference from non-aerosol consideration condition. Also note that missing OH reactivity in Yokohama only took 8%, which is a quarter of the fraction in Tsukuba campaign.

Figure 3.7 compares the relationship between ozone production potential and NO_x in Yokohama. Similar to Tsukuba's case, only when NO_x was less than 20 ppbv, the aerosol uptake effects become important, so does the missing OH reactivity's contribution. As mentioned before, in most of the cases, Φ from aerosol consideration is approximately equal to that from non-aerosol consideration except when NO_x below 20 ppbv and ozone production potential above 2 ration. When NOx exceeds 50 ppbv, missing OH reactivity was diagnosed to be negative in sometime, this can explain those cases in which missing OH reactivity caused decreases in ozone production.

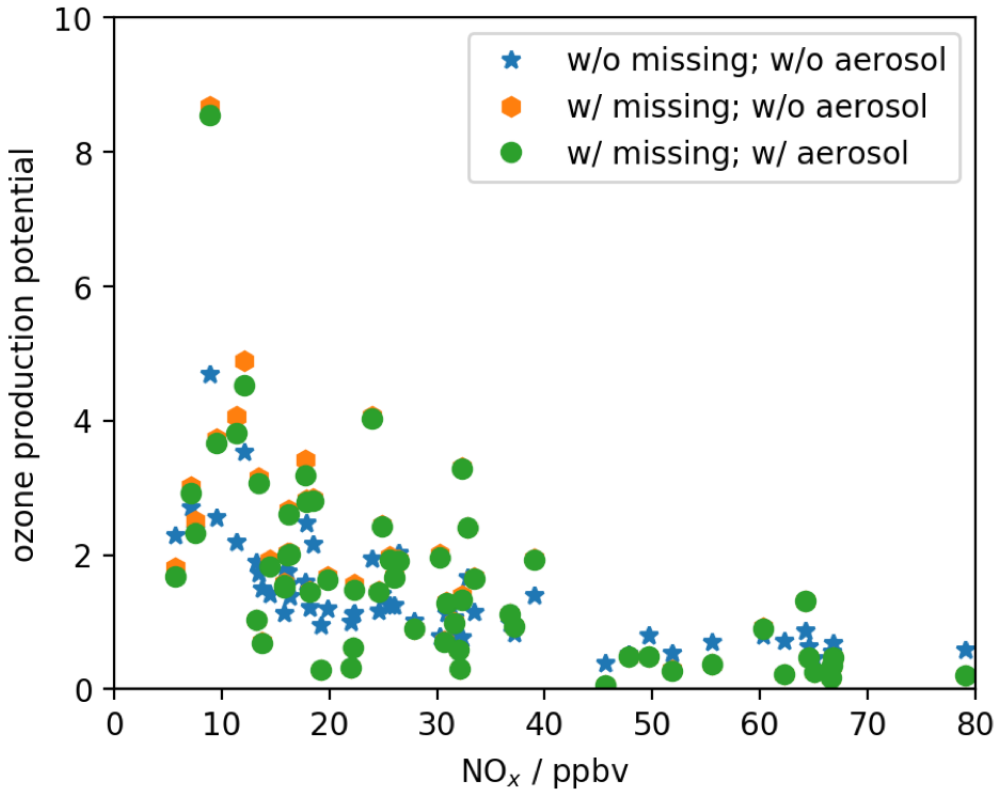

Figure 3.7: Ozone production potential only from calculated OH reactivity (in blue star); from total OH reactivity without considering aerosol uptake effects (in orange hexagon); and from total OH reactivity with aerosol uptake effects (in green circle) versus NO_x concentration in **Yokohama – campaign**.

3.2.6 Ozone production analysis in Kyoto

Kyoto campaign was expected as the cleanest urban area among the three campaigns, in which the smallest averaged total OH reactivity was obtained. NO_x concentration and other trace species mixing ratios were much lower compared with Yokohama and also Tsukuba. Therefore, the ozone production sensitivity analysis might exhibit quite different mechanism compared with other two campaigns. A similar estimation method for ozone production potential was applied in Kyoto, note that the loss rate of HO_2 radicals was assessed from the real-time surface area of particles and real-time uptake coefficient of HO_2. Although in Kyoto campaign, the real-time uptake coefficient of RO_2 derived from isoprene was continuously measured. Like previous assay, the loss rate of RO_2 radicals on aerosol was not considered. The concentration of peroxy radicals in Kyoto campaign was extrapolated from ozone mixing ratios based on an empirically model proposed by [Kanaya et al., 2007].

As Figure 3.8 shows, there are fluctuations of daily maximal ozone production potential (with aerosol consideration) through the whole observation, amongst which 8^{th}, 9^{th}, and 12^{th} indicated the lowest Φ daily peak approximately 2 ration compared to the largest daily peak equals 20 ration on 6^{th}. Specifically, on 8^{th} and 9^{th}, the overall ozone production potential was concentrated at low level. The lowest humidity and second lowest temperature were reported on 8^{th}, and 9^{th}, respectively. Less humid and cooler meteorological conditions might explain constrained ozone production potential in Kyoto compared with other normal days. The largest discrepancy between aerosol consideration and non-aerosol consideration was present in Kyoto campaign, with the average Φ from total OH reactivity, non-aerosol consideration equals 9 ration, while Φ from total OH reactivity, aerosol consideration to be 7.7 ration. When removing the contribution of missing OH reactivity, the mean ozone production potential is 3.9 ration with aerosol consideration. Although this is the overall case, on 5^{th} and 12^{th}, the contribution from missing OH reactivity was much smaller than that from the aerosol. The reason for such a distinct characteristics might lie on the meteorological and anthropogenic conditions because both days were Saturday and received similar air masses originated from the lake area.

Figure 3.9 exhibits the NO_x dependence on Φ. NO_x in Kyoto was less than 20 ppbv, and Φ from three different conditions showed similar tendencies as that in Tsukuba while more addictive to the transition regime. With the increasing of NO_x especially above 2.5 ppbv, ozone

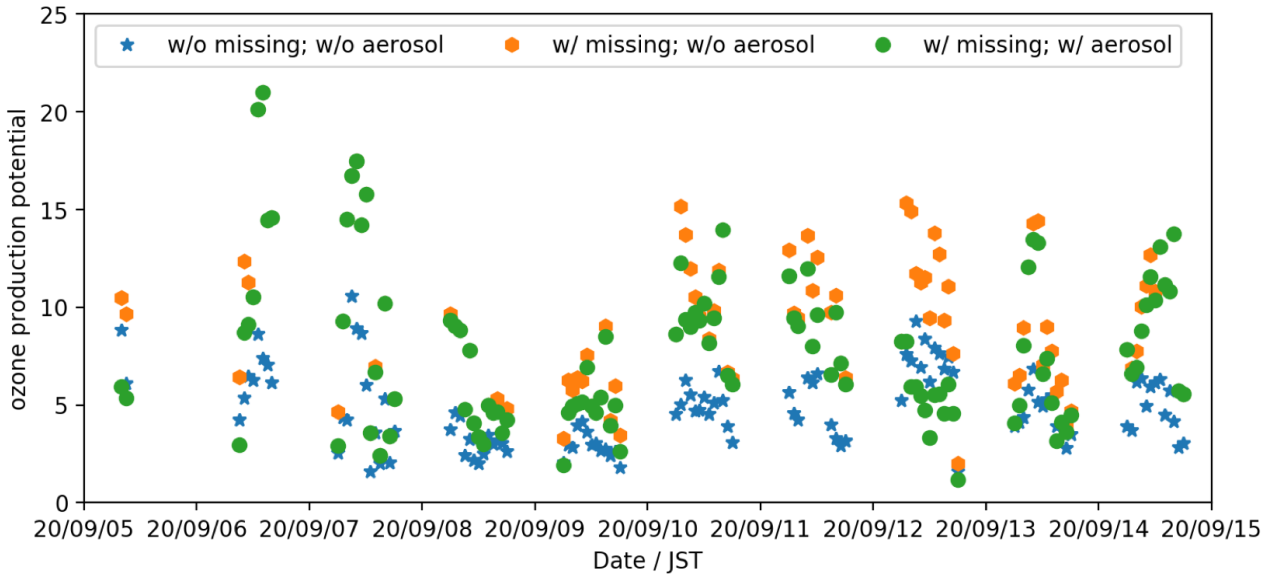

Figure 3.8: Temporal variations of the daytime (06:00-18:00) ozone production potential estimated only from calculated OH reactivity (in blue star); from total OH reactivity without considering aerosol uptake effects (in orange hexagon); and from total OH reactivity with aerosol uptake effects (in green circle) in **Kyoto – campaign**.

production potential declined quickly. In the range of NO_x below 2.5 ppbv, ozone production potential indicating as the transition regime with an increase first and then turn into decrease. The aerosol uptake effects were more important when NO_x concentration varied between 2.5 and 5 ppbv, and caused bigger difference in Φ value. Compared with aerosol uptake effects, missing OH reactivity is more critical in improving ozone production in Kyoto, especially missing OH reactivity also takes an important fraction.

3.2.7 A brief comparison of ozone production in three campaigns

The ozone production sensitivity was compared in terms of their behavior and characteristics under contrasting situations. Firstly, the potential ratio of Φ from total OH reactivity with aerosol consideration over that without aerosol consideration from three campaigns was plotted together in Figure 3.10. Secondly, ozone production rate according to (3.21) and (3.22) was provided for a comparable discussion.

The aerosol uptake effects on ozone production potential versus NO concentration was displayed in Figure 3.10, in which three locations were plotted in series and also together. Generally, there is a positive correlation between NO and the ratio range, a higher level of NO revealed with limited range of ratio which is also pretty high. For instance, in Yokohama NO

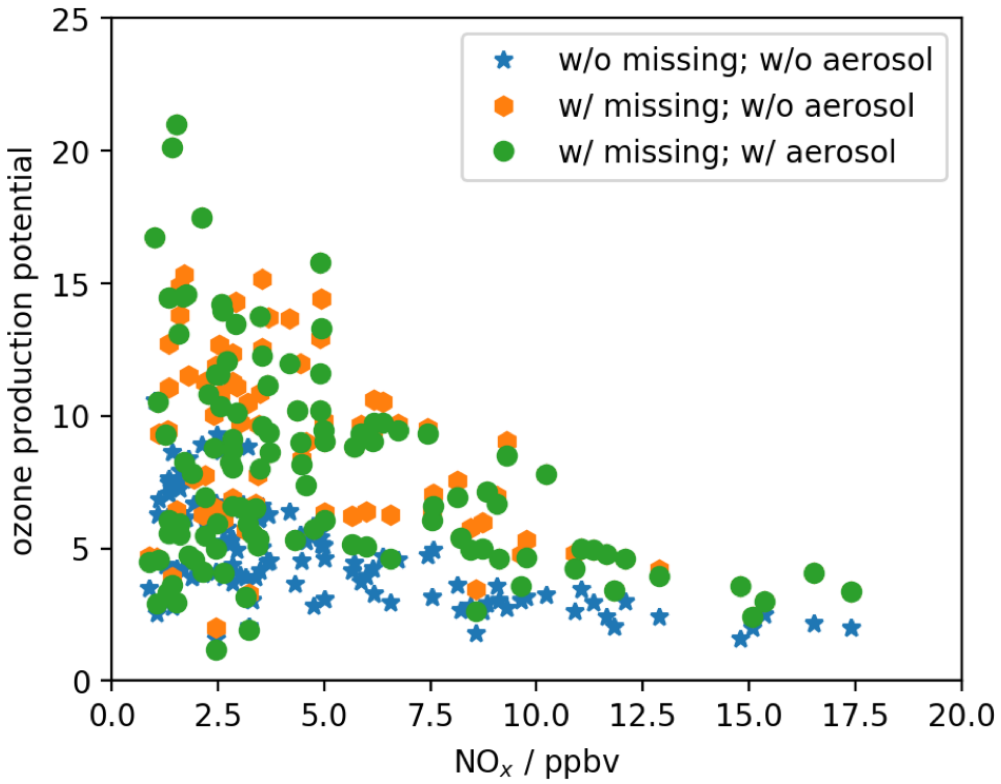

Figure 3.9: Ozone production potential only from calculated OH reactivity (in blue star); from total OH reactivity without considering aerosol uptake effects (in orange hexagon); and from total OH reactivity with aerosol uptake effects (in green circle) versus NO_x concentration in **Kyoto – campaign**.

ranged from 1 to 40 ppbv compared with the ratio varied from 0.92 to 1. The NO in Kyoto was quite low which mostly distributed below 1 ppbv and the ratio increased from 0.4 to 0.9 when NO increased. Tsukuba, as compared in the last graph, located more in the transition region, with NO dominantly varied over 0.5-2, and the ratio from 0.85 to 1. From the combination of three campaigns result, the relationship between aerosol uptake effects and NO concentration could be disclosed. The loss rate of peroxy radicals on particles would only be important when NO less than 1 ppbv. On the other hand, radicals would be terminated efficiently via the gas-phase reactions.

The result of ozone production rate, estimated from three campaigns, was compared with NO in Figure 3.11. Note that the real-time NO concentration in Yokohama and Kyoto were used due to its relatively high/low levels. Only in Tsukuba, NO was extrapolated from a stable NO/NO_x ratio multiplied by real-time NO_x concentration to avoid interconversion of NO into NO_2. The peroxy radicals concentration in Tsukuba and Kyoto was estimated from ozone concentration according to an empirical model from [Kanaya et al., 2007], while the concentration in Yokohama was extrapolated from a quasi-steady state of HO_x radicals.

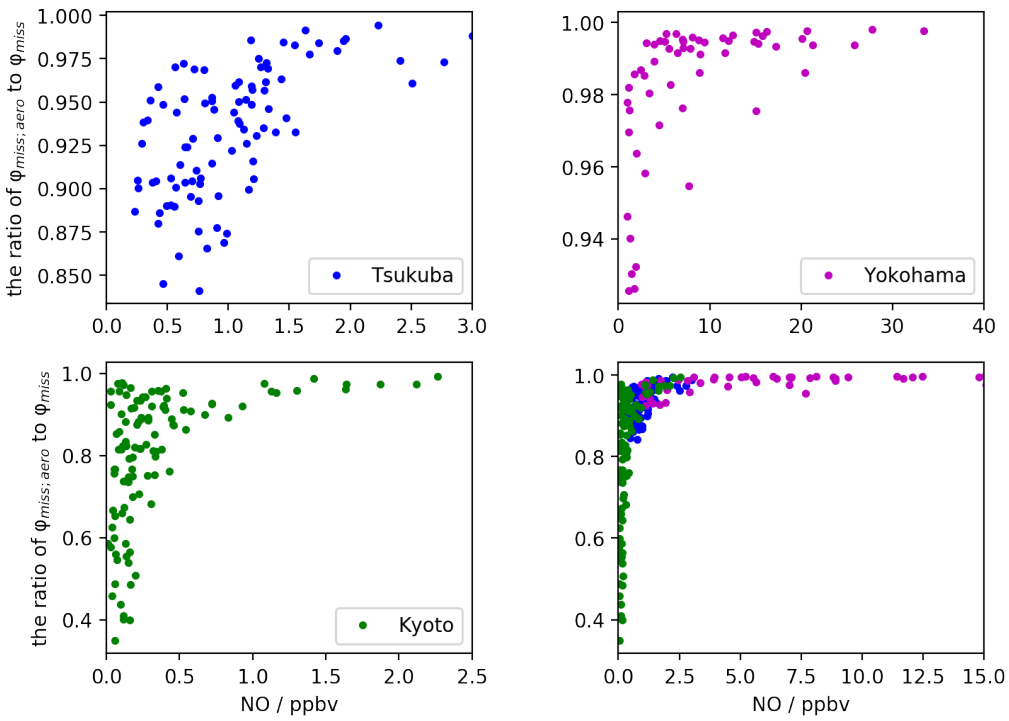

Figure 3.10: The ratio of ozone production potential Φ from total OH reactivity considering aerosol uptake to not considering uptake versus NO concentration in three campaigns.

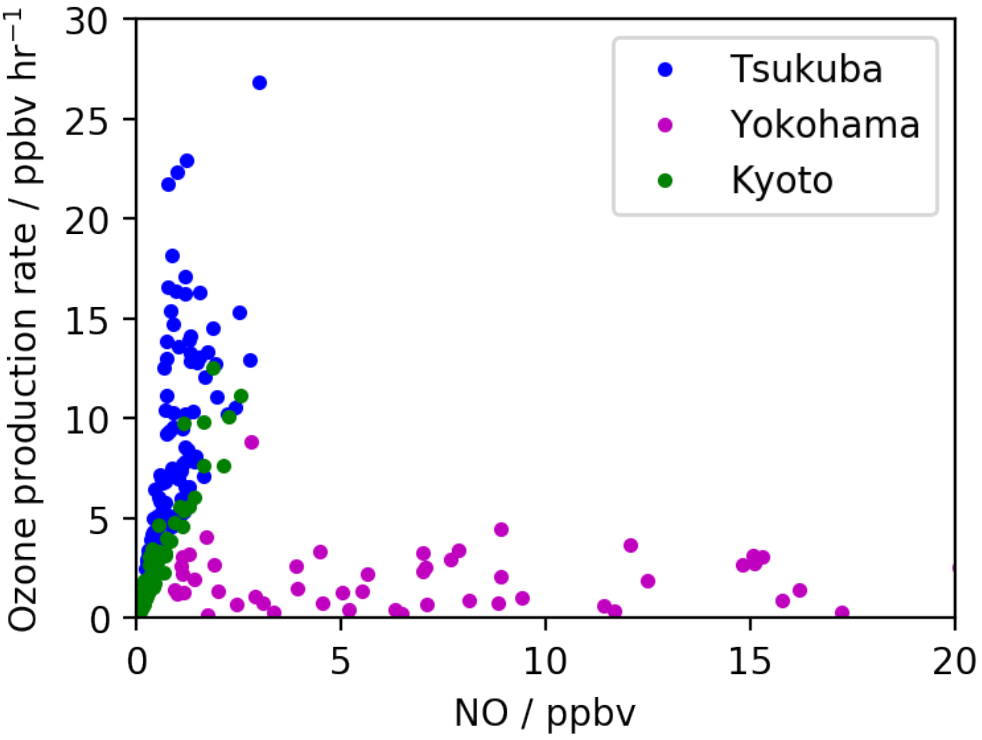

Figure 3.11: A comparative result between ozone production rate and NO concentration among three field studies.

The ozone production rate, as colored differently in locations in Figure 3.11, displayed contrasting behaviors based on NO concentration. Because of high NO concentration, ozone production rate was limited in Yokohama with an average of 2.2 ppbv hr^{-1} and mostly distributed below 5 ppbv hr^{-1}. The ozone production rate in Kyoto and Tsukuba was much higher specific in Tsukuba with highest value above 25 ppbv hr^{-1}. Ozone production rate in Kyoto was less than 15 ppbv hr^{-1}. From the positive correlation exhibited in Tsukuba and Kyoto, it was found that in the case when NO was less than 3 ppbv, ozone production rate will increase with NO. Owing to the local VOCs level, different maxima ozone production rate in Tsukuba and Kyoto were obtained.

3.3 Ozone regime sensitivity

Ozone, plays an important role in the troposphere considering its impacts on human, vegetation, and the ecosystem [Nuvolone et al., 2018]; [Monks et al., 2015]; [Van Dingenen et al., 2009]; [Krupa et al., 2001]. NO_x and VOCs, as the pivotal precursors of ozone, have to be investigated carefully. Researchers have divided the ozone isopleth diagram into two regime: VOC-limited (VOC-sensitive) and NO_x-limited (NO_x-sensitive) [Finlayson-Pitts and Pitts Jr, 1999]. The VOC-limited regime indicates that ozone production will be strengthened or mitigated by corresponding increasing or reducing of VOCs, and also by decreasing or increment of NO_x. Compared to that, in NO_x-limited regime, ozone production will increase with the increasing of NO_x, as showed in Figure 3.12. Note that in the Figure 3.12 the transition line was estimated from the ratio of [VOCs] over [NO_x], which should vary from case to case. Hence, to explore the ozone production mechanism precisely, especially based on the chemistry of HO_x cycle is substantial to effectively mitigate ozone.

The sensitivity of ozone production rate to its precursor, either VOCs or NO_x, was first given by [Kleinman et al., 1997], and further developed by assuming a proportional NO from NO_x [Kleinman et al., 2001]; [Kleinman, 2005]. The relative sensitivity of $P(O_3)$ was then advanced by [Sakamoto et al., 2019] via considering the HO_2 radical uptake effects on particles. Moreover, [Sakamoto et al., 2019] also proposed an absolute sensitivity by multiplying $P(O_3)$ with the relative sensitivity to judge the change in the value of $P(O_3)$ caused by its precursors increasing.

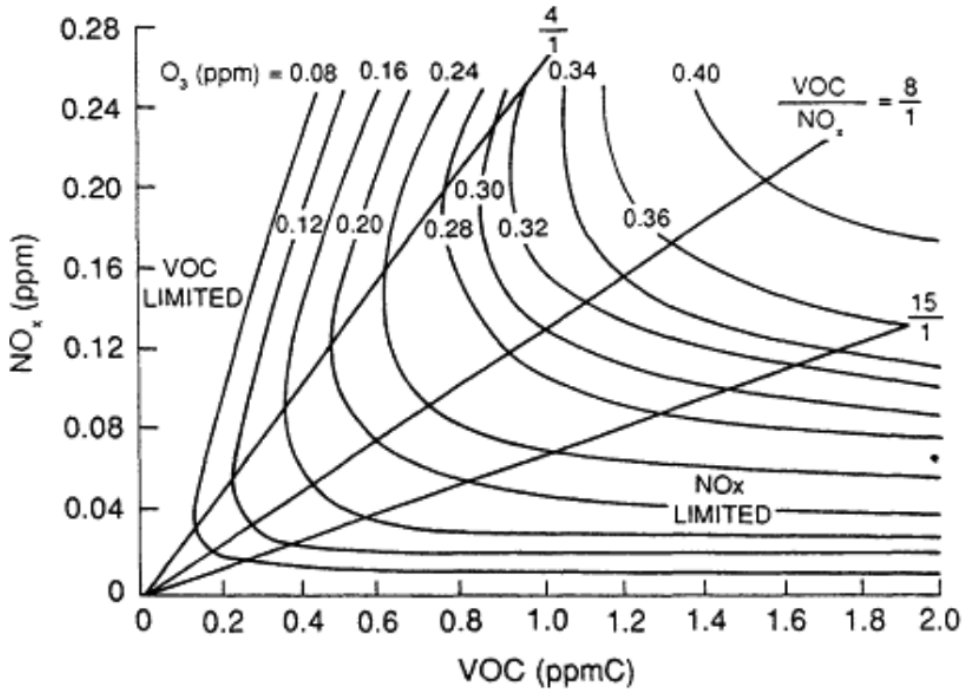

Figure 3.12: Typical ozone isopleths as a function of VOCs and NO_x used in EPA's empirical kinetic modeling approach (EKMA) [Dodge, 1977].

Firstly, the calculation of relative $P(O_3)$ will be described in detail based on the traditional approach proposed by [Kleinman et al., 1997]. Then the aerosol uptake effects will be included and the absolute sensitivity should be expanded from the calculation by [Sakamoto et al., 2019] in Subsection 3.3.1. Finally, the results of ozone sensitivity in Tsukuba (Subsection 3.3.2), Yokohama (Subsection 3.3.3), and Kyoto campaigns (Subsection 3.3.4) will be introduced thoroughly.

3.3.1 Derivation of $P(O_3)$ sensitivity

Ozone production rate, as explained in (3.21) and (3.22), firmly depends on the way to estimate peroxy radicals concentration. Owing to the quasi-steady state of all HO_x radicals, the radicals propagation Q should equal to the sum of all radicals sinks.

$$Q = L_R^* + L_N(+L_p) \tag{3.25}$$

In (3.25), the parameter Q represents the total radicals production rate, and L_R^* is the bimolecular radical-radical reactions loss rate, as displayed in (3.26). In principle, L_R^* should include peroxide formation and bimolecular radical-radical reactions such as OH + HO_2. How-

ever, the later is much less important and hence be disregarded in the calculation. L_N is radical loss rate via NO_x mainly considering the termination reaction of OH with NO_2, as explained in (3.27), in which k_N is the rate constant of OH with NO_2 and $P(NORO_2)$ means the formation of organic nitrate, which can be ignored. L_p is the aerosol uptake effects, which will be introduced in detail later.

$$L_R = 2k_{eff}([XO_2])^2 \tag{3.26}$$

$$L_N = k_N[OH][NO_2] + P(RONO_2) \tag{3.27}$$

In (3.26), k_{eff} is an effective rate constant for peroxide formation.

$$k_{eff} = k_{HO2-HO2}(\frac{[HO_2]}{[XO_2]})^2 + k_{HO2-RO2}\frac{[HO_2]}{[XO_2]}\frac{[RO_2]}{[XO_2]} \tag{3.28}$$

From (3.26) and (3.25), the $[XO_2]$ can be extrapolated, and $P(O_3)$ in (3.21) can be rewrote as in (3.29). k_t has been explained in (3.22).

$$P(O_3) = k_t\sqrt[2]{\frac{Q-L_N}{2k_{eff}}}[NO] \tag{3.29}$$

(3.29) is the foundation of ozone regime analysis, a detailed mathematic transformation will be introduced hereinafter based on (3.29). The final goal of ozone sensitivity analysis is to figure out the change rate of $P(O_3)$ should be either more sensitive to NO_x or VOCs. The results are considered to be critically important in order to mitigate ozone effectively and scientifically.

$$\frac{dlnP(O_3)}{dln[NO]} = \frac{\frac{dP(O_3)}{P(O_3)}}{\frac{d[NO]}{[NO]}} \tag{3.30}$$

$$lnP(O_3) = ln\frac{k_t}{(2k_{eff})^{\frac{1}{2}}} + \frac{1}{2}ln(Q-L_N) + ln\alpha[NO_x] \tag{3.31}$$

From (3.29), we can obtain the relative sensitivity by differentiating (3.31) with respect to $[NO_x]$ or [VOCs], as showed in (3.32), and (3.33), respectively. [NO] in (3.29) was replaced by $\alpha[NO_x]$ in (3.31). The simplified model equation is provided in (3.30).

$$\frac{\partial lnP(O_3)}{\partial ln[NO_x]} = -\frac{1}{2}\frac{\partial L_N}{(Q-L_N)}\frac{[NO_x]}{\partial[NO_x]} + 1 \tag{3.32}$$

$$\frac{\partial lnP(O_3)}{\partial ln[VOCs]} = -\frac{1}{2}\frac{\partial L_N}{(Q-L_N)}\frac{[VOCs]}{\partial[VOCs]} \tag{3.33}$$

Note that from (3.31) to (3.32) and (3.33), Q only depends on radicals precursors like ozone and formaldehyde, and the dependence of k_t and k_{eff} on [NO_x], [VOCs] is basically quite small and therefore have been ignored.

In the condition where HO_x cycle propagation is more important than initiation, the consumed OH radicals finally will be regenerate via HO_2 reaction with NO. Therefore, such procedure can be manipulated as (3.34) when HO_x cycle reactions are active. Note that this equation is not suitable in clean area, where [NO_x] is pretty low, and $\frac{L_N}{Q}$ is close to zero.

$$k_i[OH][VOCs] = k_{HO2-NO}[HO_2][NO] \tag{3.34}$$

Combine (3.34) into (3.27), the sink rate L_N can be rewrite as in (3.35). The parameter P($RONO_2$) can be ignored in further calculation because its integral is pretty small.

$$L_N = k_N(1-\alpha)[NO_x]\frac{P(O_3)}{k_i[VOCs]} + P(RONO_2) \tag{3.35}$$

$$lnL_N = ln(1-\alpha)k_N\frac{1}{k_i[VOCs]} + lnP(O_3) + ln(NO_x) \tag{3.36}$$

Similar as before, we can differentiating (3.36) with respect to [NO_x] or [VOCs].

$$\frac{\partial lnL_N}{\partial ln[NO_x]} = 1 + \frac{\partial lnP(O_3)}{\partial ln[NO_x]} \tag{3.37}$$

$$\frac{\partial lnL_N}{\partial ln[VOCs]} = \frac{\partial lnP(O_3)}{\partial ln[VOCs]} - 1 \tag{3.38}$$

From (3.32), (3.37), we can extrapolate (3.39), in which the relative sensitivity of ozone production in terms of [NO_x] is clear from L_N/Q. The same calculation approach was used from (3.33) and (3.38) for that from [VOCs], as displayed in (3.40).

$$\frac{\partial lnP(O_3)}{\partial ln[NO_x]} = \frac{1-\frac{3L_N}{2Q}}{1-\frac{L_N}{2Q}} \tag{3.39}$$

$$\frac{\partial lnP(O_3)}{\partial ln[VOCs]} = \frac{\frac{L_N}{2Q}}{1-\frac{L_N}{2Q}} \tag{3.40}$$

(3.39) and (3.40) are the relative $P(O_3)$ sensitivity presented by a simple expression via L_N/Q. [Kleinman et al., 2001] also proposed an expression for L_N/Q. Firstly, combine (3.25) and (3.26), an equation in the form of L_N/Q can be obtained.

$$Q(1-L_N/Q) = 2k_{eff}([XO_2])^2 \tag{3.41}$$

$$\beta = \frac{[HO_2]}{[XO_2]} \tag{3.42}$$

Substituting (3.34) into (3.41), and replace $[XO_2]$ by $[HO_2]$.

$$1-L_N/Q = 2k_{eff}Q(\frac{k_i[VOCs]L_N}{k_{HO2-NO}k_N\beta[NO][NO_2]Q})^2 \tag{3.43}$$

(3.43) can be solved by the root formula, as displayed in (3.44).

$$\frac{L_N}{Q} = -\frac{a}{2} + \frac{\sqrt[2]{a^2+4a}}{2} \tag{3.44}$$

Where,

$$a = (\frac{1}{2k_{eff}Q})(\frac{k_{HO2-NO}k_N\beta[NO][NO_2]}{k_i[VOCs]})^2 \tag{3.45}$$

The consideration of L_p will be added hereinafter. L_p should be estimated from effective uptake coefficient, k_{p_XO2}, which has been explained in (3.23), and peroxy radicals concentration. The estimation is based on the prerequisite in which $L_p \gg L_R$.

$$L_p = k_{p\_XO2}[XO_2] \tag{3.46}$$

Substituting (3.46) and (3.26) into (3.25).

$$[XO_2] = \frac{Q-L_N}{2k_{eff}[XO_2]+k_{p\_XO2}} \tag{3.47}$$

By substituting (3.47) into (3.21), $P(O_3)$ can be expressed as follow.

$$P(O_3) = k_t\frac{Q-L_N}{2k_{eff}[XO_2]+k_{p\_XO2}}[NO] \tag{3.48}$$

The logarithm of (3.48) can be expressed as,

$$lnP(O_3) = ln\frac{k_t}{2k_{eff}[XO_2] + k_{p\_XO2}} + ln(Q - L_N) + ln\alpha[NO_x] \tag{3.49}$$

From (3.49), the relative sensitivity with k_p consideration can be derived by differentiating with respect to [NO_x] or [VOCs].

$$\frac{\partial lnP(O_3)}{\partial ln[NO_x]} = 1 - \frac{\partial L_N}{Q - L_N}\frac{[NO_x]}{\partial [NO_x]} \tag{3.50}$$

$$\frac{\partial lnP(O_3)}{\partial ln[VOCs]} = -\frac{\partial L_N}{Q - L_N}\frac{[VOCs]}{\partial [VOCs]} \tag{3.51}$$

Substituting (3.37), and (3.38) into (3.50), and (3.51), respectively. The relative $P(O_3)$ sensitivity can be obtained as exhibited in (3.52) and (3.53).

$$\frac{\partial lnP(O_3)}{\partial ln[NO_x]} = 1 - \frac{2L_N}{Q} \tag{3.52}$$

$$\frac{\partial lnP(O_3)}{\partial ln[VOCs]} = \frac{L_N}{Q} \tag{3.53}$$

(3.39), (3.40), (3.52), and (3.53) expressed the relative $P(O_3)$ sensitivity with respect to [NO_x] and [VOCs] in the condition of $L_R \gg L_p$, and $L_p \gg L_R$, respectively. [Sakamoto et al., 2019] combines both conditions via using the ratio of $L_p/(L_p + L_R)$.

$$\chi = \frac{L_p}{L_p + L_R} \tag{3.54}$$

$$\frac{\partial lnP(O_3)}{\partial ln[NO_x]} = (1 - \chi)\frac{1 - \frac{3L_N}{2Q}}{1 - \frac{L_N}{2Q}} + \chi(1 - \frac{2L_N}{Q}) \tag{3.55}$$

$$\frac{\partial lnP(O_3)}{\partial ln[VOCs]} = (1 - \chi)(\frac{\frac{L_N}{2Q}}{1 - \frac{L_N}{2Q}}) + \chi\frac{L_N}{Q} \tag{3.56}$$

As mentioned before, the absolute $P(O_3)$ sensitivity can be obtained by the $P(O_3)$ multiply with (3.55) or (3.56).

$$P(O_3)\frac{\partial lnP(O_3)}{\partial ln[Y]} = \frac{\partial P(O_3)}{\partial ln[Y]} \tag{3.57}$$

When (3.55) equals (3.56), the regime transition point can be explored, in which $L_N/Q_{transition}$

can be expressed as in (3.58).

$$\frac{L_N}{Q}_{transition} = \frac{(3\chi+4) \pm \sqrt{(3\chi+4)^2 - 24\chi}}{6\chi} \tag{3.58}$$

Similarly, when $\frac{\partial lnP(O_3)}{\partial ln[NO_x]}$ in (3.55) equals zero, the ozone production sensitivity turns into the transition regime, as defined as L_N/Q_{zero} exhibiting in (3.59).

$$\frac{L_N}{Q}_{zero} = \frac{(2\chi+3) \pm \sqrt{(2\chi+3)^2 - 16\chi}}{4\chi} \tag{3.59}$$

Another approach to figure out $L_N/Q_{transition}$ and L_N/Q_{zero} could be from (3.39), (3.40), (3.52), and (3.53). In the condition of $L_R \gg L_p$, $L_N/Q = \frac{1}{2}$ when (3.39) equals (3.40). On the other hand, in the condition of $L_p \gg L_R$, from (3.52) and (3.53), we know that L_N/Q equals $\frac{1}{3}$.

$$\frac{L_N}{Q}_{transition} = (1-\chi)\frac{1}{2} + \chi\frac{1}{3} \tag{3.60}$$

Using a similar way, we can get (3.62) by assuming (3.39) and (3.52) equal zero in the condition of $L_R \gg L_p$, and $L_p \gg L_R$, respectively.

$$\frac{L_N}{Q}_{zero} = (1-\chi)\frac{2}{3} + \chi\frac{1}{2} \tag{3.61}$$

From (3.47), (3.34), and (3.27), $\frac{L_N}{Q}$ can be expressed as in (3.62).

$$\frac{L_N}{Q} = \frac{1}{1 + (\frac{(2k_{eff}[XO_2] + k_{p\_XO2})k_i[VOCs]}{k_N k_{HO2-NO}\beta[NO][NO_2]})} \tag{3.62}$$

3.3.2 Ozone regime sensitivity in Tsukuba campaign

The relative ozone production sensitivity was estimated in Tsukuba campaign and has been reported in [Sakamoto et al., 2019]. Here estimates the relative and absolute ozone production sensitivity using the aforementioned calculation. The time series of L_N/Q calculated from (3.62) with the loss rate of aerosol uptake were displayed in Figure 3.13. The reference line in black indicating $L_N/Q_{transition}$, in red indicating L_N/Q_{zero} were added to distinguish the regime of NO_x-limited or VOCs-limited explicitly. The region between L_N/Q_{zero} and $L_N/Q_{transition}$ indicates the transition regime, below $L_N/Q_{transition}$ refers to NO-limited regime, and above L_N/Q_{zero} is

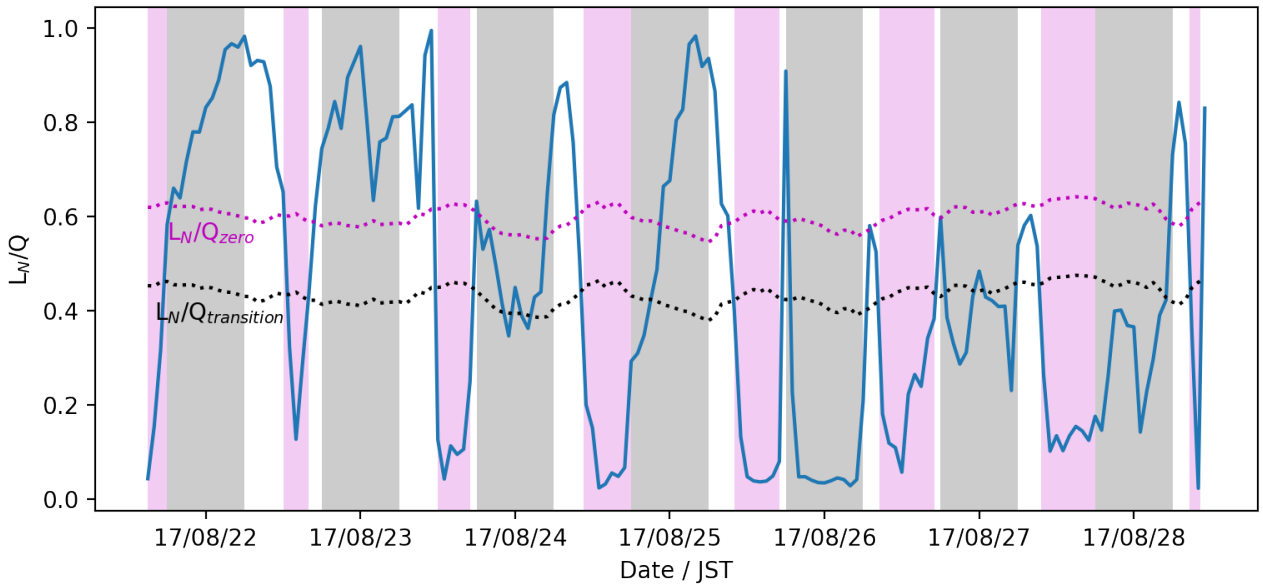

Figure 3.13: Temporal variations of L_N/Q including aerosol uptake effects in **Tsukuba – campaign**. The black shaded area indicates nighttime, and pink shaded area highlights NO_x-limited regime. Dashed line depicts the transition regime.

VOCs-limited regime. It can be found that during the observation, the site generally is VOCs-limited regime according to the aforementioned ozone production potential results. However, from Figure 3.13, non-shaded areas indicating VOCs-limited regime which showed up during the morning and then turned into NO_x-limited regime in the afternoon. Although time to time, the relative ozone sensitivity changes, the morning regime dominated the whole campaigns' ozone production.

The effects of missing OH reactivity and aerosol uptake in the estimated relative $P(O_3)$ sensitivity were displayed in Figure 3.14 and Figure 3.15, respectively. The change of the regime occurred on 22^{nd} from missing OH reactivity, as shaded in orange. On the other hand, the aerosol uptake effects turned VOC-limited regime into NO_x-limited more frequently in short-term, as highlighted in green area in Figure 3.15. In a VOC-limited region, aerosol uptake effects can suppress the production of ozone, reduction was specifically obvious in the early morning. Compared to that, in NO_x-sensitivity region, the reduction impacts were constrained by aerosol, which might lead to an increase of ozone production.

The accumulated daily absolute $P(O_3)$ sensitivity as showed in Figure 3.16 compares the integrated ozone production sensitivity attributed from [NO_x] or [VOCs]. Quite large ozone production sensitivity appeared on 22^{nd}, 23^{rd}, and 25^{th}, during this period polluted air masses passed from Tokyo and its surrounding areas flowed to the observational site. Although gener-

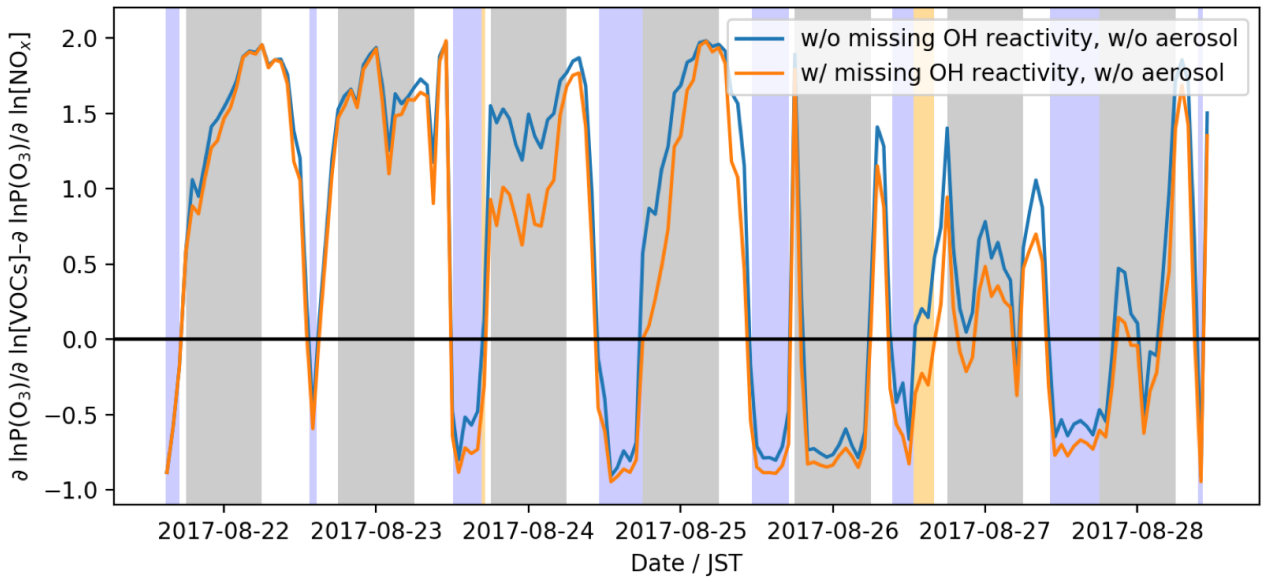

Figure 3.14: Time series of the difference between relative $P(O_3)$ sensitivity with respect to [VOCs] and $[NO_x]$ compared in the group of no missing OH reactivity consideration and with missing OH reactivity consideration in **Tsukuba – campaign**.

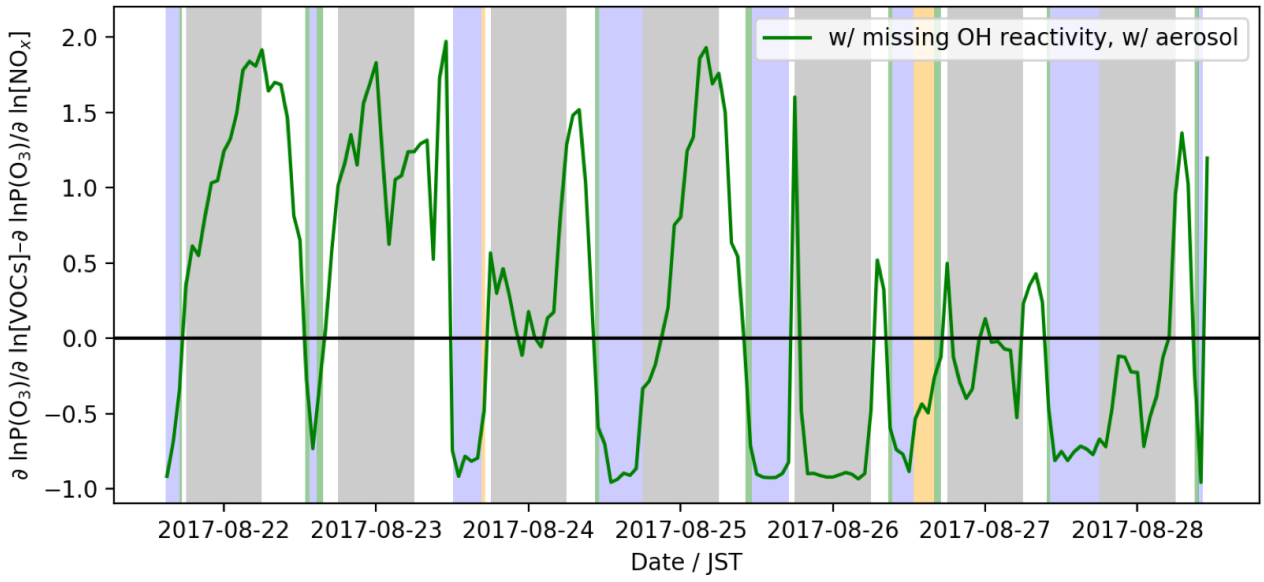

Figure 3.15: Time series of the difference between relative $P(O_3)$ sensitivity with respect to [VOCs] and $[NO_x]$ estimated with both missing OH reactivity and aerosol uptake effects in **Tsukuba – campaign**.

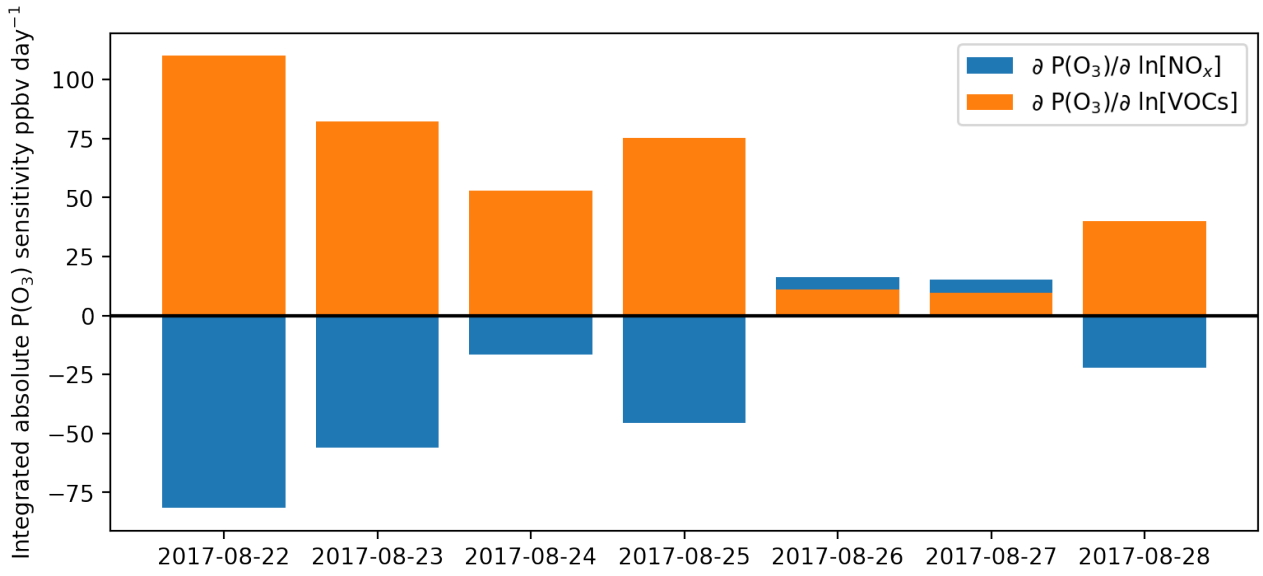

Figure 3.16: Integrated absolute $P(O_3)$ sensitivity to NO_x and VOCs during the daytime for the whole observation period in **Tsukuba – campaign**.

ally NO_x had negative contributions to ozone production sensitivity, the total ozone production on site should be determined by VOCs level because of the dominant VOC-limited regime. However, on 26^{th} and 27^{th}, NO_x exhibited positive contribution to the ozone production which outdid the contribution from VOCs. As highlighted in Figure 2.2, 26^{th} and 27^{th} were on weekend while clean air mass originated from the lake area also blowed the measurement site. Although in Figure 3.14, NO_x-sensitive regime appeared every afternoon while only on 26^{th} and 27^{th}, VOC-sensitive condition got surpassed by NO_x-sensitive regime according to the integrated ozone production sensitivity analysis.

3.3.3 Ozone regime sensitivity in Yokohama campaign

Same estimation approach was conducted based on the dataset of Yokohama campaign, however, because of extremely high NO_x concentration in Yokohama. The ozone production sensitivity results are quite different from Tsukuba's. First, as showed in Figure 3.17, the overall ratio of L_N/Q based on the consideration of L_p was above 0.95, which is much larger than the transition value per ca. The reference transition lines were not plotted in Figure 3.17 because they located much lower than the ratio. Therefore, the ozone production sensitivity could always be VOCs-limited regime. It is noteworthy to mention that a relative wide range (0.95-1) of L_N/Q appeared on the initial several days before 29^{th}.

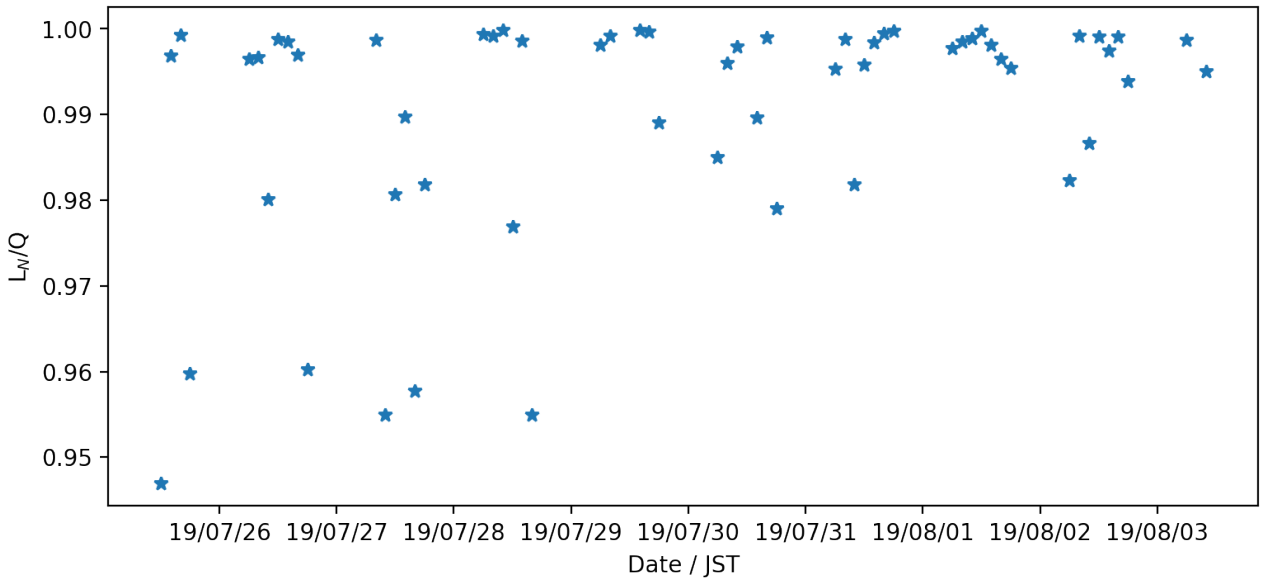

Figure 3.17: Diurnal variations of L_N/Q with HO_2 radicals loss considering aerosol uptake in **Yokohama – campaign**.

The relative $P(O_3)$ sensitivity over partial [NO_x] or partial [VOCs] in logarithmic scale was compared from non-aerosol effects and aerosol effects, as showed in Figure 3.18. Since Yokohama suffered from high NO_x condition, distinctive behavior between NO_x and VOCs was exhibited in which the NO_x only contributed to ozone production negatively. When compare the impacts of aerosol uptake in NO_x and VOCs group, various fluctuations in NO_x-sensitive indicating that aerosol uptake loss procedure had larger effects in NO_x contribution, which, as a result, can reduce the mitigation effect of ozone production importantly. As for VOCs contribution, there is scarce difference between the group with and without aerosol uptake.

The level of integrated absolute $P(O_3)$ sensitivity in Yokohama campaign was much lower compared with that in Tsukuba. In Yokohama the value distributed from zero to 8 ppbv hr^{-1} while in Tsukuba it can be as high as over 60 ppbv hr^{-1}, which is in daily average below 20 ppbv day $^{-1}$ compared to 110 ppbv day^{-1}. Owing to the relative small absolute $P(O_3)$ sensitivity throughout the campaign, there were no big variations from day to day, except the maximal value only appeared on 2^{nd}. Such a spike showed up together with polluted air mass initiated from Tokyo area, however, same air mass also came on 1^{st}, while the accumulated absolute ozone production was only half the amount. The reason for such a difference was not clear. The absolute $P(O_3)$ sensitivity with respect to NO_x and VOCs delineated similar conclusion as that to relative $P(O_3)$ sensitivity, generally VOCs positively contributed to ozone production

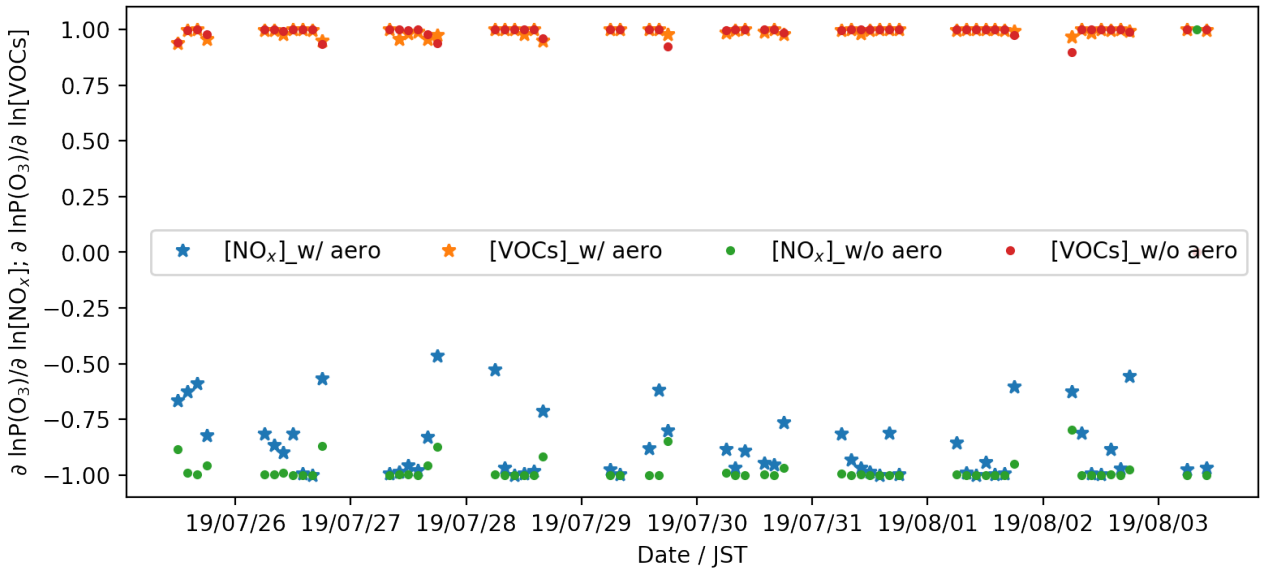

Figure 3.18: Temporal variations of relative $P(O_3)$ sensitivity with respect to $[NO_x]$ or [VOCs] with aerosol uptake and without aerosol uptake in **Yokohama – campaign**.

and NO_x constrained the $P(O_3)$. Since no NO_x-limited regime was obtained in Yokohama, the whole period could belong to VOCs-limited regime due to high NO_x concentration in-situ.

3.3.4 Ozone regime sensitivity in Kyoto campaign

The time series of the ratio L_N/Q (considering the aerosol uptake effects) during the daytime in Kyoto campaign was displayed in Figure 3.20. In Kyoto, the ratio varies greatly from time to time. When L_N/Q is smaller than the $L_N/Q_{transition}$, corresponding area was highlighted in pink refers to NO_x-limited. Except on 8^{th} and 14^{th}, all other days contain some time as NO_x-limited regime. There was a period that pertained to the transition regime almost everyday, as indicating between the red dashed line and black dashed line. Dislike the appearance that NO_x-limited only existed in the second-half of the day in Tsukuba, Kyoto observed NO_x-limited regime with varied hours of the day. This can be explained as the general low level of NO_x in Kyoto compared to the comparatively low level in the afternoon in Tsukuba. However, even NO_x-limited regime frequently controls the ozone production sensitivity, Kyoto campaign was dominantly influenced by VOC-limited regime and also transition regime in low NO_x conditions considering much larger contributions to the formation of ozone in-situ was stimulated by VOCs rather than NO_x.

Figure 3.21 expressed the discrepancy of relative ozone production sensitivity between calcu-

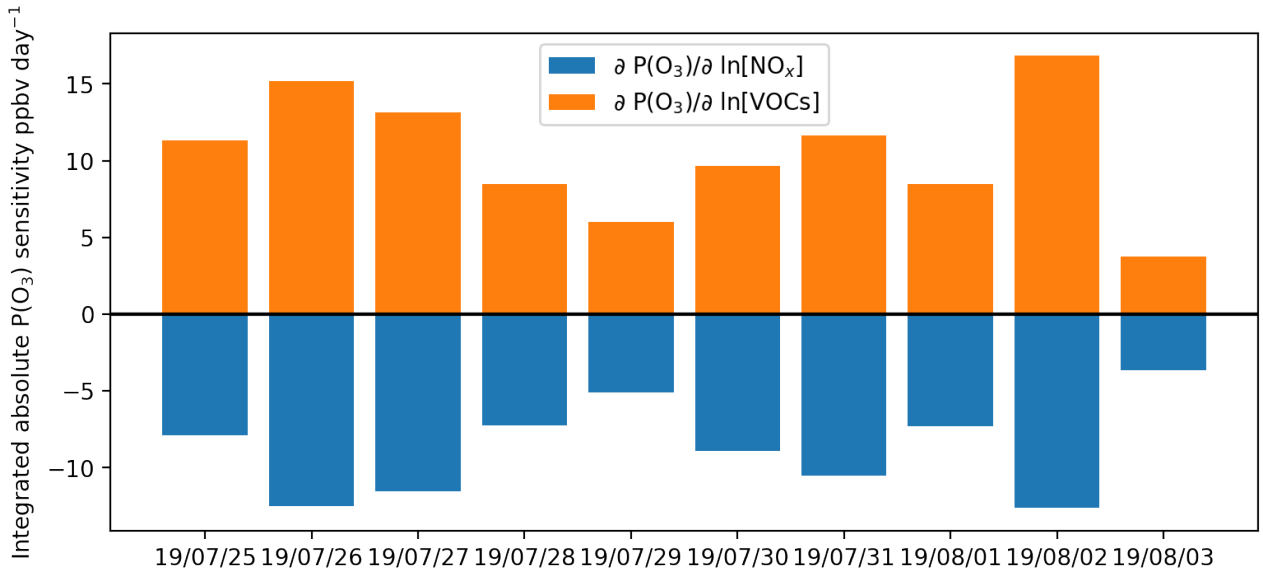

Figure 3.19: Absolute $P(O_3)$ sensitivity during the daytime compared from $[NO_x]$ and [VOCs] in **Yokohama – campaign**.

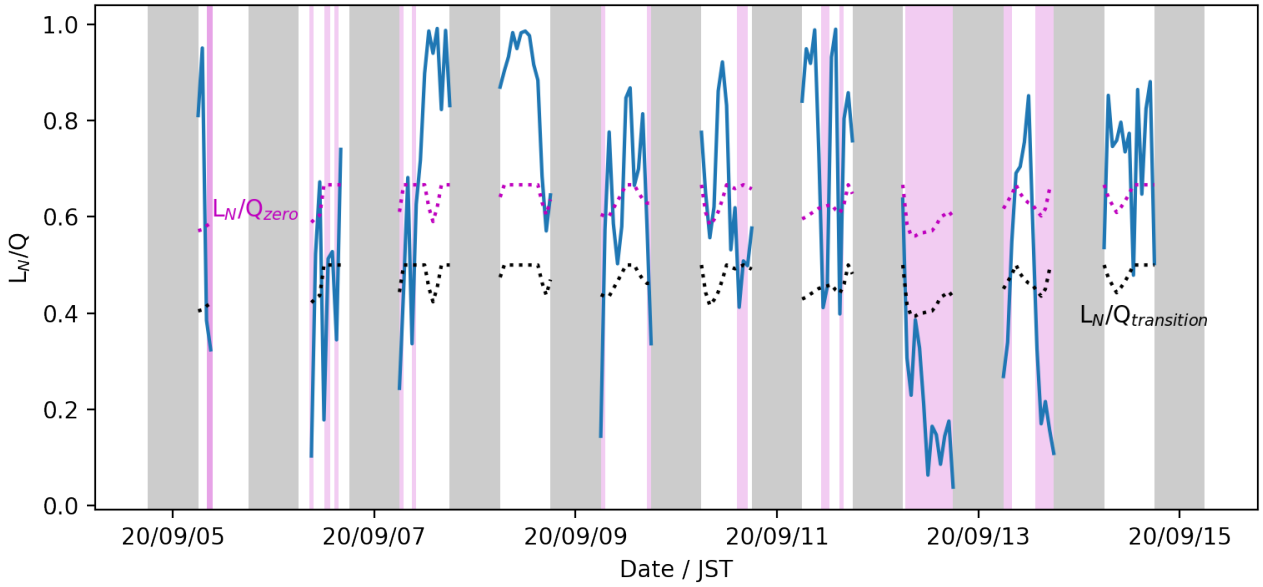

Figure 3.20: Temporal variations of L_N/Q with aerosol uptake consideration in **Kyoto – campaign**. Black shaded area indicates night time, and pink shade area means the NO_x-limited regime.

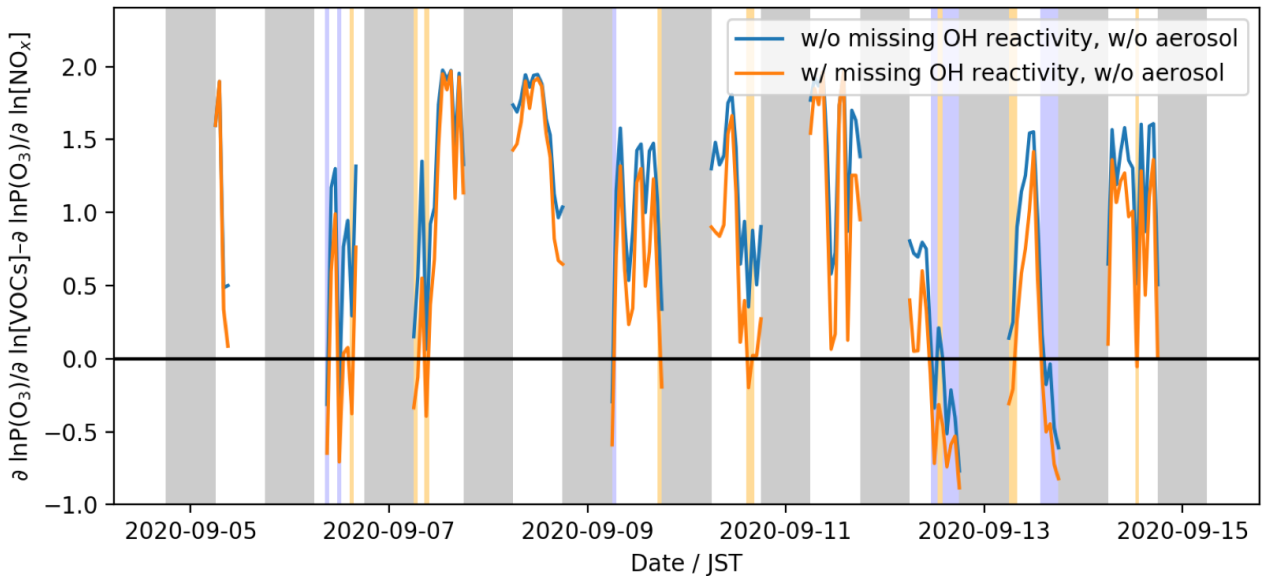

Figure 3.21: Time series of the relative $P(O_3)$ sensitivity with respect to $[NO_x]$ or [VOCs] compared in the group with aerosol uptake effects and without aerosol uptake effects in **Kyoto – campaign**.

lated OH reactivity and total OH reactivity in temporal scale. NO_x-limited regime was marked in blue color when estimated the result from calculated OH reactivity and in orange when take missing OH reactivity into account. NO_x-limited regime dominated on the afternoon of 12^{th} and 13^{th}. Figure 3.22 shaded the aerosol effects-altered regions in green, same color as that in Tsukuba's case, from which the day of 12^{th} was totally converted into NO_x-limited regime. Identical alternation of regime was found in Kyoto as that in Tsukuba. The aerosol uptake consideration had a decreasing effects in VOCs contribution while strengthened the reduction of ozone production in NO_x attribution. According to the aerosol uptake effects in ozone production sensitivity from both Tsukuba and Kyoto campaigns, it could be concluded as that the particles can expand NO_x-limited regime period for hours. Although the changing trigger stays unclear, NO_x concentration and aerosol conditions (mass concentration, chemical compositions such as transition metal, and size distributions) might be the key to disclose the mechanism.

The daily integrated absolute $P(O_3)$ sensitivity was displayed in Figure 3.23, in which high ozone production rate appeared on 7^{th} and 8^{th} when polluted air masses transported from Osaka arrived in Kyoto. The highest accumulated ozone production appeared on 8^{th}, which is as high as 60 ppbv day^{-1}. Although 13^{th} and 15^{th} experienced same direction of air masses (see Figure 2.27), elevated ozone production rate was not found on these days. The result on 15^{th} was lost due to calibration. NO_x elucidated limited positive impacts on ozone production on 6^{th} and 12^{th},

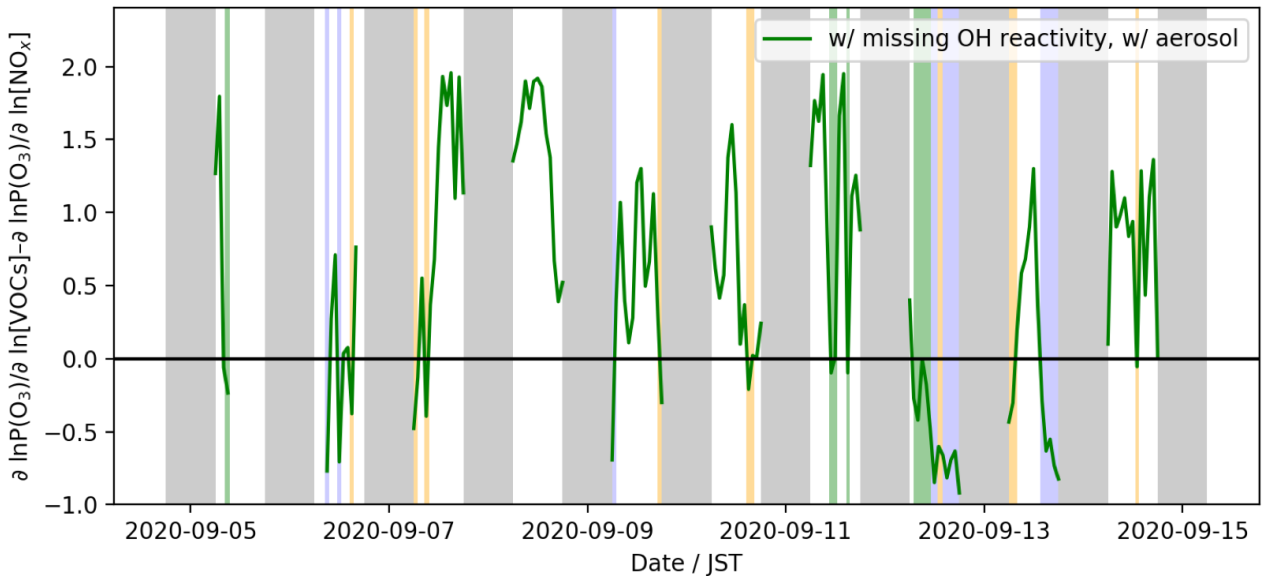

Figure 3.22: Time series of the relative $P(O_3)$ sensitivity with respect to $[NO_x]$ or [VOCs] compared in the group with aerosol uptake effects and without aerosol uptake effects in **Kyoto – campaign**.

while the dominate contribution of ozone production came from VOC-limited and transition regime with relatively low NO_x concentrations in Kyoto. Generally, ozone production rate in Kyoto was not high compared with the case in Tsukuba, this might be caused by relatively low level of NO_x and VOCs, as Kyoto is quite clean as described in Section 2.3.

3.3.5 A brief comparison over Tsukuba, Yokohama, and Kyoto campaigns

Figure 3.24 shows the relationship between L_N/Q and [NO], there is no [NO] dependence in Yokohama while [NO] was pretty high. In Tsukuba and Kyoto, L_N/Q indicates a positive corresponding relationship with [NO], especially in the case when [NO] is below 1 ppbv. The L_N/Q droped from 1 to 0.4 quickly when [NO] ranges from 0.2-1 ppbv, this range was reported to be the transition regime in Tsukuba [Sakamoto et al., 2019]. It has to be noted that although the calculation methods are same in this work and [Sakamoto et al., 2019], several parameters, including the ratio of HO_2 to XO_2, in the condition were set differently, therefore discrepancy might exist in the result. When compare the scattered points in Tsukuba and in Kyoto, comparable trends can be found in both cases while the result in Kyoto located at the left side of that in Tsukuba. This indicates both lower level of NO_x and peroxy radicals in Kyoto. Considering L_N/Q was estimated from (3.62), except [NO], other factors like k_i[VOCs], k_{eff}[XO_2], k_{p_XO2} should be much smaller in Kyoto campaign. Which means a larger L_N/Q should exist in Kyoto

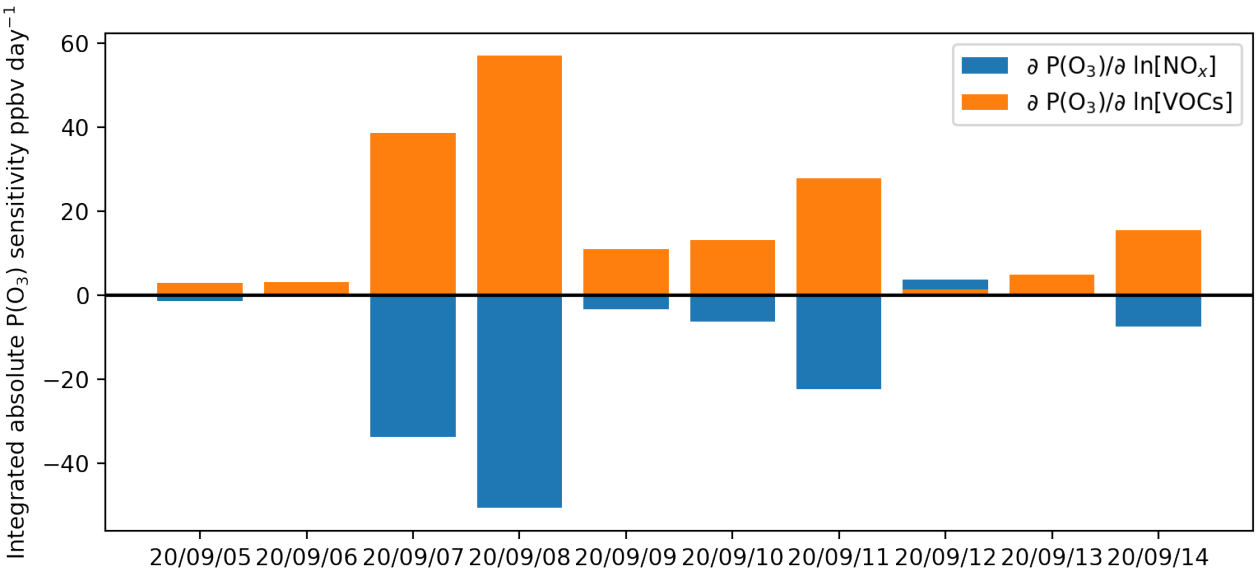

Figure 3.23: Absolute $P(O_3)$ sensitivity with respect to $[NO_x]$ or [VOCs] in **Kyoto – campaign**.

than in Tsukuba under same NO concentration condition. In fact, according to the calculation, the results in Figure 3.24 match with this hypothesis.

Another aspect can be discussed here is the elevated absolute $P(O_3)$ sensitivity, which appeared together with polluted air masses on site. While polluted air masses cannot always bring high absolute $P(O_3)$ sensitivity, therefore there might be some unknown factor concurrently worked on the ozone production rate. It might be the meteorological conditions or other joint local emissions or both, which has to be studied in the future.

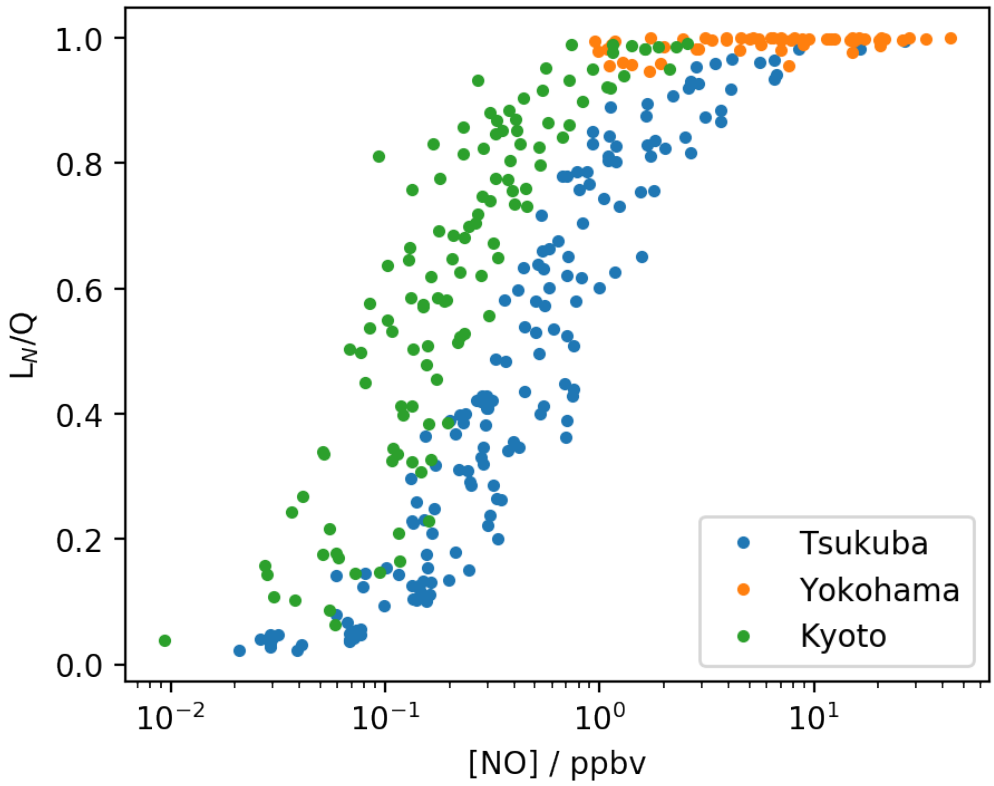

Figure 3.24: Dependence of L_N/Q ratio on [NO] with the consideration of aerosol uptake effects compared in three campaigns.

Chapter 4

Summary, conclusions, and outlook

Three intensive field studies focusing on total OH reactivity and OH-reactants measurements were conducted in different locations of Japan. The first location Tsukuba is approximately 50 km away from Tokyo, second site Yokohama situates at a seaside industrial area, and the last campaign observed a relative clean urban area, Kyoto. Total OH reactivity ranking was as expected, in a descending order as follows: 12.9 s^{-1} (35.3% of missing OH reactivity) in Tsukuba, 11.4 s^{-1} (7.7% of missing) in Yokohama, and 8.5^{-1} (40.4% of missing) in Kyoto. Although quite similar commercial instrumentations were used in the three campaigns, chemical analysis of OH reactivity makes distinctions in the result of missing OH reactivity, indicating the different existence of unknown VOCs in the air. When explore the source of missing OH reactivity, OVOCs derived from AVOCs and BVOCs indicated a moderate corresponding relationship with missing OH reactivity in Tsukuba. However, in Yokohama, the generation of secondary products was quite limited despite the fact that measured OVOCs importantly attributed to total OH reactivity. Last but not least, Kyoto observed the lowest total OH reactivity, at the same time reported with highest fraction of missing OH reactivity, and the later showed a close relationship with BVOCs itself. When investigating the mixing ratio of the air, total OH reactivity measurement and concurrent detection of trace species help to provide insights on the unknown VOCs in situ. As the results in the three campaigns, different properties of the air composition especially among the unknown trace species is essential to further study the secondary products generation such as ozone and aerosol.

Ozone production sensitivity in three field cases was rigorously estimated from the perspectives of chain length, ozone production potential, ozone production rate, and ozone regime

sensitivity. The most lasting HO_x cycle reactions was obtained in Kyoto from relatively long chain length. However, the ozone production rate was larger in Tsukuba due to a higher level of VOCs and slightly higher concentrations of NO_x than Kyoto. Note that generally NO_x concentration was lower in Kyoto than Tsukuba, but the difference could be quite limited when compared with Yokohama. Missing OH reactivity contribution and heterogenous effects of the HO_2 uptake on the aerosol were compared in terms of ozone production potential and ozone regime sensitivity. Simply put, the higher level of missing OH reactivity it is, the greater it can make in amount in terms of ozone production potential. The largest ozone production potential was gained in Kyoto, followed by Tsukuba, and the smallest in Yokohama. Missing OH reactivity could enhance the ozone production potential up to a factor of four in Kyoto, which should be the upper limit of ozone production. Compare to that, Tsukuba indicated a similar tendency while smaller contributions from missing OH reactivity, while the maximal increase equals a factor of three. In Yokohama, the general ozone production potential was constrained from both total OH reactivity and calculated OH reactivity, and missing OH reactivity's attribution was the smallest approximately 10%. Heterogenous effects of aerosol uptake on ozone production exhibited the same descending order in the three places as the potential per ca. Almost no obvious difference can be found in Yokohama either considering aerosol or not. However, in the cleanest urban site Kyoto, aerosol uptake effects on ozone production potential can be as high as one factor. Ozone regime sensitivity result separates ozone isopleth diagram into either VOC-limited or NO_x-limited regime. In the case of Yokohama, all the period belonged to VOC-limited because of high NO_x condition. In Tsukuba and Kyoto, although the dominant regime is VOC-limited, NO_x-limited regime can be found time to time. Specifically, NO_x-limited regimes appeared frequently in the afternoon in Tsukuba, compared to that, NO_x-limited can be any hour of the day in Kyoto's case. Tsukuba and Kyoto indicated same influences derived from aerosol uptake effects, in which aerosol consideration converted VOC-limited into NO_x-limited condition. Although aerosol uptake made no effort in altering the regime in Yokohama, still, much larger influence could be there when consider ozone production sensitivity derived from NO_x.

Future work will be stressed in the exploration of missing OH reactivity in clean urban area to the relationship with BVOCs. Either from primary unknown BVOCs or secondary

products derived from BVOCs could be feasible directions. As for ozone production sensitivity, the current analysis only considers aerosol uptakes of HO_2 radicals, leading us to think of a diversity of RO_2 which can enhance the aerosol effects on ozone's generation. Also, the transformation of ozone regime mechanism from aerosol uptake in Tsukuba and Kyoto calls for further investigation. Given the fact that ozone pollution acts as one of the most hazardous air pollution issues in many urban areas currently, the practice of ozone mitigation should pay extra attention to these VOC-limited regime conditions. Since in the reduction of the main precursors NO_x, an increase of ozone might occur. Thus, a joint-control of both NO_x and VOCs is essential to avoid that. The analysis of ozone production sensitivity in-situ is urgently required.

A.1 Other radicals measurement by LP-LIF

LP-LIF technique can be improved to detect other radicals except for OH. Hydroperoxy and peroxy radicals are also possible for detection by chemical conversion method after converting these radicals into OH. Although such a method is quite limited and suffers from interference since it cannot differentiate RO_2 from HO_2. The successful detection make it possible to give a step forward in the atmospheric chemistry field.

This section explains fundamental chemistry used in peroxy radicals measurement in the first A.1.1. The difference between RO_2 and HO_2 reaction pathway is stressed. Following this, A.1.2 discusses the virtual experimental problem and the approach to solve RO_2 radicals detection obstacle by addition of O_2. The experimental results were stated and also the influence of O_2 addition was explored. Then, A.2 and A.3 briefly indicate the implementation of peroxy radicals detection, to further measure the reaction of peroxy radicals with NO_x. This pathway is known as one of the most important destruction processes for peroxy radicals and also vital to understand NO_x behavior in the troposphere.

A.1.1 Basic principles

RO_2 and HO_2 radicals are measured as OH radicals via chemical conversion method. In HO_2's case, excessive CO (10 sccm) is injected in the reaction cell to produce artificial HO_2 by converting OH to HO_2, as showed in (1). Following this, HO_2 is reconverted into OH in the detection cell, where extra NO is added in LIF cell (2).

$$OH + CO + O_2 \longrightarrow HO_2 + CO_2 \tag{1}$$

$$HO_2 + NO \longrightarrow OH + NO_2 \tag{2}$$

Before detecting the reactivity of HO_2 radicals, the spectrum of OH converted from HO_2 was recorded to obtain the optimum wavelength for LIF signal. Normally, excess CO is added right before NO injection to make sure that all OH radicals in reaction cell should be converted into HO_2 radicals. Then HO_2 will react with NO in LIF cell to re-generate OH radicals. Reaction of HO_2 with NO occurs quickly with recommended rate coefficient at room temperature equals 8.2×10^{-12} cm^3/molecule s [Burkholder et al., 2019]. Finally the sampled OH signal can be

analyzed, which comes from HO_2 radical. By using this method, both HO_2 concentration and reactivity can be detected indirectly.

RO_2 radicals can be measured by similar method as HO_2 by differentiating initial trace species injection in reaction cell (3) & (4). As for RO_2 detection, more NO and possibly extra O_2 is needed in LIF cell since RO_2 radicals require a longer reaction pathway to firstly form HO_2 via (5) & (6) and then re-form OH (2).

$$OH + RH \longrightarrow R + H_2O \tag{3}$$

$$R + O_2 \longrightarrow RO_2 \tag{4}$$

$$RO_2 + NO \longrightarrow RO + NO_2 \tag{5}$$

$$RO + O_2 \longrightarrow RCHO + HO_2 \tag{6}$$

RO_2 is measured by similar routine as HO_2. Two different representative VOCs (ethane and isoprene) were selected to conduct the experiment. The reason why chose such trace species are 1)ethane is not active, therefore ethane derived RO_2 radicals are difficult for measurement; 2)isoprene is quite active, and acts as one of the most important BVOCs in the air. By testing with these two model VOCs, we can apply LIF-FAGE to all other RO_2 detection. The room temperature rate constants for C_2H_5OO and isoprene-derived RO_2 with NO are recommended to be 8.7×10^{-12} cm^3/molecule s [Burkholder et al., 2019] and 8.8×10^{-12} cm^3/molecule s [Miller et al., 2004], respectively, which is quite close to that with HO_2 (2).

A.1.2 O_2 addition

From the comparison between (2) and (5) (6), we know that the detection process in RO_2 case has to get through a longer pathway. Specifically, (6) is known as the rate-limiting step, such as the rate coefficient of (6) in C_2H_5O's case was reported to be 1.0×10^{-14} [Burkholder et al., 2019], which is over ten times smaller than reaction (5). To enhance the detection efficiency of RO_2 radicals especially inactive RO_2 like C_2H_5OO, an excess of O_2 (0-4 SLM; maximal 3.1×10^{16} molecules cm^{-3}) was injected into LIF cell to improve the rate-limiting step (6) and increase the signal of RO_2 detection. The result is exhibited in Figure 1, oxygen mixed with nitrogen

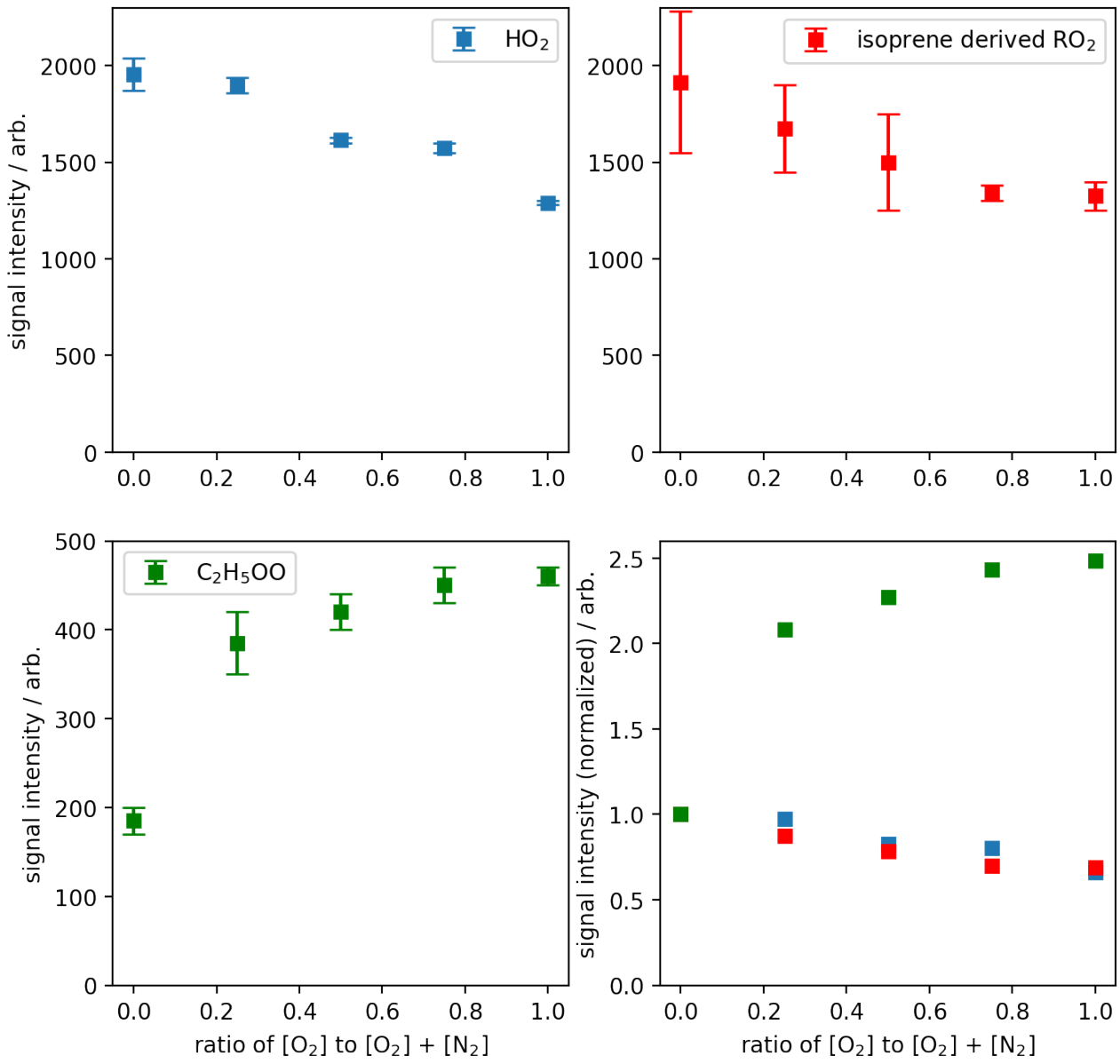

Figure 1: O_2 dependence results of the LIF intensity on HO_2, C_2H_5OO, and isoprene derived RO_2 radicals. The last graph compares three groups results together with normalized y-value.

was injected in LIF cell, in which the ratio of oxygen varied from 0 to 1. Y-axis in four graphs indicates LIF signal intensity where initial three plots come from HO_2, C_2H_5OO, and isoprene derived RO_2. In the last graph, all three groups were compared in normalized LIF intensity.

As Figure 1 shows, the LIF intensity from HO_2 decreased with the injection of increasing oxygen. To avoid the pressure's change in LIF cell, oxygen is mixed with nitrogen under a stable total flow rate of 4 SLM. HO_2's signal declined with increasing oxygen, this is because the excited OH quenching rate with oxygen differs from nitrogen. And isoprene derived RO_2 signal indicates a similar tendency as HO_2 which were compared in the last graph in Figure 1 after normalizing the LIF intensity. Quenching rate should be the major factor that determines

the detection of HO_2 and isoprene derived RO_2 radicals. Contrarily, C_2H_5OO displayed an upwind trend with increasing O_2 ratio, indicating that rate-limiting step (4) was proceeded efficiently and compensated for the quenching rate loss for the signal.

A.2 Application 1: RO_2 reactions with NO_2

After the successful detection of RO_2 was achieved, the rate constants of simple RO_2 radicals with NO_2 under atmospheric conditions were measured by LP-LIF technique. A.2 will express the measurement and calculation in detail. Two of the simplest RO_2 radicals (CH_3OO and C_2H_5OO) were selected as the target species.

$$CH_3OO + NO_2 \underset{k_{1r}}{\overset{k_{1f}}{\rightleftharpoons}} CH_3OONO_2 \tag{7}$$

$$C_2H_5OO + NO_2 \underset{k_{2r}}{\overset{k_{2f}}{\rightleftharpoons}} C_2H_5OONO_2 \tag{8}$$

The reactions of RO_2 with NO_2 as displayed in (7) and (8), are reversible reactions. Under ambient conditions, the concentration of NO_2 was much higher than RO_2, around two to three orders of magnitude larger than radicals. Therefore, the process was treated as pseudo-first-order reaction. Note that there would be a loss process due to the wall effects in LP-LIF causing interference on the analysis, as indicated in (9) and (10).

$$RO_2 \xrightarrow{k_d} \text{loss} \tag{9}$$

$$RO_2NO_2 \xrightarrow{k_d'} \text{loss} \tag{10}$$

$$RO_2 + NO_2 \underset{k_r}{\overset{k_f}{\rightleftharpoons}} RO_2NO_2 \tag{11}$$

The loss rate could be determined by the direct measurement of the decay rate without NO_2 addition in the system. A detailed description on the calculation of rate constant of RO_2 with NO_2 (11) based on the measurement of NO_2 dependence will be provided.

$$\frac{d[RO_2]}{dt} = -(k_d + k_f)[RO_2] + k_r[RO_2NO_2] \tag{12}$$

$$\frac{d[RO_2NO_2]}{dt} = -(k_r + k_d^{'})[RO_2NO_2] + k_f[RO_2] \tag{13}$$

$$\frac{d}{dt}\frac{d[RO_2]}{dt} = -(k_d + k_f)\frac{d[RO_2]}{dt} + k_r\frac{d[RO_2NO_2]}{dt} \tag{14}$$

Substituting (12) and (13) into (14), an equation on $[RO_2]$ can be written as follows.

$$\frac{d}{dt}\frac{d[RO_2]}{dt} + (k_d + k_f + k_r + k_d^{'})\frac{d[RO_2]}{dt} + (k_r k_d + k_d k_d^{'} + k_d^{'} k_f)[RO_2] = 0 \tag{15}$$

From (15), the analysis will be separated into 1)$k_d = k_d^{'}$, and 2)$k_d \neq k_d^{'}$ two cases.

A.2.1 $k_d = k_d^{'}$

In the first case, (15) can be merged into (16), where t = $\frac{d[RO_2]}{dt}$.

$$t^2 + (2k_d + k_f + k_r)t + k_d(k_d + k_f + k_r) = 0 \tag{16}$$

$$(t + k_d)(t + k_d + k_f + k_r) = 0 \tag{17}$$

The concentration of $[RO_2]$ in terms of time can be expresses as,

$$[RO_2] = C_1 e^{-k_d t} + C_2 e^{-(k_d + k_f + k_r)t} \tag{18}$$

To figure out the parameter of C_1 and C_2, the moment t = 0 was used. C_1, C_2 can be expressed by $[RO_2]_0$, k_f, and k_r.

$$[RO_2]_0 = C_1 + C_2 \tag{19}$$

Substituting (12) and (18), $k_r[RO_2NO_2]$ could be rewritten.

$$k_r[RO_2NO_2] = k_f C_1 e^{-k_d t} - k_r C_2 e^{-(k_d + k_f + k_r)t} \tag{20}$$

$$[RO_2NO_2]_0 = k_f C_1 - k_r C_2 = 0 \tag{21}$$

Combining (19) and (21), C_1 and C_2 could be expressed as,

$$C_1 = \frac{k_r}{k_f + k_r}[RO_2]_0 \tag{22}$$

$$C_2 = \frac{k_f}{k_f + k_r}[RO_2]_0 \tag{23}$$

Substituting (22) and (23) into (18), the concentration of [RO_2] will be as follows,

$$[RO_2] = \frac{k_r}{k_f + k_r}[RO_2]_0 e^{-k_d t} + \frac{k_f}{k_f + k_r}[RO_2]_0 e^{-(k_d + k_f + k_r)t} \tag{24}$$

Combining (20) and (24), the concentration of [RO_2NO_2] can be exhibited as (25).

$$[RO_2NO_2] = \frac{k_f}{k_f + k_r}[RO_2]_0 e^{-k_d t} - \frac{k_f}{k_f + k_r}[RO_2]_0 e^{-(k_d + k_f + k_r)t} \tag{25}$$

A.2.2 $\mathbf{k}_d \neq \mathbf{k}_d^{'}$

In the case where $k_d \neq k_d^{'}$, (15) will be merged into a different formula, as displayed in (26), in which t $= \frac{d[RO_2]}{dt}$.

$$t^2 + (k_d + k_f + k_r + k_d^{'})t + (k_d k_d^{'} + k_r k_d + k_f k_d^{'}) = 0 \tag{26}$$

Here, t_1 and t_2 represent the root of the quadratic formula in (26). And t_1 and t_2 can be written as,

$$t_1 = \frac{-(k_d + k_f + k_r + k_d^{'}) + \sqrt{(k_d + k_f + k_r + k_d^{'})^2 - 4(k_d k_d^{'} + k_r k_d + k_f k_d^{'})}}{2} \tag{27}$$

$$t_2 = \frac{-(k_d + k_f + k_r + k_d^{'}) - \sqrt{(k_d + k_f + k_r + k_d^{'})^2 - 4(k_d k_d^{'} + k_r k_d + k_f k_d^{'})}}{2} \tag{28}$$

Therefore, [RO_2] equals,

$$[RO_2] = C_1 e^{t_1 t} + C_2 e^{t_2 t} \tag{29}$$

(19) still suits the current case, and the expression for $[RO_2NO_2]_0$ will be different.

$$k_r[RO_2NO_2] = t_1 C_1 e^{t_1 t} + t_2 C_2 e^{t_2 t} + (k_d + k_f)(C_1 e^{t_1 t} + C_2 e^{t_2 t}) \tag{30}$$

At the beginning of the reaction when t = 0,

$$[RO_2NO_2]_0 = C_1(t_1 + k_d + k_f) + C_2(t_2 + k_d + k_f) = 0 \tag{31}$$

Combining (19) and (31), C_1 and C_2 can be expressed as,

$$C_1 = \frac{-(t_2 + k_d + k_f)}{t_1 - t_2}[RO_2]_0 \tag{32}$$

$$C_2 = \frac{t_1 + k_d + k_f}{t_1 - t_2}[RO_2]_0 \tag{33}$$

Hence, (29) can be rewritten as follows,

$$[RO_2] = \frac{-(t_2 + k_d + k_f)}{t_1 - t_2}[RO_2]_0 e^{t_1 t} + \frac{t_1 + k_d + k_f}{t_1 - t_2}[RO_2]_0 e^{t_2 t} \tag{34}$$

Combining (30), (32), and (33), the concentration of $[RO_2NO_2]$ could be displayed as in (35).

$$[RO_2NO_2] = \frac{t_1 + k_d + k_f}{k_r(t_1 - t_2)}[RO_2]_0(-(t_2 + k_d + k_f)e^{t_1 t} + (t_2 + k_d + k_f)e^{t_2 t}) \tag{35}$$

A.2.3 Kinetics of RO_2 + NO_2

The reaction of RO_2 with NO might interfere the detection of RO_2 with NO_2, this part will be discussed in A.3. Other side reactions such as $O(^3P)$ with NO_2, peroxy radicals self-reactions, and R radicals with NO_2 could be disregarded because of their extremely low level [Kohno et al., 2020].

The detailed detection and estimation of the kinetics of CH_3OO + NO_2 and C_2H_5OO + NO_2 has been published in the article by [Kohno et al., 2020]. Note that double exponential fitting equation as in (24) and (34) was utilized to extrapolate the corresponding rate constant. The result might vary from different fitting ranges, k_d's relationship with $k_d^{'}$, and the way to calculate $k_d^{'}$. Here, only the kinetics of CH_3OO + NO_2 will be discussed, for further result on C_2H_5OO + NO_2 could refer to [Kohno et al., 2020].

In the measurement procedure, zero air was replaced by pure N_2 and O_2 from the cylinders. k_d was estimated from the background decay rate, as displayed in Figure 2. The single exponential fitting started from 0.05 s, and before that time, the rapid decay rate was caused by OH reacting with methane in the system. From Figure 2, the loss rate of CH_3OO was estimated to be 1.77 s^{-1}. Note that [Kohno et al., 2020] reported k_{d,CH_3OO} equals 1.53 s^{-1}. The discrepancy might come from the different endpoints of the fitting range.

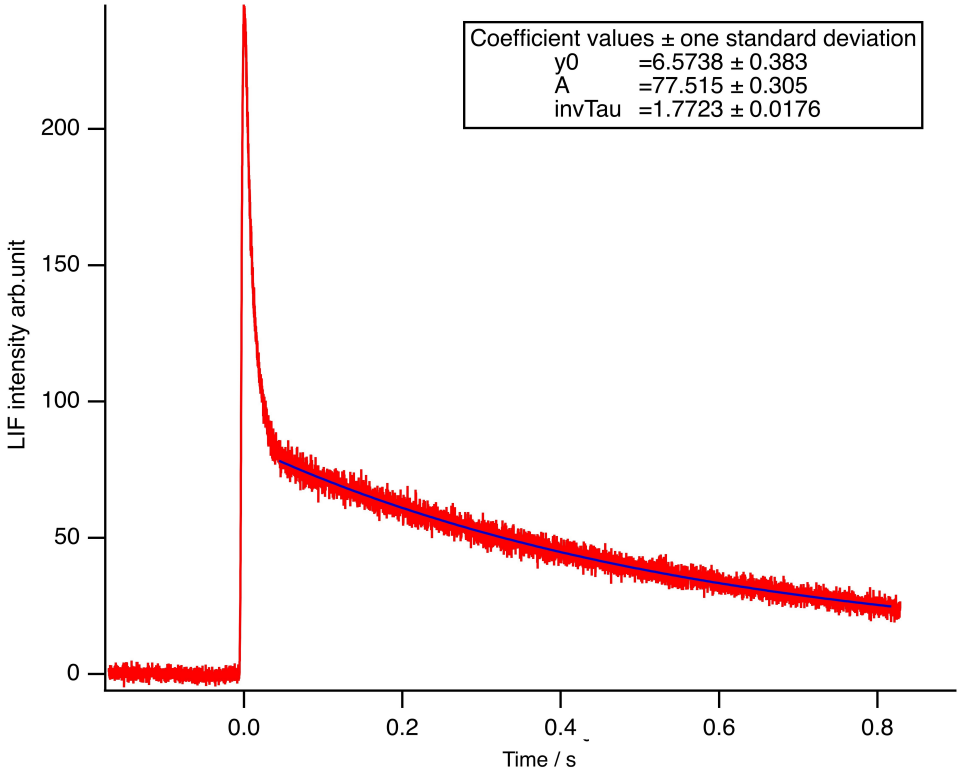

Figure 2: Time profile of the CH_3OO detected by LP-LIF without the injection of NO_2.

Similarly, the CH_3OO radicals decay profile was compared under a series of NO_2 addition, as exhibited in Figure 3. The concentration of NO_2 ranges from 0.7 to 2.2×10^{12} molecule cm^{-3}. Double exponential fitting function was used to specify the parameter in (24) in which assume $k_d = k_d^{'}$, or in (34) in which $k_d \neq k_d^{'}$. Figure 4 displayed the result based on a fix k_d of 1.77 s^{-1}, and k_d should be equal to $k_d^{'}$. The double exponential fitting range for the result in Figure 4 covers the whole range after 0.05 s.

In Figure 4, the rate constant of CH_3OO + NO_2 can be obtained from the slope since the reaction was treated as pseudo-first-order rate. According to the slope, the rate constant of CH_3OO with NO_2 could be 3.3 ± 0.2 × 10^{-12} cm^3 $molecule^{-1}s^{-1}$. Compared with the corresponding rate constant of 3.9 ± 0.3 × 10^{-12} cm^3 $molecule^{-1}s^{-1}$ by [Kohno et al., 2020], and recommended with k = 4.0× 10^{-12} cm^3 $molecule^{-1}s^{-1}$ at 298 K and 1 bar of air by IUPAC, the values are close to each other. Note that the reported value in [Kohno et al., 2020] was extrapolated from the case that $k_d \neq k_d^{'}$, and they also compared with the case of $k_d = k_d^{'}$ in which rate constant should be slightly smaller.

$k_d^{'}$ presents the background decay rate of CH_3OONO_2, which is hard to detect directly. Therefore, the Graham's law is used to predict the rate of effusion of CH_3OONO_2 from that

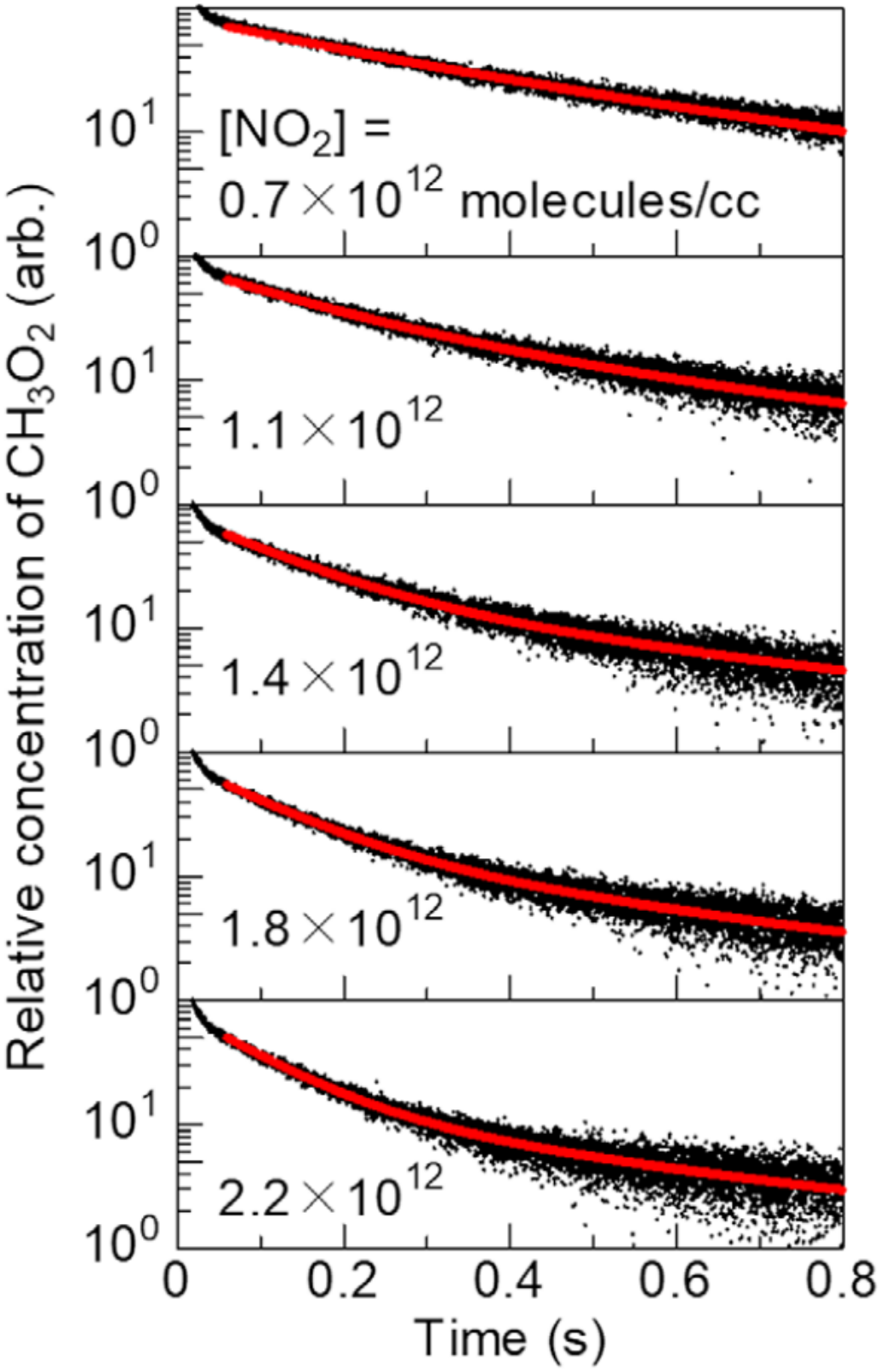

Figure 3: Time profile of the CH_3OO detected by LP-LIF with the injection of NO_2. Figure adapted from [Kohno et al., 2020].

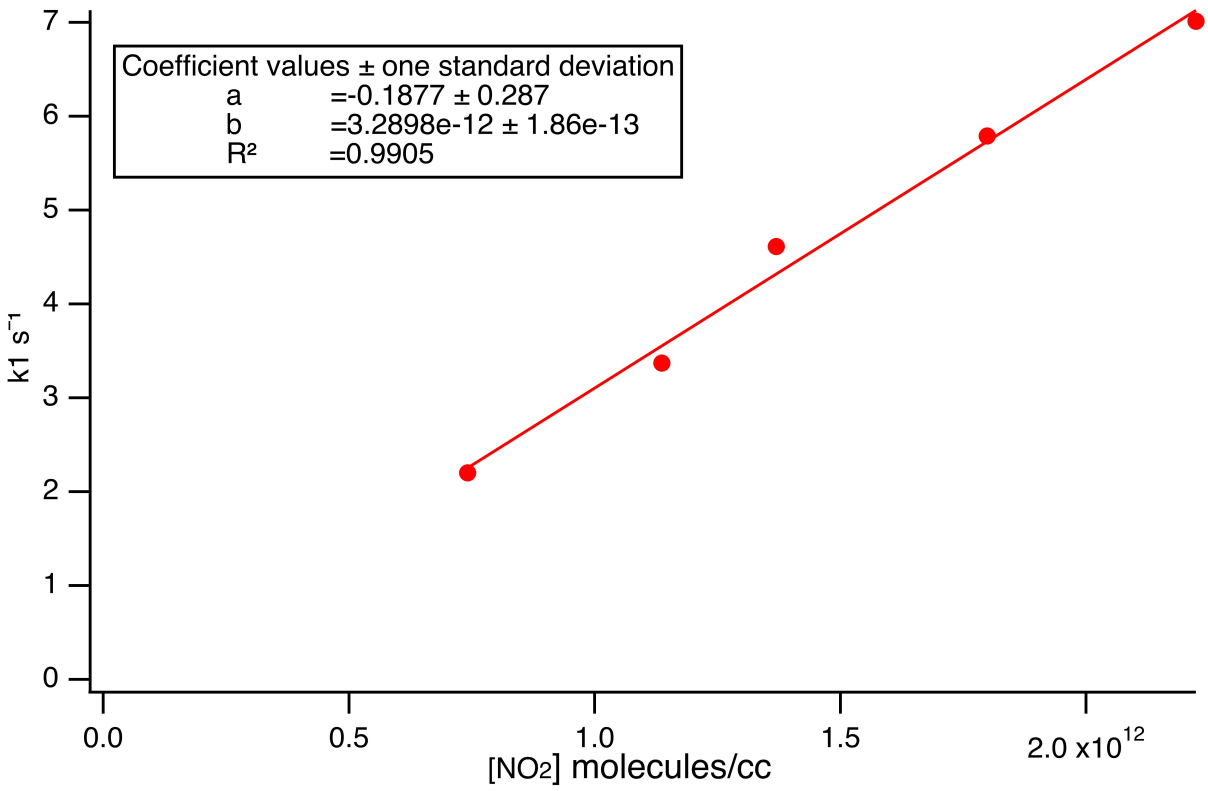

Figure 4: NO_2 dependence of the reaction rate for $CH_3OO + NO_2$.

of CH_3OO. As explained in (36), the rate of effusion of a gas is inversely proportional to the square root of the mass of its molecule.

$$\frac{Rate_{CH_3OONO_2}}{Rate_{CH_3OO}} = \sqrt{\frac{M_{CH_3OO}}{M_{CH_3OONO_2}}} \tag{36}$$

Where, $Rate_x$ is the rate of effusion for the gas x and M_x is the molar mass of x. Hence, k'_d in the case of CH_3OO, equals 1.26 s^{-1} when k_d = 1.77 s^{-1}, and equals 1.09 s^{-1} when k_d = 1.53 s^{-1} according to the Graham's law.

The current section explains the analyzing details of the kinetics of RO_2 with NO_2. As aforementioned discussions, fitting conditions and the parameter solutions have to be carefully chosen considering their effects to master the final result. [Kohno et al., 2020] provided one of the optimal examples to follow, which also made the result pretty close to previous literature. A.2 will stop here and guide the readers of interest to find answers for future kinetics of RO_2 + NO_2 by practice.

A.3 Application 2: RO_2 reactions with NO

This section will explain the kinetics of RO_2 + NO in case of isoprene. Isoprene was chosen for this study because it has larger molecular weight, which is easier to generate the complex RO_2NO, and get removed from the HO_x cycle. The reaction of isoprene derived RO_2 radicals with NO occurs rapidly and there are mainly two pathway channels, as showed in (37) and (38).

$$C_5H_8OHO_2 + NO \longrightarrow C_5H_8OHO + NO_2 \tag{37}$$

$$C_5H_8OHO_2 + NO \longrightarrow C_5H_8OHONO_2 \tag{38}$$

The reaction as displayed in (37) is the dominant channel, which acts as part of the HO_x cycle, and the rate constant of (37) is reportedly (2.5 ± 0.5) × 10^{-11} $cm^3molecule^{-1}s^{-1}$ at 3-4 Torr and 295 K [Reitz et al., 2002]. However, the rate constant in (38) is 6.0 × 10^{-14} cm^3 $molecule^{-1}s^{-1}$ at 100 Torr and 298 K [Patchen et al., 2007]. Another study conducted under same conditions measured (38) directly and reported the rate constant to be 8.8 ± 1.2 ×10^{-12} $cm^3molecule^{-1}s^{-1}$ [Miller et al., 2004].

From Figure 5, the rate constant extrapolated from decay rate measured by LP-LIF in relation to injected NO concentration was exhibited, in which the k = 1.01× 10^{-12} cm^3 $molecule^{-1}s^{-1}$. The experimental conditions is 1 bar and 298 K.

According to the field study in Yokohama as introduced in Subsection 2.2.3, the interconversion of NO into NO_2 in the sampling procedure has to be considered. During the measurement of isoprene derived RO_2 with NO, the reaction (37) could lead to NO_2 production. On the other hand, because of O_2 addition during the detection, RO could also react with O_2 to form HO_2, HO_2 as a result, can oxidize NO and form NO_2 ultimately.

The NO_2 concentration inside reaction cell was detected by CAPS. Based on the injected NO concentration and detected NO_2 concentration in the reaction cell, the real NO concentration in reaction cell can be estimated by assuming the total amount of NO_x is equal to the initial NO concentration. Figure 6 showed the real concentration of NO compared with NO_2 inside of the reaction cell. Obviously, the concentration of NO_2 was one factor larger than NO, indicating the reaction of RO_2 + NO_2 must have interfered with the detection.

An experiment was then conducted to test the impurity of the NO cylinder by using a NO_2

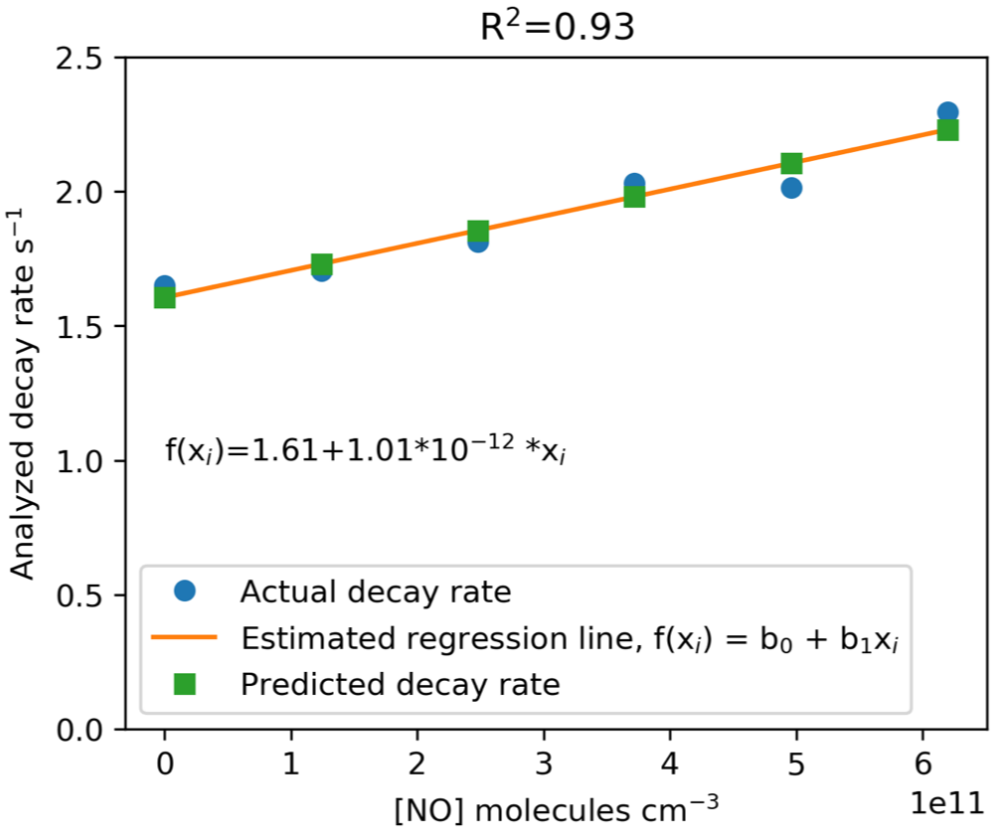

Figure 5: NO dependence of the reaction rate for $C_5H_8OHO_2$ + NO at 1 bar and 298 K.

scrubber after the cylinder tank. Figure 5 and Figure 7 compared the result of decay rate w/o and w/ the NO_2 scrubber, respectively. From the fitting equation, the extrapolated rate constants in two conditions were almost same, which means that the NO was not oxidized in the cylinder.

The detected decay rate was then analyzed with the real NO concentration inside of the reaction cell. Moreover, because NO_2 concentration was much higher than NO, the decay rate caused by RO_2 radicals reacting with NO_2 was subtracted. The rate constant from C_2H_5OO with NO_2 reported by [Kohno et al., 2020] was utilized. Figure 8 showed the results of measured decay rate and corrected decay rate from RO_2NO_2. As a conclusion, it can be found that the effects of (38) could be disregarded. Although a downwind trend is perplexing, the conclusion of the rate constant of (38) under the current experimental conditions should be unchangeable.

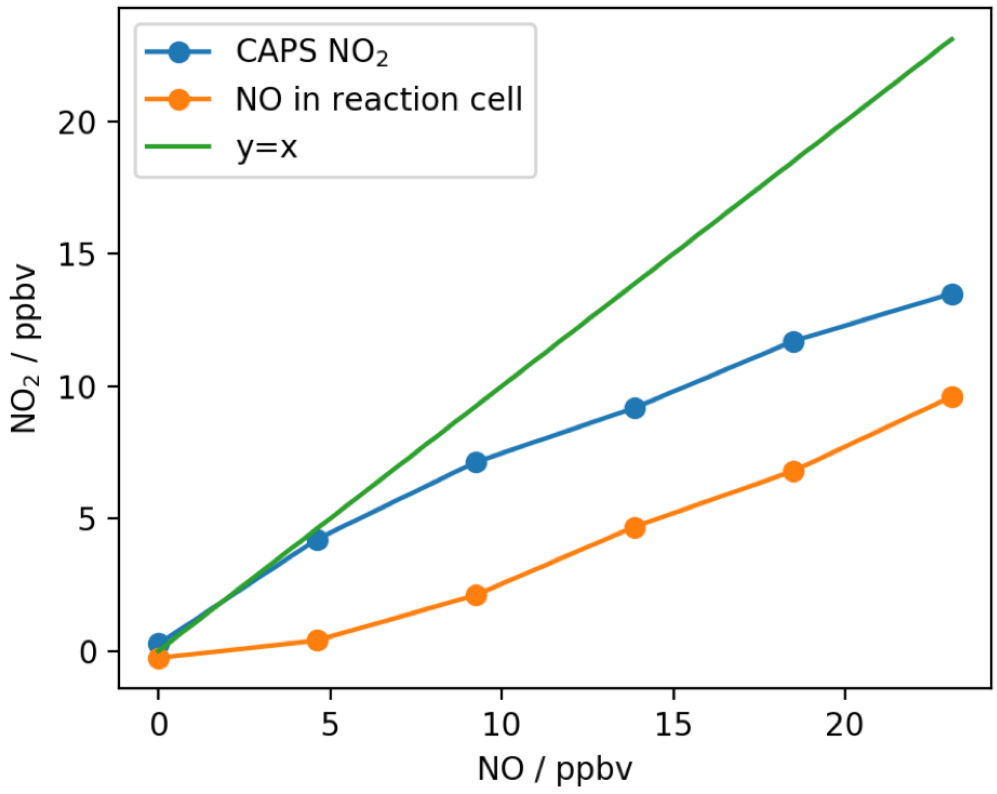

Figure 6: Real concentration of NO and NO_2 in the reaction cell.

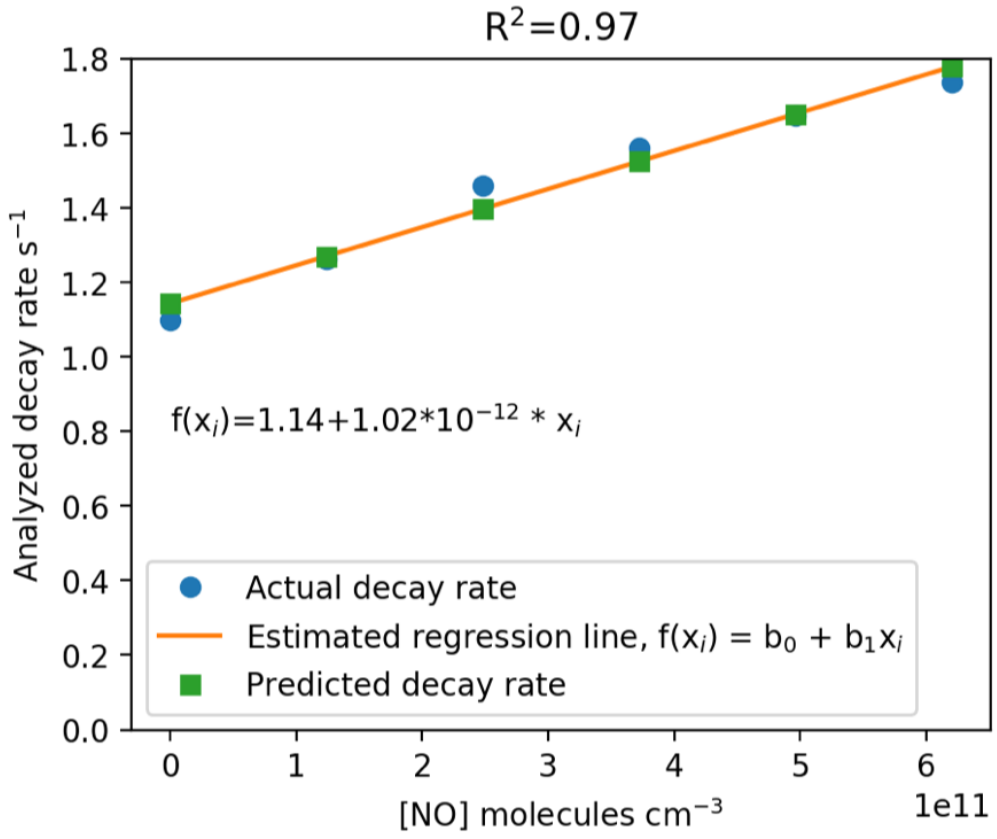

Figure 7: NO dependence of the reaction rate with NO_2 scrubber after the NO cylinder tank.

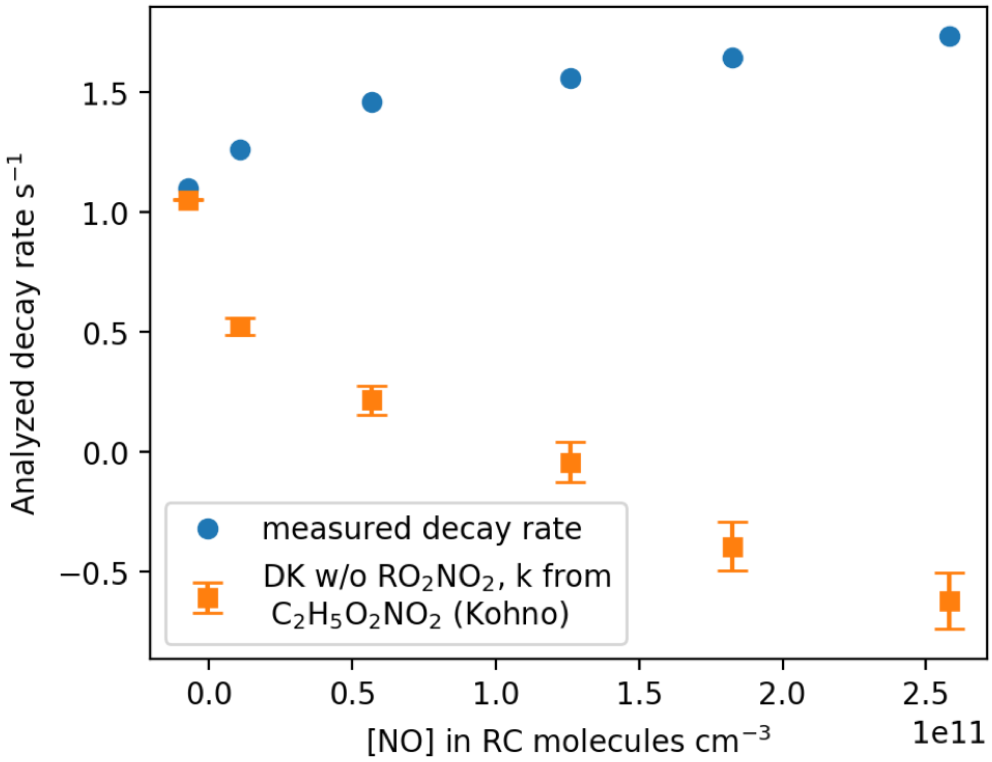

Figure 8: Decay rate of C_5H_7OHOO + NO corrected from the reaction pathway of C_5H_7OHOO + NO_2.

Bibliography

[Akimoto et al., 2002] Akimoto, H., Kawamura, K., Nakazawa, T., and Washida, N. (2002). *The chemistry of the tropospheric air and earth environment (in Japanese)*. Scientific society press (Japan).

[Altshuller, 1983] Altshuller, A. (1983). Natural volatile organic substances and their effect on air quality in the united states. *Atmospheric Environment*, 17(11):2131–2165.

[Andersen et al., 2018] Andersen, S. O., Sherman, N. J., Carvalho, S., and Gonzalez, M. (2018). The global search and commercialization of alternatives and substitutes for ozone-depleting substances. *Comptes Rendus Geoscience*, 350(7):410–424.

[Armerding et al., 1995] Armerding, W., Comes, F., and Schülke, B. (1995). O(^{1}D) quantum yields of ozone photolysis in the uv from 300 nm to its threshold and at 355 nm. *The Journal of Physical Chemistry*, 99(10):3137–3143.

[Atkinson, 1986] Atkinson, R. (1986). Kinetics and mechanisms of the gas-phase reactions of the hydroxyl radical with organic compounds under atmospheric conditions. *Chemical Reviews*, 86(1):69–201.

[Atkinson et al., 2004] Atkinson, R., Baulch, D., Cox, R., Crowley, J., Hampson, R., Hynes, R., Jenkin, M., Rossi, M., and Troe, J. (2004). Evaluated kinetic and photochemical data for atmospheric chemistry: Volume I-gas phase reactions of O_x, HO_x, NO_x and SO_x species. *Atmospheric chemistry and physics*, 4(6):1461–1738.

[Ball et al., 1997] Ball, S. M., Hancock, G., Martin, S. E., and de Moira, J. C. P. (1997). A direct measurement of the O(^{1}D) quantum yields from the photodissociation of ozone between 300 and 328 nm. *Chemical physics letters*, 264(5):531–538.

[Bauer et al., 2001] Bauer, D., D'Ottone, L., and Hynes, A. J. (2001). O(^{1}D) quantum yields from O_3 photolysis in the near uv region between 305 and 375 nm. *Physical Chemistry Chemical Physics*, 2(7):1421–1424.

[Berndt et al., 2018] Berndt, T., Scholz, W., Mentler, B., Fischer, L., Herrmann, H., Kulmala, M., and Hansel, A. (2018). Accretion product formation from self-and cross-reactions of RO_2 radicals in the atmosphere. *Angewandte Chemie International Edition*, 57(14):3820–3824.

[Berresheim et al., 2000] Berresheim, H., Elste, T., Plass-Dülmer, C., Eiseleb, F., and Tannerb, D. (2000). Chemical ionization mass spectrometer for long-term measurements of atmospheric OH and H_2SO_4. *International Journal of Mass Spectrometry*, 202(1-3):91–109.

[Brock and Watson, 1980] Brock, J. and Watson, R. (1980). Ozone photolysis: Determination of the O(^{3}P) quantum yield at 266 nm. *Chemical Physics Letters*, 71(3):371–375.

[Brown and Stutz, 2012] Brown, S. S. and Stutz, J. (2012). Nighttime radical observations and chemistry. *Chemical Society Reviews*, 41(19):6405–6447.

[Burkholder et al., 2019] Burkholder, J., Sander, S., Abbatt, J., Barker, J., Cappa, C., Crounse, J., Dibble, T., Huie, R., Kolb, C., Kurylo, M., et al. (2019). Chemical kinetics and photochemical data for use in atmospheric studies; evaluation number 19. Technical report, Pasadena, CA: Jet Propulsion Laboratory, National Aeronautics and Space Administration.

[Chatani et al., 2018] Chatani, S., Yamaji, K., Sakurai, T., Itahashi, S., Shimadera, H., Kitayama, K., and Hayami, H. (2018). Overview of model inter-comparison in Japan's study for reference air quality modeling (J-STREAM). *Atmosphere*, 9(1):19.

[Chen et al., 2001] Chen, W., Kuze, H., Uchiyama, A., Suzuki, Y., and Takeuchi, N. (2001). One-year observation of urban mixed layer characteristics at Tsukuba, Japan using a micro pulse lidar. *Atmospheric Environment*, 35(25):4273–4280.

[Di Carlo et al., 2004] Di Carlo, P., Brune, W. H., Martinez, M., Harder, H., Lesher, R., Ren, X., Thornberry, T., Carroll, M. A., Young, V., Shepson, P. B., et al. (2004). Missing OH reactivity in a forest: Evidence for unknown reactive biogenic VOCs. *Science*, 304(5671):722–725.

[Dodge, 1977] Dodge, M. (1977). Combined use of modeling techniques and smog chamber data to derive ozone-precursor relationships. In *International conference on photochemical oxidant pollution and its control: Proceedings*, volume 2, pages 881–889. US Environmental Protection Agency, Environmental Sciences Research Laboratory Research Triangle Park, International conference on photochemical oxidant pollution and its control: Proceedings.

[Dolgorouky et al., 2012] Dolgorouky, C., Gros, V., Sarda-Esteve, R., Sinha, V., Williams, J., Marchand, N., Sauvage, S., Poulain, L., Sciare, J., and Bonsang, B. (2012). Total OH reactivity measurements in Paris during the 2010 MEGAPOLI winter campaign. *Atmospheric Chemistry and Physics*, 12(20):9593–9612.

[Emmerson et al., 2007] Emmerson, K. M., Carslaw, N., Carslaw, D., Lee, J. D., McFiggans, G., Bloss, W. J., Gravestock, T., Heard, D. E., Hopkins, J., Ingham, T., et al. (2007). Free radical modelling studies during the UK TORCH Campaign in summer 2003. *Atmospheric Chemistry and Physics*, 7(1):167–181.

[EPA, 2021] EPA, P. O. (2021). EPA moves forward with phase down of climate-damaging hydrofluorocarbons.

[Finlayson-Pitts and Pitts Jr, 1999] Finlayson-Pitts, B. J. and Pitts Jr, J. N. (1999). *Chemistry of the upper and lower atmosphere: theory, experiments, and applications*. Elsevier.

[Fuchs et al., 2017] Fuchs, H., Tan, Z., Lu, K., Bohn, B., Broch, S., Brown, S. S., Dong, H., Gomm, S., Häseler, R., He, L., et al. (2017). OH reactivity at a rural site (Wangdu) in the North China Plain: contributions from OH reactants and experimental OH budget. *Atmospheric Chemistry and Physics*, 17(1):645–661.

[Fuhrer et al., 2016] Fuhrer, J., Val Martin, M., Mills, G., Heald, C. L., Harmens, H., Hayes, F., Sharps, K., Bender, J., and Ashmore, M. R. (2016). Current and future ozone risks to global terrestrial biodiversity and ecosystem processes. *Ecology and evolution*, 6(24):8785–8799.

[Haber and Weiss, 1934] Haber, F. and Weiss, J. (1934). The catalytic decomposition of hydrogen peroxide by iron salts. *Proceedings of the Royal Society of London. Series A-Mathematical and Physical Sciences*, 147(861):332–351.

[Hansen et al., 2015] Hansen, R. F., Blocquet, M., Schoemaecker, C., Léonardis, T., Locoge, N., Fittschen, C., Hanoune, B., Stevens, P., Sinha, V., and Dusanter, S. (2015). Intercomparison of the comparative reactivity method (CRM) and pump–probe technique for measuring total OH reactivity in an urban environment. *Atmospheric Measurement Techniques*, 8(10):4243–4264.

[Heard, 2021] Heard, D. (2021). The FAGE Technique. www.fage.leeds.ac.uk/atmospheric-measurements/the-fage-technique/. accessed 01 apr. 2021.

[Hellen et al., 2006] Hellen, H., Hakola, H., Pirjola, L., Laurila, T., and Pystynen, K.-H. (2006). Ambient air concentrations, source profiles, and source apportionment of 71 different C2–C10 volatile organic compounds in urban and residential areas of Finland. *Environmental science & technology*, 40(1):103–108.

[Ingham et al., 2009] Ingham, T., Goddard, A., Whalley, L., Furneaux, K., Edwards, P., Seal, C., Self, D., Johnson, G., Read, K., Lee, J., et al. (2009). A flow-tube based laser- induced fluorescence instrument to measure OH reactivity in the troposphere. *Atmospheric Measurement Techniques*, 2(2):465–477.

[Jiang et al., 2019] Jiang, Z., Zheng, X., Zhai, H., Wang, Y., Wang, Q., and Yang, Z. (2019). Seasonal and diurnal characteristics of carbonyls in the urban atmosphere of Changsha, a mountainous city in south-central China. *Environmental Pollution*, 253:259–267.

[Jun et al., 2000] Jun, P., Gillenwater, M., and Barbour, W. (2000). CO_2, CH_4, and N_2O emissions from transportation–water-borne navigation. *Good Practice Guidance and Uncertainty Management in National Greenhouse Gas Inventories, Intergovernmental Panel on Climate Change, Paris, France*, pages 71–92.

[Junkermann and Burger, 2006] Junkermann, W. and Burger, J. (2006). A new portable instrument for continuous measurement of formaldehyde in ambient air. *Journal of Atmospheric and Oceanic Technology*, 23(1):38–45.

[Kanaya, 1997] Kanaya, Y. (1997). Development on the instrument for tropospheric OH radicals measurement by laser induced fluorescence technique (in Japanese). Master's thesis, University of Tokyo.

[Kanaya et al., 2007] Kanaya, Y., Cao, R., Akimoto, H., Fukuda, M., Komazaki, Y., Yokouchi, Y., Koike, M., Tanimoto, H., Takegawa, N., and Kondo, Y. (2007). Urban photochemistry in central Tokyo: 1. Observed and modeled OH and HO_2 radical concentrations during the winter and summer of 2004. *Journal of Geophysical Research: Atmospheres*, 112(D21).

[Kanno et al., 2006] Kanno, N., Tonokura, K., and Koshi, M. (2006). Equilibrium constant of the HO_2-H_2O complex formation and kinetics of HO_2 + HO_2-H_2O: Implications for tropospheric chemistry. *Journal of Geophysical Research: Atmospheres*, 111(D20).

[Kimbrough et al., 2017] Kimbrough, S., Owen, R. C., Snyder, M., and Richmond-Bryant, J. (2017). NO to NO_2 conversion rate analysis and implications for dispersion model chemistry methods using Las Vegas, Nevada near-road field measurements. *Atmospheric Environment*, 165:23–34.

[Kleinman, 2005] Kleinman, L. I. (2005). The dependence of tropospheric ozone production rate on ozone precursors. *Atmospheric Environment*, 39(3):575–586.

[Kleinman et al., 1997] Kleinman, L. I., Daum, P. H., Lee, J. H., Lee, Y.-N., Nunnermacker, L. J., Springston, S. R., Newman, L., Weinstein-Lloyd, J., and Sillman, S. (1997). Dependence of ozone production on NO and hydrocarbons in the troposphere. *Geophysical Research Letters*, 24(18):2299–2302.

[Kleinman et al., 2001] Kleinman, L. I., Daum, P. H., Lee, Y.-N., Nunnermacker, L. J., Springston, S. R., Weinstein-Lloyd, J., and Rudolph, J. (2001). Sensitivity of ozone production rate to ozone precursors. *Geophysical Research Letters*, 28(15):2903–2906.

[Kleist et al., 2012] Kleist, E., Mentel, T., Andres, S., Bohne, A., Folkers, A., Kiendler-Scharr, A., Rudich, Y., Springer, M., Tillmann, R., and Wildt, J. (2012). Irreversible impacts of heat on the emissions of monoterpenes, sesquiterpenes, phenolic BVOC and green leaf volatiles from several tree species. *Biogeosciences*, 9(12):5111–5123.

[Kohno et al., 2020] Kohno, N., Li, J., Sakamoto, Y., and Kajii, Y. (2020). Rate constants of CH_3O_2 + NO_2 <=> $CH_3O_2NO_2$ and $C_2H_5O_2$ + NO_2 <=> $C_2H_5O_2NO_2$ reactions under atmospheric conditions. *International Journal of Chemical Kinetics*.

[Kondo et al., 2008] Kondo, Y., Morino, Y., Fukuda, M., Kanaya, Y., Miyazaki, Y., Takegawa, N., Tanimoto, H., McKenzie, R., Johnston, P., Blake, D., et al. (2008). Formation and transport of oxidized reactive nitrogen, ozone, and secondary organic aerosol in Tokyo. *Journal of Geophysical Research: Atmospheres*, 113(D21).

[Kovacs et al., 2003] Kovacs, T., Brune, W., Harder, H., Martinez, M., Simpas, J., Frost, G., Williams, E., Jobson, T., Stroud, C., Young, V., et al. (2003). Direct measurements of urban OH reactivity during Nashville SOS in summer 1999. *Journal of Environmental Monitoring*, 5(1):68–74.

[Kovacs and Brune, 2001] Kovacs, T. A. and Brune, W. H. (2001). Total OH loss rate measurement. *Journal of Atmospheric Chemistry*, 39(2):105–122.

[Kroll and Seinfeld, 2008] Kroll, J. H. and Seinfeld, J. H. (2008). Chemistry of secondary organic aerosol: Formation and evolution of low-volatility organics in the atmosphere. *Atmospheric Environment*, 42(16):3593–3624.

[Krupa et al., 2001] Krupa, S., McGrath, M. T., Andersen, C. P., Booker, F. L., Burkey, K. O., Chappelka, A. H., Chevone, B. I., Pell, E. J., and Zilinskas, B. A. (2001). Ambient ozone and plant health. *Plant Disease*, 85(1):4–12.

[Last et al., 1994] Last, J. A., Sun, W.-M., and Witschi, H. (1994). Ozone, NO, and NO_2: oxidant air pollutants and more. *Environmental Health Perspectives*, 102(suppl 10):179–184.

[Lee et al., 2009] Lee, J. D., Young, J. C., Read, K. A., Hamilton, J. F., Hopkins, J. R., Lewis, A. C., Bandy, B. J., Davey, J., Edwards, P., Ingham, T., et al. (2009). Measurement and calculation of OH reactivity at a United Kingdom coastal site. *Journal of atmospheric chemistry*, 64(1):53–76.

[Li et al., 2020] Li, J., Sakamoto, Y., Kohno, N., Fujii, T., Matsuoka, K., Takemura, M., Zhou, J., Nakagawa, M., Murano, K., Sadanaga, Y., et al. (2020). Total hydroxyl radical reactivity measurements in a suburban area during AQUAS–Tsukuba campaign in summer 2017. *Science of The Total Environment*, 740:139897.

[Lou et al., 2010] Lou, S., Holland, F., Rohrer, F., Lu, K., Bohn, B., Brauers, T., Chang, C., Fuchs, H., Häseler, R., Kita, K., et al. (2010). Atmospheric OH reactivities in the Pearl River

Delta–China in summer 2006: measurement and model results. *Atmospheric Chemistry and Physics*, 10(22):11243–11260.

[Lu et al., 2013] Lu, K., Hofzumahaus, A., Holland, F., Bohn, B., Brauers, T., Fuchs, H., Hu, M., Häseler, R., Kita, K., Kondo, Y., et al. (2013). Missing OH source in a suburban environment near Beijing: observed and modelled OH and HO_2 concentrations in summer 2006. *Atmospheric Chemistry and Physics*, 13(2):1057–1080.

[Lu et al., 2010] Lu, K., Zhang, Y., Su, H., Brauers, T., Chou, C. C., Hofzumahaus, A., Liu, S. C., Kita, K., Kondo, Y., Shao, M., et al. (2010). Oxidant (O_3 + NO_2) production processes and formation regimes in Beijing. *Journal of Geophysical Research: Atmospheres*, 115(D7).

[Luecken et al., 2018] Luecken, D., Napelenok, S., Strum, M., Scheffe, R., and Phillips, S. (2018). Sensitivity of ambient atmospheric formaldehyde and ozone to precursor species and source types across the United States. *Environmental science & technology*, 52(8):4668–4675.

[Lui et al., 2017] Lui, K., Ho, S. S. H., Louie, P. K., Chan, C., Lee, S., Hu, D., Chan, P., Lee, J. C. W., and Ho, K. (2017). Seasonal behavior of carbonyls and source characterization of formaldehyde (HCHO) in ambient air. *Atmospheric Environment*, 152:51–60.

[Maliniemi et al., 2021] Maliniemi, V., Nesse Tyssøy, H., Smith-Johnsen, C., Arsenovic, P., and Marsh, D. R. (2021). Ozone super recovery cancelled in the antarctic upper stratosphere. *Atmospheric Chemistry and Physics Discussions*, pages 1–15.

[Mao et al., 2009] Mao, J., Ren, X., Brune, W., Olson, J., Crawford, J., Fried, A., Huey, L., Cohen, R., Heikes, B., Singh, H., et al. (2009). Airborne measurement of OH reactivity during INTEX-B. *Atmospheric Chemistry and Physics*, 9(1):163–173.

[Mao et al., 2010] Mao, J., Ren, X., Chen, S., Brune, W. H., Chen, Z., Martinez, M., Harder, H., Lefer, B., Rappenglück, B., Flynn, J., et al. (2010). Atmospheric oxidation capacity in the summer of Houston 2006: comparison with summer measurements in other metropolitan studies. *Atmospheric Environment*, 44(33):4107–4115.

[Martinez et al., 2003] Martinez, M., Harder, H., Kovacs, T., Simpas, J., Bassis, J., Lesher, R., Brune, W., Frost, G., Williams, E., Stroud, C., et al. (2003). OH and HO_2 concentrations,

sources, and loss rates during the Southern Oxidants Study in Nashville, Tennessee, summer 1999. *Journal of Geophysical Research: Atmospheres*, 108(D19).

[Matsui et al., 2009] Matsui, H., Koike, M., Takegawa, N., Kondo, Y., Griffin, R., Miyazaki, Y., Yokouchi, Y., and Ohara, T. (2009). Secondary organic aerosol formation in urban air: Temporal variations and possible contributions from unidentified hydrocarbons. *Journal of Geophysical Research: Atmospheres*, 114(D4).

[Matsumi and Kawasaki, 2003] Matsumi, Y. and Kawasaki, M. (2003). Photolysis of atmospheric ozone in the ultraviolet region. *Chemical reviews*, 103(12):4767–4782.

[McDonald et al., 2018] McDonald, B. C., De Gouw, J. A., Gilman, J. B., Jathar, S. H., Akherati, A., Cappa, C. D., Jimenez, J. L., Lee-Taylor, J., Hayes, P. L., McKeen, S. A., et al. (2018). Volatile chemical products emerging as largest petrochemical source of urban organic emissions. *Science*, 359(6377):760–764.

[Michoud et al., 2015] Michoud, V., Locoge, N., and Dusanter, S. (2015). Detailed characterization of a Comparative Reactivity Method (CRM) instrument for ambient OH reactivity measurements: experiments vs. modeling. In *EGU General Assembly Conference Abstracts*, page 5756.

[Miller et al., 2004] Miller, A. M., Yeung, L. Y., Kiep, A. C., and Elrod, M. J. (2004). Overall rate constant measurements of the reactions of alkene-derived hydroxyalkylperoxy radicals with nitric oxide. *Physical Chemistry Chemical Physics*, 6(13):3402–3407.

[Mollner et al., 2010] Mollner, A. K., Valluvadasan, S., Feng, L., Sprague, M. K., Okumura, M., Milligan, D. B., Bloss, W. J., Sander, S. P., Martien, P. T., Harley, R. A., et al. (2010). Rate of gas phase association of hydroxyl radical and nitrogen dioxide. *Science*, 330(6004):646–649.

[Monks, 2005] Monks, P. S. (2005). Gas-phase radical chemistry in the troposphere. *Chemical Society Reviews*, 34(5):376–395.

[Monks et al., 2015] Monks, P. S., Archibald, A., Colette, A., Cooper, O., Coyle, M., Derwent, R., Fowler, D., Granier, C., Law, K. S., Mills, G., et al. (2015). Tropospheric ozone and its precursors from the urban to the global scale from air quality to short-lived climate forcer. *Atmospheric Chemistry and Physics*, 15(15):8889–8973.

[Morino et al., 2011] Morino, Y., Ohara, T., Yokouchi, Y., and Ooki, A. (2011). Comprehensive source apportionment of volatile organic compounds using observational data, two receptor models, and an emission inventory in Tokyo metropolitan area. *Journal of Geophysical Research: Atmospheres*, 116(D2).

[Muller et al., 2018] Muller, J., Elste, T., Plass-Dülmer, C., Stange, G., Holla, R., Claude, A., Englert, J., Gilge, S., and Kubistin, D. (2018). A novel semi-direct method to measure OH reactivity by chemical ionization mass spectrometry (CIMS). *Atmospheric Measurement Techniques*, 11(7):4413–4433.

[Myriokefalitakis et al., 2008] Myriokefalitakis, S., Vrekoussis, M., Tsigaridis, K., Wittrock, F., Richter, A., Brühl, C., Volkamer, R., Burrows, J., and Kanakidou, M. (2008). The influence of natural and anthropogenic secondary sources on the glyoxal global distribution. *Atmospheric Chemistry and Physics*, 8(16):4965–4981.

[Nakashima et al., 2010] Nakashima, Y., Kamei, N., Kobayashi, S., and Kajii, Y. (2010). Total OH reactivity and VOC analyses for gasoline vehicular exhaust with a chassis dynamometer. *Atmospheric Environment*, 44(4):468–475.

[Nakashima et al., 2014] Nakashima, Y., Kato, S., Greenberg, J., Harley, P., Karl, T., Turnipseed, A., Apel, E., Guenther, A., Smith, J., and Kajii, Y. (2014). Total OH reactivity measurements in ambient air in a southern Rocky mountain ponderosa pine forest during BEACHON-SRM08 summer campaign. *Atmospheric Environment*, 85:1–8.

[Nakashima and Sadanaga, 2017] Nakashima, Y. and Sadanaga, Y. (2017). Validation of in situ measurements of atmospheric nitrous acid using incoherent broadband cavity-enhanced absorption spectroscopy. *Analytical Sciences*, 33(4):519–524.

[Nash, 1953] Nash, T. (1953). The colorimetric estimation of formaldehyde by means of the Hantzsch reaction. *Biochemical Journal*, 55(3):416–421.

[Nölscher et al., 2016] Nölscher, A. C., Yáñez-Serrano, A. M., Wolff, S., De Araujo, A. C., Lavrič, J., Kesselmeier, J., and Williams, J. (2016). Unexpected seasonality in quantity and composition of Amazon rainforest air reactivity. *Nature communications*, 7(1):1–12.

[Nuvolone et al., 2018] Nuvolone, D., Petri, D., and Voller, F. (2018). The effects of ozone on human health. *Environmental Science and Pollution Research*, 25(9):8074–8088.

[Orlando et al., 2003] Orlando, J. J., Tyndall, G. S., and Wallington, T. J. (2003). The atmospheric chemistry of alkoxy radicals. *Chemical reviews*, 103(12):4657–4690.

[Parker et al., 2011] Parker, A. E., Amédro, D., Schoemaecker, C., and Fittschen, C. (2011). OH radical reactivity measurements by FAGE. *Environmental Engineering & Management Journal (EEMJ)*, 10(1).

[Patchen et al., 2007] Patchen, A. K., Pennino, M. J., Kiep, A. C., and Elrod, M. J. (2007). Direct kinetics study of the product-forming channels of the reaction of isoprene-derived hydroxyperoxy radicals with NO. *International Journal of Chemical Kinetics*, 39(6):353–361.

[Pope et al., 2005] Pope, F. D., Smith, C. A., Davis, P. R., Shallcross, D. E., Ashfold, M. N., and Orr-Ewing, A. J. (2005). Photochemistry of formaldehyde under tropospheric conditions. *Faraday discussions*, 130:59–72.

[Pöschl et al., 2007] Pöschl, U., Rudich, Y., and Ammann, M. (2007). Kinetic model framework for aerosol and cloud surface chemistry and gas-particle interactions–Part 1: General equations, parameters, and terminology. *Atmospheric Chemistry and Physics*, 7(23):5989–6023.

[Qian et al., 2019] Qian, X., Shen, H., and Chen, Z. (2019). Characterizing summer and winter carbonyl compounds in Beijing atmosphere. *Atmospheric Environment*, 214:116845.

[Ramasamy et al., 2016] Ramasamy, S., Ida, A., Jones, C., Kato, S., Tsurumaru, H., Kishimoto, I., Kawasaki, S., Sadanaga, Y., Nakashima, Y., Nakayama, T., et al. (2016). Total oh reactivity measurement in a bvoc dominated temperate forest during a summer campaign, 2014. *Atmospheric Environment*, 131:41–54.

[Ramasamy et al., 2018] Ramasamy, S., Nagai, Y., Takeuchi, N., Yamasaki, S., Shoji, K., Ida, A., Jones, C., Tsurumaru, H., Suzuki, Y., Yoshino, A., et al. (2018). Comprehensive measurements of atmospheric OH reactivity and trace species within a suburban forest near Tokyo during AQUAS–TAMA campaign. *Atmospheric Environment*, 184:166–176.

[Reitz et al., 2002] Reitz, J., McGivern, W., Church, M., Wilson, M., and North, S. (2002). The fate of the hydroxyalkoxy radical in the OH-initiated oxidation of isoprene. *International journal of chemical kinetics*, 34(4):255–261.

[Ren et al., 2006] Ren, X., Brune, W. H., Oliger, A., Metcalf, A. R., Simpas, J. B., Shirley, T., Schwab, J. J., Bai, C., Roychowdhury, U., Li, Y., et al. (2006). OH, HO_2, and OH reactivity during the PMTACS–NY Whiteface Mountain 2002 campaign: observations and model comparison. *Journal of Geophysical Research: Atmospheres*, 111(D10).

[Ren et al., 2003a] Ren, X., Harder, H., Martinez, M., Lesher, R. L., Oliger, A., Shirley, T., Adams, J., Simpas, J. B., and Brune, W. H. (2003a). HO_x concentrations and OH reactivity observations in New York City during PMTACS-NY2001. *Atmospheric Environment*, 37(26):3627–3637.

[Ren et al., 2003b] Ren, X., Harder, H., Martinez, M., Lesher, R. L., Oliger, A., Simpas, J. B., Brune, W. H., Schwab, J. J., Demerjian, K. L., He, Y., et al. (2003b). OH and HO_2 chemistry in the urban atmosphere of New York city. *Atmospheric Environment*, 37(26):3639–3651.

[Roehl et al., 1994] Roehl, C. M., Orlando, J. J., Tyndall, G. S., Shetter, R. E., Vazquez, G. J., Cantrell, C. A., and Calvert, J. G. (1994). Temperature dependence of the quantum yields for the photolysis of NO_2 near the dissociation limit. *The Journal of Physical Chemistry*, 98(32):7837–7843.

[Sadanaga et al., 2017] Sadanaga, Y., Kawasaki, S., Tanaka, Y., Kajii, Y., and Bandow, H. (2017). New system for measuring the photochemical ozone production rate in the atmosphere. *Environmental science & technology*, 51(5):2871–2878.

[Sadanaga et al., 2005] Sadanaga, Y., Yoshino, A., Kato, S., and Kajii, Y. (2005). Measurements of OH reactivity and photochemical ozone production in the urban atmosphere. *Environmental science & technology*, 39(22):8847–8852.

[Sadanaga et al., 2004] Sadanaga, Y., Yoshino, A., Watanabe, K., Yoshioka, A., Wakazono, Y., Kanaya, Y., and Kajii, Y. (2004). Development of a measurement system of OH reactivity in the atmosphere by using a laser-induced pump and probe technique. *Review of Scientific Instruments*, 75(8):2648–2655.

[Sakamoto et al., 2019] Sakamoto, Y., Sadanaga, Y., Li, J., Matsuoka, K., Takemura, M., Fujii, T., Nakagawa, M., Kohno, N., Nakashima, Y., Sato, K., et al. (2019). Relative and Absolute Sensitivity Analysis on Ozone Production in Tsukuba, a City in Japan. *Environmental science & technology*, 53(23):13629–13635.

[Saliba et al., 2000] Saliba, N. A., Mochida, M., and Finlayson-Pitts, B. J. (2000). Laboratory studies of sources of HONO in polluted urban atmospheres. *Geophysical Research Letters*, 27(19):3229–3232.

[Sanchez et al., 2018] Sanchez, D., Jeong, D., Seco, R., Wrangham, I., Park, J.-H., Brune, W. H., Koss, A., Gilman, J., de Gouw, J., Misztal, P., et al. (2018). Intercomparison of OH and OH reactivity measurements in a high isoprene and low NO environment during the SouthernOxidant and Aerosol study. *Atmospheric Environment*, 174(227–236).

[Sato et al., 2017] Sato, K., Nakashima, Y., Morino, Y., Imamura, T., Kurokawa, J.-i., and Kajii, Y. (2017). Total OH reactivity measurements for the OH-initiated oxidation of aromatic hydrocarbons in the presence of NO_x. *Atmospheric Environment*, 171:272–278.

[Seeley et al., 1993] Seeley, J. V., Jayne, J. T., and Molina, M. J. (1993). High pressure fast-flow technique for gas phase kinetics studies. *International journal of chemical kinetics*, 25(7):571–594.

[Sheehy et al., 2010] Sheehy, P., Volkamer, R., Molina, L. T., and Molina, M. J. (2010). Oxidative capacity of the Mexico City atmosphere–Part 2: A RO_x radical cycling perspective. *Atmospheric Chemistry and Physics*, 10(14):6993–7008.

[Shirley et al., 2006] Shirley, T., Brune, W., Ren, X., Mao, J., Lesher, R., Cardenas, B., Volkamer, R., Molina, L., Molina, M. J., Lamb, B., et al. (2006). Atmospheric oxidation in the Mexico City Metropolitan Area (MCMA) during April 2003. *Atmospheric Chemistry and Physics*, 6(9):2753–2765.

[Shukla et al., 2008] Shukla, J., Misra, A., Sundar, S., and Naresh, R. (2008). Effect of rain on removal of a gaseous pollutant and two different particulate matters from the atmosphere of a city. *Mathematical and Computer Modelling*, 48(5-6):832–844.

[Sinha et al., 2008] Sinha, V., Williams, J., Crowley, J., and Lelieveld, J. (2008). The Comparative Reactivity Method–a new tool to measure total OH Reactivity in ambient air. *Atmospheric Chemistry and Physics*, 8(8):2213–2227.

[Smith et al., 2000] Smith, G. D., Molina, L. T., and Molina, M. J. (2000). Temperature Dependence of $O(^1D)$ Quantum Yields from the Photolysis of Ozone between 295 and 338 nm. *The Journal of Physical Chemistry A*, 104(39):8916–8921.

[Smith et al., 2002] Smith, G. D., Molina, L. T., and Molina, M. J. (2002). Measurement of radical quantum yields from formaldehyde photolysis between 269 and 339 nm. *The Journal of Physical Chemistry A*, 106(7):1233–1240.

[Stavrakou et al., 2009a] Stavrakou, T., Müller, J.-F., Smedt, I. D., Roozendael, M. V., Kanakidou, M., Vrekoussis, M., Wittrock, F., Richter, A., and Burrows, J. (2009a). The continental source of glyoxal estimated by the synergistic use of spaceborne measurements and inverse modelling. *Atmospheric Chemistry and Physics*, 9(21):8431–8446.

[Stavrakou et al., 2009b] Stavrakou, T., Müller, J.-F., Smedt, I. D., Roozendael, M. V., Van Der Werf, G., Giglio, L., and Guenther, A. (2009b). Global emissions of non-methane hydrocarbons deduced from sciamachy formaldehyde columns through 2003–2006. *Atmospheric Chemistry and Physics*, 9(11):3663–3679.

[Svensson et al., 1987] Svensson, R., Ljungström, E., and Lindqvist, O. (1987). Kinetics of the reaction between nitrogen dioxide and water vapour. *Atmospheric Environment*, 21(7):1529–1539.

[Takahashi et al., 1996] Takahashi, K., Matsumi, Y., and Kawasaki, M. (1996). Photodissociation Processes of Ozone in the Huggins Band at 308- 326 nm: Direct Observation of $O(^1D_2)$ and $O(^3P_j)$ products. *The Journal of Physical Chemistry*, 100(10):4084–4089.

[Talukdar et al., 1998] Talukdar, R. K., Longfellow, C. A., Gilles, M. K., and Ravishankara, A. (1998). Quantum yields of $O(^1D)$ in the photolysis of ozone between 289 and 329 nm as a function of temperature. *Geophysical Research Letters*, 25(2):143–146.

[Tan et al., 2019] Tan, Z., Lu, K., Hofzumahaus, A., Fuchs, H., Bohn, B., Holland, F., Liu, Y., Rohrer, F., Shao, M., Sun, K., et al. (2019). Experimental budgets of OH, HO_2, and

RO_2 radicals and implications for ozone formation in the Pearl River Delta in China 2014. *Atmospheric chemistry and physics*, 19(10):7129–7150.

[Tanner and Zielinska, 1994] Tanner, R. L. and Zielinska, B. (1994). Determination of the biogenic emission rates of species contributing to VOC in the San Joaquin Valley of California. *Atmospheric Environment*, 28(6):1113–1120.

[Thornton et al., 2002] Thornton, J., Wooldridge, P., Cohen, R., Martinez, M., Harder, H., Brune, W., Williams, E., Roberts, J., Fehsenfeld, F., Hall, S., et al. (2002). Ozone production rates as a function of NO_x abundances and HO_x production rates in the Nashville urban plume. *Journal of Geophysical Research: Atmospheres*, 107(D12):ACH–7.

[Tiwari et al., 2010] Tiwari, V., Hanai, Y., and Masunaga, S. (2010). Ambient levels of volatile organic compounds in the vicinity of petrochemical industrial area of Yokohama, Japan. *Air Quality, Atmosphere & Health*, 3(2):65–75.

[Trolier and Wiesenfeld, 1988] Trolier, M. and Wiesenfeld, J. R. (1988). Relative quantum yield of $O(^1D_2)$ following ozone photolysis between 275 and 325 nm. *Journal of Geophysical Research: Atmospheres*, 93(D6):7119–7124.

[Van Dingenen et al., 2009] Van Dingenen, R., Dentener, F. J., Raes, F., Krol, M. C., Emberson, L., and Cofala, J. (2009). The global impact of ozone on agricultural crop yields under current and future air quality legislation. *Atmospheric Environment*, 43(3):604–618.

[Volkamer et al., 2010] Volkamer, R., Sheehy, P., Molina, L. T., and Molina, M. J. (2010). Oxidative capacity of the Mexico City atmosphere–Part 1: A radical source perspective. *Atmospheric Chemistry and Physics*, 10(14):6969–6991.

[Volkamer et al., 2005] Volkamer, R., Spietz, P., Burrows, J., and Platt, U. (2005). High-resolution absorption cross-section of glyoxal in the UV–vis and IR spectral ranges. *Journal of Photochemistry and Photobiology A: Chemistry*, 172(1):35–46.

[Watson et al., 2001] Watson, J. G., Chow, J. C., and Fujita, E. M. (2001). Review of volatile organic compound source apportionment by chemical mass balance. *Atmospheric Environment*, 35(9):1567–1584.

[Whalley et al., 2021] Whalley, L. K., Slater, E. J., Woodward-Massey, R., Ye, C., Lee, J. D., Squires, F., Hopkins, J. R., Dunmore, R. E., Shaw, M., Hamilton, J. F., et al. (2021). Evaluating the sensitivity of radical chemistry and ozone formation to ambient VOCs and NO_x in Beijing. *Atmospheric Chemistry and Physics*, pages 2125–2147.

[Whalley et al., 2016] Whalley, L. K., Stone, D., Bandy, B., Dunmore, R., Hamilton, J. F., Hopkins, J., Lee, J. D., Lewis, A. C., and Heard, D. E. (2016). Atmospheric OH reactivity in central London: observations, model predictions and estimates of in situ ozone production. *Atmospheric Chemistry and Physics*, 16(4):2109–2122.

[Williams et al., 2016] Williams, J., Keßel, S. U., Nölscher, A. C., Yang, Y., Lee, Y., Yáñez-Serrano, A. M., Wolff, S., Kesselmeier, J., Klüpfel, T., Lelieveld, J., et al. (2016). Opposite OH reactivity and ozone cycles in the Amazon rainforest andmegacity Beijing: subversion ofbiospheric oxidant control by anthropogenic emissions. *Atmospheric Environment*, 125:112–118.

[Yang et al., 2021] Yang, X., Lu, K., Ma, X., Liu, Y., Wang, H., Hu, R., Li, X., Lou, S., Chen, S., Dong, H., et al. (2021). Observations and modeling of OH and HO_2 radicals in Chengdu, China in summer 2019. *Science of The Total Environment*, 772:144829.

[Yang et al., 2018] Yang, X., Xue, L., Wang, T., Wang, X., Gao, J., Lee, S., Blake, D. R., Chai, F., and Wang, W. (2018). Observations and explicit modeling of summertime carbonyl formation in Beijing: identification of key precursor species and their impact on atmospheric oxidation chemistry. *Journal of Geophysical Research: Atmospheres*, 123(2):1426–1440.

[Yang et al., 2017] Yang, Y., Shao, M., Keßel, S., Li, Y., Lu, K., Lu, S., Williams, J., Zhang, Y., Zeng, L., Nölscher, A. C., et al. (2017). How the OH reactivity affects the ozone production efficiency: Case studies in Beijing and Heshan, China. *Atmospheric Chemistry and Physics*, 17(11):7127–7142.

[Yoshino et al., 2012] Yoshino, A., Nakashima, Y., Miyazaki, K., Kato, S., Suthawaree, J., Shimo, N., Matsunaga, S., Chatani, S., Apel, E., Greenberg, J., et al. (2012). Air quality diagnosis from comprehensive observations of total OH reactivity and reactive trace species in urban central Tokyo. *Atmospheric Environment*, 49:51–59.

[Yoshino et al., 2006] Yoshino, A., Sadanaga, Y., Watanabe, K., Kato, S., Miyakawa, Y., Matsumoto, J., and Kajii, Y. (2006). Measurement of total OH reactivity by laser-induced pump and probe technique-comprehensive observations in the urban atmosphere of Tokyo. *Atmospheric Environment*, 40(40):7869–7881.

[Yu et al., 1999] Yu, J., Cocker, D. R., Griffin, R. J., Flagan, R. C., and Seinfeld, J. H. (1999). Gas-phase ozone oxidation of monoterpenes: Gaseous and particulate products. *Journal of Atmospheric Chemistry*, 34(2):207–258.

[Zannoni et al., 2016] Zannoni, N., Gros, V., Lanza, M., Sarda, R., Bonsang, B., Kalogridis, C., Preunkert, S., Legrand, M., Jambert, C., Boissard, C., et al. (2016). OH reactivity and concentrations of biogenic volatile organic compounds in a Mediterranean forest of downy oak trees. *Atmospheric Chemistry and Physics*, 16(3):1619–1636.

[Zhang et al., 2016] Zhang, Y., Wang, X., Wen, S., Herrmann, H., Yang, W., Huang, X., Zhang, Z., Huang, Z., He, Q., and George, C. (2016). On-road vehicle emissions of glyoxal and methylglyoxal from tunnel tests in urban Guangzhou, China. *Atmospheric Environment*, 127:55–60.

[Zhou et al., 2020] Zhou, J., Murano, K., Kohno, N., Sakamoto, Y., and Kajii, Y. (2020). Real-time quantification of the total HO_2 reactivity of ambient air and HO_2 uptake kinetics onto ambient aerosols in Kyoto (Japan). *Atmospheric Environment*, 223:117189.

[Zhou et al., 2021] Zhou, J., Sato, K., Bai, Y., Fukusaki, Y., Kousa, Y., Ramasamy, S., Takami, A., Yoshino, A., Nakayama, T., Sadanaga, Y., et al. (2021). Kinetics and impacting factors of HO_2 uptake onto submicron atmospheric aerosols during a 2019 air quality study (AQUAS) in Yokohama, japan. *Atmospheric Chemistry and Physics Discussions*, pages 1–28.

Acknowledgements

On closing this thesis, I'd like to express my sincerest gratitude to the people hereinafter.

First of all, my deepest appreciation goes to my supervisor Professor Yoshizumi Kajii, for providing me valuable guidance and rigorous discussion in research, for encouraging me in being a female researcher for career, for supporting me during my tough time of life, for his open-minded, charming, and generous personalty. I also thank Assist. Prof Yosuke Sakamoto with my warmest regard. He is always there being willing to help and having efficient discussions with me. I'm sincerely grateful to Dr. Nanase Kohno and Dr. Kentaro Murano, both of them are my indispensable mentors who provided me necessary instructions in researches and who shared me precious life experience in person. Our ex-researcher Dr. Maho Nakagawa is my important companion who inspired me with courage, confidence and kindness. I really appreciate the warm-hearted support from our secretary Ishida san, for her help in routine affairs, in my conference procedure, and business reimbursement. I'm grateful to meet my dearest Malian sister Mme. Alimata Sidibe, the coolest lab mate M. Huy Gia Pham, and all Kajii-members in Kyoto. Merci boucoup, C'est la via avec Kyoto.

Next, I would like to appreciate all the support and help from all of my co-authors in the article. On submitting the dissertation and relevant documentary. All of them have provided me prompt and kind support. I express my sincerest gratitude to Assoc. Prof Yasuhiro Sadanaga, Assoc. Prof Yoshihiro Nakashima, Dr. Kei Sato, Dr. Akinori Takami, Dr. Ayako Yoshino, Assoc. Prof Tomoki Nakayama, Assoc. Prof Shungo Kato, Dr. Jun Zhou, Mr. Kohei Matsuoka, Mr. Tomihide Fujii, and Ms. Marina Takemura.

In addition, I thank Dr. Christa Fittschen and Dr. Coralie Schoemaecker from Lille University, them shepherded me into the field of atmospheric chemistry during my Internship in 2017. I'm so grateful to meet all members from the PC2A lab and in Lille University. At the same time, I express my highest respect and gratefulness to Dr. Yasuhiro Sadanaga, Dr. Kei

Sato, Dr. Yoshihiro Nakashima, and Dr. Yukiko Fukusaki for their crucial participation in the field campaigns, for great help in my article-writing. Specifically, I owe my recognition to the National Institute for Environmental Studies for the Tsukuba-campaign and the Yokohama Environmental Studies Institute for the Yokohama-campaign.

Moreover, I give my heartfelt thanks to the BAI XIAN Asia Institute and the TOKYU Foundation for their financial support during my Master and PhD courses. Those friends I met and those things I learned from the BXAI summer program in Peking University and TOKYU monthly activities will let me benefit all my life.

At last, I extend my thanks to my family. This dissertation is a farewell gift for my grandpa. I'm so proud to be the granddaughter, the daughter, and the wife of my loves. Thanks for all their support, love, and authenticity.